https://ntrs.nasa.gov/search.jsp?R=19660027476 2020-03-24T01:57:32+00:00Z

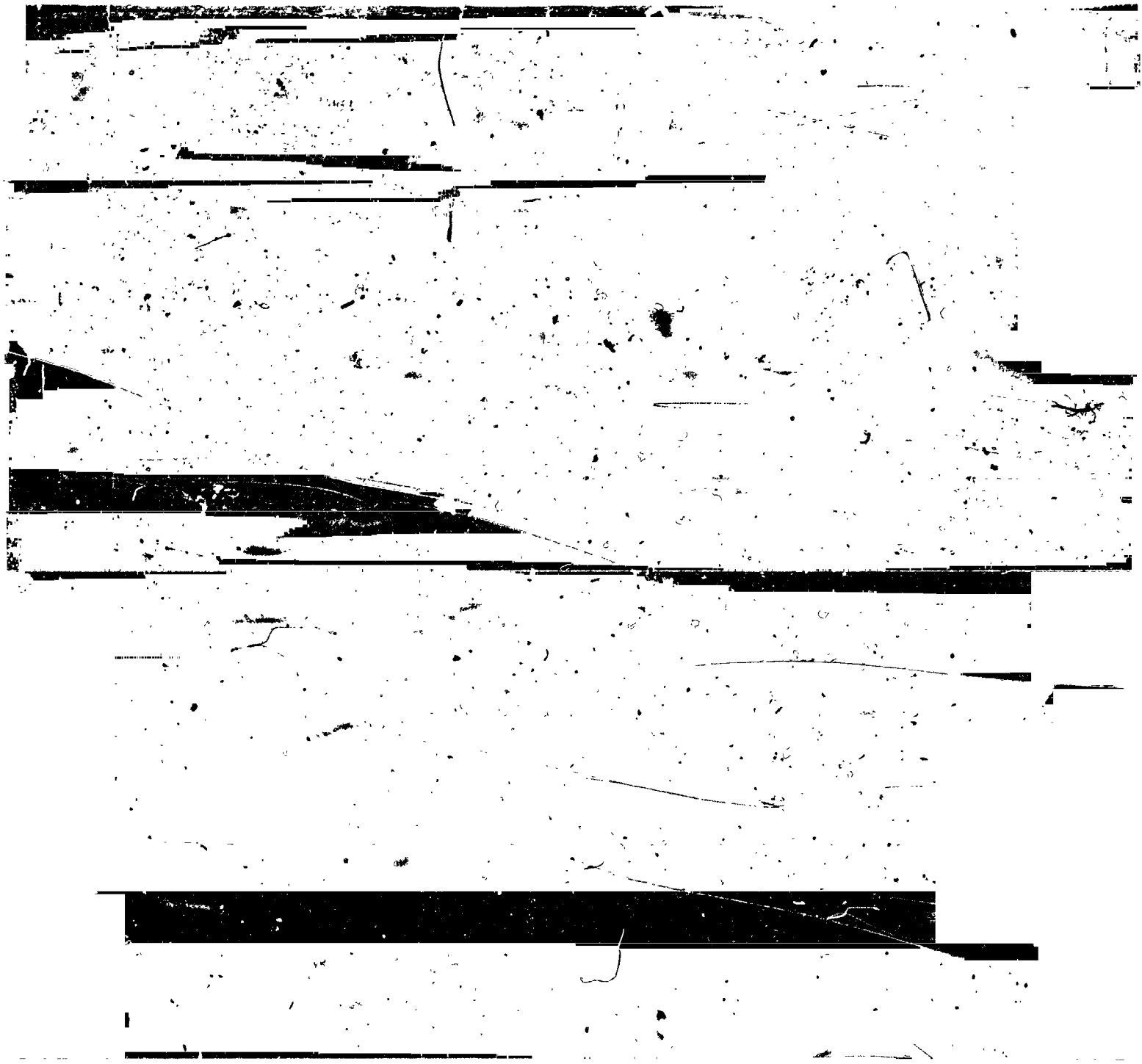

HUGHES

HUGHES AIRCRAFT COMPANY

RESEARCH ON GRAVITATIONAL MASS SENSORS

15 OCTOBER 1964 through 15 APRIL 1966

HUGHES RESEARCH LABORATORIES • MALIBU

GPO PRICE $ _____

CFSTI PRICE(S) $ _____

Hard copy (HC) 2.36

Microfiche (MF) 2.25

ff 653 July 65

FACILITY FORM 602

N66 36766 (ACCESSION NUMBER)

436 (PAGES)

CR 77933 (NASA CR OR TMX OR AD NUMBER)

N66 36778 (THRU) 1

(CODE) 2

1 (CATEGORY)

HUGHES RESEARCH LABORATORIES
Malibu, California

a division of hughes aircraft company

RESEARCH ON GRAVITATIONAL MASS SENSORS

Final Report
Contract No. NASW-1035
15 October 1964 through 15 April 1966

Robert L. Forward, Principal Investigator
Curtis C. Bell, J. Roger Morris, John M. Richardson, Larry R. Miller, and David Berman, Contributors

BLANK PAGE

TABLE OF CONTENTS

LIST OF ILLUSTRATIONS

ACKNOWLEDGMENT

The authors wish to acknowledge the patient and precise mechanical dexterity of Donald D. Boswell which enabled us to attain a high degree of accuracy on the experimental portion of this work.

BLANK PAGE

ABSTRACT

The ultimate objective of our effort on gravitational mass sensors is the development of a small, lightweight, rugged sensor to be used on lunar orbiters to measure the mass distribution of the moon and on deep space probes to measure the mass of the asteroids.

The basic concept of the gravitational mass sensor is as follows: if a system of masses and springs is rotated in the static gravitational field of a mass, the gravitational force gradient of the field will induce dynamic forces in the sensor with a frequency which is twice the rotation frequency of the sensor, while inertial effects caused by acceleration or vibration of the sensor mount will induce forces with a frequency at or near the rotational frequency. The strength and direction of the gravitational force gradient can be determined independently of the inertial forces by measuring the amplitude and phase of the vibrations induced in the sensor at the doubled frequency. Analysis shows that the sensing of the gravitational gradient will still occur even if the sensor is in free fall.

During the research program we developed sensor devices, in the form of transversely vibrating aluminum cruciform structures, which can be rapidly rotated and yet still respond to the very weak gravitational gradient fields. We have found that magnetic bearings and drives can be used to support and rotate the sensors without introducing an excessive amount of noise, and we have investigated sensor mounting concepts for isolating the gravitational gradient sensing portions of the sensors from the residual bearing noise and other external noise sources. We have developed sensor transducer, telemetering, and readout techniques which are more than adequate for the problem of reading out the small gravitationally induced motions. We have developed theoretical models of the cruciform structures which predict the behavior of ideal and nonideal sensors, and have verified the theoretical predictions with experimental data. We have measured with a stationary sensor a gravitational force of 7×10^{-12} g's while the sensor was supported in the 1 g gravitational field of the earth. This very weak force was induced in the sensor by a dynamic gravitational gradient of 1×10^{-9} sec^{-2}, (1 Eötvös unit or 3×10^{-4} of the earth's gradient). We have also experimentally demonstrated with a rotating sensor that we can measure forces down to 4×10^{-7} g's while operating in a 450 g inertial environment and a 1 g gravitational environment. The force level resulting from the earth's gravitational gradient is about one order of magnitude below this. This present noise level is not fundamental, but results because of various engineering problems — such as poor vacuum (10 μHg) and large stray magnetic fields (5 G) – associated with our prototype magnetic bearing.

The results of our experimental and theoretical work to date indicate that it is feasible to use a rotating cruciform structure to sense the gravitational gradient field of a mass. They are rugged enough to handle without caging or other precautions, and it is possible to test their operating characteristics and calibrate them with gravitational fields without requiring flight tests.

SECTION I

INTRODUCTION AND SUMMARY

A. INTRODUCTION

The basic concept of the gravitational mass sensor is as follows: if a system of masses and springs is rotated in the static gravitational field of a mass, the gravitational force gradient of the field will induce dynamic forces in the sensor with a frequency which is twice the rotation frequency of the sensor, while inertial effects due to acceleration or vibration of the sensor mount will induce forces with a frequency at or near the rotational frequency.[1-5] The strength and direction of the gravitational force gradient can be determined independently of the inertial forces by measuring the amplitude and phase of the vibrations induced in the sensor at the doubled frequency. Analysis shows that sensing of the gravitational gradient will still occur even if the sensor is in free fall.[2] Thus, by using frequency selection techniques to separate the effects of gravitation from the effects of inertia, it is possible to measure the gravitational fields of astronomical bodies from an orbiting vehicle, or to map the local gravitational field of the earth from an airplane without extensive correction for vehicle motion.

B. PROGRAM OBJECTIVES

The ultimate objective of our effort on gravitational mass sensors is the development of a small, lightweight, rugged sensor to be used on lunar orbiters to measure the mass distribution of the moon and on deep space probes to measure the mass of the asteroids.

The objective of the present research program was

1. to develop and refine experimental techniques for the measurement of gravitational and inertial fields using rotating elastic systems

2. to develop a more complete understanding of these types of sensors so that accurate predictions of sensor behavior can be made which are based on practical system configurations and measured device sensitivity.

C. SUMMARY OF PROBLEM AREAS

The major problem area can be summarized in one word — noise. This noise includes background clutter caused by external masses other than that under investigation, external electromagnetic noise and mechanical forces and vibrations, and internal thermal and electronic noise in

the sensor and amplifiers. The force of gravitational attraction is very weak, even for large masses, and every effort must be made in sensor design and operation to develop and utilize discrimination techniques which will allow the weak gravitational signal to be picked out from the background clutter and noise.

The problems of background gravitational clutter are nearly independent of the particular sensor design. It is felt that the techniques discussed in Section II-A-5 will suffice for elimination of this source of noise.

The problem of externally and internally generated electromagnetic and mechanical noise have been overcome in previous work on nonrotating gravitational sensors[6-11] (see Appendix B), and the experience gained during this work aided in the investigation of the very similar problems in rotating sensors. Some typical noise sources encountered were mechanical vibrations from motor drives and asymmetric bearings, electrostatic and magnetic pickup, turbulence of residual air in vacuum chambers, and even light pressure. Each sensor design had its own versions of these problems, and a major portion of the experimental work was spent in locating and eliminating or discriminating against these sources of extraneous noise. The noise elimination techniques invloved two levels of attack. One was to design the sensor support and rotation mechanisms so that the noise generated at a frequency which would excite the sensor was kept to a minimum level. The other was to design the sensor and mounting structure so that the noise which was generated did not reach the gravitational gradient sensing mode of the sensor.

One problem area which required special attention in the theoretical portion of the program involved the instability and cross-coupling effects which are common to mechanically rotated systems. Typical examples are given in Appendices A and E. This was a major problem at first since the only known sensor models were unstable under rotation. A stable sensor in the shape of a transversely vibrating cruciform structure was designed, but a thorough theoretical analysis (see Attachment D) was required for an understanding of the behavior of cross-coupling effects experimentally observed under rotation. Although a stable sensor design is known and understood, an unexpected problem of sensor mount instability under rotation arose. Stable mounts have been found empirically, but the behavior is still not well understood.

D. SUMMARY OF GENERAL APPROACH

The program began with parallel efforts consisting of detailed theoretical study and preliminary experimental work on sensor design. The various possible sensor configurations were investigated theoretically to determine their suitability as mass sensors under the assumed

operating conditions. Various combinations of promising sensor designs and preliminary models of sensor support and drive mechanisms were constructed and operated to verify qualitatively the sensor characteristics, develop signal readout techniques, and search for sources of instabilities and noise. No attempt was made to discover gravitational interactions at this stage.

Following the preliminary work, one of the combinations of sensor designs and sensor support and drive mechanisms was chosen as the basis for a feasibility model. It was intended that a carefully engineered version be designed and manufactured by an outside subcontractor. The remainder of the program was then to be expended in studying the feasibility model both experimentally and theoretically, locating and eliminating the sources of extraneous noise, and determining the sensitivity of the sensor design to gravitational fields.

The outside subcontractor was unable to deliver a working version of the feasibility model and it was necessary to revise the program. The preliminary design model was used for further noise and instability tests but it was not possible to use it to determine the sensitivity of the sensor to gravitational fields because of its many large noise sources. In order to measure the gravitational field sensitivity, a generator of dynamic gravitational gradient fields was constructed and the gravitational fields were used to calibrate the sensor.

E. SUMMARY OF WORK ACCOMPLISHED

The effort on the research phase of our work on gravitational mass sensors began when the completed contract was received on 26 October 1964. When the research work started, there were serious doubts concerning the physical feasibility of the concept of measuring static gravitational fields with rapidly rotating elastic systems.

The only sensor models which had been studied up to that time[1,2] would fly apart under the centrifugal forces induced by the rotation (see Appendix A).

There was no good method known for rotating the sensor while supporting it in the 1 g gravitational environment of the earth without introducing excessive vibrational noise.

Although it was obvious that an ideal sensor would not respond to anything except gravitational gradient fields, and that coupling of a nonideal sensor to external forces would be a second order effect, it was not known whether the second order noise effects could be made weaker than the first order gravitational effect. The gravitational fields which we were attempting to measure produce very small forces. The

gravitational gradient sensitivity which we wished to attain ultimately was 10^{-9} sec^{-2}, but the largest gravitational gradient signal which we could generate for test purposes was only 3×10^{-6} sec^{-2} (the gradient of the earth). The force which this gravitational gradient would produce in a typical sensor was only 10^{-3} dynes or an equivalent acceleration of 2×10^{-8} g's.

During this research program we have developed sensor designs which can resist the very strong centrifugal forces and also have the capability of measuring very weak gravitational gradient fields. We have found that magnetic bearings and drives can be used to support and rotate the sensors without introducing excessive noise, and we have investigated sensor mounting concepts for isolating the gravitational gradient sensing portions of the sensors from the residual bearing noise and other external noise sources. We have developed sensor transducer, telemetering, and readout techniques which are more than adequate for the problem of reading out the small gravitationally induced motions. We have developed theoretical models of the cruciform structures which predict the behavior of ideal and nonideal sensors, and have verified the theoretical predictions with experimental data.

With a stationary sensor we have measured a gravitational force of 7×10^{-12} g's while the sensor was supported in the 1 g gravitational field of the earth. This very weak force was induced in the sensor by a dynamic gravitational gradient of 10^{-9} sec^{-2} (1 Eötvös unit, or 3×10^{-4} times the earth's gradient). This demonstrates that the sensors and sensor electronics have the basic sensitivity to gravitational gradient fields which is needed for future applications, and that sensor calibration can be accomplished without resorting to a zero g environment.

We have also demonstrated experimentally with a rotating sensor that we can measure forces down to 4×10^{-7} g's while operating in a 450 g inertial environment and a 1 g gravitational environment. The force level resulting from the earth's gravitational gradient is about one order of magnitude below this. This present noise level is not fundamental, but results because of various problems — such as poor vacuum (10 mTorr) and large stray magnetic fields (5 G) — associated with our prototype magnetic bearing and the laboratory requirement that we operate the sensor in the 1 g gravitational field of the earth; rotate it with respect to the support, vacuum, and electronic systems; and maintain drive forces on it to overcome bearing and air friction. If the sensor were mounted in a spinning space vehicle, most of these problems would be eliminated immediately, and there is every reason to expect that the sensor would reach the measured sensitivity of the stationary sensor.

However, there are a number of obvious solutions to the present noise conditions induced by the laboratory environment; with sufficient care, it should be possible to eliminate nearly all of the problems and demonstrate the required degree of sensitivity in the laboratory without requiring flight tests to prove engineering feasibility.

1. Sensor and Mount Design

The first task in the research program was to design a sensor structure which would detect gravitational gradients but would not become unstable at the necessary rotation speeds. The original study[1,2] by R. L. Forward on the gravitational mass sensor was analyzed by C. C. Bell in a more general manner. (See Appendix A.) This analysis indicated that radially vibrating sensor structures generally are incapable of measuring the gravitational force gradient because the radial spring constant is not sufficiently strong to resist the centrifugal forces at the necessary rotation speeds.

After further study, it was found that the most promising form of sensor was a transversely vibrating cruciform shaped spring-mass system (see Fig. 1). The gradient of the gravitational field interacts with the masses on the ends of the arms and causes differential torques (Fig. 2(a)). As the sensor rotates, the direction of the applied torque varies at a frequency which is twice the rotation frequency of the sensor.[5] The spring constant in the transverse direction is chosen so that the sensor is resonant at the driving frequency of the applied differential torques. The centrifugal force on the sensor masses is resisted, in this design, by the longitudinal spring constant of the arm. The readout of the sensor vibrations is accomplished by sensing the dynamic strains in the sensor arms with barium titanate piezoelectric strain transducers. A number of different cruciform sensor heads were designed and studied experimentally. They all demonstrated the desired structural stability under high rotation speed.

The basic cruciform structure design was studied extensively, both experimentally and theoretically (see Section II-B). It was found that the sensor structure had four basic modes of vibration,[12] one, the tuning fork mode (Fig. 2(a)), which is excited by gravitational force gradients; one (Fig. 2(b)) which is excited by angular accelerations; and two degenerate modes (Fig. 2(c)) which are excited by forces applied to the sensor mount. Experimental and theoretical studies showed that if the sensor has a small central mass and is well isolated from other masses by suspension from a weak spring, the gravity gradient sensing mode is the lowest in frequency and is well separated from the other vibrational modes.[12]

To protect the gravitational gradient sensing mode from excitation by acoustic, electric, magnetic, and light gradients, and to protect the sensor electronics from electromagnetic pickup, the sensor was to be mounted inside a corotating vacuum chamber (see Fig. 1). When the sensor was mounted in the chamber, two new translational modes appeared which were lower than the gravity gradient sensing mode frequency. These modes involved the total mass of the sensor working against the spring constant of the mount and the mass of the chamber.

M 3615

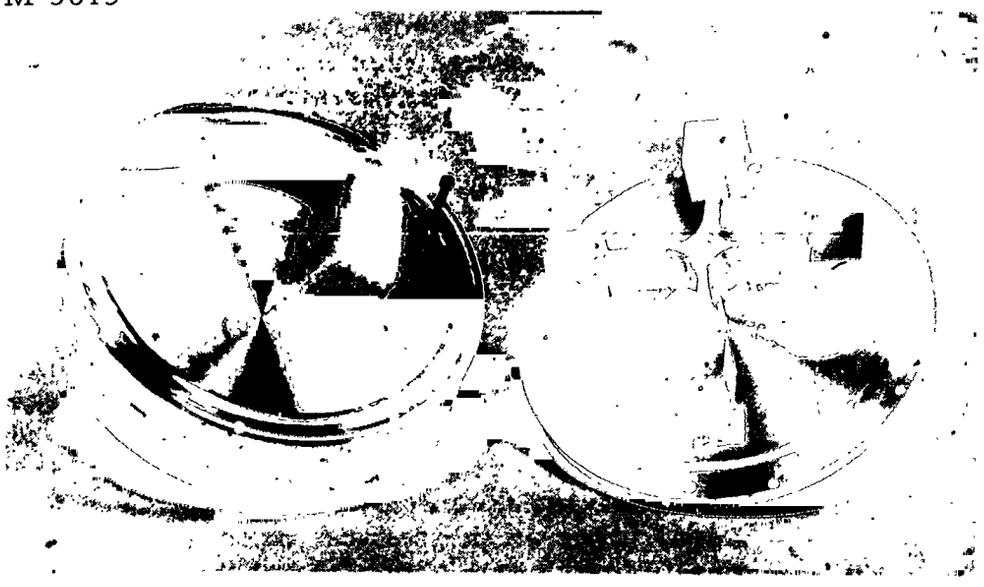

Fig. 1. Five-inch diameter cruciform gravitational mass sensor.

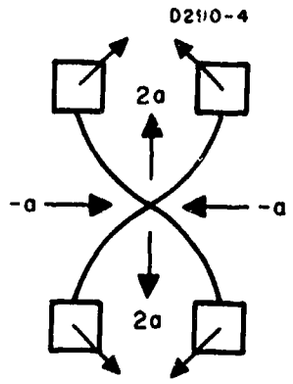

(a)

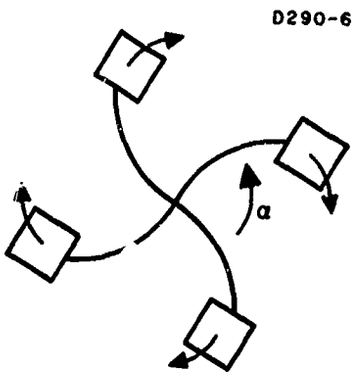

(b)

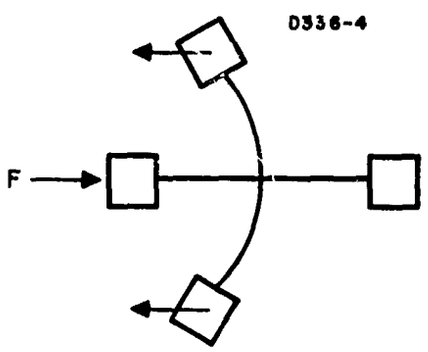

(c)

Fig. 2. Sensor vibrational modes.

Experimental studies involving a number of different mounting structures revealed a complex interaction of behavior between the two sensor translational modes and the two mount translational modes. The sensor mode frequencies depended upon the mount mode frequencies, and the two pairs of modes would split and shift in frequency when the sensor was rotated. Sometimes they would shift close enough to the gravitational gradient sensing mode that frequency separation was difficult. In addition, it was found that all the modes had a tendency to shift upward with increasing rotation speed. A detailed experimental and theoretical study to understand the vibrational mode behavior was carried out.[12] This work (presented in Attachment D) develops a mathematical model of a rotating, spring mounted, cruciform gravitational gradient sensor; equations were obtained which describe the behavior of the normal mode frequencies of the sensor-mount system as a function of the system parameters and the rotation speed. The equations agree well with the data from actual sensors and can be used to aid in the design of optimum mount-sensor structures. Based on the analysis, new sensor designs were constructed which proved to have better mode separation and less sensitivity to rotation shift.

The analysis indicated that for best frequency separation and noise isolation, the mount frequency should be low; however, most of the soft mounts investigated were unstable under rotation and allowed the cruciform to fly out under the centrifugal force until it touched the chamber walls. A stiff mount would hold the sensor, but the vibration sensitive modes would be very close to the gravitational gradient sensing mode. The sensor mount which gave the best frequency separation and still permitted operation at the desired rotational rates was an ultracentrifuge type suspension (see Fig. 3). This is suitable for the preliminary laboratory work; but it was not possible to operate the sensor in a corotating vacuum chamber with this technique, and it is obviously not suitable for all orientation operation. Other mounting techniques were studied (see Section II-C and Appendix E), but further effort must be devoted to designing a mount which is stable under rotation at all orientations and can operate in a corotating vacuum chamber, but which also allows for good sensor isolation and adequate mode separation.

With an experimentally verified sensor-mount analytical model available, it was possible to make a realistic analysis of the effect of external vibrations and sensor imperfections on system performance. This work by D. Berman[13] is given in Attachment F. The analytical model and the analysis were generalized to include the effects of differences in arm lengths, sensing masses, and spring constants; the effects of attaching the mount at a point other than at the center of mass of the sensor head; and the effects of vibrations applied to the mounting structure. The analysis shows that the gravitational gradient sensing mode of an ideal sensor responds only to gravitational gradient forces and does not respond

Fig. 3. Sensor rotating on rubber band suspension under magnetic bearing.

to externally applied forces of any type or magnitude. A nonideal sensor responds to external forces if they are dynamic vibrations with frequency components at 1Ω or 3Ω (where Ω is the rotational frequency); it does not respond to constant linear accelerations. The response occurs because a portion of the driving forces is coupled into the gravitational gradient sensing mode by the asymmetries of the sensor. This response of the sensor at 2Ω to vibrations with a frequency of 1Ω and 3Ω occurs because of the rotating coordinate system of the sensor. A transverse 1Ω vibration can be treated as a linear combination of a right- and left-handed circularly polarized vibration. The component rotating in a direction opposite to that of sensor rotation is rotating at a rate of 2Ω in the sensor coordinate system; the opposite component is rotating at the same rate as the sensor and is therefore a static force in the frame of reference of the sensor. Bearing forces resulting from unbalanced rotors fortunately belong to this second (or unobservable) class of 1Ω motions; for this reason, we have been able to measure forces of 4×10^{-7} g's even with an unbalanced rotor in a relatively crude bearing.

This analysis of a nonideal sensor gives us design data for the development of sensor-mount designs and allows us to make calculations of the second order effects of external forces on the sensor operation. The analysis indicates that to achieve low noise levels in a high vibrational level environment, it will be necessary to design both the bearing and the sensor mount with a soft restoring force, and care will have to be taken with sensor symmetry.

2. Bearings and Drives

The second major task in the program was to investigate various types of bearings and drive mechanisms and determine their suitability for the problem of smoothly rotating the sensor structures. The primary concern in the bearing was not the friction, but the generation of high frequency electromagnetic or acoustic noise which would disturb the sensor.

Preliminary models of a precision ball bearing structure, an air bearing and motor structure, and a magnetic bearing and motor structure were made and investigated (see Section II-D). The ball bearing had the obvious expected noise caused by the discrete nature of the bearing structure. The air bearing was found to have a broad band noise spectrum because of the turbulence of the air flowing through the bearing. The magnetic bearing was extremely quiet and seemed quite suitable for the purpose. The preliminary single axis model used for the tests was quite rudimentary in design and had a number of problems, such as large stray magnetic fields and poor stability.

The noise introduced by the synchronous drive motor in the magnetic bearing structure was found to be of negligible importance. The noise was barely observable when minimum drive voltages were used, and even this small amount was eliminated by the use of a phase locked asynchronous drive invented by L. R. Miller (see Section II-E).

These preliminary tests and considerations of the potential future use of the sensors indicated that a stable, three-axis magnetic bearing was required which could be operated in any orientation and which had low magnetic flux leakage at the position of the sensor. Arrangements were made with a subcontractor to construct a well designed three-axis magnetic bearing and drive for use in the feasibility model. The subcontractor was able to obtain a stable three-axis bearing; despite two contract extensions however, the subcontractor was not able to obtain a rotation speed greater than 1500 rpm. Thus, the feasibility model scheduled to be examined during the last third of the contract was never available for study, and it was necessary to use the preliminary model for study of noise and instability under rotating conditions.

3. Sensor Electronics

Although the gravitational forces which we are measuring are very weak and the corresponding motions in the sensors are very small (10^{-7} to 10^{-12}cm), the conversion of these motions into electrical voltages and the amplification and recording of the signals was not a real problem. The electronic techniques used in this program (Section II-E) closely followed some previous work on gravitational radiation antennas (see Appendix B) which had led to the development of piezoelectric transducer techniques for the measurement of motions as small as 3×10^{-14} cm.

The vibrations of the sensor arms are converted to electric signals by placing strain transducers on the arms. The units used have been Glennite SC-2, barium titante ceramic, piezoelectric transducers manufactured by Gulton Industries. These transducers have the advantages of small size (1/2 in. by 1/8 in. by 0.011 in.), high capacity (1000 pF), and high voltage to strain output (7×10^4 V/cm/cm).

The voltages from the strain transducers are typically in the low microvolt region (a sensor arm motion of 10^{-9} cm produces about 1 μV). When the sensors are being calibrated and are stationary, the voltages can be measured by any of a number of commercially available tuned amplifiers, such as the Princeton Applied Research JB-4 Lock-In Amplifier, which has a noise level of about 1 nV.

When the sensor is rotating with respect to the laboratory, it is necessary to develop techniques to feed the voltages to the recording units. A standard slip ring proved satisfactory for the initial tests. No electrical noise was found to be generated since the circuits were dry, but the brushes introduced mechanical vibrational noise.

To send the signal voltages from the rotating sensor without degrading the signal or introducing noise into the sensor, a corotating minature telemetering unit designed and built by J. R. Morris proved quite satisfactory for the noise and instability test runs.

4. Noise Sources

During our many tests with rotating and nonrotating sensors, we have discovered and investigated a number of noise sources. They include the following:

1. mechanical vibrations applied to the sensor mount which are generated by drive motors, asymmetric bearings, air turbulence, and other sources inside the sensor bearing and drive, as well as by acoustic and vibrational sources external to the sensor bearing and drive

2. differential forces applied directly to the sensor head, which arise from coupling of the sensor arms to acoustic noise, turbulence in the residual air of the vacuum chamber, magnetic eddy current forces, and light pressure

3. pickup in the transducer leads and sensor electronics from electromagnetic coupling to stray electrostatic and magnetostatic fields, and to ac induction fields from the bearings and drive motors.

The major source of noise was the mechanical vibration. The effect of the mechanical vibrations applied to the sensor mount is summarized in Section I-E-1 and is treated in more detail in Section II. In general, these noise effects were observable when we used poor bearings, stiff sensor mounts, and/or high synchronous motor drive levels. They were found to be negligible compared with other noise sources when the sensor was mounted on a soft suspension and rotated in a good (i.e., magnetic) bearing by a drive motor using a low level phase locked asynchronous drive source.

The coupling of external acoustic noise to the sensor head occurs even when the sensor is stationary, and it was found to be negligible if the sensor was operated in a moderate vacuum (10 mTorr). However, this vacuum level is not sufficiently low to prevent excitation of the sensor when it is rotated inside a stationary vacuum chamber. The differential rotation of the sensor and chamber walls creates turbulence

in the residual air in the chamber, which results in the generation of an appreciable amount of noise. The turbulence noise source will be eliminated when the sensor is operated with a corotating vacuum chamber, but this mode of operation was not attained during the noise tests because of sensor mount stability problems.

Magnetic fields can interact with the arms of the sensor either through direct coupling to any magnetic properties of the sensor arm material or through eddy current forces. The sensors were mostly made of aluminum, which is nonmagnetic. Magnetic coupling was observed with one design which was made with brass weights and stainless steel screws, but the coupling disappeared when brass screws were used. Eddy current coupling between the rotating sensor and the stray magnetic fields of the preliminary model of the magnetic bearing was found to be an appreciable source of noise. The stray fields of about 5 to 10 G cause forces in each arm of about 30 dyn, which is many orders of magnitude larger than the force (10^{-3} dyn) induced by the earth's gravitational gradient. The primary effect of the 30 dyn force is a constant torque, which is not a noise problem, but the unavoidable asymmetries in the field produce dynamic forces on the arms at the rotation frequency and its harmonics. An attempt was made to improve the magnetic flux return in the preliminary model of the magnetic bearing, but it did not succeed in appreciably reducing the stray flux levels. The solution is to use a bearing of different design and with well engineered magnetic circuitry.

During some of our test runs at low noise levels, it was found that the noise increased when the strobe light was used. This was traced to the effects of light pressure on the sensor arms. A standard penlight would produce a 1.5 to 2 times increase in sensor output when it was directed at one side of the rotating sensor. This noise source is completely eliminated when the sensor is operated inside an opaque vacuum chamber.

Pickup in the sensor electronics and the transducer leads was a continuing problem during the series of tests. It was easy to investigate and eliminate this source of noise since it did not have the resonant response of the sensor. Pickup from the electrostatic fields generated by static charges on the teflon buffer plates in the chamber was eliminated by removing the plates. The stray magnetic fields from the bearing could not be eliminated, but the pickup from the lead wires rotating through the field was reduced to acceptable levels by using twisted or shielded leads and differential preamplifiers. The induction fields at harmonics of 60 cps from the bearing were negligible compared with other noise sources and were eliminated with hum filters. The effect of the induction coupling of the drive motor fields to the sensor electronics was eliminated by using a phase locked asynchronous drive so that the frequencies of the induced voltages were considerably higher than the sensor response frequency.

The effect of these various noise sources was to place limitations on the achievable sensor sensitivity under various operating conditons. A combination of acoustic noise coupling and thermal amplifier noise was felt to be the limiting factor under the stationary conditions during calibration. The force levels measured were very low (7×10^{-12} g's) and the residual noise did not prevent us from measuring a gravitational gradient field sensitivity of the sensor (10^{-9} sec^{-2}) which was that desired for anticipated applications. A combination of residual air turbulence forces and magnetic eddy current forces coupling directly into the sensor arms was felt to be the limiting factor under rotating condtions. The force levels measured under these conditions were low (4×10^{-7} g's), but not low enough to enable the static gravitational gradient field of the earth or test objects to be seen.

5. Gravitational Calibration

One of the objectives of the research program (Section I-B) was to develop a complete understanding of these sensors, including a measurement of their sensitivity to gravitational gradient fields, so that accurate predictions of sensor behavior could be made for future applications which were based on measured device parameters rather than theoretical extrapolations. Since the preliminary design model of the magnetic bearing was too noisy to use for measurement of the gravitational sensitivity of the sensor, it was necessary to construct a generator of dynamic gravitational gradient fields and use these fields to calibrate the sensor[14] (see Section II-G and Attachment E).

The gravitational gradient field generator is a flat aluminum cylinder 14 cm in diameter, with four holes which can be filled with slugs of different density to create a rotating mass quadrupole moment. The generator was mounted on the air bearing supported motor originally used to rotate a sensor chamber for bearing noise tests (see Fig. 4), and rotated at a nominal speed of 44 rps (2640 rpm) which was half the sensor response frequency. Because of the bisymmetric mass distribution, the dynamic gravitational gradient fields generated were at a frequency of 88 Hz, or twice the rotation rate.

The sensors to be tested were hung from a spring mount inside their evacuated vacuum chambers, the chambers suspended from the ceiling and the generator placed underneath. An iron shield plate and spring mounting of the generator sufficed for acoustic and magnetic isolation since most of the nongravitationional noises were generated at the rotation frequency rather than the gravitational gradient frequency. Data were taken with four different mass distributions varying from 0 to 1000 g and separation distances varying from 4.8 to 15 cm. The excellent agreement of the data ($\pm 3\%$) with the theoretical predictions for changes in field strength and phase, and generator-sensor separtion distance, rules out any appreciable nongravitational coupling.

M4181

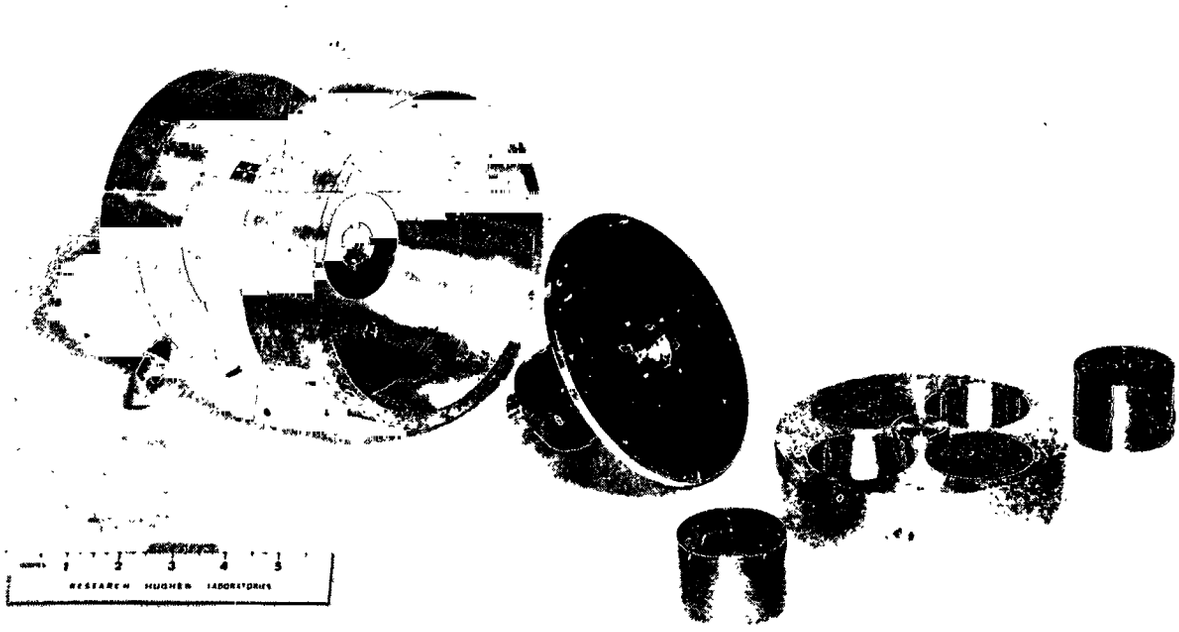

Fig. 4. Dynamic gravitational gradient field generator.

The minimum gravitational gradient field strength measured was 10^{-9} sec^{-2} (1 Eötvös unit or 3×10^{-4} of the earth's gradient). The equivalent gravitational force exerted on each of the sensor arms by this field was 2.4×10^{-7} dynes or an equivalent acceleration of 7×10^{-12} g's.

F. SUMMARY OF REMAINING PROBLEM AREAS

During the research phase of our work we have isolated a number of problem areas which need more detailed engineering investigation. We must

1. develop a stable, driftless, well-engineered, three-axis magnetic suspension with low magnetic flux leakage
2. thoroughly investigate sensor mounting techniques
3. improve the sensor design using the design data developed during the re earch phase
4. study the effects of sensor design errors on the coupling of external noises into the gravitational gradient sensing mode
5. continue study of noise sources under rotating conditions.

SECTION II

EXPERIMENTAL AND THEORETICAL PROGRAM

The experimental and theoretical work carried out on our program on gravitational mass sensors is presented in this section. Together with the appendices and the attachments to this report, it represents a complete discussion of the status of the program to date and includes all the relevant material in the quarterly progress reports and the publications prior to the work on the contract.

A. THEORY OF GRAVITATIONAL GRADIENT SENSORS

1. Introduction

In order to measure the mass of an object at a distance,[1-5] when both the object and the sensor are in free fall, and in order to determine the attitude of a spacecraft in orbit around the earth without using external referents,[15-27] it is necessary to develop force measuring instruments which will allow us to distinguish between the effects of gravitational forces and inertial reaction forces. At first glance it might be assumed that Einstein's principle of equivalence might preclude such a differentiation, since basically it states that there is no way to distinguish between a gravitational field and an accelerated reference frame. However, the principle of equivalence is valid only for uniform gravitational fields or an infinitesimal region of the reference frame.[28] The principle of equivalence can be applied over a larger region only when the gravitational field is uniform over that region. In reality, however, the gravitational field of a mass is far from uniform. Real gravitational fields have gradients in their vector field patterns. Thus, gradient sensors such as differential accelerometers can distinguish between real gravitational fields and inertial effects due to accelerated reference frames.

For almost all real situations, however, the problem is not one of a fundamental nature; rather, it is a practical one of measuring the very weak gravitational force field in the presence of the much larger inertial force fields. In order to do this, it is necessary to develop a class of sensors capable of using the differences between gravitational and inertial forces in such a way that they ignore the large inertial fields and respond only to the gravitational field.

An analysis of this problem has been carried out,[4] and is presented as Attachment B to this report. The separation of the gravitational effects from the inertial effects is accomplished by

using the physical fact that the various force fields differ in their gradient or tensor characteristics and the mathematical fact that a tensor of n^{th} rank, when examined in the rotating reference frame of a sensor, will be found to produce time-varying signals which are at n times the rotational frequency of the sensor. Because of the detailed analysis in Attachment B, only a short summary of the theory will be presented here.

2. Characteristics of Gravitational and Inertial Fields

a. Linear Acceleration Inertial Field

The linear acceleration of a vehicle of mass m by an applied force F creates a uniform inertial field in the frame of reference of the vehicle which has purely vector properties and no spatial gradients (see Fig. 5):

$$a_i = \frac{1}{m} F_i = \frac{1}{m} (F_x, F_y, F_z) . \qquad (1)$$

The accelerating force field can be detected by any force or acceleration measuring device, such as an accelerometer. Since it has no gradients, it is not sensed by a well built differential force sensor.

b. Angular Velocity Inertial Field

If the vehicle using the sensor is rotating, the rotation sets up a cylindrically symmetric inertial field (see Fig. 6).

$$a_j = \Omega^2 d_j = (\Omega^2 x, \Omega^2 y, 0) \qquad (2)$$

where Ω is the angular velocity and d is the position vector from the axis of rotation. (For purposes of clarity, we have chosen the rotation axis along the z axis.) This acceleration field has not only a radial gradient resulting from the change in the magnitude of the acceleration vector with a change in radius, but also a tangential gradient caused by the change in direction of the acceleration vector with a change in angle.

The resultant acceleration gradient field is a tensor field given by

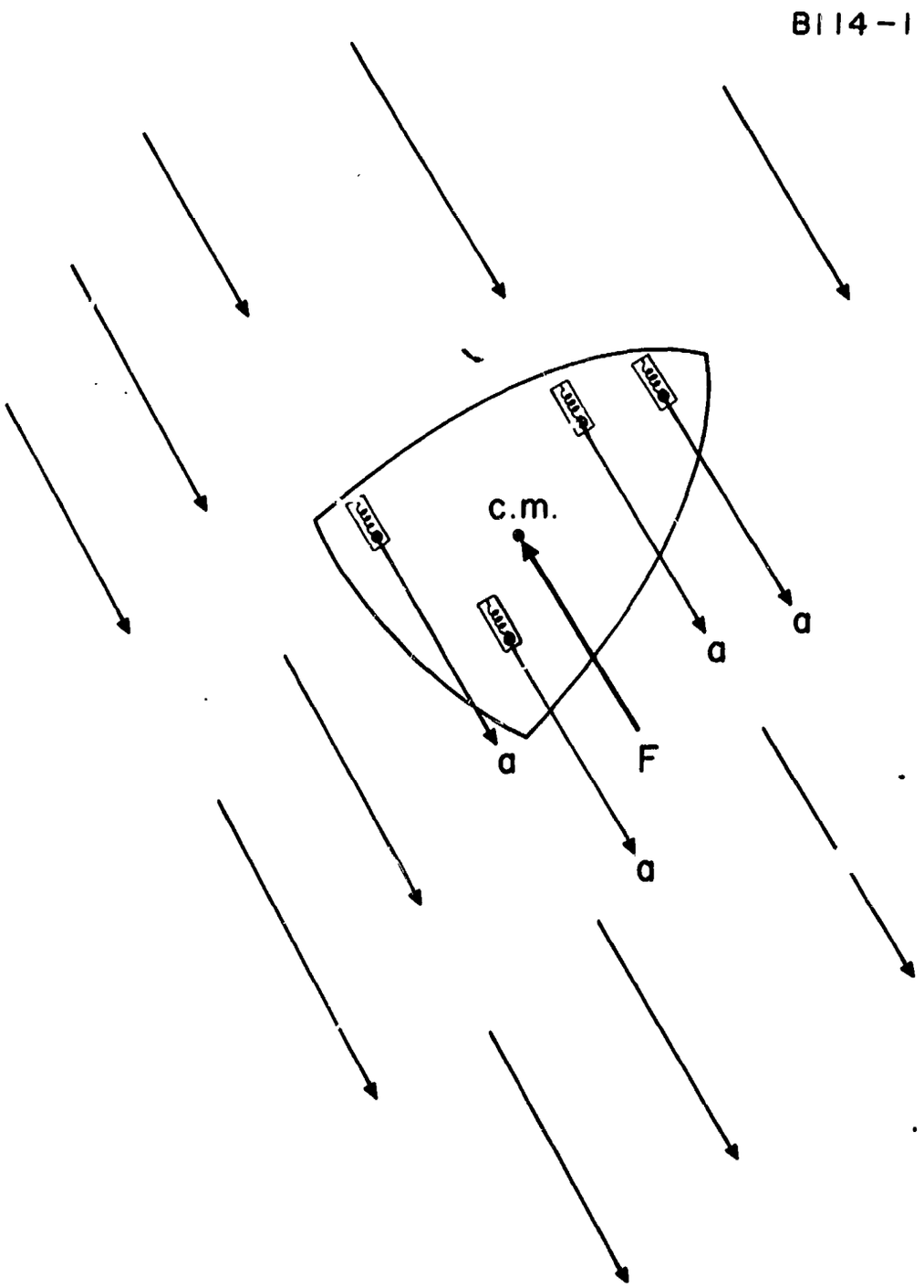

Fig. 5. The uniform inertial reaction acceleration field created by a force.

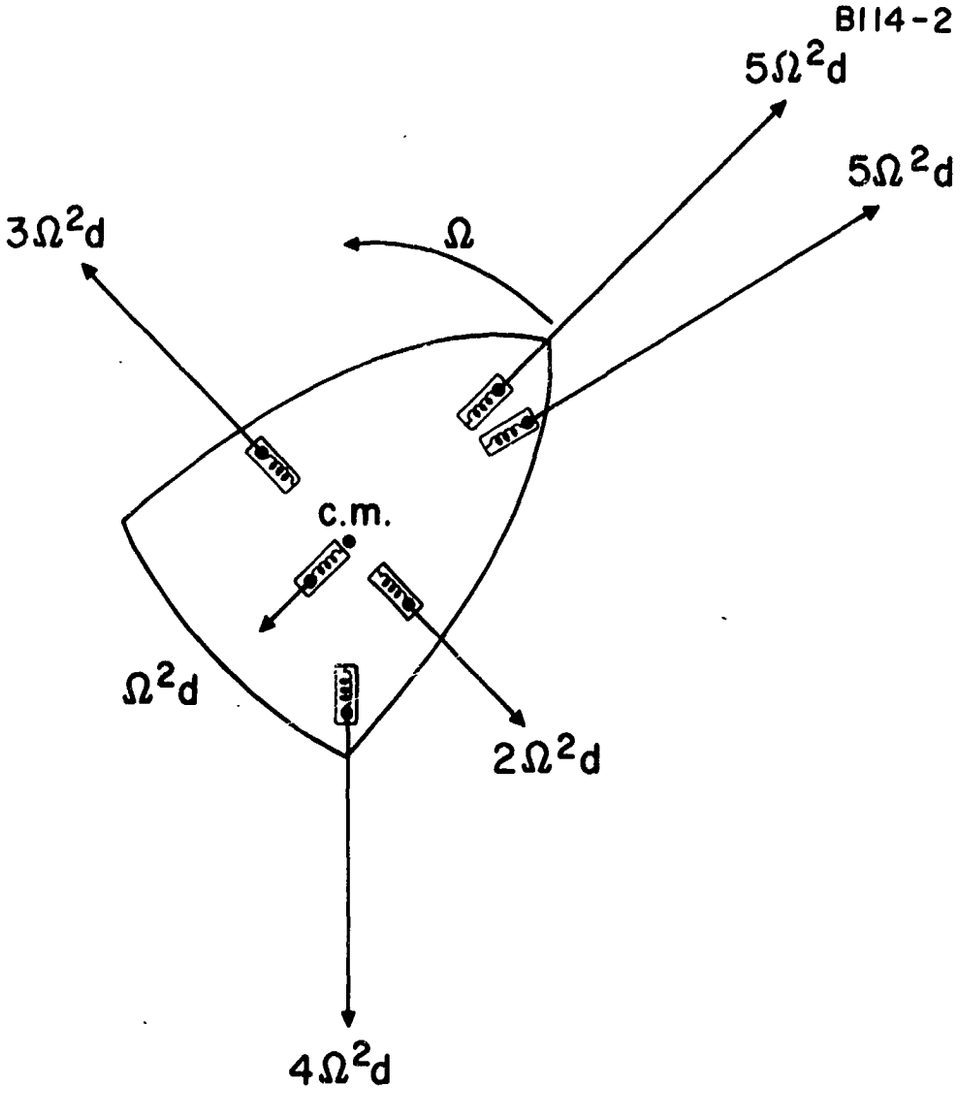

Fig. 6. The cylindrically symmetric acceleration field created by angular velocity.

$$R_{ij} = \nabla_i a_j = \begin{pmatrix} \Omega^2 & 0 & 0 \\ 0 & \Omega^2 & 0 \\ 0 & 0 & 0 \end{pmatrix}. \qquad (3)$$

This gradient is uniform and has no higher order gradients.

c. Angular Acceleration Inertial Field

If there is angular acceleration in addition to rotation about the z axis, there will be torque forces in addition to the centrifugal forces (see Fig. 7):

$$a_k = \dot{\Omega}_i \times d_j = (-\dot{\Omega}y, \dot{\Omega}x, 0) \qquad (4)$$

where $\dot{\Omega}$ is the angular acceleration and d is the position vector from the axis of rotation.

The gradient of this acceleration field is given by

$$T_{ik} = \nabla_i a_k = \begin{pmatrix} 0 & -\dot{\Omega} & 0 \\ \dot{\Omega} & 0 & 0 \\ 0 & 0 & 0 \end{pmatrix}. \qquad (5)$$

This gradient is uniform and has no higher order gradients.

d. Gravitational Field

When a gravitational field of a mass M at a distance R acts on a vehicle, it sets up a spherically symmetric acceleration field.

$$a_g = -\frac{1}{m} \nabla_g \phi \approx -\frac{GM}{R^2} \qquad (6)$$

where $\phi = -GMm/R$ is the gravitational potential.

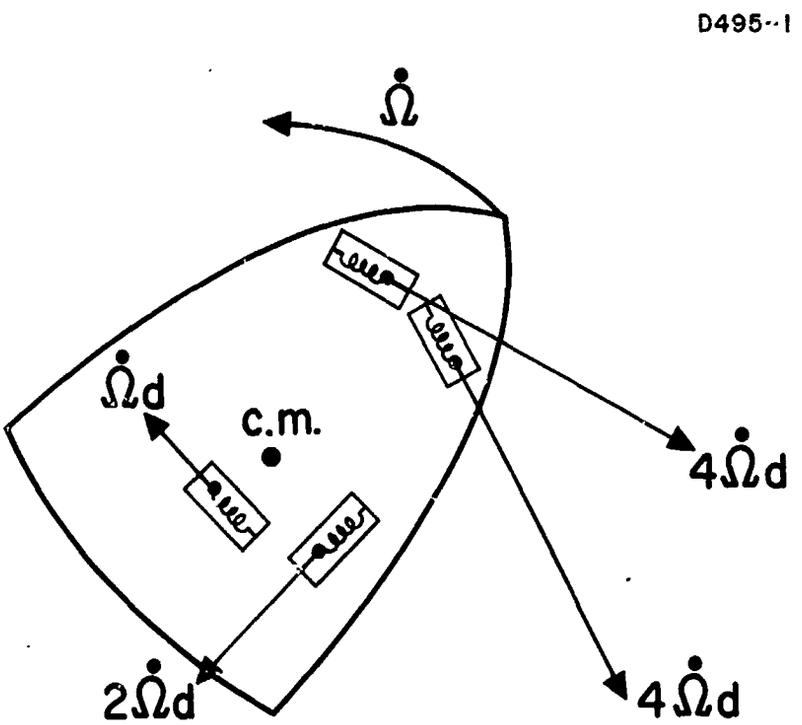

Fig. 7. The cylindrically symmetric torsional field created by angular acceleration.

If the object under measurement is in free fall with respect to the sensor, the only measurable components of the gravitational field are the gravitational force gradients which are the components of a symmetric tensor.

$$\Gamma_{ij} = \nabla_i \nabla_j \frac{\phi}{m} \approx \frac{GM}{R^3} \begin{pmatrix} 2 & 0 & 0 \\ 0 & -1 & 0 \\ 0 & 0 & -1 \end{pmatrix} \qquad (7)$$

Unlike the rotational inertial fields which have uniform force gradients and therefore no higher order gradients, there is essentially no limit to the number of higher gravitational gradients that can be measured, provided the sensor is close enough and the object under investigation is massive enough that the interaction overcomes the sensor noise. These higher order gradients are complicated tensors of high rank, and sophisticated techniques and sensors may be able to obtain a great deal of information from them. Basically they have the form

$$T_{ab\ldots n} = \frac{1}{m} \frac{\partial^n \phi}{\partial x^a \partial x^b \ldots \partial x^n} \approx \frac{GM}{R^n} . \qquad (8)$$

e. General Gravitational and Inertial Gradient Field

The general form for the gradient tensor, which includes all combinations of gravitational and inertial force gradients, is given by

$$G_{ij} = \begin{pmatrix} \Gamma_{xx} + \Omega_y^2 + \Omega_z^2 & \Gamma_{xy} - \dot{\Omega}_z - \Omega_x\Omega_y & \Gamma_{xz} + \dot{\Omega}_y - \Omega_x\Omega_z \\ \Gamma_{yx} + \dot{\Omega}_z - \Omega_y\Omega_x & \Gamma_{yy} + \Omega_z^2 + \Omega_x^2 & \Gamma_{yz} - \dot{\Omega}_x - \Omega_y\Omega_z \\ \Gamma_{zx} - \dot{\Omega}_y - \Omega_z\Omega_x & \Gamma_{zy} + \dot{\Omega}_x - \Omega_z\Omega_y & \Gamma_{zz} + \Omega_x^2 + \Omega_y^2 \end{pmatrix} \qquad (9)$$

where Γ_{ij} is the gravitational force gradient which causes a force in the i direction on an object displaced in the j direction, Ω_k is the rate of rotation about the k axis and Ω_i is the angular acceleration about the i axis.

This equation for the general form of the gradient tensor indicates that although there are no gradients resulting from linear acceleration, the gradients caused by angular velocity and angular acceleration can interfere with the measurement of the gravitational gradients.

3. Differentiation of Gravitational and Inertial Fields

As is shown above and in Attachment B, gravitational and inertial effects have different tensor characteristics. The inertial field created by acceleration is a uniform vector field and has no gradient, while the inertial fields created by rotation have uniform cylindrically symmetric tensor gradients but none of higher order. The gravitational field created by a mass is highly nonuniform, with essentially no limit to the number of higher order gradients. These differences make it theoretically possible to measure independently gravitation, rotation, and acceleration effects; to do so, some form of differential force sensor with tensor response characteristics must be used.

The differential force sensors discussed in the literature[15-26] usually consist of a spaced pair of low level accelerometers on the ends of a rod of length ℓ. In this form, the tension, compression, or torque caused by the gradient will cause the accelerometers to indicate an acceleration given by

$$a_i = \sum_{j=1}^{3} G_{ij} \ell_j \qquad (10)$$

where we have assumed that the rod is lying in the $\pm j$ direction and the accelerometers are oriented in the $\pm i$ direction. The output of a single accelerometer will also contain its response to a linear acceleration (see Fig. 8). To make a gradiometer, the outputs of the pairs of accelerometers are interconnected so that the acceleration is cancelled out, leaving only the differential or gradient forces.

The gradient forces that we are discussing are very weak for typical sensors. A gradient of 10^{-9} sec^{-2} would introduce accelerations of 3×10^{-8} cm/sec^2 (3×10^{-11} g's) in the ends of a 1 ft. long (30 cm) sensor. A very good accelerometer is capable of a linearity of only one part in 10^5, and the outputs of two accelerometers cannot be matched even to this degree of accuracy. Thus, unless it can be assured that the accelerations resulting from rotations, drag, and other forces are kept extremely low, it is not feasible to make gravitational gradiometers out of differentially balanced force sensors.

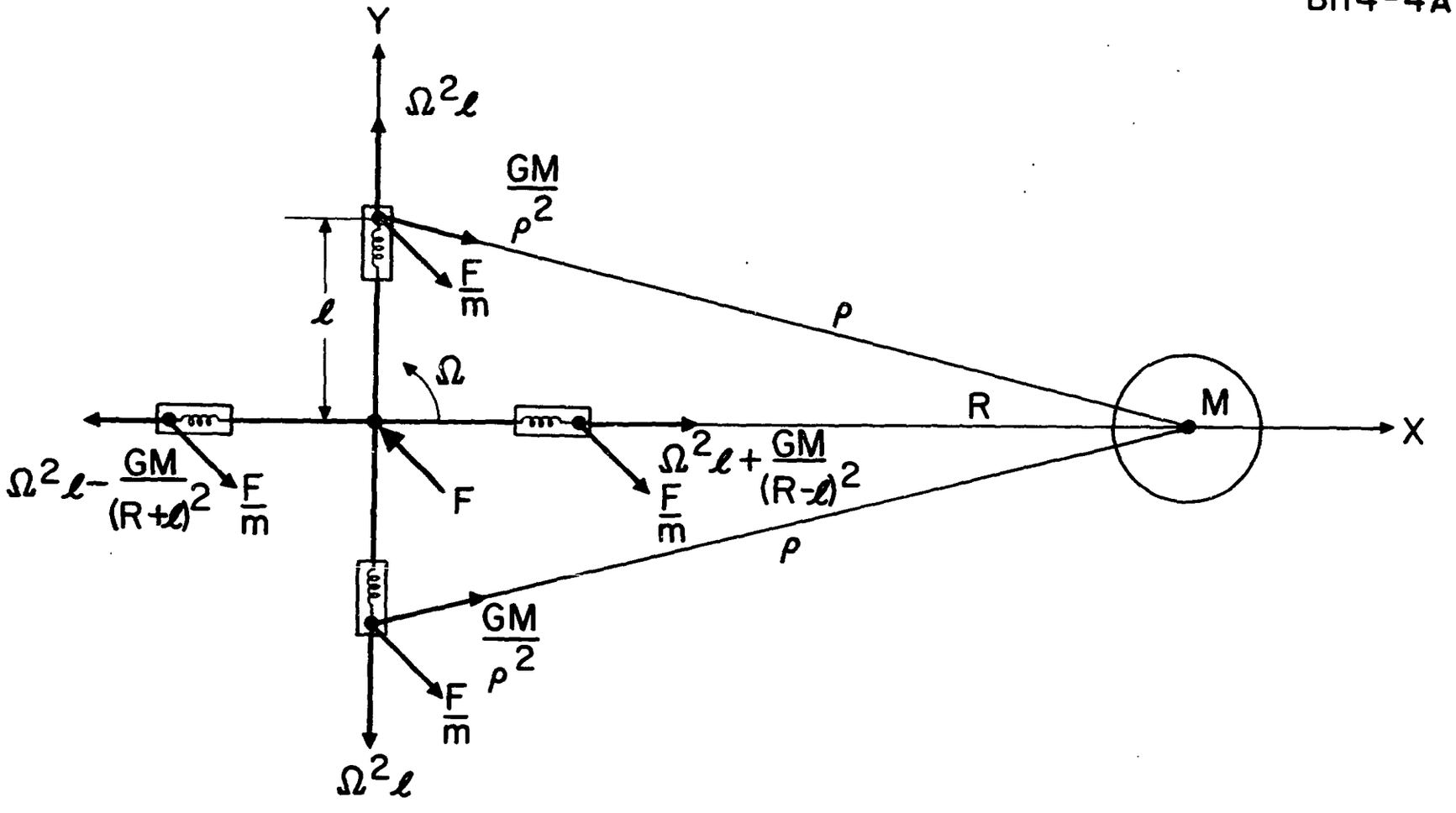

Fig. 8. Differential force sensor.

In order to make a "true" gradiometer, it is necessary to design the interaction between the spaced pairs of proof masses so that they are strongly coupled together and share the same transducer outputs. One example of such a device which is presently under investigation by the American Bosch Arma Corporation under NASA Contract NASW-1328 is the vibrating string gradiometer[27] (see Fig. 9). This is a static device consisting of two proof masses held at opposite ends of a tube (typically 1 ft. long) by means of cross axis supports and tension springs. The two proof masses share the same vibrating string transducer element. The string, which is under tension, is excited by an electromagnetic feedback loop so that it vibrates continually at its resonant frequency. The frequency of the string is proportional to the square root of the tension in the string. If the gradiometer chassis undergoes acceleration during operation, the two masses do not change their relative position, the tension of the vibrating string does not change, and the transducer frequency does not change. If the gradiometer is subjected to a gradient field, there will be differential forces applied to the two proof masses, causing them to move either closer together or farther apart, changing the tension of the string. The amount of frequency change of the string indicates the strength of the gradient.

Various versions of the basic vibrating string gradiometer design have been studied. The cross product designs which measure the torsional aspects of the gradient field (the off diagonal or xy, yz, zx terms in eq. (9)) were not considered feasible because the vibrating string gradiometer designs are sensitive to the gradients resulting from angular acceleration Ω. Their proposed designs are in-line gradiometers which measure the diagonal components of the gradient tensor.

In addition to being sensitive to rotational gradients, as are all gradiometers, the static gradiometer is also sensitive to thermal effects and cross axis coupling (which in essence implies that there is still some residual coupling to acceleration fields). The cross-axis coupling is such that it is difficult to calibrate these devices with gravitational gradient fields in the earth's 1 g acceleration environment, and a zero g flight test will be required to demonstrate engineering feasibility.

A more promising technique is a dynamic one.[1-5, 21, 25] By rotation of specially designed differential force sensors, the static spatial variations of the fields can be transformed into temporal variations in the sensor. Even though the sensor is not perfectly balanced, and has a residual response to accelerations, the various acceleration and gradient effects come out at different frequencies,[2-4] because of the rotational properties of tensors.

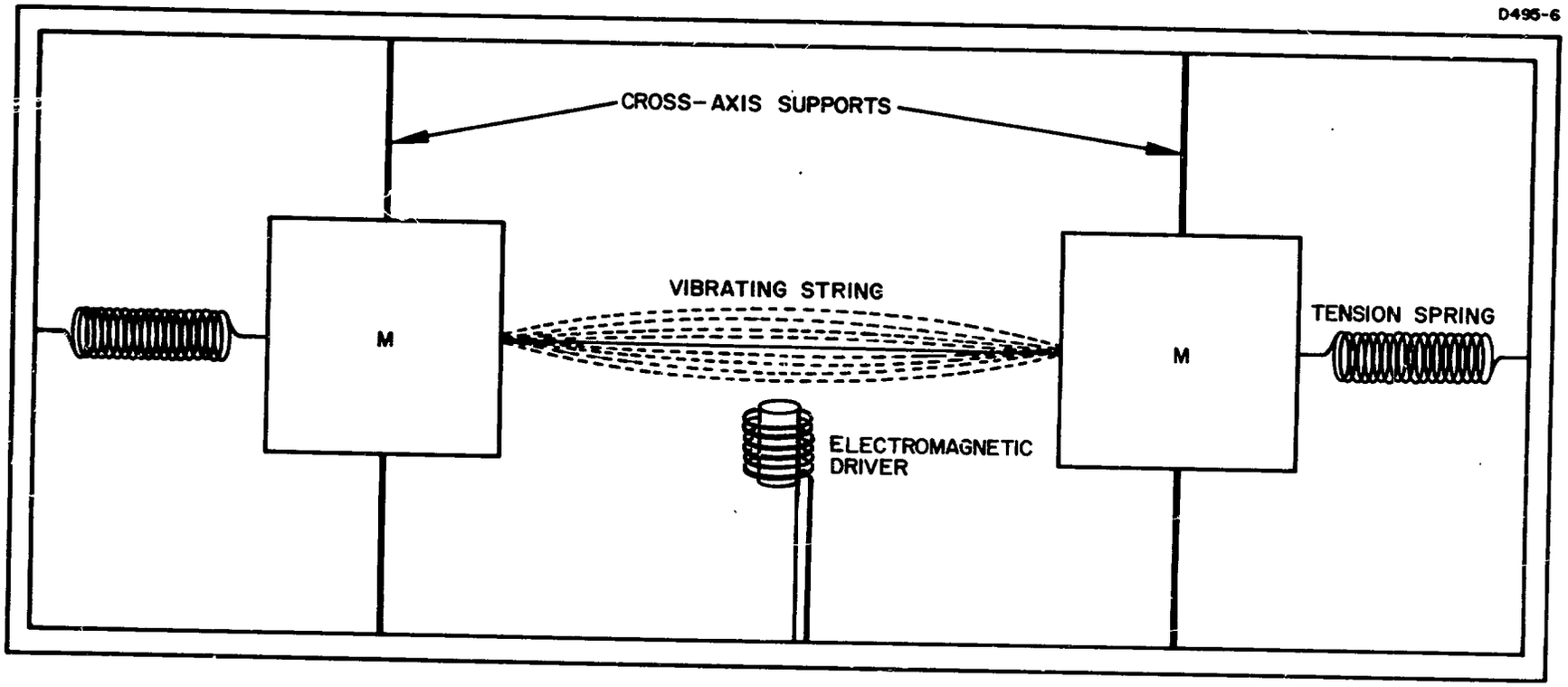

Fig. 9. Vibrating string gradiometer.

The basic concept is that forces are vectors (tensors of first rank), the gradients of forces are tensors of second rank, and higher order gradients are higher rank tensors. In general, the components of a tensor of n^{th} rank, when examined in the rotating reference frame of a sensor, will be found to have time-varying coefficients which are at n times the rotational frequency of the sensor.[4]

4. Rotating Gravitational Gradient Sensors

As was pointed out in the preceding sections, the gravitational field of a mass creates a pattern of tensions and compressions in space which differs from that of the inertial fields resulting from rotations or external forces. We have developed sensors which transform these different spatial patterns into different frequency components.

The basic gravitational sensor configuration being studied at Hughes[1-5] consists of a mass-spring system with one or more vibrational modes. The system is rotated at some subharmonic of the vibrational mode. If a nonuniform gravitational field is present, the differential forces on the sensor resulting from the gradients of the gravitational field will excite the vibrational modes of the sensor structure. In the schematic of Fig. 10, the gradient of the gravitational field excites vibrations at twice the rotation frequency of the sensor. Similar devices have been proposed by Diesel,[21-25] Kalmus,[29] and Fitzgerald,[30-31] although only the device proposed by Diesel was designed to measure the gradient of the force rather than the gravitational force itself. The other proposed devices[29-31] are similar in construction to the Hughes sensors, but in operation are more similar to the weak spring type of static accelerometer or graviometer. In this class of device, the system is rotated at its "critical speed" so that the restoring forces of the spring are exactly counterbalanced by centrifugal forces. The system is then in unstable equilibrium and a small gravitationally induced force or any other force will cause a large displacement. The Hughes sensors are operated below the "critical speed." The difference between the two types of devices is illustrated by the discussions of Den Hartog.[32]

The basic concept behind the operation of these sensors is an old one in the field of electronics, the concept of chopping. This is used extensively in dc amplifiers, where the low level dc signal is chopped, transformed into an ac signal, and then amplified and measured by phase sensitive detectors. In the gravitational sensors, the chopping of the static gravitational field is accomplished by physically rotating the sensor so that its response to the gravitational field varies with time.

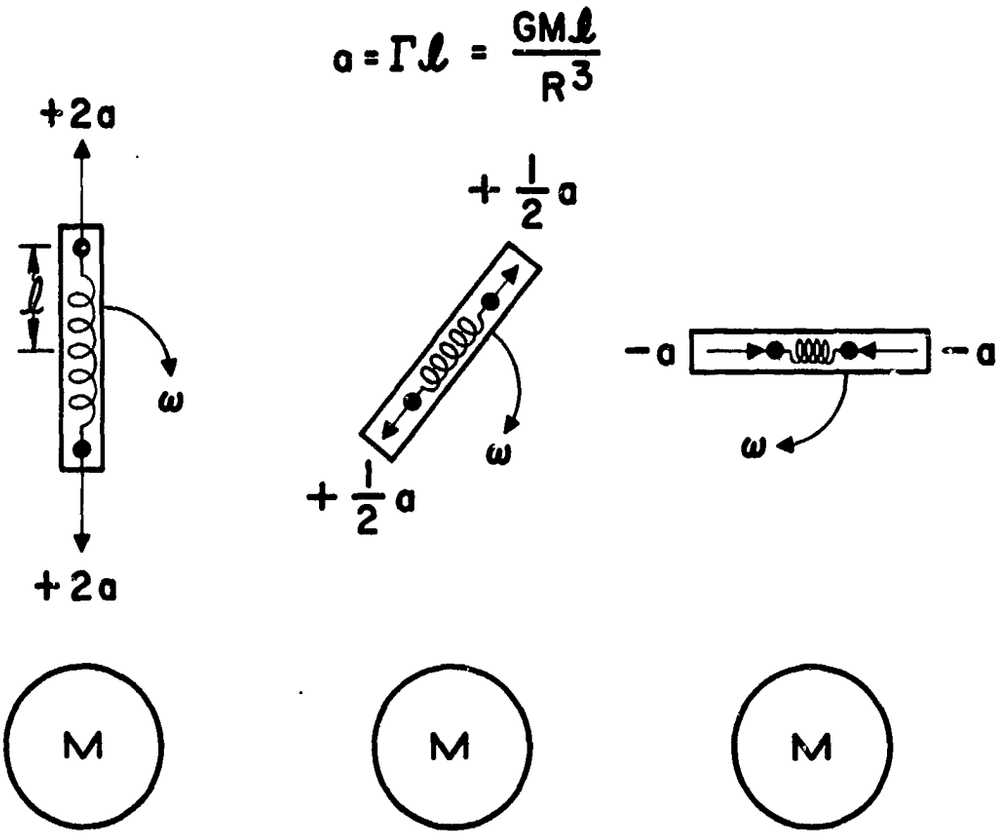

Fig. 10. Response of rotating gradient sensor to gravity gradients.

The conversion of a static gravitational interaction into a dynamic gravitational interaction occurs because the rotation of the sensor creates a rotating reference system. From the viewpoint of the sensor, the mass to be measured is somehow whirling around the sensor, attracting it first one way and then the other.

The possible sensor configurations which have been identified fall into four general classes (see Fig. 11). One has its effective length along the rotational axis and vibrates perpendicular to the rotational axis (Fig. 11(a)) and three have their effective length rotated in the plane at right angles to the rotational axis, with their vibrations either radially in the rotational plane (Fig. 11 (b)), tangentially in the rotational plane (Fig. 11 (c)), or at a right angle to the rotational plane (Fig. 11 (d)).

The case of Fig. 11(a) is common in the field of mechanics where it is known that a problem of gravitationally driven vibration exists when a drive shaft is rotated at one-half its natural vibrational frequency.[32] For our application, these gravitationally induced vibrations are not a problem, but the desired result. The case of Fig. 11(a) is sensitive to torsional gradients effective along the rotational axis.

The case of Fig. 11(b) has the characteristic that it should measure the difference between the radial gradients in the plane of rotation. A careful analysis (see Appendix A) showed, however, that because the same spring is used to generate the centripetal force and the vibrational restoring force, if we attempt to design the sensor to detect the gravitational force gradient of an object, the spring will not have enough strength to resist the centrifugal force. The sensor can be used to measure the higher order gradients, however.

The case of Fig. 11(c) has been analyzed by V. Chobotov.[33] Here again, the gravitationally induced vibrations were considered a problem. This type of sensor measures the difference between the torsional gradients in the plane of rotation.

The case of Fig. 11(d) has the characteristics that it will measure the difference between the torsional gradients perpendicular to the plane of rotation. The coupling of the centrifugal force to the vibrational system is much weaker in this case since a vibrational response does not change the angular momentum about the rotational axis.

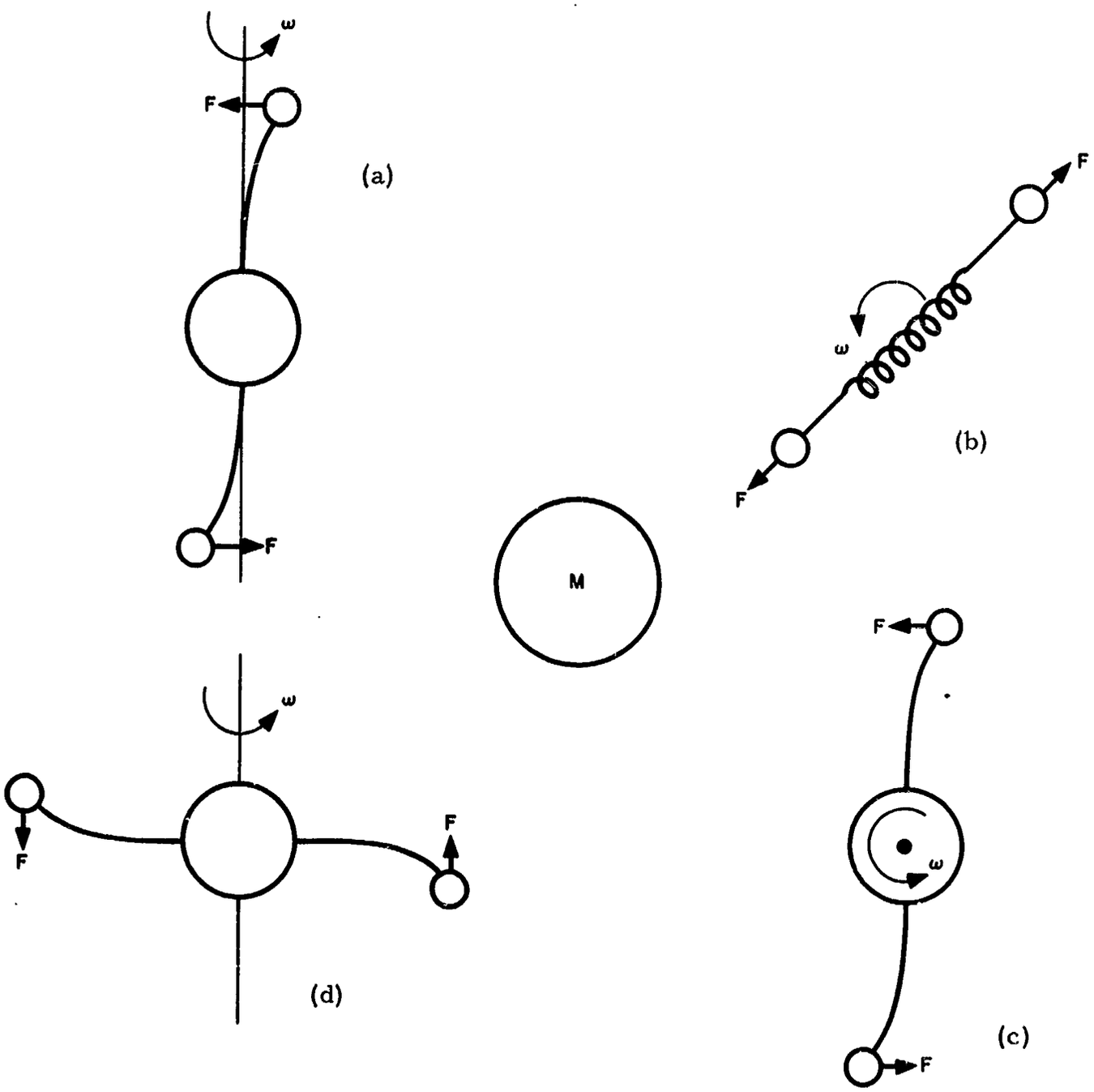

Fig. 11. Possible sensor configurations.

The most promising sensor configuration is that shown in Fig. 12. It is a variation of the type shown in Fig. 11(c) and consists of four masses on the end of four tangentially vibrating arms. The gradient of the gravitational field causes differential torques on the arms. As the sensor rotates, the direction of the applied differential torque varies at a frequency which is twice the rotation frequency of the sensor, and a phase which is related to the direction to the exciting mass (see Fig. 13). This sensor is discussed further in Section II-B.

5. Fundamental Noise Limitations

Certain noise sources apply to all gravitational gradient sensors. They are independent of engineering errors in sensor design, although different types of sensors may respond differently. These fundamental noise sources are thermal noise in the sensor, background clutter caused by gravitational gradients from masses other than that under observation, and clutter caused by rotational gradients from rotation of the sensor by the using vehicle.

a. Thermal Noise

The fundamental sensitivity of any sensor is determined by the thermal noise limitation. In practice, this limit can never be reached, but many systems can approach it very closely. This is especially true of low frequency devices, since the electronics available in this region has been highly developed and will contribute only a few degrees of extra equivalent noise temperature to the physical temperature of the sensor.

Because this basic limit is dependent upon energy considerations, its calculation depends only upon very general parameters of the sensor, such as its temperature, mass, effective length, and time of integration. The results can then be applied to all sensors, regardless of their detailed design. The basic formula states that the signal-to-noise ratio is given by the ratio of the signal energy stored in the sensor to the thermal energy (kT) present in the sensor. In a dynamic case, the signal energy is stored partly in the kinetic energy and partly in the potential energy of the spring.

$$S = KE + PE = \frac{1}{2} m\dot{\xi}^2 + \frac{1}{2} K\xi^2 \qquad (11)$$

where we assume that the amplitude of the spring extension due to the signal forces is given by[2]

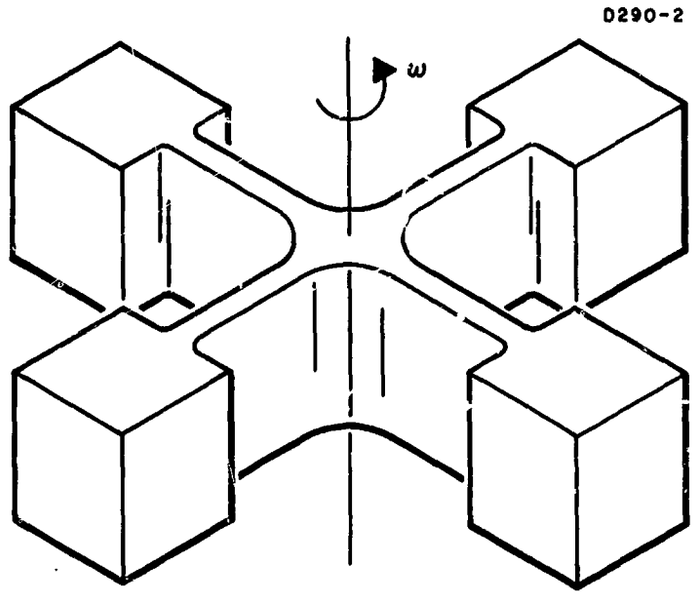

Fig. 12. Cruciform gravitational mass sensor.

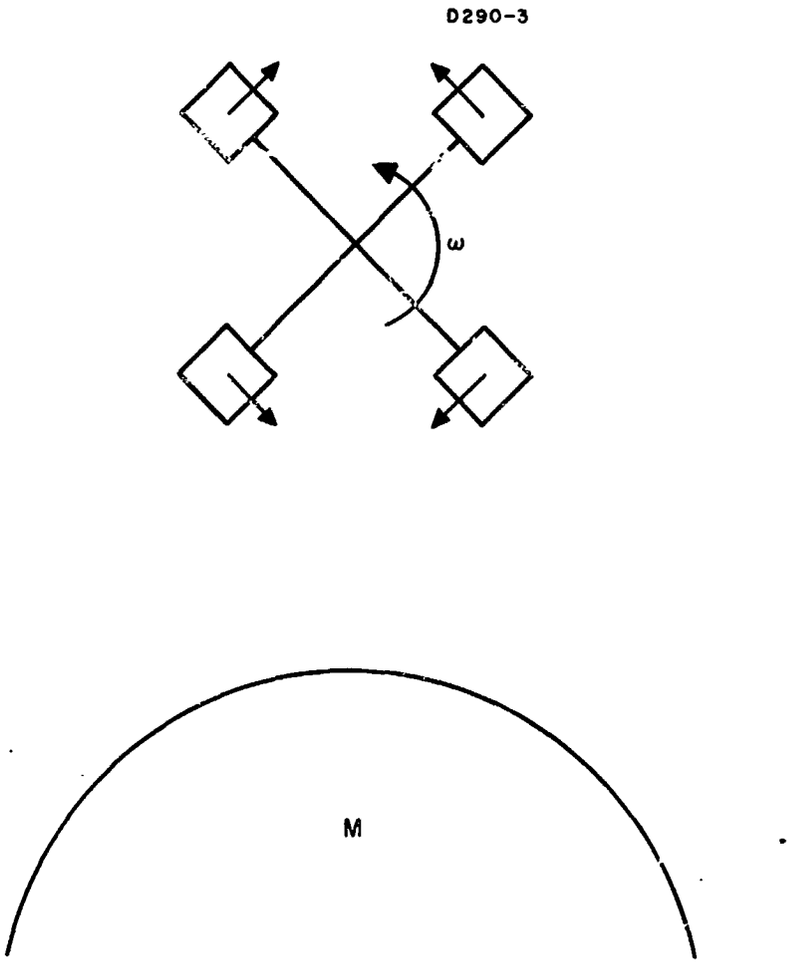

Fig. 13. Phase of 2ω vibrations.

$$\xi = \xi_o \sin \omega t \approx \frac{GM \ell \tau}{R^3 \omega} \sin \omega t \qquad (12)$$

where ℓ is the sensor length and τ the integration time. Since the spring constant, mass, and frequency are related by $K = m\omega^2$, the average stored signal energy is just

$$S = \frac{1}{2} m (\omega^2 \xi^2 \cos^2 \omega t) + \frac{1}{2} (m\omega^2) \xi_o^2 \sin^2 \omega t = m\omega^2 \xi_o^2 \qquad (13)$$

and the signal-to-noise ratio is

$$\frac{S}{N} = \frac{m\omega^2 \xi_o^2}{2kT} \qquad (14)$$

or the amplitude necessary for a specified signal-to-noise ratio is given by

$$\xi_o \approx \frac{(S/N)^{1/2}}{\omega} \left(\frac{2kT}{m}\right)^{1/2} . \qquad (15)$$

This equation, combined with (12), yields the minimum gradient that can be measured for a thermally limited sensor:

$$\Gamma = \frac{GM}{R^3} = \frac{(S/N)^{1/2}}{\ell \tau} \left(\frac{2kT}{m}\right)^{1/2} \qquad (16)$$

where S/N is the desired signal-to-noise ratio; T, m, and ℓ are the temperature, mass, and length, respectively, of the sensor; M is the mass of the object at distance R; and τ is the integration time.

For a large sensor (M = 1 kg, ℓ = 30 cm) with a long integration time (30 sec), the room temperature thermal noise limit for unity signal-to-noise ratio is a gravitational gradient of 10^{-11} sec^{-2}. For a smaller sensor (M = 80 g, ℓ = 10 cm) with a shorter integration time (3 sec), the thermal noise limit is 10^{-9} sec^{-2}, which is approximately the sensitivity level desired for future applications.

The major problem to be faced in the design, construction, and operation of any gravitational gradiometer is the identification and elimination of external and internal sources of electronic and mechanical noise so that the sensor is limited only by thermal fluctuations.

b. Background Rejection

One difficulty in using any gradiometer will be the spurious background signals generated by masses other than that under investigation. This will not always be a problem, since the sensors measure the various gradients of the gravitational field and are much more sensitive at close range. If the exact position of the object is known, phase coherent detection and correlation between two different sensors could be used to discriminate against the background clutter. With rotating sensors, partial discrimination can also be obtained by orienting the sensor rotation perpendicular to the disturbing mass.

There are ways of using the various sensors to obtain further information or better discrimination. For example, the gravitational field pattern varies nonuniformly from one measurement point to another, and a series of measurements at different distances from a mass would allow verification of the range and an unambiguous identification of the gravitationally induced signal. In addition, the primary axes of the gravitational stress pattern are oriented with respect to the line of sight to the mass being investigated, and if the sensor and the mass are in relative motion, the changing line of sight will cause phase shifts in the sensor output.

If an object (e.g., the moon) has a complex mass distribution, its gravitational field will have higher order multipole terms that will vary with relative orientation of the object and the sensor. If the sensor is in orbit around the mass, these higher order multipole terms will also show up as different frequency components, with each order at a different multiple of the orbital frequency.

The most important technique for eliminating the background clutter from all the other disturbing masses such as the sun and the using vehicle itself is to operate the sensor in the mode in which it responds preferentially to moving objects. This is done by adjusting the rotational angular frequency slightly below (or above) the proper frequency for vibrational resonance.

$$f_r = \frac{\omega_r}{2\pi} < \frac{f_v}{2} \qquad (17)$$

At this rotational rate, all the disturbing masses will be inducing vibrational forces at twice the rotational frequency and if the vibrational mode has a high Q, these forces will lie outside the acceptance bandwidth of the vibrational mode and it will not be excited

If we now operate the sensor so that there is a constant relative velocity v between it and the object to be measured, the changing line of sight is found to be equivalent to a relative increase in angular rotation. (See Figs. 14 and 15.)

$$\omega_r + \dot{\theta} \approx \omega_r + \frac{v}{b} = 2\pi\left(\frac{f_v}{2}\right) . \qquad (18)$$

Thus the detector is rotating with respect to the moving object at the proper angular rate to excite the vibrations in the bending modes, but all other inputs are off resonance.

A technique very similar to this will be valuable for laboratory testing purposes. The sensor to be tested can be rotated at a right angle to the local vertical at a rotational rate which is off resonance. A mass quadrupole test mass can then be suspended from above and spun with its rotational rate and direction chosen so that the combined rotations bring the driving forces into resonance with the vibrational mode.

In reality, of course, the discrimination obtained by this technique is only relative, and a very strong disturbing signal can still be seen even after the discrimination is effected. However, if there is relative motion between the sensor and the object to be measured, the excitation frequency will be different from that of the background clutter, and the signal from the object being measured can be detected by the beat notes which it causes. This can be illustrated by Fig. 16, which shows the response of an electromechanical analog of a sensor. The sensor analog was driven off resonance by a very strong but stable clutter signal. A simulated flyby was then made with a frequency and amplitude swept signal which was 1000 times weaker. The output of the sensor analog was then detected and the beat note of about 0.8 cps between the strong clutter signal and the stored energy from the simulated flyby was plotted. The rise time of 1.5 sec is the duration of the flyby, and the fall time of 3.0 sec is the decay time of the vibrational mode. The two passes show that the effect is repeatable, and other experiments showed the expected one-to-one relation between signal strength and beat note amplitude.

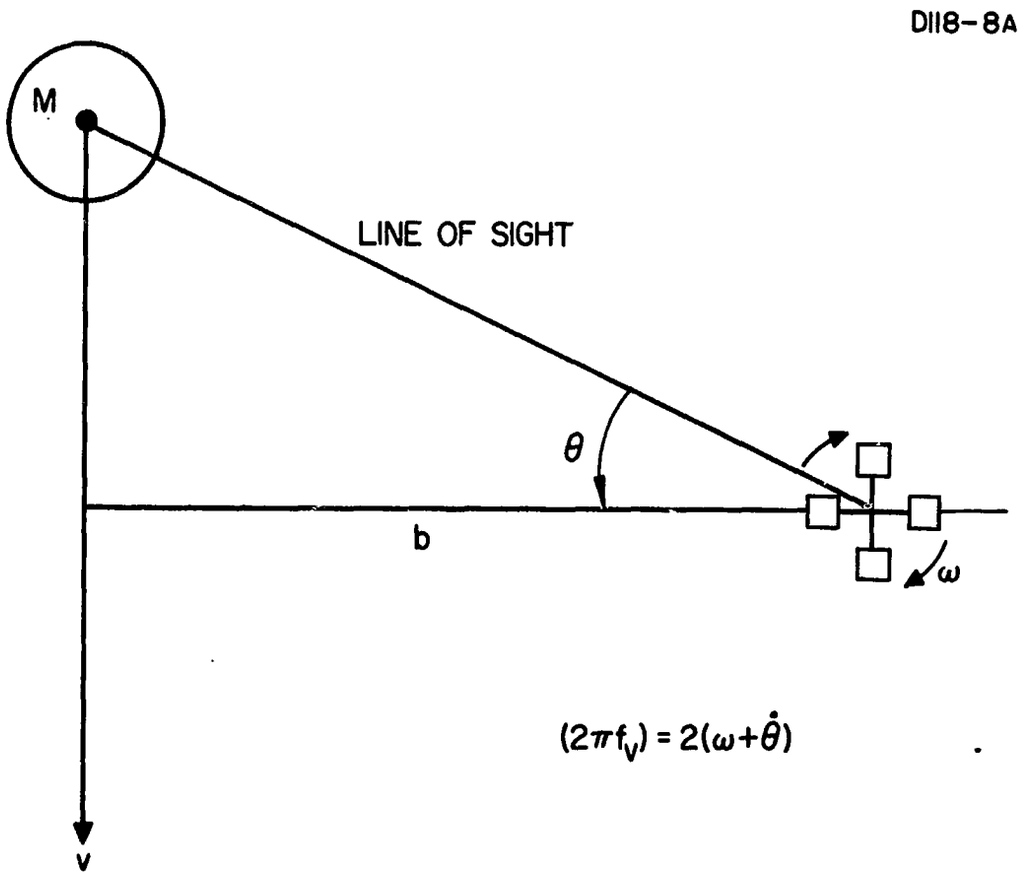

Fig. 14. Relative angular rotation due to angular velocity.

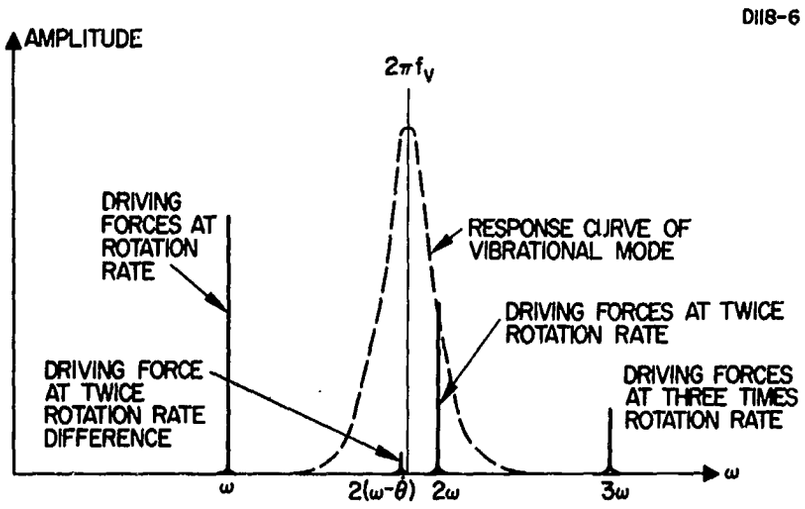

Fig. 15. Response of vibrational mode to driving forces from various sources.

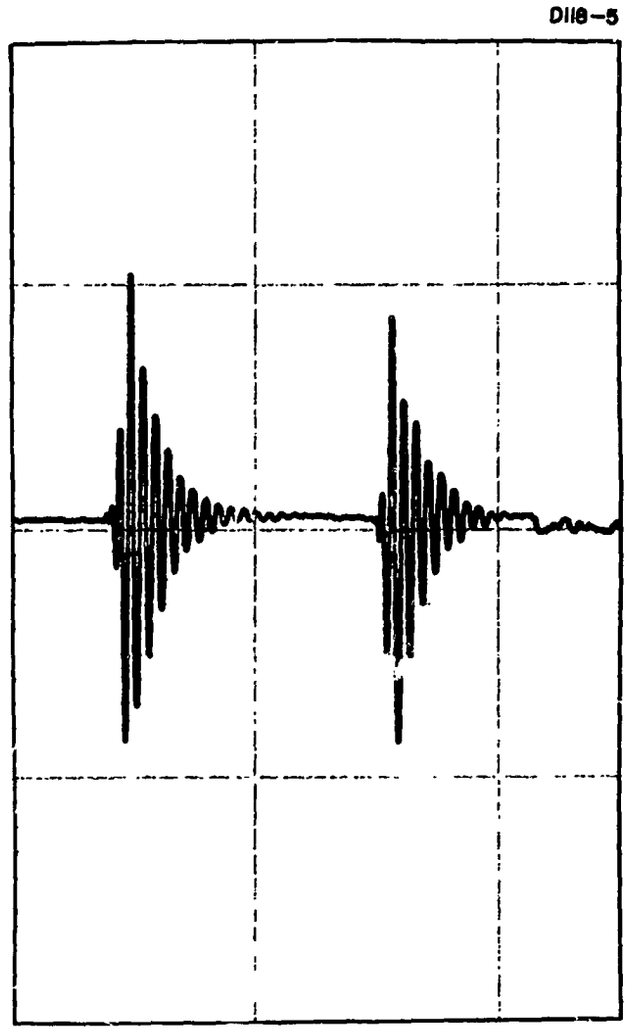

Fig. 16. Simulated flyby with constant background.

c. Rotational Gradients

The equation for the general form of the gradient tensor (eq. (9)) indicates that although there are no gradients resulting from linear acceleration, the gradients resulting from angular velocity and angular acceleration can interfere with the measurement of the gravitational gradients. The largest gravitational gradient that can be generated is approximately 10^{-5} sec^{-2} (the surface gradient of the earth is 3×10^{-6} sec^{-2}). However, for many of the proposed applications (see Section II-H), we would like to be able to measure gravitational gradients down to 10^{-9} sec^{-2}. The angular velocity which would cause an equivalent gradient is 3×10^{-5} rad/sec (6°/hour) and the angular acceleration is 10^{-9} rad/sec^2 (0.7°/hour change per hour). Both of these rotational gradients involve very small angular quantities.

The rotational gradient resulting from angular velocity is seen to enter into every term in eq. (9), and it is not possible to separate the effects completely. Thus any instrument designed to measure gravitational gradients will have to be space stabilized in some way. One approach, which is necessary for static gradiometers, is to mount the sensor on a stabilized platform.[27] The stabilization required (less than 6°/hour) is relatively easy to achieve, but it does add complexity to the system. The rotating sensors which we are investigating are not quite as susceptible to angular velocities. As we show in Section II-B, they are not sensitive to rotations in the plane of their rotation. However, they would be sensitive to torques induced by rotation of a nonspinning space vehicle or to nutation of a spinning space vehicle. However, since they and their vacuum chambers are spinning, they could act as their own gyrostabilized platform and a gimballed mount will decouple them from the torques.

The rotational gradient caused by angular acceleration is relatively easy to circumvent, since it does not enter in all the terms in eq. (9). A well designed in-line gradiometer which measures either G_{xx}, G_{yy}, or G_{zz} will not experience interference from angular acceleration (although it will see any angular velocity). The rotating sensors which we are investigating are not susceptible to angular acceleration because of their four arm design (see Section II-B).

B. SENSOR DESIGN STUDIES

The first task in the research program was to determine a sensor structure design which would detect gravitational gradients and would not become unstable at the necessary rotation speeds. The original study[1, 2] of the gravitational mass sensor by Robert L. Forward was analyzed by C. C. Bell in a more general manner (see Appendix A). This analysis indicated that radially vibrating sensor structures (Fig. 17) generally are incapable of measuring the gravitational force gradient because the radial spring constant is not strong enough to resist the centrifugal forces at the necessary rotation speeds.

After further study, it was found that the most promising form of sensor was a tangentially vibrating cruciform spring-mass system (see Fig. 18). The gradient of the gravitational field interacts with the masses on the ends of the arms and causes differential torques. As the sensor rotates, the direction of the applied torque varies at a frequency which is twice the rotation frequency of the sensor. The spring constant in the tangential direction is chosen so that the sensor is resonant at the driving frequency of the applied differential torques.

In this design, the centrifugal force on the sensor masses is resisted by the longitudinal spring constant of the arm. A number of different cruciform sensor heads were designed and studied experimentally. They all demonstrated the desired structural stability under high rotation speed.

To protect the sensor from excitation by acoustic, electric, magnetic, and light gradients, and the electronics from electromagnetic pick-up, the sensor was to be mounted inside a corotating vacuum chamber (see Fig. 19). The readout of the sensor vibrations is accomplished by sensing the dynamic strains in the sensor arms with barium titanate piezoelectric strain transducers (see Section II-E).

1. Five Inch Monolithic Cruciform Design

The first mass sensor design constructed was a cruciform machined out of a solid piece of aluminum (see Fig. 19). The arms are about 1.5 in. long, 0.75 in. wide, and 0.050 in. thick, with a 0.75 in. cube at the end for extra mass and are designed to have a natural resonant frequency of approximately 190 Hz. The over-all diameter is about 4.5 in. The four strain transducers, one on each arm, are matched to within 1 dB and have a voltage strain characteristic of 7.0×10^4 V/unit strain. The associated vacuum chamber, which is rotated with the sensor head, is 5.5 in. in diameter and 1.5 in high.

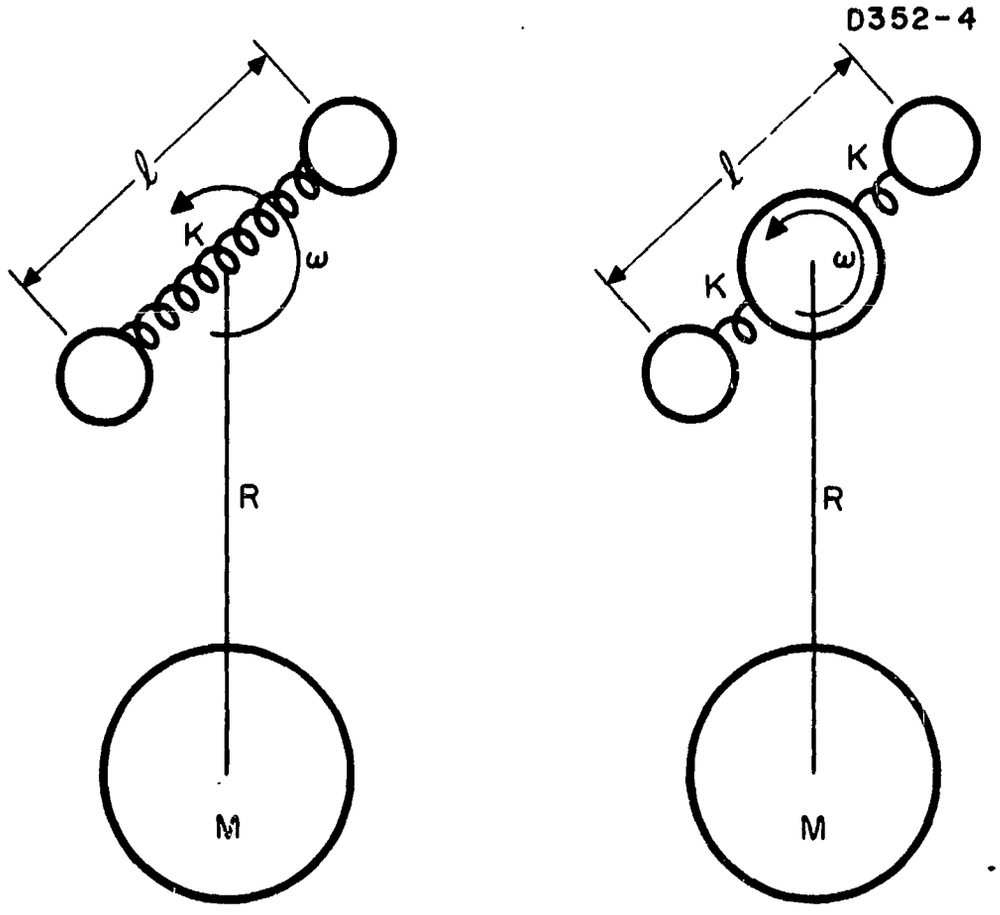

Fig. 17. Radially vibrating mass sensors.

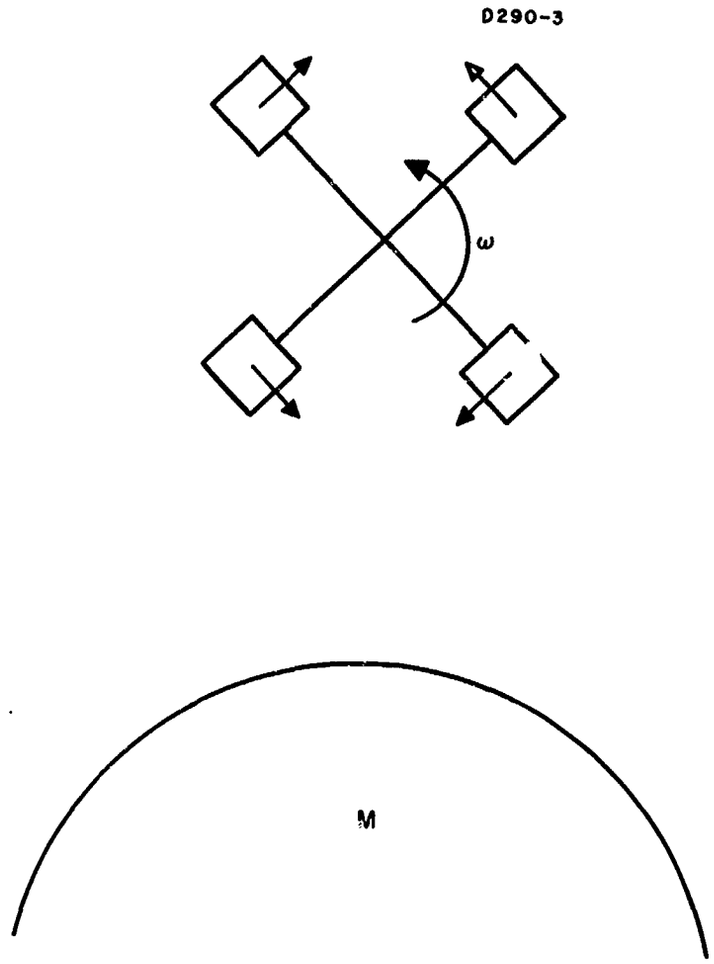

Fig. 18. Transversely vibrating cruciform mass sensor.

M 3615

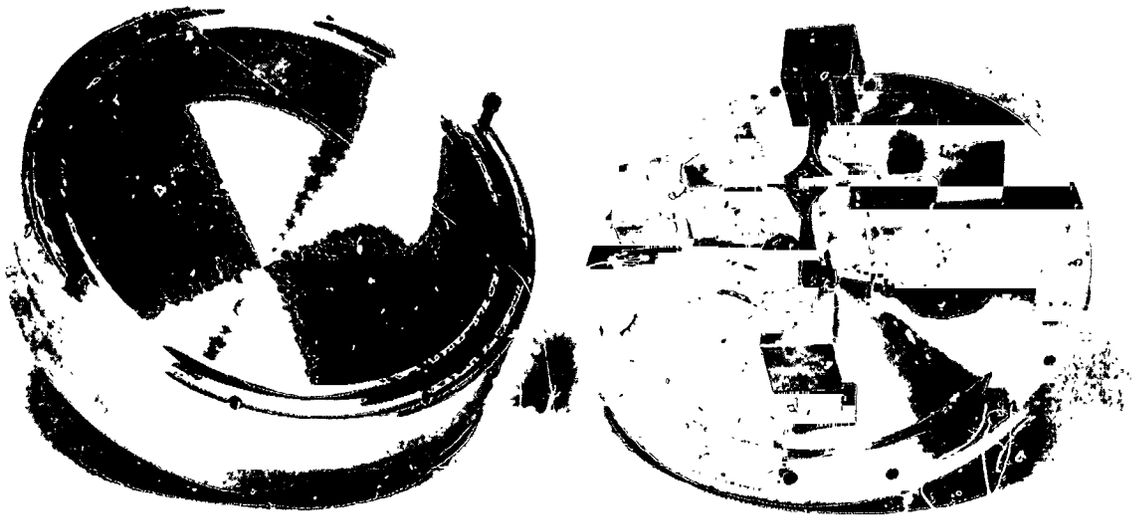

Fig. 19. Five-inch diameter cruciform gravitational mass sensor.

When the sensor head was mounted in the vacuum chamber on a stiff supporting rod, it was found that three vibrational resonant modes were present (e.g., 186.2, 187.7 and 190.1 Hz) instead of one, as expected. This was caused by the coupling of the sensor modes to the mass of the vacuum chamber through the support rod. To check this, the sensor was removed from the solid mount and suspended from its center by a wire and a rubber strip. The four primary piezoelectric strain transducers were then driven with a constant ac voltage, and the sensor response was detected with a fifth transducer. By applying properly phased driving voltages to the transducers on the various arms, it was possible to excite the various modes selectively. The results are shown in Table I.

The table shows that the various modes are all well separated from each other if the center of the sensor is not strongly coupled to a large mass. It was possible to identify the primary modes of interest from the large responses at particular modes for particular driving phase combinations. The gradient or tuning fork mode is at 189 cps, and the angular acceleration or rotational mode is at 993 cps. The tranlational acceleration or wing flapping mode was found to split into two modes at 241 and 244 cps because of the slight dimensional differences between the opposite pairs of arms. The other modes were not directly identified, but could easily be torsional modes as well as harmonics of the above vibrational modes since the transducers were not placed exactly along the central line of the arms on this sensor.

A small mass (approximately 10 g) was then added to the center mass of the cruciform, and the measurements repeated. It was found that the tuning fork mode remained the same, the translational modes each shifted downward about 10 cps, and the torsional mode shifted from 993 to 977 cps.

The results of these measurements indicated that the desired mode of operation (the tuning fork or gradient mode) has the lowest frequency of vibration and its output can be well separated from all the other vibrational modes by a simple band-pass filter if the sensor's effective central mass can be kept small. This indicated that further effort was needed on the sensor support mechanism as well as on the sensor design.

2. Adjustable Sensor Design

In addition to the monolithic sensor, an adjustable sensor head assembly was fabricated and tested (see Fig. 20). The purpose of this design was to permit separate adjustment of the various sensor parameters, such as arm length, frequency, and Q, in order to achieve better sensor symmetry than obtainable with the monolithic design. The sensor head consists of a central hub, four arms, and four adjustable

TABLE I

Driven Resonant Modes

Tuning Fork Mode D290-4		Torsional Mode D290-6		Translational Mode D366-4	
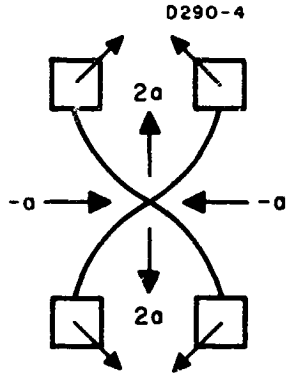		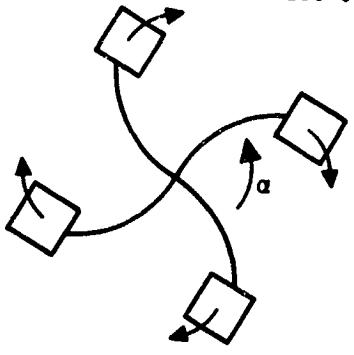		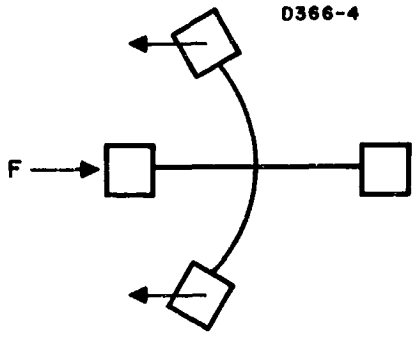	
Frequency cps	Output mV	Frequency cps	Output mV	Frequency cps	Output mV
189.0	37	188.8	11.2	188.8	2
243.8	6	244.3	4.2	241 244.4	27
845.5	6.5	849.5	5.7	845.5	7
869.0	2.5	869.0	<1	869.0	1
992.9	13	993.0	58	993.0	4.5
1745	40	1745	52	1745	33
1989	16	1949	7	1949	8.8
2048	17	2084	22	2039 2084	1.5 9

M 4131

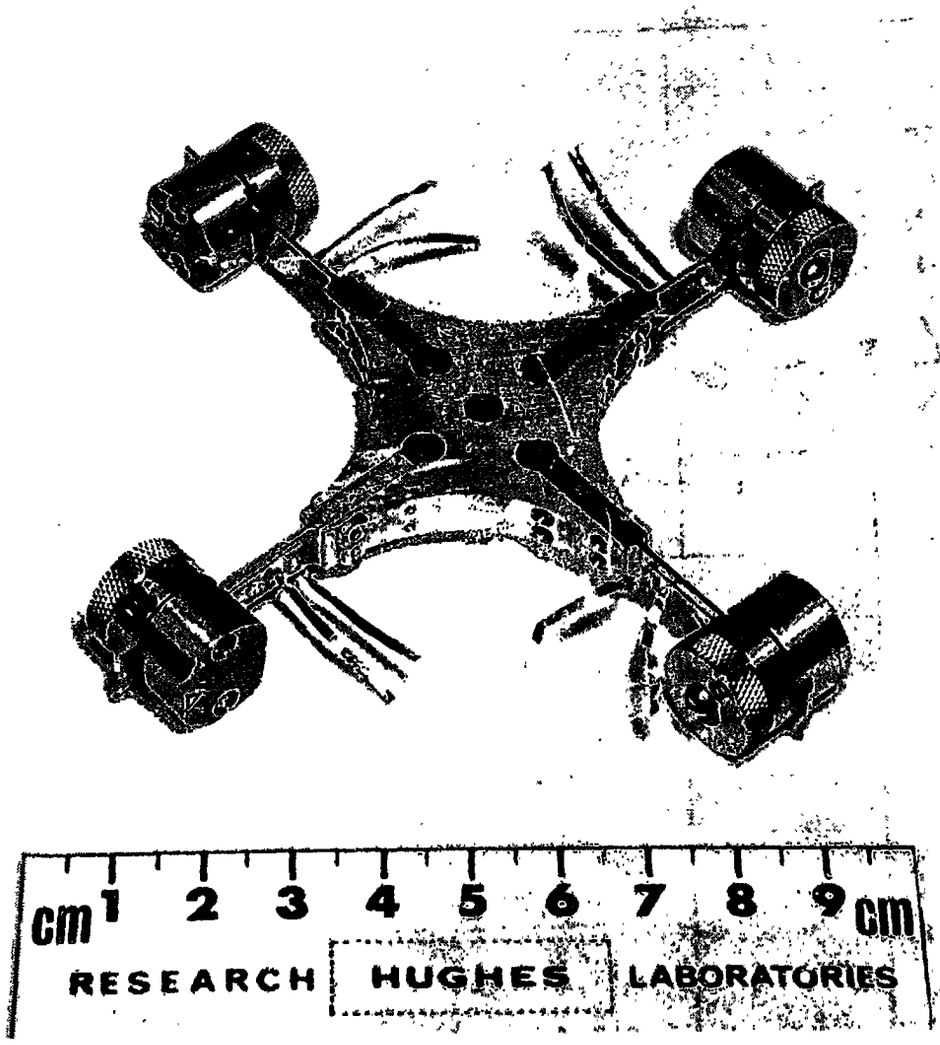

Fig. 20. Adjustable sensor.

mass assemblies. The hub is designed to clamp the arms rigidly for good cross coupling and yet allow the arm and mass assembly to be moved in and out about 0.070 in. for mass balance of the final assembly. The arms (see Fig. 21) have a 0.125 in. thick base where they fasten to the hub and an outer bending portion that is 0.030 in. thick and about 0.70 in. long. The over-all diameter (4.5 in.) and weight (100 g) of the new assembly is approximately the same as the monolithic design. The adjustable masses, which clamp onto the ends of the arms, consist of two small masses and a double eccentric which can be adjusted to vary the effective length of the arm and yet maintain a center of mass coincidence with the center line of the arm. Pv moving the masses, the effective length of the arm can be varied from 0.60 to 0.78 in. to yield a frequency shift of several cycles about the design frequency of 100 cps.

This particular design was tested and showed the same mode behavior as the monolithic sensor. Because of its lower design frequency it was used for most of the rotation tests described in Section II-C and Attachment D. However, it was difficult to prevent the various parts from shifting under the centrifugal force during rotation.

3. Multiple Radius Tests

Because an increase in the center mass of the cruciform has a tendency to converge the frequencies of the various vibrational modes, it is desirable to keep the center mass as small as possible by minimizing the radii of curvature of the fillets between the arms. The original purpose of this fillet was to prevent high stresses at the joints between the arms (which might affect the Q) and to provide coupling between the arms so that they would act as a single resonant structure rather than as four independent arms.

To test the effect of the radius of curvature on the Q of the sensor and the coupling between the arms, three aluminum cruciforms were constructed which had the same dimensions except for the radius of curvature at the center (see Fig. 22). These sensors were also made larger (8 to 12 in.) than the earlier sensors in order to become familiar with the behavior of large, low frequency devices.

Cruciform No. 4 (Fig. 22(a)) had a radius of curvature of 2 in. with an over-all diameter of 12.3 in. Cruciform No. 5 (Fig. 22(b)) had a radius of curvature of 1 in. and a diameter of 10.3 in. Cruciform No. 6 (Fig. 22(c)) had a radius of only 0.25 in. and an over-all diameter of 8.8 in. Despite the large variation in size, they all had the same resonant frequency since the arm length (measured from the fillet boundary) was kept constant.

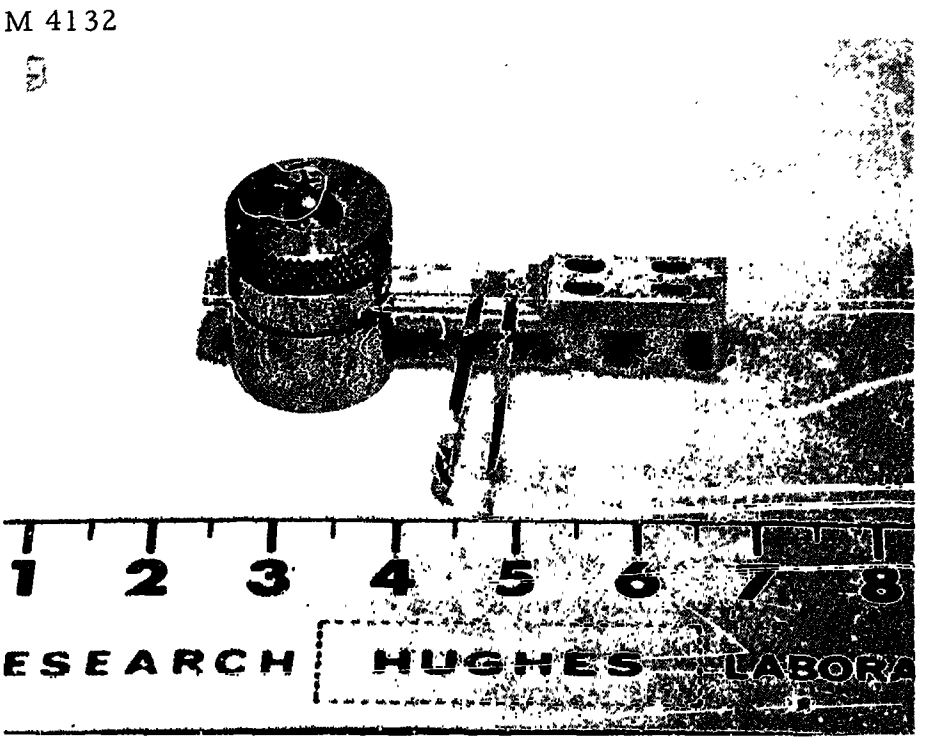

Fig. 21. Detail of sensor arm.

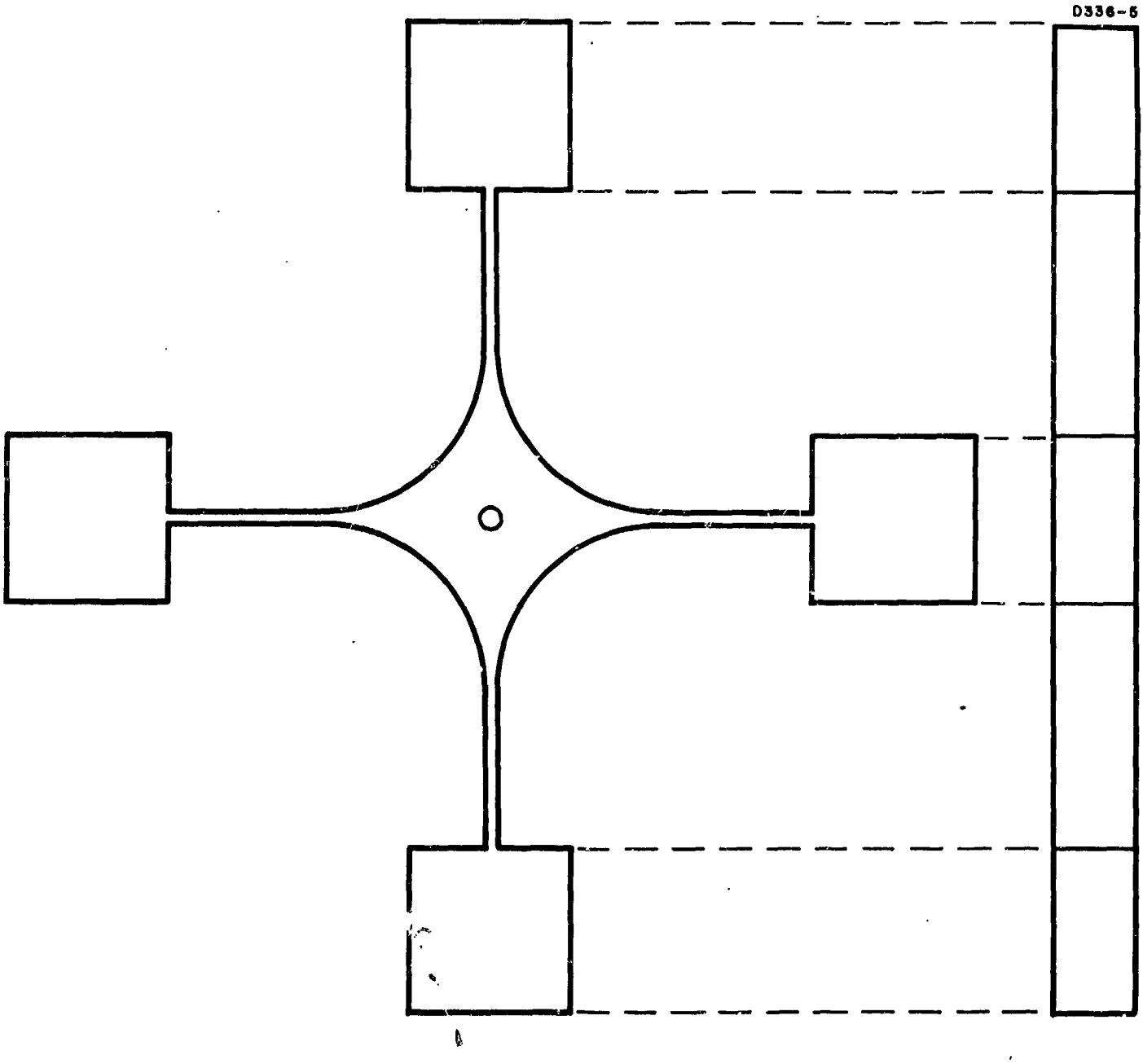

Fig. 22(a). Sensor cruciform (two inch radius).

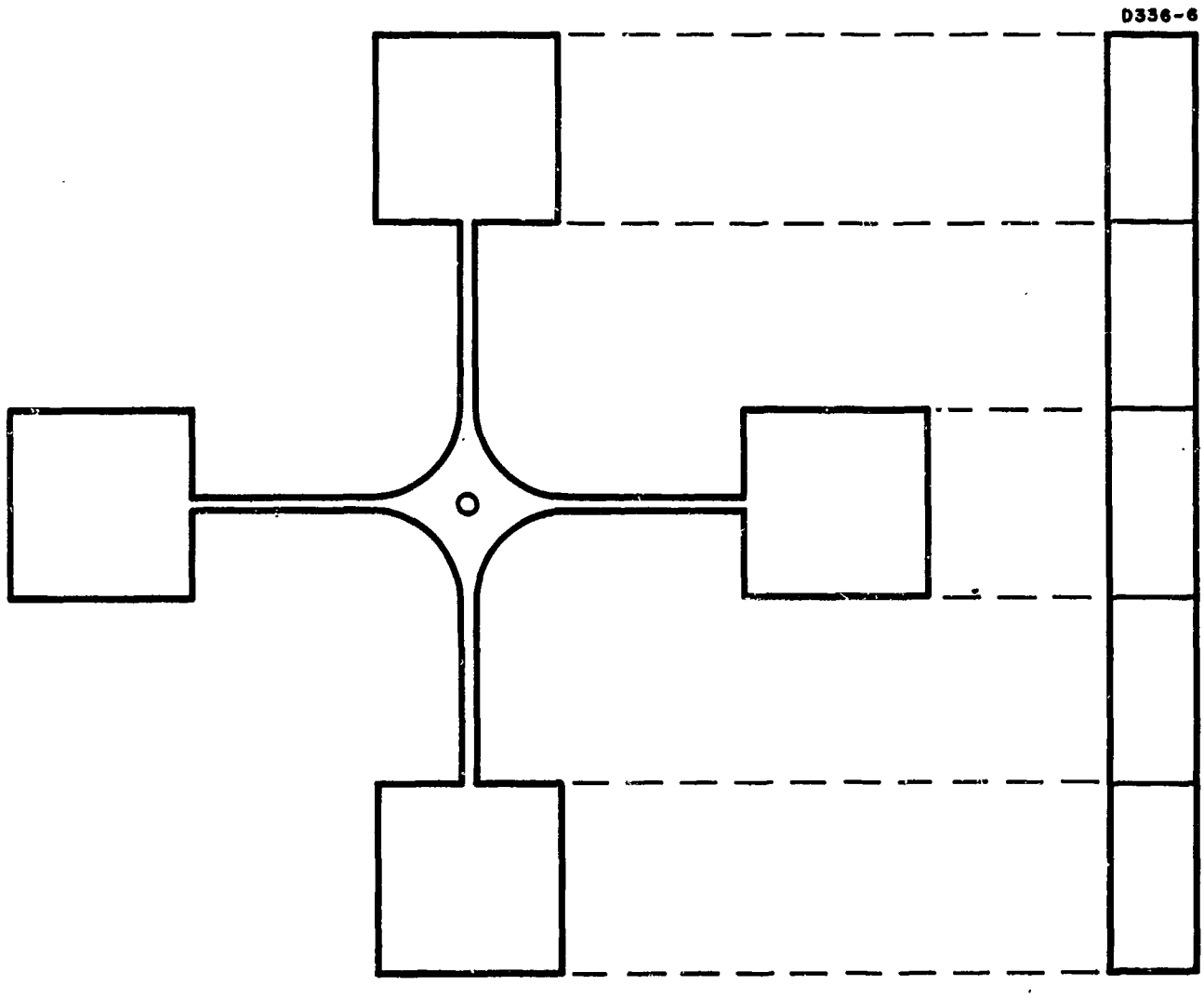

Fig. 22(b). Sensor cruciform (one inch radius).

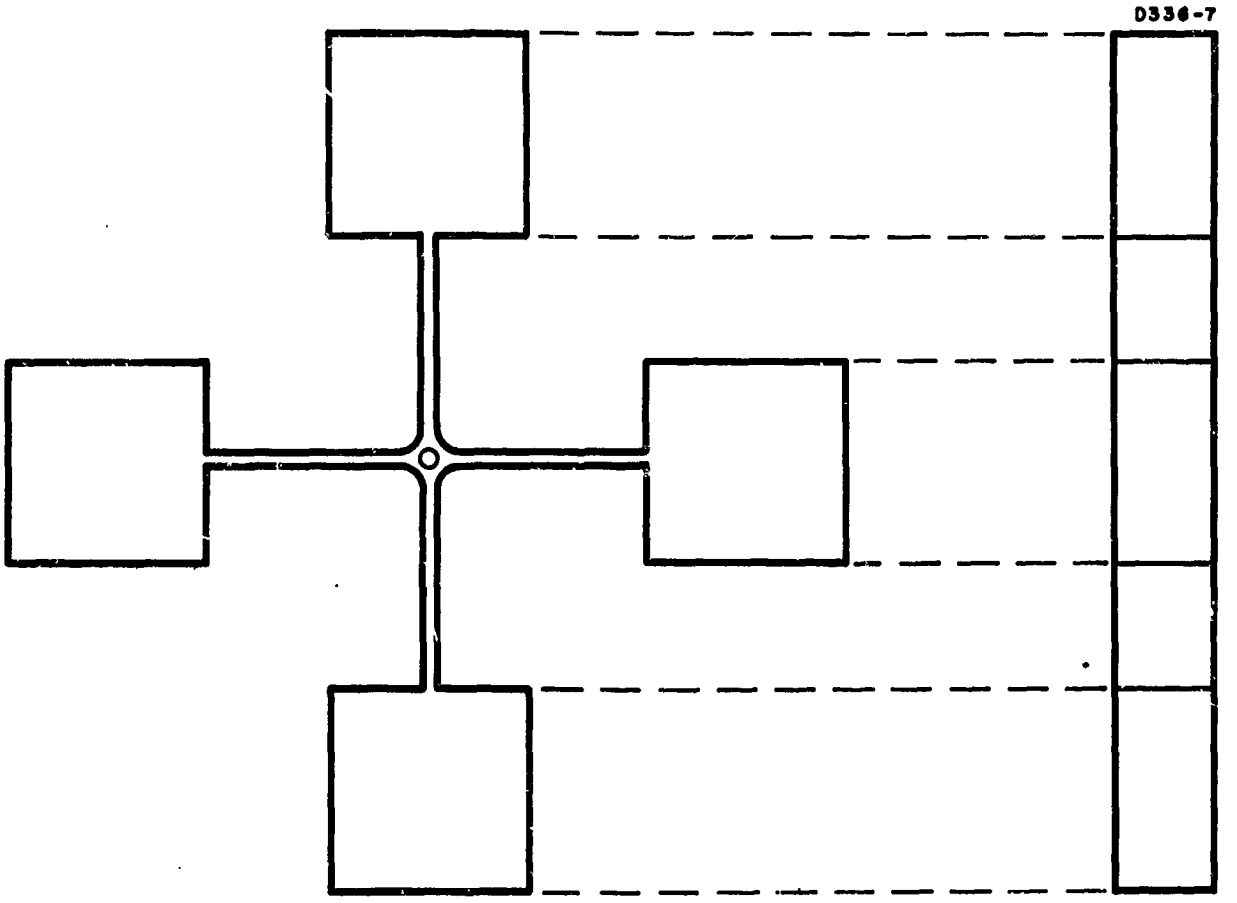

Fig. 22(c). Sensor cruciform (one quarter inch radius).

Barium titanate strain transducers were attached to the arms, and the cruciforms were suspended at the center of mass by a small wire and a rubber strip to give minimum external coupling. The results shown in Table II were obtained by driving the various modes with an external ac voltage.

TABLE II

Mode Frequencies for Large Cruciforms

Sensor	Tuning Fork Mode, cps	Translational Mode, cps	Torsional Mode, cps
Cruciform No. 4 (2 in. radius)	20.2	25.2	511
Cruciform No. 5 (1 in. radius)	20.1	26.5	930
Cruciform No. 6 (1/4 in. radius)	20.8	28.5	1698

There appeared to be no significant difference in the Q of the various units.

The major effect on the Q was found to be a result of damping from the barium titanate strain transducers on the arms. With two large (SC-4) transducers, the Q of cruciform No. 6 was 160, with one large transducer it was 235, and with one small (SC-1) transducer the Q rose to 435.

Various tests were also run in air and in vacuum with the other conditions held constant. There was no apparent difference in Q or in the resonant frequency. The only effect noted was the lack of acoustical noise excitation in the vacuum.

The conclusions drawn from the above tests were that the primary cause of damping in the present sensors is the losses in the strain transducers and that the sensor with the smallest radius of curvature had the greatest frequency separation between the various vibrational modes because of its smaller center mass. Since the smaller radius does not seem to affect the other properties of the sensor, the later sensors were designed with small radii of curvature than the initial designs.

4. Study of Sensor Mode Behavior Under Rotation

As a result of the initial experimental work, it was realized that the cruciform shaped gravitational mass sensors have four primary oscillation modes which involve the spring constant of the bending arms. These are the gravitational gradient sensing or tuning fork mode, a torsional mode, and two translational modes. In addition, there are other modes involving the higher harmonics of these primary modes, as well as oscillations involving the sensor mounting structure. All of the modes were found to shift in a complicated manner under rotation. In order to better understand the behavior of the sensors and to develop a theory of operation which would allow us to design better sensors, a combined theoretical and experimental study of the vibrational mode behavior of rotating cruciform sensors was carried out.

The theoretical analysis (see Attachment D) is quite detailed and includes not only an analysis of the sensor but also it interaction with its mounting structure. The model used in the analysis was not that of one of the actual sensors, but was chosen to be as general as possible while still retaining the important features of the actual sensors. The model (Fig. 23) assumes a central mass M and four smaller masses m at the ends of four arms of length a; these arms are pivoted at a distance b from the center of the sensor. The central mass is assumed to be attached to a rotating axis through an axially symmetric spring of spring constant K. (The model shows four coil springs; the experiment used a flexible shaft.) To simplify the analysis the axis was assumed to remain fixed in position at the origin of the inertial reference frame, while rotating at a constant angular frequency of Ω. The central mass M, since it is attached to the rotating axis through springs, is not constrained to the origin but its center of mass is in general at the position $\vec{R}$ and its speed of rotation varies about Ω by a small amount $\dot{\phi}$ due to the interaction with the vibrating arms. The masses at the ends of the arms participate in the general rotation of the sensor and also can vibrate through a small angle α_n with respect to the rotating reference frame.

Because of the detailed analysis of this model which is available in Attachment D, only a summary of the sensor vibrational mode behavior is given here. We are primarily interested in the sensor behavior, without the complication of the interaction of the sensor modes with the mount modes; therefore, we will take those portions of the analysis which apply when the mount spring constant is essentially zero.

Each mode of vibration of the sensor corresponds to a particular combination of arm phase and amplitude. The four primary modes of interest are the gravity gradient sensing mode (see Fig. 24(a))

$$A_g = \frac{a}{2} (\alpha_1 - \alpha_2 + \alpha_3 - \alpha_4) \ , \qquad (19)$$

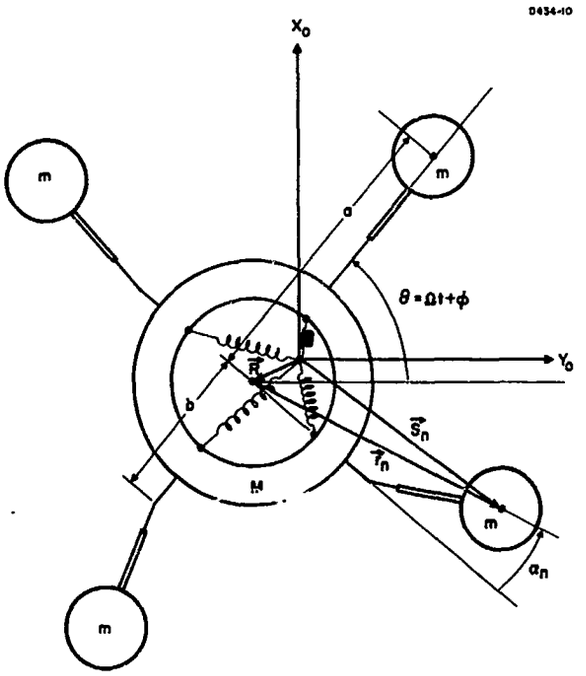

Fig. 23. Model of rotating cruciform sensor on spring mount.

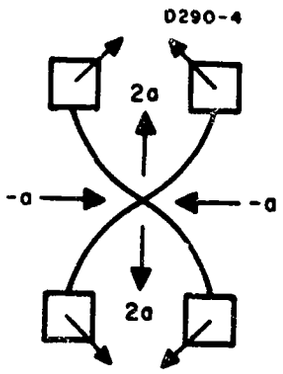

(a)

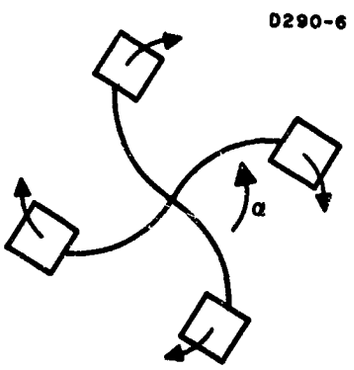

(b)

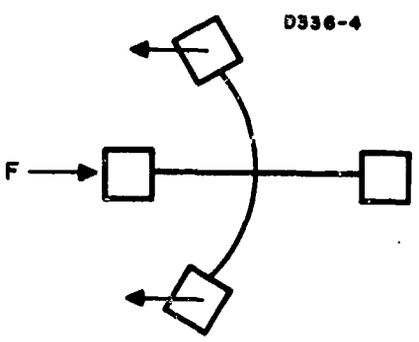

(c)

Fig. 24. Sensor vibrational modes.

the torsional mode (see Fig. 24(b))

$$A_t = \frac{a}{2}(\alpha_1 + \alpha_2 + \alpha_3 + \alpha_4) \ , \tag{20}$$

and the two orthogonal translational modes (see Fig. 24(c))

$$A_+ = \frac{a}{\sqrt{2}}(\alpha_3 - \alpha_1) \tag{21}$$

$$A_- = \frac{a}{\sqrt{2}}(\alpha_4 - \alpha_2) \ . \tag{22}$$

The two translational modes can also be expressed in terms of right and left handed circulating translational modes which are complex combinations of the orthogonal modes

$$A_r = \frac{1}{\sqrt{2}}(A_+ + iA_-) = \frac{a}{2}(-\alpha_1 - i\alpha_2 + \alpha_3 + i\alpha_4) \tag{23}$$

$$A_\ell = \frac{1}{\sqrt{2}}(A_+ - iA_-) = \frac{a}{2}(-\alpha_1 + i\alpha_2 + \alpha_3 - i\alpha_4) \tag{24}$$

When the sensor equations of motion (see Attachment D) are solved in terms of these mode amplitudes, we obtain equations giving the frequencies of the various modes. The frequency of the gravitational gradient sensing mode (see Fig. 24(a)) is given by the spring constant k and mass of the arms as modified by the centrifugal rotation

$$\omega_g^2 = \frac{k}{m} + \frac{b}{a - b}\Omega^2 \ . \tag{25}$$

We note here that the frequency of this mode is not constant but shifts upward under rotation. This effect is borne out by the experimental results and is due to the increase in the effective spring constant from the centrifugal force acting on the sensor arms as gravity on a pendulum. However, the centrifugal force does not simulate gravity exactly since it is not a uniform field but is directed radially outward. If the pivot point of the arm were at the center of rotation (b = 0), the frequency of the mode would be independent of the rotational speed, since the mass on the end of the arm would not see any variation in the centrifugal potential as the arm vibrated.

When we solve the equation for the torsional vibration (see Fig. 24(b)), we find that the natural frequency of the torsional mode is related to the gradient sensing mode frequency by

$$\omega_t^2 = \left(\frac{I + 4ma^2}{I} \right) \omega_g^2 \quad . \tag{26}$$

Here we note that the torsional mode frequency starts off higher than the gradient sensing mode frequency, provided the moment of inertia I of the central mass is not too large, and increases with rotation speed in the same manner. This behavior is borne out by the experimental results. An isolated sensor usually has a sufficiently small central mass that the torsional mode frequency is considerably higher than the gradient sensing mode frequency and rises with increasing rotation speed. However, if the sensor is firmly attached to a large sensor chamber, the torsional mode frequency shifts down toward the gradient sensing mode frequency.

When we solve the equations of motion for the two translational modes (see Fig. 24(c)), (assuming that the sensor is isolated from its chamber by a soft mount), we find that the frequencies of the translational modes are also related to the gravitational gradient sensing mode frequency, but by a more complicated relation than in the torsional case

$$(\omega_\pm \pm \Omega)^2 + \frac{M + 4m}{2m} \left(\omega_g^2 - \omega_\pm^2 \right) = 0 \quad . \tag{27}$$

In order to examine the behavior of the translational mode frequencies, a series of plots of mode response frequencies $\omega_\pm$ as a function of rotation speed Ω was made (see Fig. 25).

For the case where the central mass of the sensor is negligible ($M << m$), the sensor translational modes start at $\omega_\pm = \sqrt{2}\ \omega_g$ and then split as the sensor starts rotating. When the rotation speed is at the desired operating point ($2\Omega = \omega_g$), the two sensor translational modes are at

$$\omega = \frac{1}{2} \left(\sqrt{10} \pm 1 \right) \omega_g \tag{28}$$

or

$$\omega_+ = 2.081\ \omega_g \tag{29a}$$

$$M << m \quad .$$

$$\omega_- = 1.081\ \omega_g \tag{29b}$$

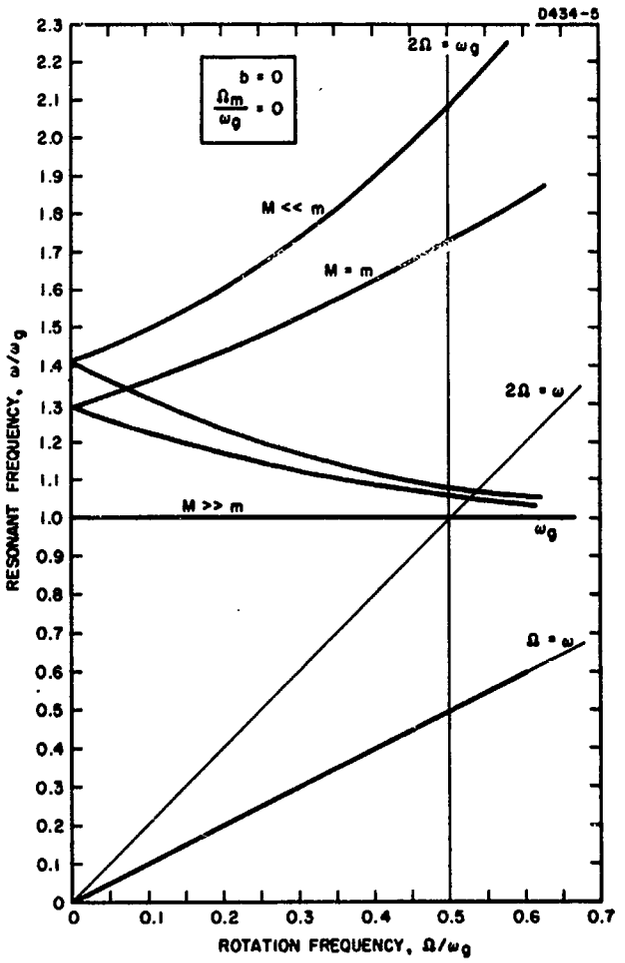

Fig. 25. Predicted translational mode splitting ($\Omega_m = 0$).

If the mass of the central hub is increased so that $M = m$, the sensor translational mode starts out at $\omega_{\pm} = 1.29\ \omega_g$ and again splits under rotation in the same manner. At the desired operating speed the two frequencies are

$$\omega_+ = 1.728\ \omega_g \qquad (30a)$$

$$M = m \quad .$$

$$\omega_- = 1.062\ \omega_g \qquad (30b)$$

For a large central mass $M >> m$, the sensor translational modes start out at

$$\omega_{\pm} = \omega_g \qquad M >> m \qquad (31)$$

and do not split under rotation.

From this set of curves we see that it is desirable to keep the central mass of the sensor as small as possible. In this manner we can obtain a higher degree of frequency separation between the gravity gradient sensing mode at ω_g and the vibration sensitive translational modes. As a practical matter it is difficult to make the central mass smaller than the arm masses, and in most of our sensors $M \approx m$.

In order to check the theoretical predictions a set of sensor resonant frequency data was taken on a rotating cruciform hanging from a rubber band (see Fig. 26). The rubber band had a very low natural frequency, and therefore $\Omega_m = 0$. There was an instability at low rotation rates; however, after this was passed and the sensor was rotated above the resonance point, it was very stable. The data are plotted in Fig. 27. Four points from the data (large points) were then used to determine the four sensor parameters (k/m), $(b/a - b)$, $(I + 4ma^2/I)$, and $\mu = (M + 4m/2m)$.

These parameters were then used in the three theoretical equations

$$\omega_g^2 = \frac{k}{m} + \frac{b}{a - b}\ \Omega^2 \qquad (32)$$

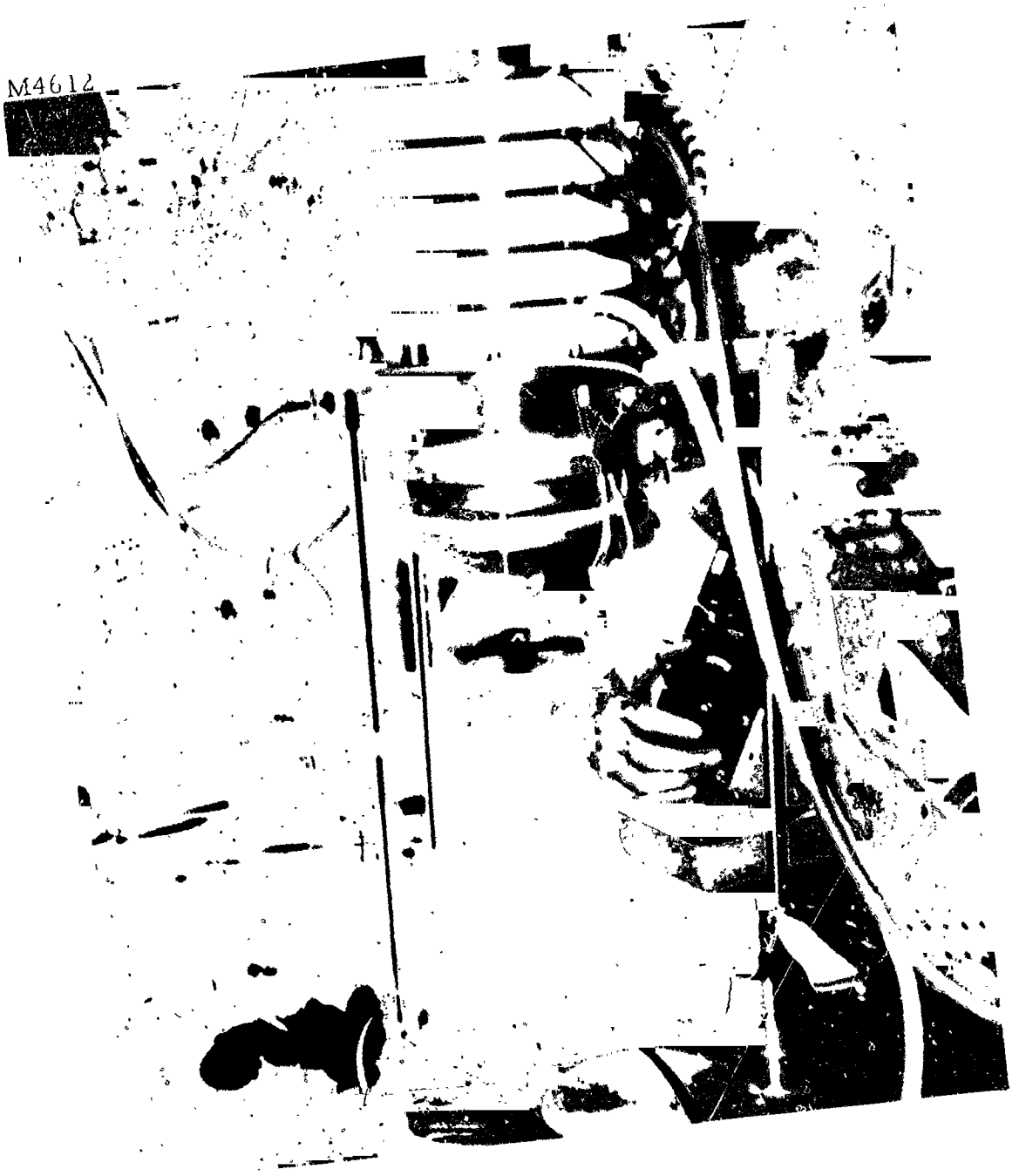

Fig. 26. Sensor rotating on rubber band suspension under magnetic bearing.

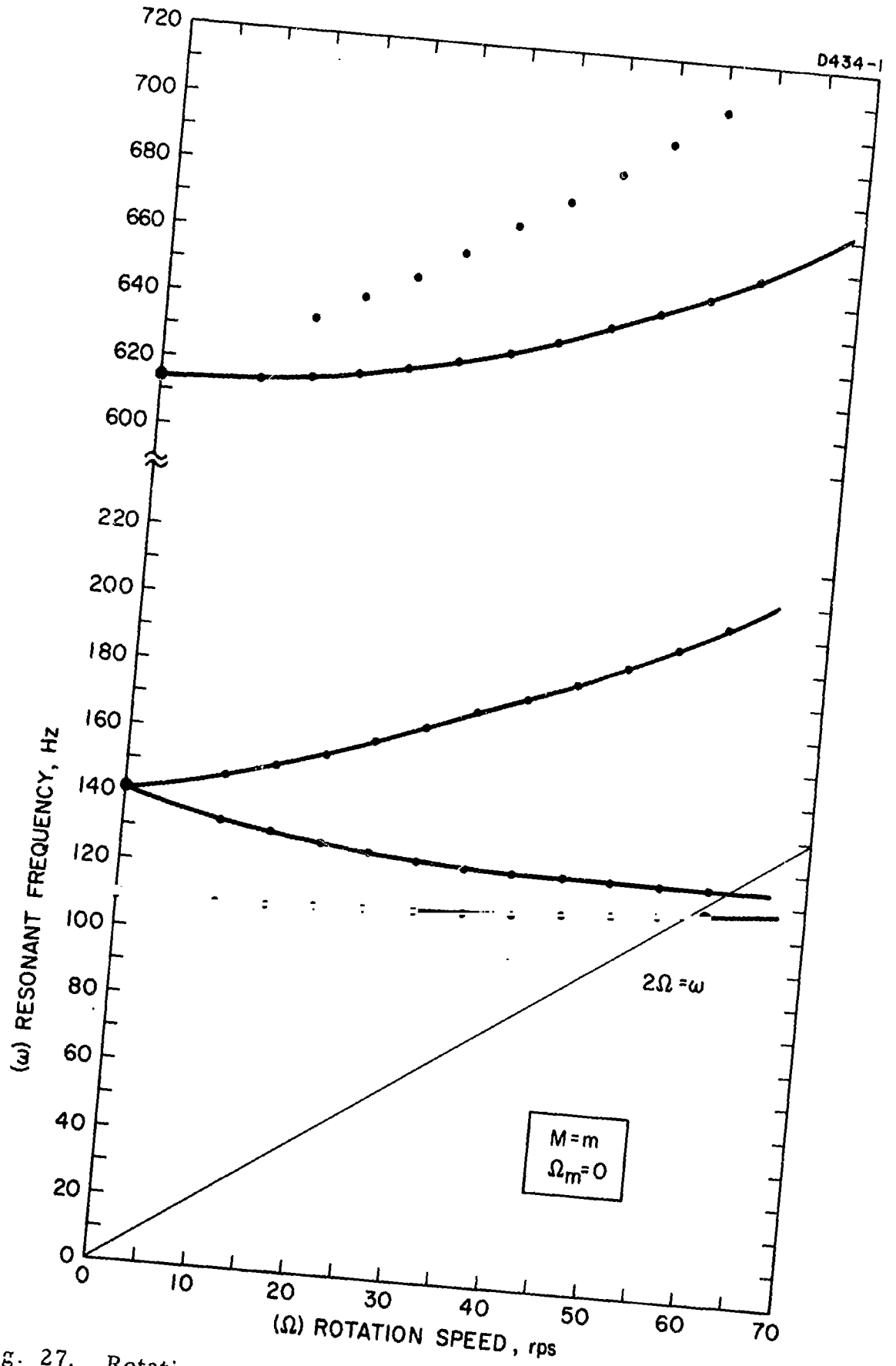

Fig. 27. Rotating sensor system resonant modes on soft mount.

$$\omega_t^2 = \left(\frac{I + 4ma^2}{I}\right) \omega_g^2 \tag{33}$$

$$(\omega_{\pm} \pm \Omega)^2 + \mu (\omega_g^2 - \omega_{\pm}^2) = 0 \tag{34}$$

to obtain the theoretical curves. The agreement with the data is excellent. The highest set of data seems to be the upper half of a split torsional mode. It is believed to result from the effect of the moment of inertia of the arm masses which was neglected in the theoretical calculations.

5. Seven Inch Monolithic Cruciform Design

The analytical work reported above and in Attachment C and D provided a theoretical basis for the operation of the sensor, the results of which are in close agreement with data taken on actual sensors. Based on this theory, it was decided that the performance of the sensor could be improved in the following ways:

- To improve mode separation, a small ratio of central mass of the sensor to the outer masses is required.
- To minimize the effect of centrifugal force on the resonance curves, the distance from the center of rotation of the sensor to the bending point in the arm should be a minimum compared with the sensor effective radius.
- To maximize the sensitivity to the gravity gradient field, the effective sensor radius should be maximized.

Based on the above points, a new sensor was designed as illustrated in Fig. 28. This new sensor was designed to have a maximum end mass to center mass ratio, central bending of the arms, and a large effective radius to help optimize output. In addition, by including an adjustable brass slug in each end mass, it was possible to adjust the effective radius of each arm in order to match the translational modes of the sensor.

M4572

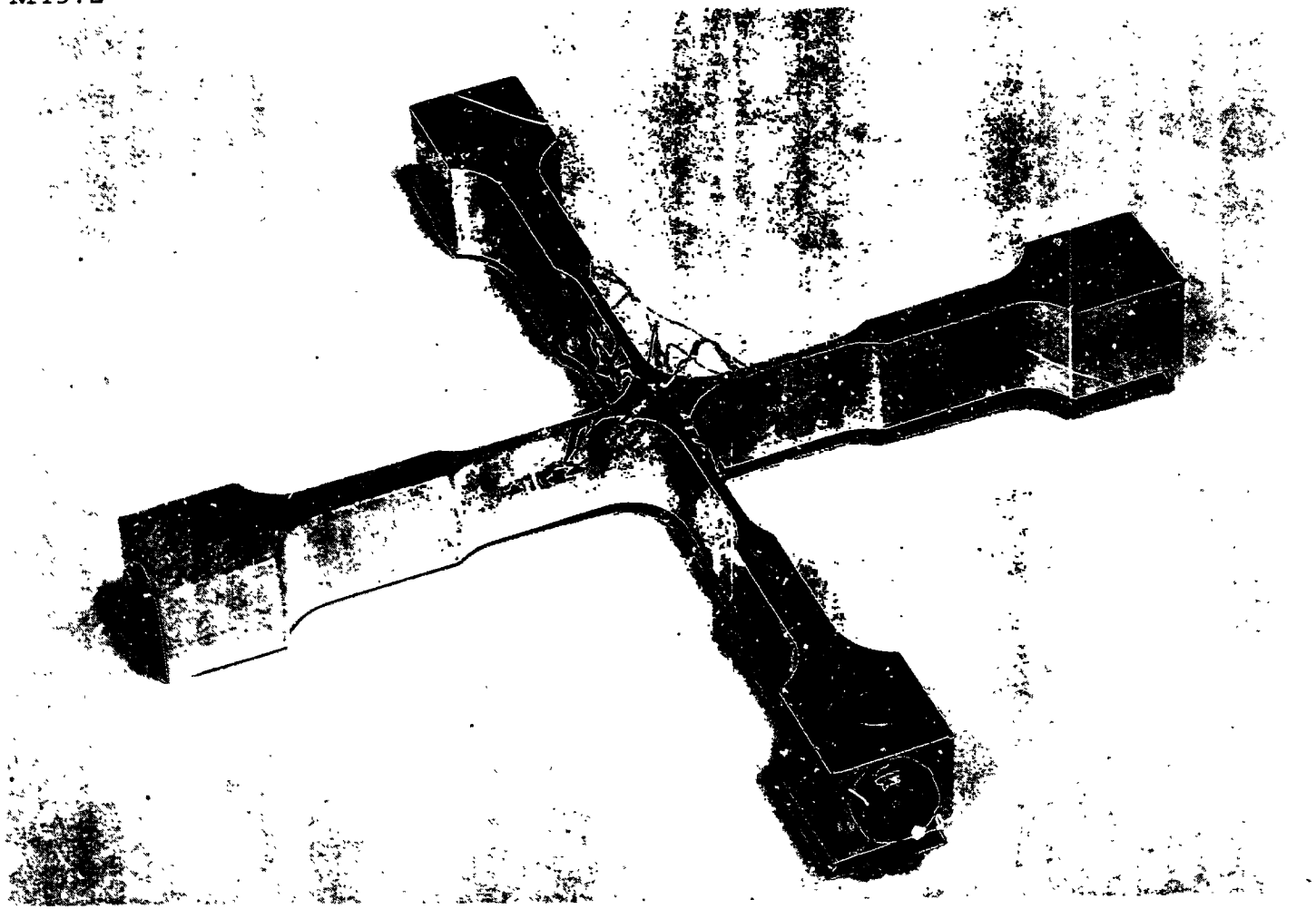

Fig. 28. Seven inch diameter cruciform sensor.

The sensor was fabricated from 0. 75 in. thick 6061 aluminum tooling plate. The total mass of the cruciform is 170 g with an overall length of 6. 75 in. The end masses are 0. 75 in. cubes drilled and tapped to receive 0. 50 in. diameter brass adjusting slugs The central hub, which has a mass of less than 10 g, is bored and tapped to accept a collet and chuck assembly for mounting to a torsion wire mount. The bending portion of the arm, which is about 1. 0 in. long, is placed as close to the hub as possible, and the effective bending point is about 0. 75 in. from the center. The bending portion is approximately 0. 075 in. thick to give a natural frequency of about 100 Hz with end masses of 40 g; including brass slugs. The cruciform is mounted in a corotating vacuum chamber 7. 75 in. o. d. by 2. 5 in. high with a wall thickness of 0. 25 in. Both lucite and aluminum chambers have been made.

The new sensor was found to be superior to the original designs in a number of ways. It had a higher Q (400 compared with 100 to 150), a larger initial frequency separation ratio between the translational modes and the gravitational gradient sensing mode (1. 31 compared with 1. 21 to 1. 26), and less sensitivity to frequency shift under rotation (3% compared with 6 to 16%). The curves of frequency shift of the gravitational gradient modes as a function of rotation for three different sensors are shown in Fig. 29. The frequency shift of 3% for the new sensor at operating speed, ($2\Omega = \omega_g$) agrees fairly well with that calculated from (25)

$$\frac{\omega_g}{\omega_o} = \left[1 + \frac{b}{a-b}\left(\frac{2\Omega}{\omega_o}\right)^2\right]^{1/2} \approx 1 + \frac{1}{2}\left(\frac{0.750}{3.375 - 0.750}\right)\left(\frac{1}{2}\right)^2$$

$$\approx 1.035 \quad . \qquad (35)$$

6. Gravitational Gradient Sensitivity

One of the important sensor design parameters is the response of the sensor to gravitational gradient fields. A theoretical analysis of the response of a rotating cruciform sensor structure to various gravitational and inertial forces was carried out early in the program. It was presented as a paper at the AIAA Second Annual Meeting in San Francisco on 26 July 1965 by C. C. Bell.[5] The paper is included as Attachment C to this report.

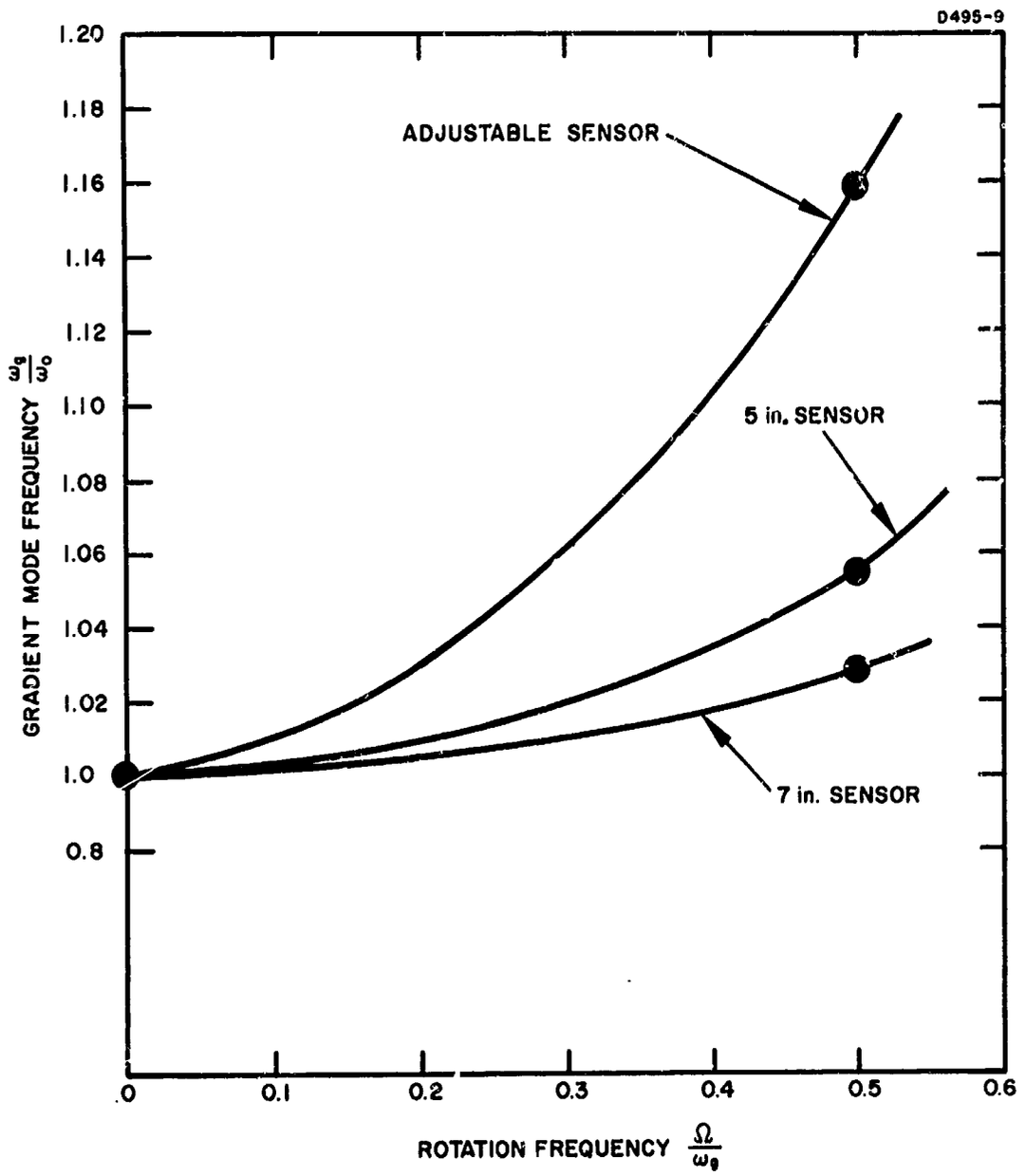

Fig. 29. Gravity gradient mode frequency shift under rotation.

The analysis showed that the gradient sensing or tuning fork mode of the sensor is driven only by the gravitational gradient forces at 2ω; all of the other gravitational forces had canceled out. A more important aspect of the analysis showed that the gradient sensing mode is independent of the motions of the center of mass of the sensor and therefore is independent of external inertial or vibrational forces or torques on the sensor which must necessarily act through the motions of the hub.

Because of the detailed analysis available in Attachment C, the work will not be repeated here; however, the results obtained will be used to calculate the response of the sensors to the gravitational gradient field of a mass.

The equation for the maximum deflection Δ_{max} of the sensor arms is given by (see eq. (43) of Attachment C):

$$\Delta_{max} = \frac{3GM}{2R^3} r \frac{Q}{(2\omega)^2} \sin 2\omega t \qquad (36)$$

where $3GM/2R^3 \sin 2\omega t$ is the spatially varying component of the gravitational gradient of a mass M at a distance R, r is the effective radius of the sensor or the distance from the center of mass of one of the arms to the center of mass of the whole sensor, Q is the quality factor of the sensor, and ω is the rotation speed.

Note that the deflection of the sensor arms depends only on the effective radius, frequency, and Q of the sensor and not upon its mass or other parameters. The same equation was also obtained in previous analyses for the response of radially vibrating structures.[2] For typical sensors, the maximum deflection usually is less than 10^{-9} cm or 0.1 Å; this is much smaller than a wavelength, which means that optical detection techniques cannot be used. It was found in previous work (see Appendix B) that it is possible to measure ac mechanical displacements down to 10^{-14} cm by using piezoelectric strain transducers to measure the ac strains in the body caused by these displacements.

However, when we use strain transducers to measure the response of the sensor, we find that the amount of strain in the sensor arm produced by a given deflection is a strong function of the details of design of the sensor arm. As shown by (22), (25), (36), and (44) of Attachment C, the strain ϵ_{max} in the arm is given by

$$\epsilon_{max} = \frac{M_A c}{EI} = \frac{-V_B (b + L) c}{EI} = \frac{(b + L) c \Delta_{max}}{\left(\frac{L^3}{3} + bL^2 + b^2 L\right)} \qquad (37)$$

where M_A, V_B, b, and L are as defined in Fig. 7 of Attachment C, I is the moment of inertia, c is the half thickness of the arms, and E is Young's modulus.

The strain calculated by (37) is the maximum strain at the hub. The actual strain measured by the barium titanate strain transducers is an averaged strain which depends upon its position along the sensor arm. According to beam deflection theory, the strain in an end loaded beam of uniform cross section is a maximum at the clamped end and decreases linearly to zero at the point where the force is applied. Thus, to determine the effective strain measured by the strain transducer, it is necessary only to determine its position x along the arm starting from the center of the end mass

$$\epsilon = \frac{x}{L + b} \epsilon_{max} \cdot \qquad (38)$$

The voltage V given out by the piezoelectric transducers when experiencing the strain ϵ is given by

$$V = \epsilon\sigma = \frac{3GM}{2R^3} \frac{Q}{(2\omega)^2} \frac{x\,c\,r}{\left(\frac{L^3}{3} + bL^2 + b^2L\right)} \sigma \sin 2\omega t \qquad (39)$$

where σ is the transducer "gauge" factor. For the barium titanate transducers we have been using, this factor has been 7×10^4 V/in./in. (see Section II-E).

We now wish to calculate the output to be expected from the sensor structures we have been using. We will assume that for laboratory purposes we can use the gravitational gradient of the earth so that $3GM/2R^3 = 2.3 \times 10^{-6}$ sec^{-2}. Then if we take the following experimental parameters for the sensors, we obtain the results shown in Table III. The four different sensors are as follows:

Sensor A — The cut down monolithic sensor which was used to generate the noise curves shown in Figs. 59 and 60.

Sensor B — The adjustable sensor used to obtain the gravitational calibration data in Attachment E.

Sensor C — The 7 in. monolithic sensor used to take the noise curve in Fig. 61 and the later gravitational calibration data.

Sensor D — A 7 in. monolithic sensor with the arm thickness reduced to lower the natural frequency to 50 Hz.

TABLE III

Calculation of Sensor Response

Sensor	Frequency f, H_z	Rotation Speed ω, rad/sec	Quality Factor Q	Effective Radius r, cm	Arm Half Thickness, cm	Arm Length L, cm	End Mass Radius b, cm	Strain Factor x/r	Maximum Deflection Δ, 10^{-9} cm	Maximum Strain, ϵ 10^{-11}	Voltage Output V, μV (μVrms)
A	117	368	100	4.4	0.070	2.3	1.2	0.7	1.9	3.25	1.6 (1.1)
B	88.5	278	120	5.0	0.038	1.8	0.3	0.6	4.6	12	5.1 (3.6)
C	107	335	445	7.2	0.100	2.4	4.2	0.9	17	16	10 (7)
D	50	156	275	7.2	0.059	2.4	4.2	0.9	46	25	16 (11)

The results of Table III indicate that the 7 in. monolithic sensors designed to give better mode separation and less frequency shift also give a higher voltage output for a given gravitational gradient input. The output is not quite as large as might be expected from the increase in Q and size, but this is because of the sensitivity of the strain to the detailed sensor design (see (37)). Notice that sensor C has an arm deflection which is almost four times that of sensor B, but the maximum strains are nearly equal.

The differences between sensor C and sensor D are instructive. The two sensors are identical except that the arm thickness on D was lowered to 0.059 cm from 0.100 cm. This lowered the frequency to 50 Hz, which causes the deflection to increase substantially despite the slight decrease in Q at the lower frequency. However, the conversion of deflection to strain is a function of the arm thickness, so that the net increase in strain or voltage output is not great.

Table III and eqs. (36) and (37) indicate that it is desirable to operate the sensors at low frequencies. However, the increased sensitivity must be balanced against the engineering problems of vibration isolation, transducer impedance, signal filtering, and sensor size, all of which become more troublesome at lower frequencies.

C. SENSOR MOUNT STUDIES

One problem in constructing a feasibility model of a rotating gravitational mass sensor is devising a structure to mount the sensor head to the rotation mechanism. This problem was originally thought to be minor compared with that of developing a sensor head which would be stable under rotation; however, it turned out to be the source of many of our experimental difficulties. At the present time, it is the major limiting uncertainty in our work, and the mount behavior is still not as well understood as that of the sensor.

The mounting structures involved three major areas of study and investigation: (1) the interaction of the mount vibrational modes with the sensor vibrational modes; (2) the stability of the mount structures under rotation; and (3) the vibrational isolation characteristics of the mount-sensor system.

It was originally thought that the mount problem would be minor because of the knowledge that the gradient sensing mode of the sensor, being of tensorial character, would be independent of any effects occurring at its center of mass. It is true that the gravitational gradient sensing mode frequency is not changed by a change in mount stiffness, and the mode is not excited directly by motions of the mount. However, as we shall see below, the mount stiffness affects the translational modes of the sensor, and the various translational modes shift under rotation until it is difficult to separate them from the gravitational gradient mode. The vibrations of the mount excite the translational modes, which then couple through the sensor imperfections into the gravitational gradient mode. These interactions can both be eliminated by using a soft mount, but then we encounter the problem of mount instability under rotation.

1. Sensor-Mount Vibrational Mode Interaction

A major problem with cruciform gravitational mass sensors lies in maintaining adequate frequency separation between the various vibration sensitive resonant modes of the sensor system and the gravitational gradient sensing mode of the cruciform sensing head. If this frequency separation can be maintained, it will be possible to use narrow band amplifiers to separate the gravitationally driven sensor response from the inertially driven responses.

In the initial experimental work (see Section II-B), it was found that if the sensor has a small central mass and is well isolated from other masses by suspension from a weak spring, the gravity gradient sensing mode is the lowest in frequency and is well separated from the rest of the vibrational modes. However, when a mount with a weak spring constant is used it becomes difficult to rotate the sensor

up to the desired operating speed because the mount cannot resist the centrifugal forces. When the mount stiffness is increased to resist the centrifugal force, two new translational modes formed by the spring constant of the mount and the total mass of the sensor become important. These modes cause the two translational modes in the sensor head to shift upward, helping to solve the mode separation problem. Under rotation, however, the translational modes split; at the desired rotational speed, they become close enough to the gradient sensing mode to make frequency selection techniques difficult.

A combined program of theoretical analysis and experimental study of the vibrational mode behavior of various combinations of sensors and sensor mounts was undertaken in an attempt to understand this behavior. This work is presented in detail in Attachment D. In this attachment we develop a mathematical model of a rotating, spring mounted, cruciform gravitational gradient sensor and obtain equations describing the behavior of the normal mode frequencies of the system as a function of the system parameters and the rotation speed. These equations agree well with the data from actual sensors and can be used to aid in the design of optimum mount-sensor structures. The theory and experiment indicate that it is possible to operate a sensor at the desired rotation speed of one-half of the gradient sensing mode frequency and still maintain adequate frequency separation between the vibration sensitive translational modes and the gradient sensing mode. Because of the detailed discussion in Attachment D, only a summary of the sensor-mount mode behavior is presented here.

a. Theoretical Analysis

The model used for the theoretical analysis is that shown in Fig. 23 of Section II-B. The sensor has a central mass M and four smaller masses m at the ends of four arms of length a; these arms are pivoted at a distance b from the center of the sensor. The central mass is assumed to be attached to a rotating axis through an axially symmetric spring of constant K. The axis was assumed to remain fixed in position at the origin, while rotating at a constant angular frequency Ω. The central mass is at the position $\vec{R}$, and its speed of rotation varies about Ω by a small amount $\dot{\phi}$. The masses at the ends of the arms also can vibrate through a small angle α_n with respect to the rotating reference frame.

The Lagrangian of this system in terms of the vibrational mode amplitudes of the sensor (A_g, A_t, A_-, and A_+) and the motions of the center of mass (x, y) is given by (see eq. (26) of Attachment D)

$$L = \mu[\dot{x}^2 + \dot{y}^2 + 2\Omega(x\dot{y} - y\dot{x}) + (\Omega^2 - \Omega_m^2)(x^2 + y^2)] +$$

$$\sqrt{2}(\dot{x} - \Omega y)(\dot{A}_+ - \Omega A_-) + \sqrt{2}(\dot{y} + \Omega x)(\dot{A}_- + \Omega A_+) +$$

$$\frac{1}{2}\left(\frac{I + 4ma^2}{m}\right)\dot{\theta}^2 + 2a\dot{\theta}\dot{A}_t + \frac{1}{2}(\dot{A}_g^2 + \dot{A}_t^2 + \dot{A}_+^2 + \dot{A}_-^2) -$$

$$\frac{1}{2}\omega_g^2 (A_g^2 + A_t^2 + A_+^2 + A_-^2) \tag{40}$$

where we have defined the following constants as

- the gradient sensing mode frequency

$$\omega_g^2 = \frac{k'}{m} = \frac{k}{m} + \frac{b}{a-b}\Omega^2 , \tag{41}$$

- the reduced mass of the sensor in the translational mode

$$\mu = \frac{M + 4m}{2m} , \tag{42}$$

- and the mount translational frequency

$$\Omega_m^2 = \frac{K}{M + 4m} . \tag{43}$$

The equations of motion derived from this Lagrangian for the gravitational gradient sensing mode and the torsional mode are independent of the mount parameters and were discussed in Section II-B.

The equations of motion for the four translational modes cannot be solved independently since the sensor modes interact with the mount motions. For example, the equations of motion for the sensor translational modes involve both the x and y motions of the mount:

$$\frac{d}{dt}\frac{\partial L}{\partial \dot{A}_+} - \frac{\partial L}{\partial A_+} = \sqrt{2}[\ddot{x} - 2\Omega\dot{y} - \Omega^2 x] + \ddot{A}_+ + \omega_g{}^2 A_+ = 0 \quad (44)$$

$$\frac{d}{dt}\frac{\partial L}{\partial \dot{A}_-} - \frac{\partial L}{\partial A_-} = \sqrt{2}[\ddot{y} + 2\Omega\dot{x} - \Omega^2 y] + \ddot{A}_- + \omega_g{}^2 A_- = 0 \quad (45)$$

and the equations of motion for the mount motions involve all of the translational mode amplitudes:

$$\frac{d}{dt}\frac{\partial L}{\partial \dot{x}} - \frac{\partial L}{\partial x} = 2\mu[\ddot{x} - 2\Omega\dot{y} - (\Omega^2 - \Omega_m{}^2)x] + \sqrt{2}[\dot{A}_+ - 2\Omega A_- - \Omega^2 \dot{A}_+] = 0 \quad (46)$$

$$\frac{d}{dt}\frac{\partial L}{\partial \dot{y}} - \frac{\partial L}{\partial y} = 2\mu[\ddot{y} + 2\Omega\dot{x} - (\Omega^2 - \Omega_m{}^2)y] + \sqrt{2}[\ddot{A}_- + 2\Omega\dot{A}_+ - \Omega^2 A_-] = 0 . \quad (47)$$

However, we can obtain a partial separation of the modes if we define a right- and a left-hand circularly polarized mode for the translational motions of the mount

$$R = \frac{1}{\sqrt{2}}(x + iy) \quad (48)$$

$$L = \frac{1}{\sqrt{2}}(x - iy) \quad (49)$$

along with the right- and left-hand modes for the sensor

$$A_r = \frac{1}{\sqrt{2}}(A_+ + iA_-) \quad (50)$$

$$A_\ell = \frac{1}{\sqrt{2}}(A_+ - iA_-) . \quad (51)$$

These can then be used to express the four equations of motion (eqs. (44) to (47)) in an equivalent form

$$2\mu\left[\ddot{R} + 2i\Omega\dot{R} - (\Omega^2 - \Omega_m{}^2)\,R\right] + \sqrt{2}\left[\ddot{A}_r + 2i\Omega\dot{A}_r - \Omega^2 A_r\right] = 0 \quad (52)$$

$$2\mu\left[\ddot{L} - 2i\Omega\dot{L} - (\Omega^2 - \Omega_m{}^2)\,L\right] + \sqrt{2}\left[\ddot{A}_\ell - 2i\Omega\dot{A}_\ell - \Omega^2 A_\ell\right] = 0 \quad (53)$$

$$\ddot{A}_r + \omega_g{}^2 A_r + \sqrt{2}\left[\ddot{R} + 2i\Omega\dot{R} - \Omega^2 R\right] = 0 \quad (54)$$

$$\ddot{A}_\ell + \omega_g{}^2 A_\ell + \sqrt{2}\left[\ddot{L} - 2i\Omega\dot{L} - \Omega^2 L\right] = 0\ . \quad (55)$$

Notice that instead of all four mode amplitudes appearing in each equation indicating coupling between all four modes as they did in (44) to (47), we now find that the right hand circularly polarized mount mode interacts only with the right hand sensor mode, and the two left hand modes interact similarly.

The equations now only have to be solved in pairs, and the only difference between the two pairs of equations is the direction of rotation $\pm\,\Omega$.

The solution to these equations is found in Attachment D and is

$$(\omega \pm \Omega)^4 + \mu(\omega_g{}^2 - \omega^2)\left[(\omega \pm \Omega)^2 - \Omega_m{}^2\right] = 0\ . \quad (56)$$

The four solutions to this fourth order equation in ω then give us the vibrational frequencies of the four translational modes as a function of the rotation rate Ω, the mass ratio of the sensor masses $\mu = (M + 4m)/2m$, the basic mount frequency $\Omega_m^2 = K/(M + 4m)$, and the frequency of the gradient sensing mode ω_g. Since the gradient sensing mode frequency is also a function of rotation speed, we can express the dependence on Ω directly if we wish:

$$(\omega \pm \Omega)^4 + \frac{M + 4m}{2m}\left(\frac{k}{m} + \frac{b}{a-b}\Omega^2 - \omega^2\right)\left[(\omega \pm \Omega)^2 - \frac{K}{M + 4m}\right] = 0\ . \quad (56a)$$

In general it is necessary to use a computer to find the solutions to (56); however, under certain simplified conditions the equation reduces in order and can be solved.

The case of negligible mount interaction ($\Omega_m = 0$) was discussed in Section II-B. It was shown that the maximum frequency separation between the gravitational gradient sensing mode and the lower of the split translational modes of the sensor at the desired rotational speed was

$$\omega_- = 1.081\,\omega_g , \tag{57}$$

and the difference was decreased as the central mass increased.

When the mount stiffness is made appreciable, eq. (56) predicts a number of interesting interactions between the sensor and the mount. As the basic mount frequency is increased, the sensor translational modes are pushed upward away from the gravity gradient sensing mode, thus helping to maintain adequate frequency separation.

However, if the basic mount frequency is made higher, we find that when the mount resonance splits under rotation and the higher mode becomes very close to the gradient sensing mode at the desired operating speed ($\Omega = 1/2\ \omega_g$). A typical curve showing these effects appears in Fig. 30. Other curves for different mount frequencies are given in Attachment D.

Since our sensors are designed to be rotated at a rate which is half of the gradient sensing mode vibration frequency, we also calculated solutions to (56), assuming that $\Omega = 1/2\,\omega_g$ but varying the mass ratio and the basic mount frequency Ω_m (see Fig. 31). From these curves we see that changing the mass ratio does not aid appreciably in obtaining frequency separation.

b. Experimental Comparison for Stationary Sensors

If we assume that the sensor and mount are not rotating ($\Omega = 0$), eq. (56) simplifies somewhat to become

$$\omega^4 + \mu\,(\omega_g^2 - \omega^2)\,(\omega^2 - \Omega_m^2) = 0 . \tag{58}$$

When this is plotted for $\mu = 3.07$ ($M/m = 2.15$), we obtain the curves shown in Fig. 32. The light lines $\omega_\pm$ and Ω_m indicate the behavior of the sensor translational modes and the mount translational modes if they did not interact with each other.

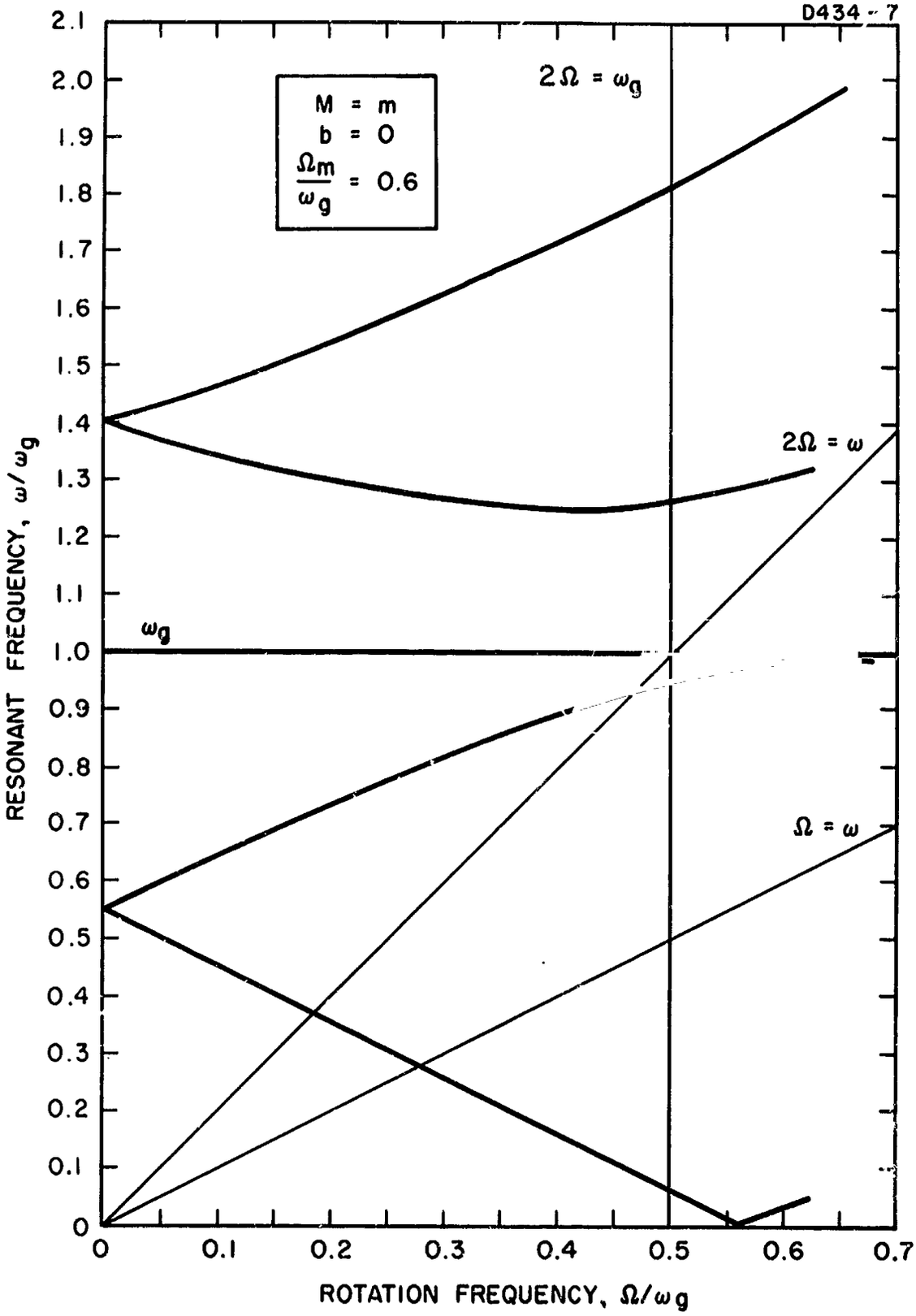

Fig. 30. Predicted translational mode splitting ($\Omega_m = 0.6\ \omega_g$).

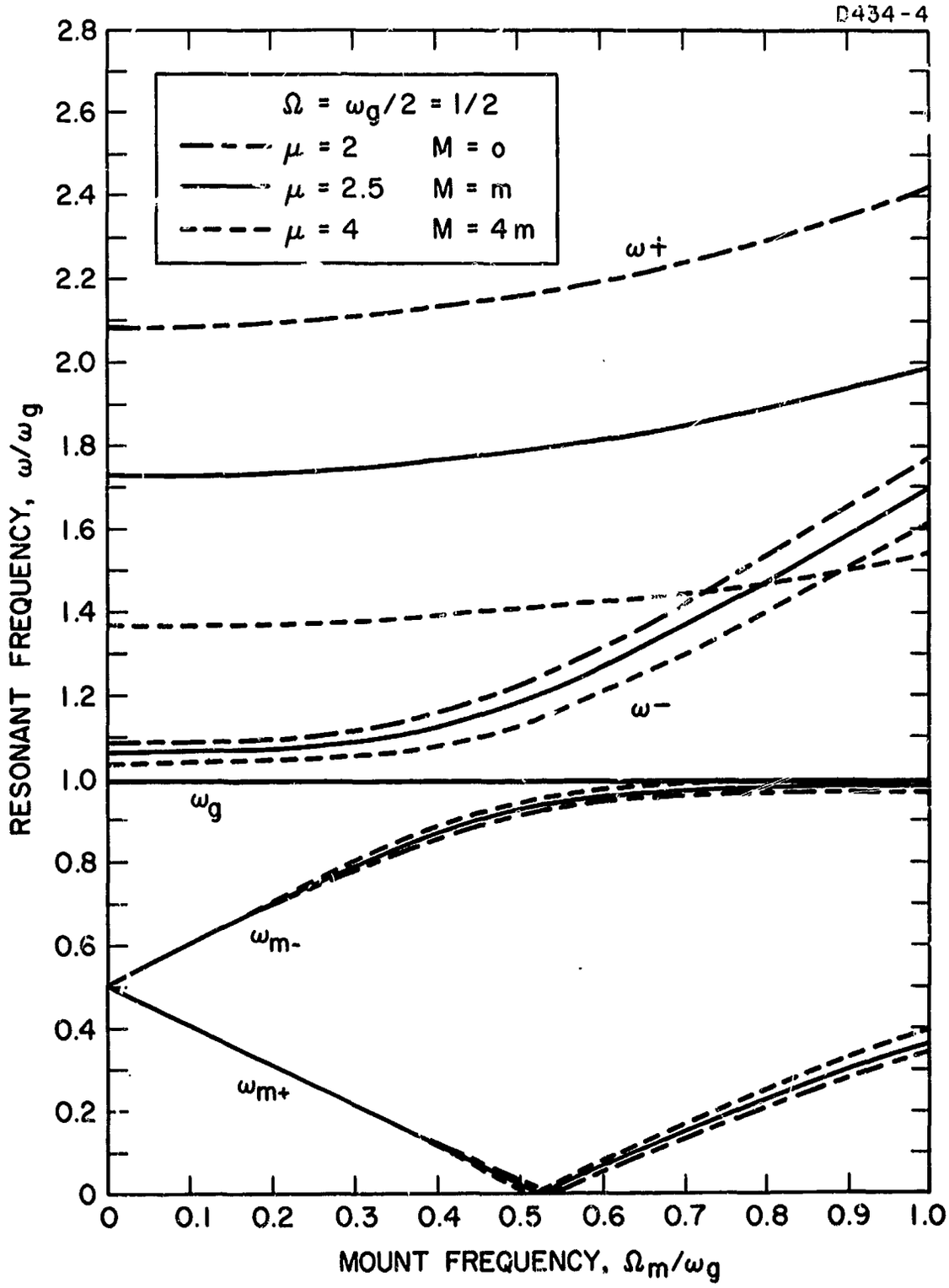

Fig. 31. Predicted translational mode splitting ($\Omega = 1/2\ \omega_g$).

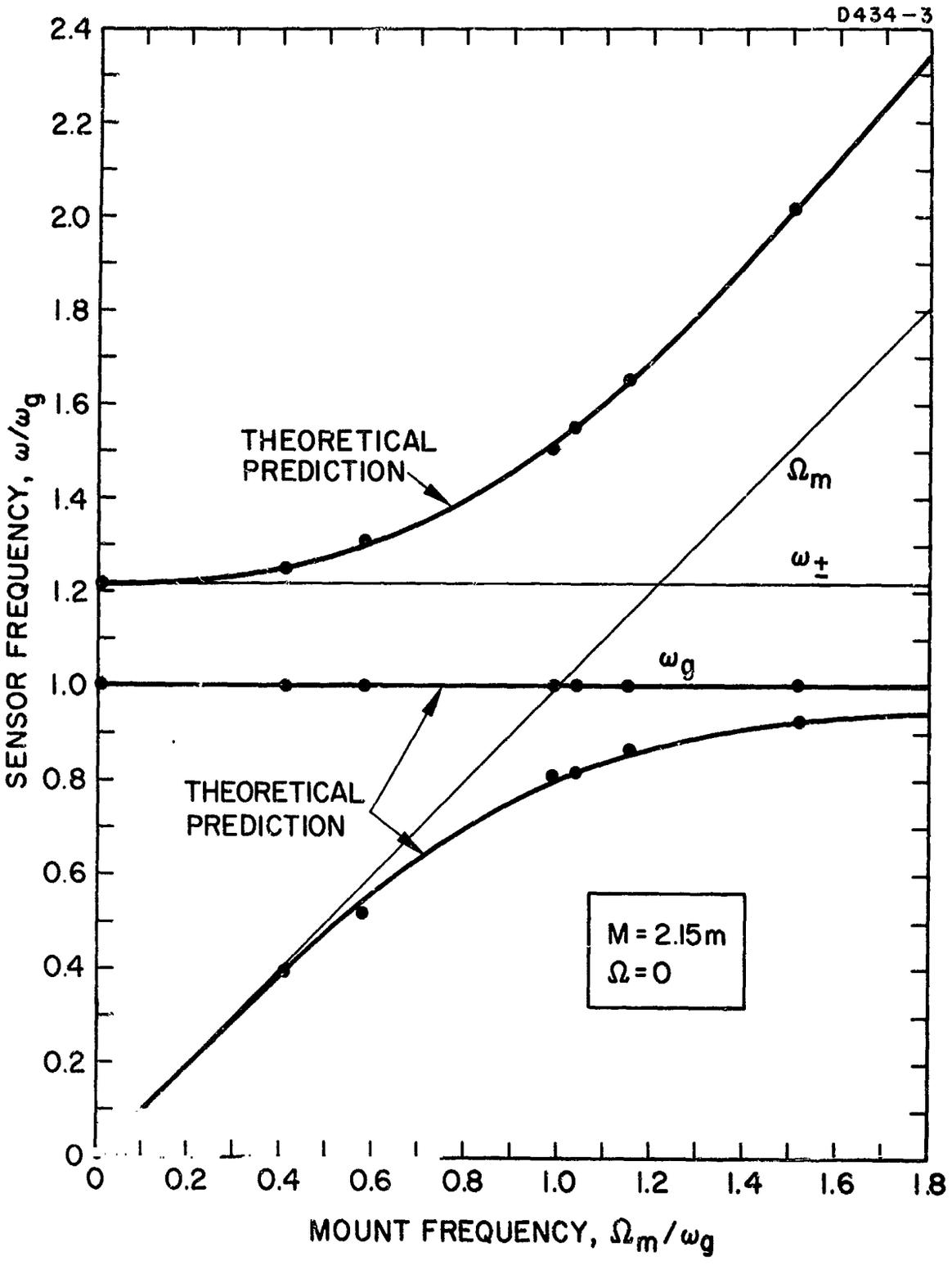

Fig. 32. Mount-sensor interaction (nonrotating).

One of our sensors had been tested with a number of possible mounts. The frequency data from these tests were normalized and are plotted as the points in Fig. 32. The agreement between theory and experiment is excellent. This curve can be used to determine the basic mount frequency when the three resonant frequencies of the interacting system are known, and will aid in the optimum mount design.

c. Experimental Comparison Under Rotation

Only one set of frequency data is available for a rotating sensor on a fairly rigid mount. The mounting structure was a wire attached to the sensor at the center and held at the ends by the lid and base of a sensor vacuum chamber. The data are shown in Fig. 33. The two translational modes of the sensor and the two translational modes of the mount were not the same at zero rotation speed. This indicates that the sensor had a considerable asymmetry in construction.

Five data points were taken for this curve in order to determine the sensor parameters and the mount frequency. These parameters were then used in (32), (33), and (56) to obtain the theoretical curves.

Although the theoretical curves have the same general behavior as the actual measured data, the fit does not approach that of Figs. 27 and 32. It is believed that this results primarily because the torsion wire is not a linear spring; its spring constant depends upon the tension in the wire and the tension was increasing during rotation because of the centrifugal force acting on the unbalance in the sensor.

2. Mount Vibrational Isolation Characteristics

With a proper mounting structure the sensor can be vibrationally isolated from external noise sources acting through the mount. For an ideal sensor, the amount of vibrational isolation obtained from the mount is not important, because the gravitational gradient mode of an ideal sensor does not respond to vibrations (see Section III of Attachment F). However, a nonideal sensor responds to external vibrations through various second order effects. These second order coupling effects are described in detail in Attachment F. The mount vibrational isolation characteristics are also discussed in this analysis as part of the more detailed study of the vibrational response characteristics of the entire sensor-mount system.

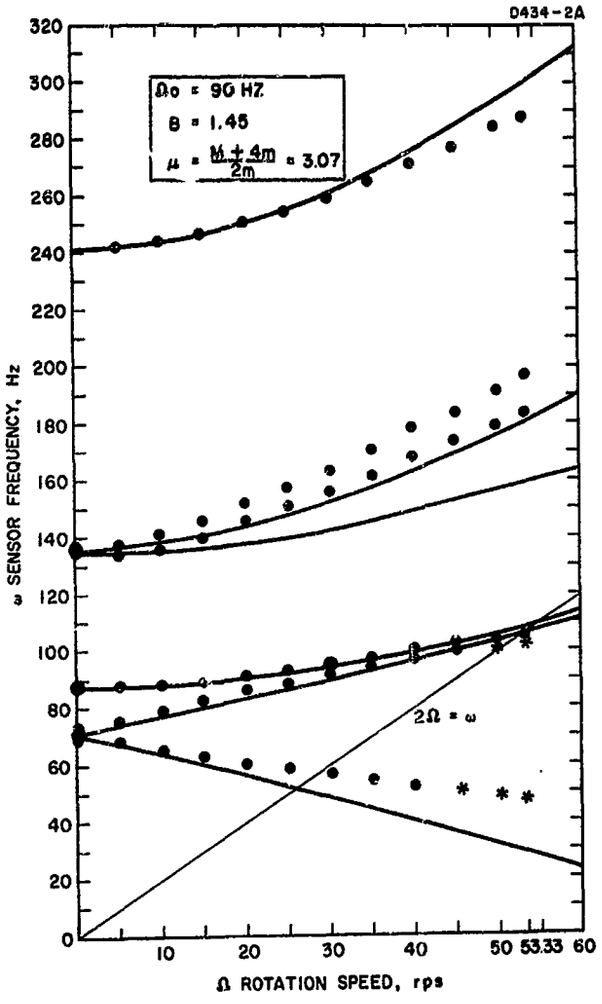

Fig. 33. Rotating sensor resonant modes on hard mount.

In general the analysis shows that the vibration isolation of the mounting structure improves as the inverse square of the mount frequency (see Fig. 34); therefore a soft mounting structure not only gives better mode frequency separation but also better vibrational isolation. This result was anticipated from our work on vibration isolation problems, and has been borne out in all of our experimental noise studies.

3. Mount Stability Under Rotation

Mount stability under rotation was one of our most difficult problems. Although a number of stable mounts have been found and used, they have various disadvantages; unfortunately, we do not completely understand their behavior. It is essential that mount stability be studied theoretically and experimentally in the next phase of the program.

The first sensor mount used in our work was a thick rod about 1/8 in. in diameter which was pressed through the central hole in the 5 in. monolithic cruciform sensor (see Fig. 35). This mount was obviously stable under rotation; however, the strong coupling of the sensor to the sensor chamber by the mount brought the translational modes so close to the gravitational gradient sensing mode that mode separation by frequency filtering was almost impossible. Although it was necessary to abandon this mounting structure early in the program, it has no fundamental faults. If the sensor chamber, its telemetering unit, and bearing axle were designed to weigh approximately the same as a sensor arm mass, and the vacuum chamber was suspended and rotated in a soft bearing (such as a magnetic bearing), the vibrational modes of the system would be well separated and there would be no mount instability problem.

Because of our problems with the solid mount, we next investigated a series of double ended torsion wire mounting structures. These consisted of a wire connected to the top and bottom of the vacuum chamber and to the center of the sensor (see Fig. 36). A large number of these mounts were constructed with different wire thicknesses varying from 0.006 in. to 0.040 in. diameter. Data were then taken on the frequency behavior of the vibrational mode under rotation.

These modes behave generally as predicted by the equations developed in Attachment D. The sensor translational modes at 0 rpm are pushed up as the torsion wire becomes thicker; with increased rotation, the translational modes split, and the gravitational gradient mode shifts upward.

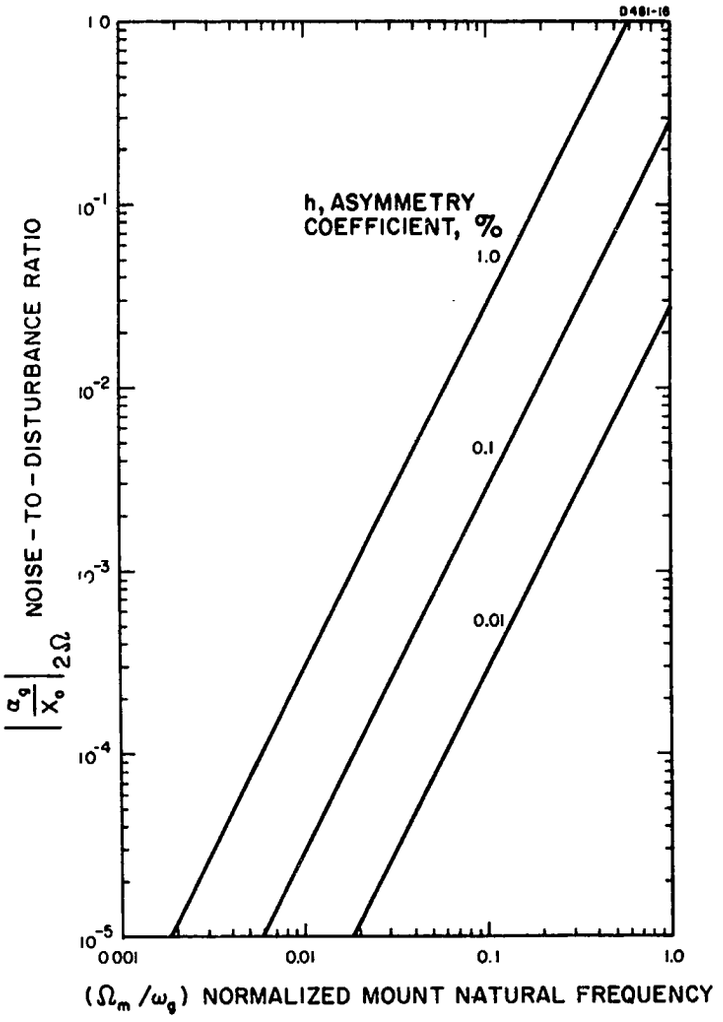

Fig. 34. Gravitational mode response (at gravity-sensing frequency) due to external disturbance of Ω negative circulation.

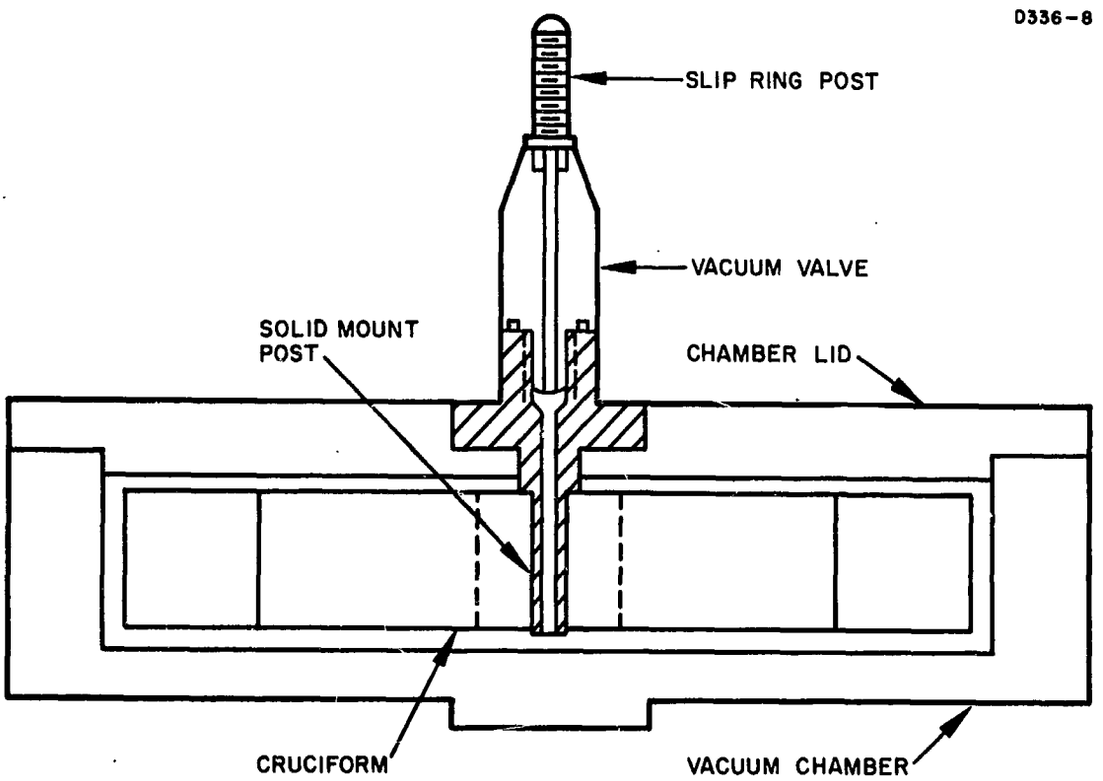

Fig. 35. Solid mount.

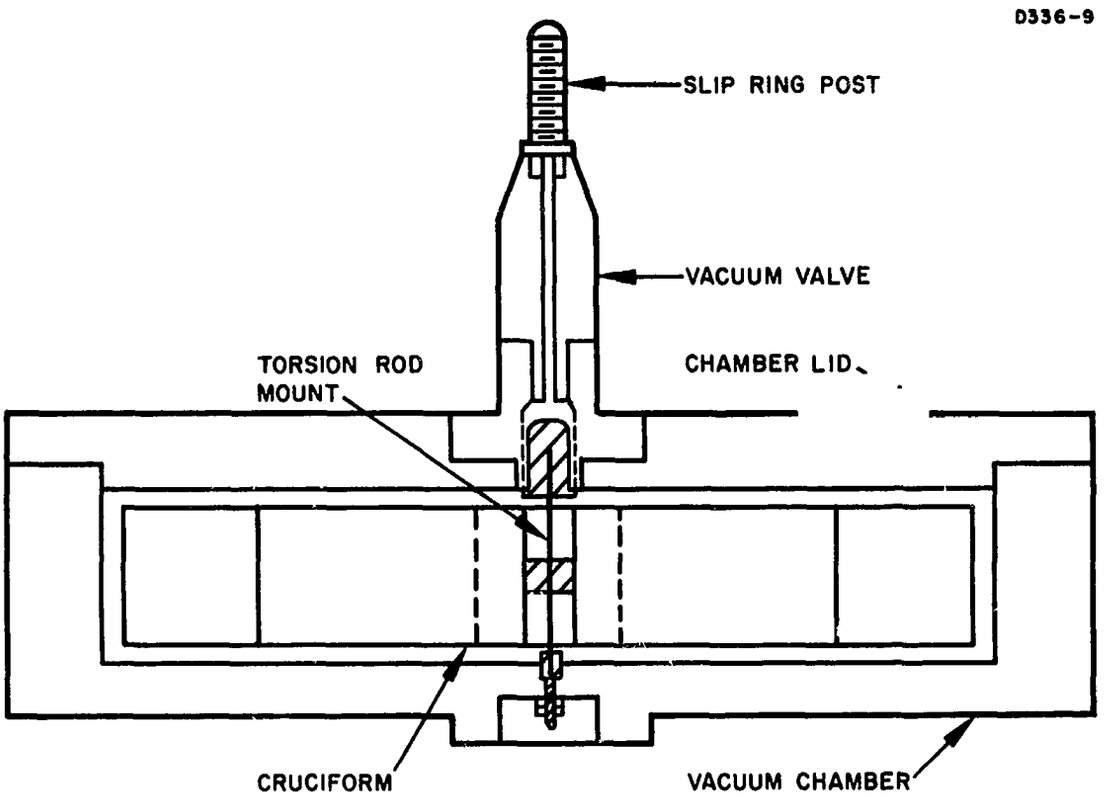

Fig. 36. Torsion mount.

During testing of the 0.012 and 0.016 in. torsion wires, the sensor speed could not be increased above 2700 and 3000 rpm, respectively, because the small diameter torsion wires were too weak to withstand the centrifugal force and keep the sensor head from flying out from the center (see Fig. 37). With the 0.020 in. torsion wire, however, the sensor could attain the desired operating speed. The graph (Fig. 27) shows that the gravitational gradient sensing mode is distinguishable at about 3 Hz above the upper mount translational mode frequency. However, the separation is not as great as would be desired, and the entire system operation was marginal. If we increased the mount thickness, the mode separation became even poorer; if we decreased the mount thickness, the mount became unstable.

Because of the problems encountered with a double-ended torsion wire mount for the sensor, a single-ended sensor mount was investigated. This consists of a very thin, low frequency mount operated far above its translational resonance point in a manner similar to an ultracentrifuge (see Figs. 26 and 38). The preliminary tests with a fine wire support gave good results. After a small amount of excursion as the rotation frequency passed through the mount resonance (typically at a few rps), the sensor was very stable and could be operated for hours without problems. The vibrational modes measured were found to be exactly those predicted by Attachment D for very low mount frequencies (see Fig. 27). Thin wires, rubber bands, and plastic tubing have also been used in this mount. The rubber and plastic mounts proved to be better for noise tests because of their low longitudinal stiffness which transmitted less vertical vibrational noise than the wire mount.

This mount was quite suitable for laboratory work, and most of our noise data were taken with it; however, it has a number of faults. Because it is single ended, it depends upon the earth's gravitational acceleration for stability, which makes it obviously unsuitable for either zero g or all orientation operation. In addition, it was not possible to achieve the ultracentrifuge type of operation unless the wire was quite long. This prevented sensor operation within a corotating vacuum chamber because the available chambers were too short to accommodate the mount. This caused a considerable problem in the noise tests because the sensor would windmill through the residual air in the stationary vacuum chamber, causing turbulence. This "vacuum turbulence" was one of the dominant noise sources in our final noise tests.

The ultracentrifuge suspension, however, did demonstrate that it was possible to stably rotate a sensor on a soft mount at a rotation rate well above the mount resonance frequency. To achieve the same benefits of good vibration isolation and vibrational mode frequency separation and to achieve all-axis orientation and short

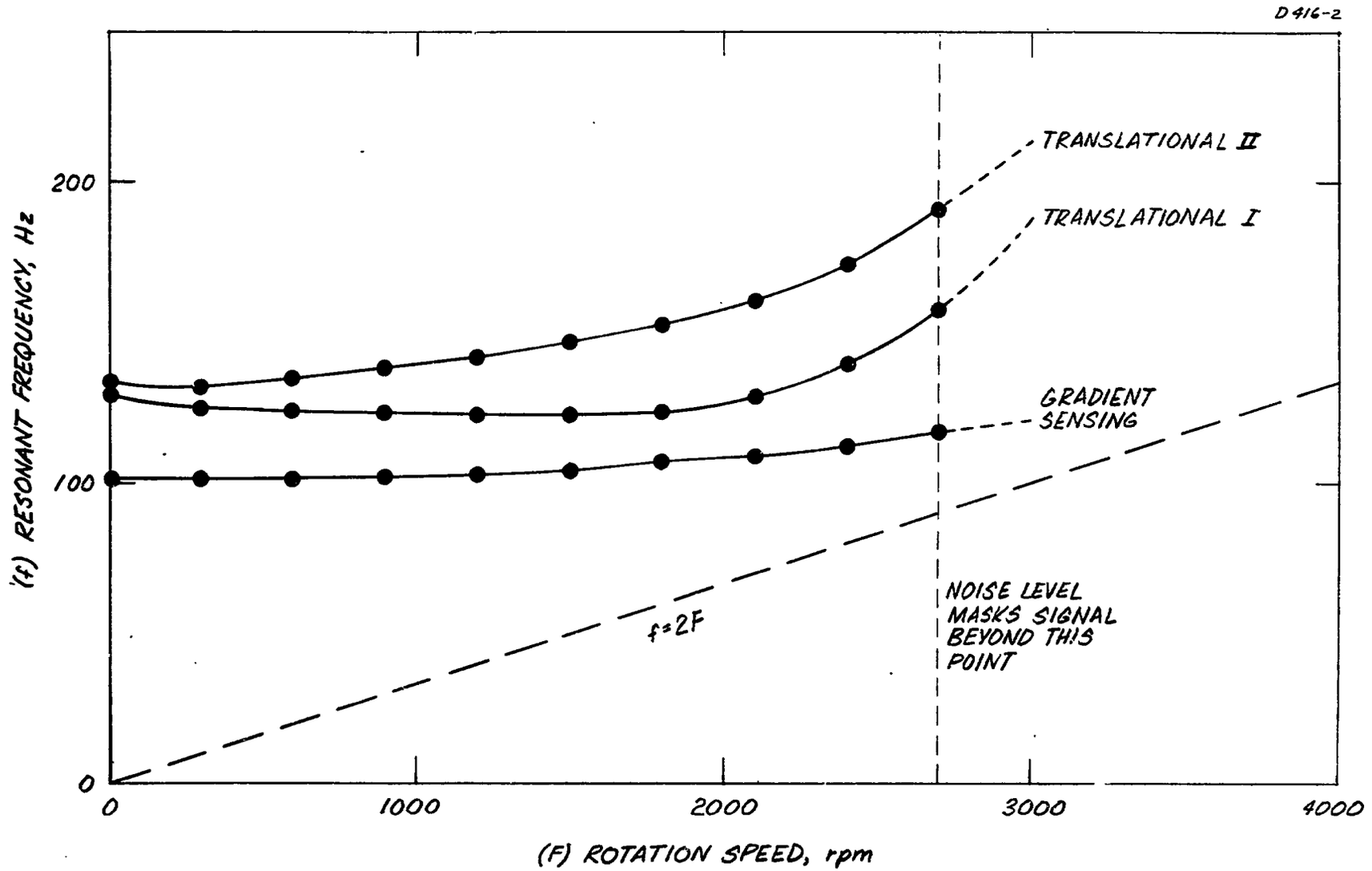

Fig. 37. Resonant modes of 100 Hz cruciform on 0.012 in. torsion wire.

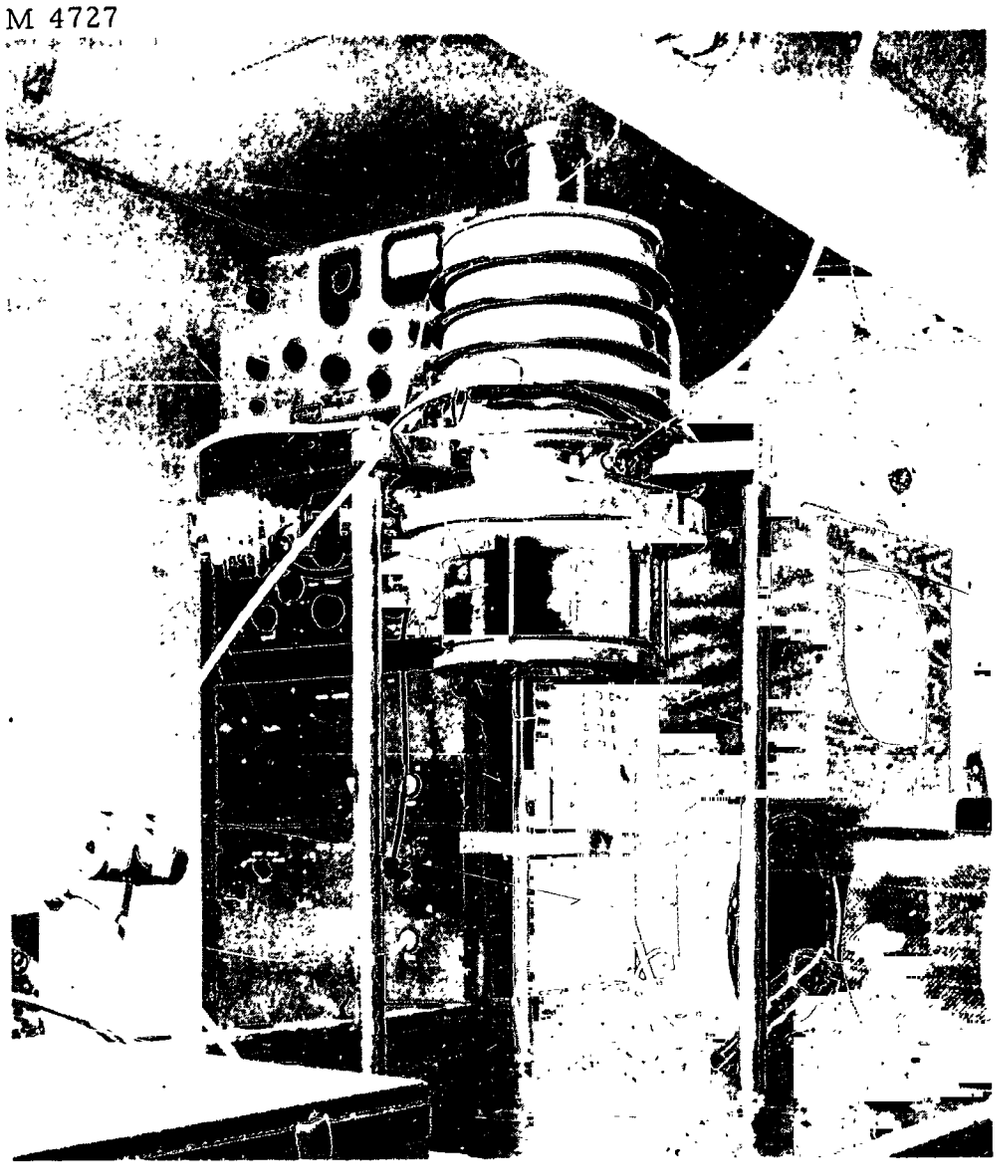

Fig. 38. Ultracentrifuge mount.

mount length, another sensor mounting structure was developed (see Fig. 39). This mount consists of coil springs mounted between the sensor head and the corotating vacuum chamber.

The study of this mounting structure was begun late in the program, and only preliminary results are available. The theoretical study of the stability of this system was begun, and the preliminary results are presented in Appendix E. These preliminary mathematical results indicate that the structure should be unstable at any rotation speed above its critical resonance. This is not borne out by the experimental results, however.

Several different four and eight spring mounts with various spring constants were investigated using a 7 in. monolithic cruciform sensor in a large lucite vacuum chamber mounted on an air bearing motor. The spring mount frequencies varied from 5 to 25 Hz. In a typical test with an eight spring mount, a region of instability appeared as the chamber rotation speed was increased, with the sensor leaving the center of rotation slightly as the rotation frequency passed through the mount frequency. As the rotation speed increased, the sensor would return to the center of rotation and would rotate stably. The mount was even capable of running through the mount resonance to the stable region when tilted at an angle of 15° to the horizontal (the limit being imposed by the air bearing side thrust limitations), demonstrating that mount operation is not dependent upon or affected by gravitational acceleration. However, when the rotation frequency was increased even more, a precession would begin and the system would become unstable.

In other tests with only four springs, the system could be brought up to a speed that was above the mount resonance and would appear stable; when left for many minutes, however, it would develop a precession and become unstable. It has not yet been determined whether this "metastable" behavior is basic to the mount or is an artifact caused by line transients or other effects.

The tests on these mounts were limited by lack of time and the desire to avoid damage to the air bearing, which would seize up whenever an instability developed at high speeds.

A number of unsolved questions remain, and a number of permutations of the basic mounting structure have not yet been investigated. We have not determined the role of gyro effects in cross coupling between the mount springs and in the basic stability of the mount, and we have not yet investigated the behavior when the springs are attached to the center of rotation of either the sensor or the vacuum chamber rather than at points off the rotation axis.

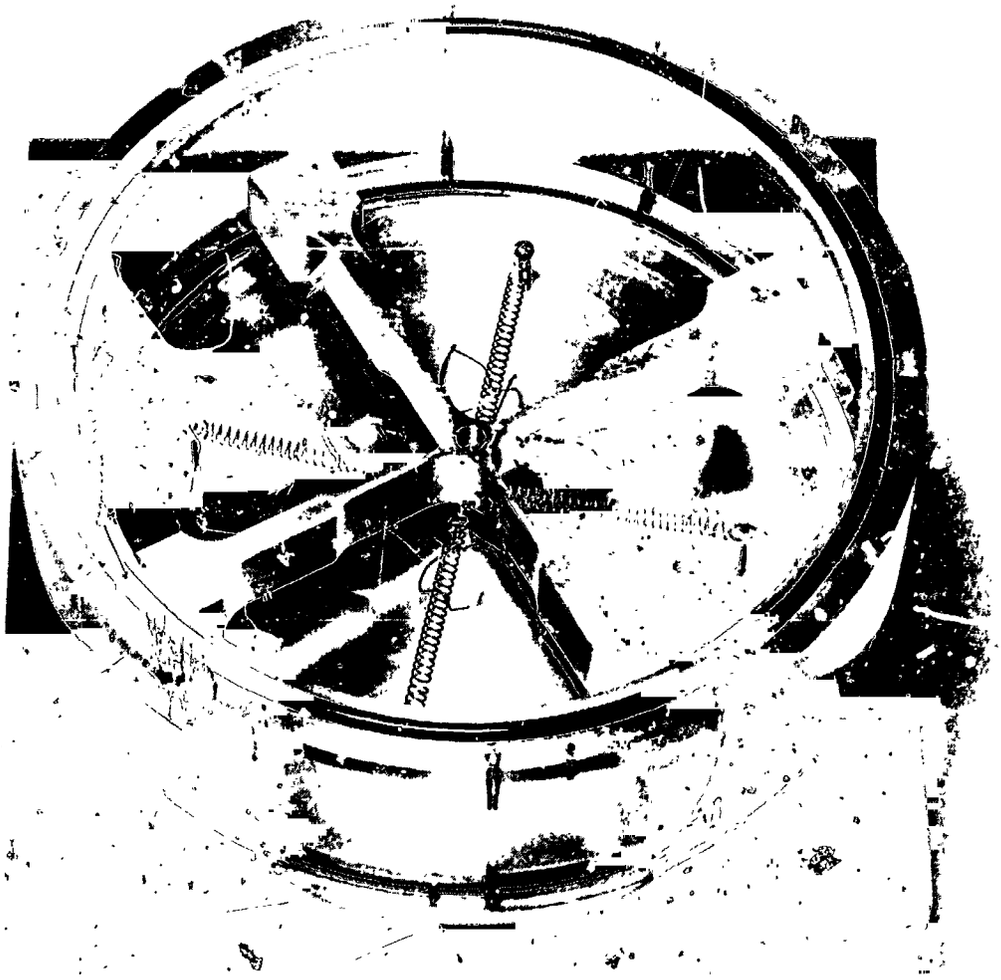

Fig. 39. Coil spring mount.

We have investigated an eight spring mount, and a mount with four springs all on one side (see Fig. 39), but we have not studied four center mounted springs, two springs, or two pairs of springs on opposite sides, either in parallel or at 90° with each other.

This preliminary work indicates that the low frequency coil spring mount is stable above its mount resonant frequency; since it is a low frequency mount, it should have the advantages of the ultracentrifuge suspension as well as being compact and capable of being operated in any position. Therefore, it appears suitable as a mounting structure for future gravitational mass sensors. A number of uncertainties exist, however, and its behavior is not yet completely understood. A theoretical model of mount stability, backed by experimental data, must be developed in order to have a basis for the design of optimum mount structures for future sensors.

D. BEARING AND DRIVE STUDIES

A major task in the program was the investigation of various types of bearings and drive mechanisms and the determination of their suitability for smoothly rotating the sensor structures. The primary concern of this investigation was to find a bearing and drive which generated a minimum amount of high frequency electromagnetic, acoustic, and vibrational noise which would disturb the sensor. Preliminary models of three different bearing structures were constructed and investigated. These were a precision ball bearing structure with an air drive and a motor drive, an air bearing with a motor drive, and a magnetic bearing with a motor drive.

1. Mechanical Bearing

The first bearing constructed on the program was a simple mechanical bearing consisting of a well aligned frame which held two gyro quality precision ball bearing races (see Fig. 40). The sensor chamber shafts were made to fit in the bearings, and the entire rotor structure was reground after assembly to insure that the center axis of the chamber corresponded to the center axis of the shaft The sensor was mounted in the chamber on a solid mount (see Fig. 35) and had vibrational resonances near 190 Hz. The chamber could be driven either by an air jet injected at an angle through the air port (the small hole to the left in Fig. 40(b)) or by a synchronous motor through an elastic coupling to the shaft. We did not expect this bearing to be a low noise bearing, but were primarily interested in using it for a study of sensor stability under rotation and an investigation of the feasibility of using slip rings for readout of the signals.

The sensor and vacuum chamber were placed in the ball bearing mount and driven by air pressure to a rotational speed of about 6000 rpm (100 rps). The unfiltered, unamplified resonant response of the sensor at this speed was about 100 mV; this was entirely a result of the vibrational noise from the ball bearings, which were emitting an audible noise. The resonant frequency of the response was at about 200 Hz, which was higher than the resonant response at 0 rpm.

The rotor with the sensor in it was then dynamically balanced to a center of mass location within 5 μin. of the center of rotation. This balancing brought the magnitude of the noise output down to approximately 20 mV, the resonant response still being at 200 Hz. The bearing noise was no longer audible, but vibrations could be felt with the hand. It was not feasible to consider balancing the rotor to a much greater degree of accuracy and these preliminary results with the mechanical bearing confirmed our original supposition that ball bearings do not have a low noise output because of their discrete structure.

M 3677

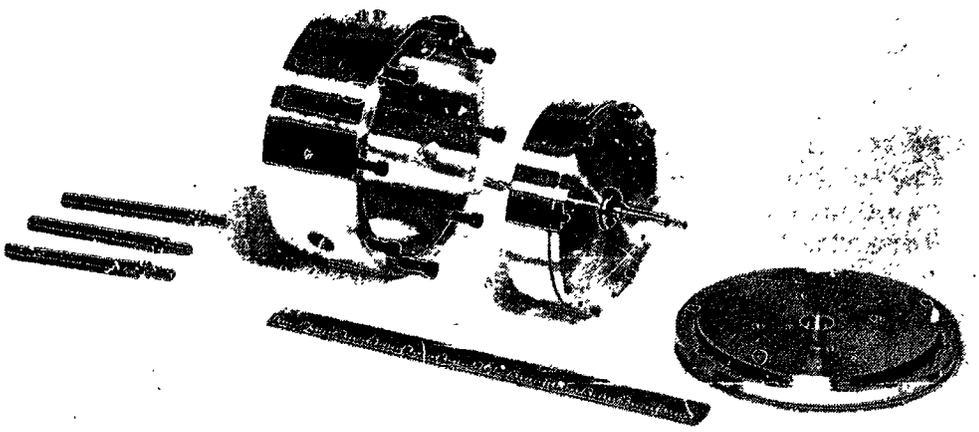

(a) Exploded view.

M 3676

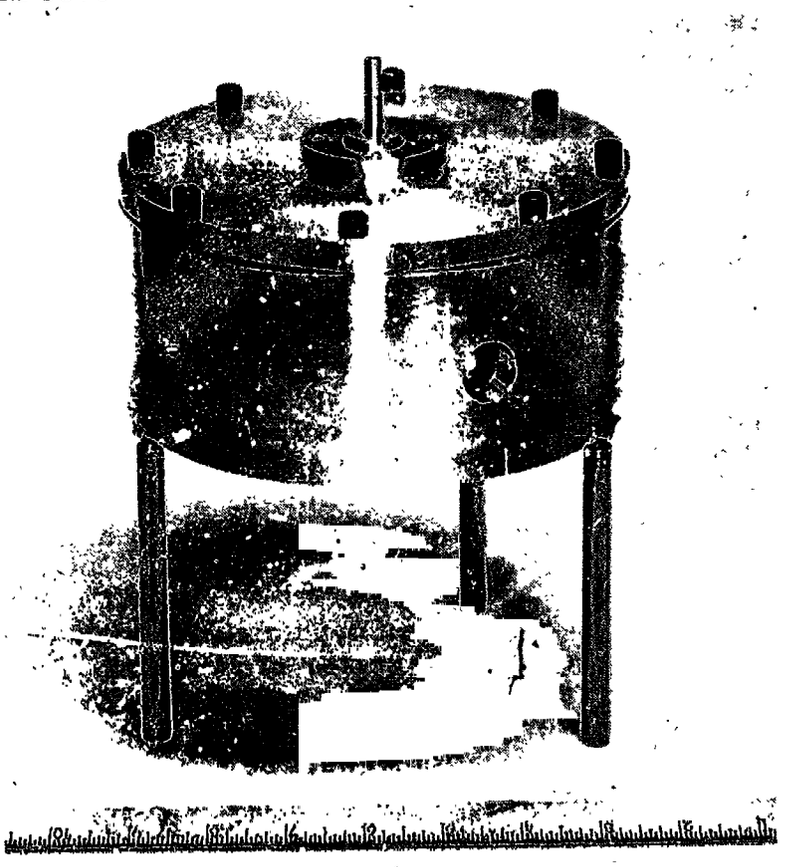

(b) Assembled test setup.

Fig. 40. Ball bearing motor mount and frame with rotor structure.

Our work with this bearing demonstrated that the cruciform sensor design was structurally capable of rotation at the necessary speeds and had no unknown resonance behavior to cause instability. This study also gave us our first indications that the frequency of the sensor modes would shift slightly under rotation. The tests indicated that the commercially purchased slip rings worked quite well at these speeds and voltages; that it was possible not only to extract clean signals from the sensor while rotating, but also to drive the sensor transducers through the slip rings to excite the sensor vibrational modes.

2. Air Bearing

An air bearing support and drive was constructed for us by the Hughes Aerospace Group in Culver City. The support structure consisted of a table supported both vertically and horizontally by an air bearing formed with a rotor tube sitting on a channeled stator (see Fig. 41). The rotor tube also has a magnetic hysteresis ring which is excited and driven by a synchronous motor stator constructed around the outside (see Fig. 42). The sensor chamber is then mounted on top of the rotor table, and the voltages from the sensor are removed through the slip rings on the top (see Fig. 43). The primary reason for the construction of this support and drive unit was to discover and investigate sources of vibrational noise in air bearings.

The synchronous motor drive worked very well, had considerable torque, could be run up to speed rapidly, and was not difficult to synchronize. The air bearing had very low friction, as was to be expected; during the operational checks, however, two instabilities were discovered. One was a lateral dynamic resonance whose frequency varied with air pressure; the other was a vertical instability which was inaudible at low operating pressures, but which could be heard at pressures above 40 psi.

The lateral resonance would occur at speeds just short of the desired rotational speeds when the rotor table was loaded with the sensor chamber. By adjusting the pressure while running up to speed, however, it was possible to pass through this resonance without damage to the rotor. If the sensor had been designed to work at a lower frequency (100 Hz instead of 200 Hz), this lateral resonance would not have been a problem.

The vertical instability was more serious however. It occurred at all speeds, was nearly independent of the speed of rotation, and would even occur with a stationary, but levitated, table. The noise level introduced into the sensor by these vibrations was large enough to cause a sensor output in the millivolt range.

Fig. 41. Air bearing support and drive (exploded view).

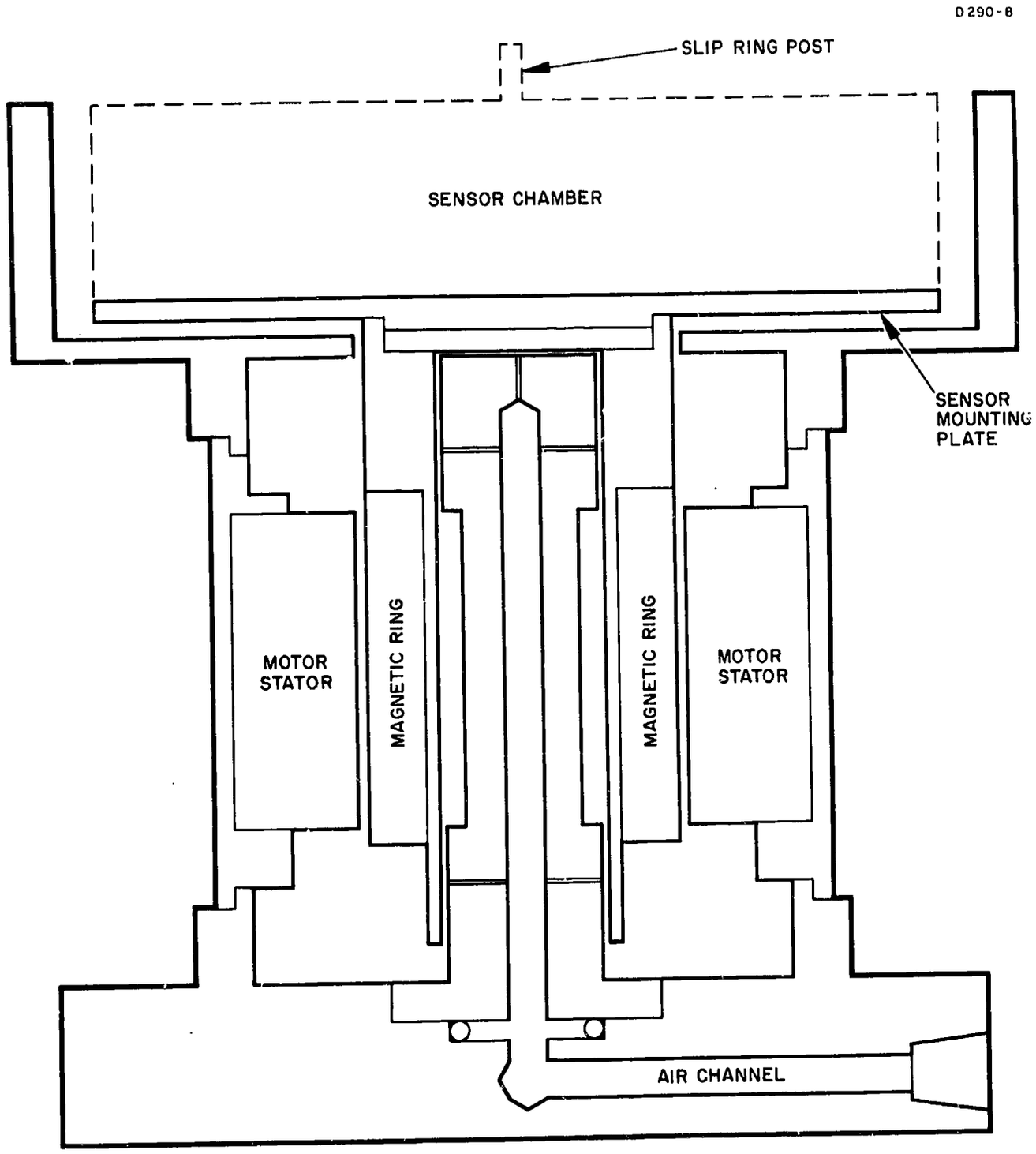

Fig. 42. Sensor air support and synchronous motor assembly.

M 3821

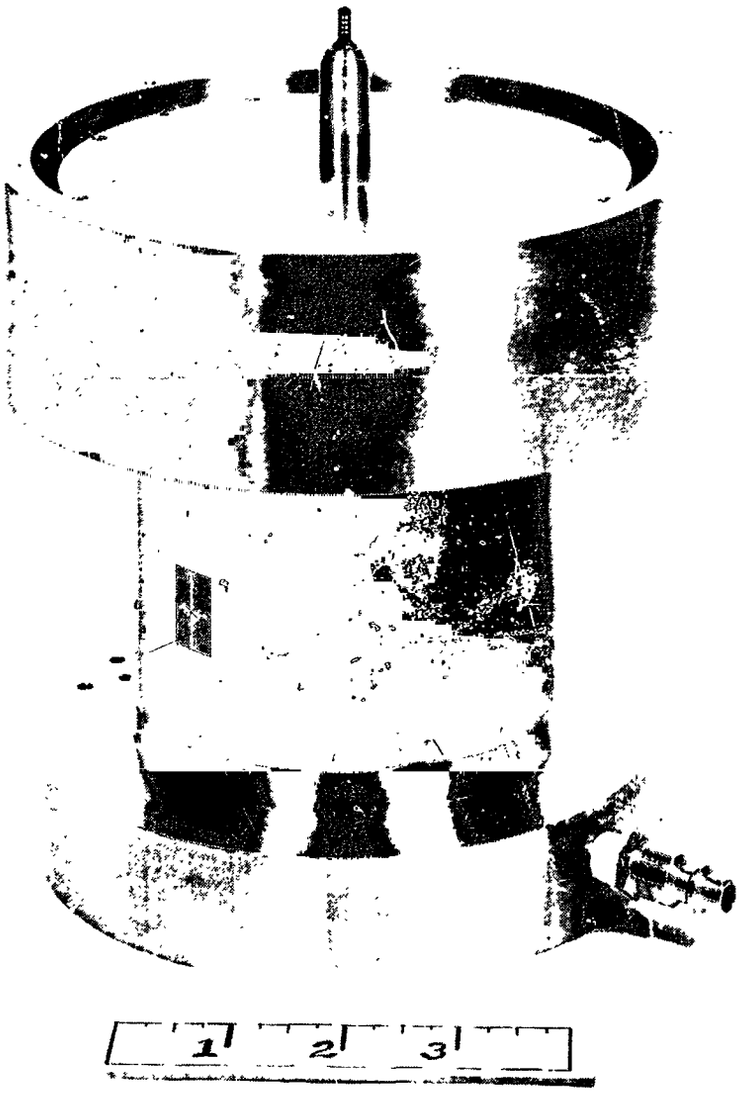

Fig. 43. Air bearing support and drive (assembled).

In order to better understand the cause of the vertical vibrations, an analysis of the air bearing characteristics was undertaken by C. C. Bell and J. R. Morris. The analysis is presented in Appendix C; it shows that the bearing structure generally has two possible positions of equilibrium for a given air pressure. The vertical vibrations occur as the table alternates between these two positions. In addition, for a certain rotor-stator configuration, the calculation indicated that the two equilibrium positions would reduce to a single position. Based on these theoretical results a new air bearing stator was designed with spot face diameters of 0.202 in. The rotor tube was honed to fit this stator, and tests were made with various clearances between the rotor tube and stator. With a gap of 0.0001 to 0.0004 in., the table levitates quite well and there is no evidence of the vibratory resonance. As the radial gap is increased from 0.0004 to 0.0006 in., the bearing characteristics start to deteriorate; at 0.0006 in. gap and 95 psig air pressure, the table will develop a vibratory resonance. Because of the danger of the bearing seizure at very narrow gaps, the primary rotor tube with the hysteresis ring was honed to 0.00045 in. as a compromise.

Upon completion of the air bearing table rework, noise level spectrum data were taken using a torsion bar mounted cruciform sensor inside a vacuum chamber supported on the air bearing table. The voltages generated by a transducer on one of the arms were taken directly out through the slip rings to a General Radio tuned preamplifier. Since the primary concern was to find and investigate the sources of noise, no attempt was made in these or any of the other noise tests to balance either the sensor or the sensor chamber or to use phase cancellation on the signals from different arms.

The first tests on the air bearing table were made without rotation. Data were taken using two different diameter rotor tubes at three different pressures. These data are shown in Fig. 44. Generally the noise peak at 220 cps (the translational mode frequency) and the over-all noise level increase as pressure and the radial gap between rotor tube and stator increase. This would indicate that the noise level is a function of the mass rate of flow of the air through the bearing. This is borne out by the fact that if we calculate the mass rate of flow ratio for tests 2 and 3, where the noise levels are the same, we find that the mass rate of flow is also the same.

The mass rate of flow ratio is given by

$$\frac{\dot{m}_2}{\dot{m}_3} = \frac{g_2 v_2}{g_3 v_3} \tag{59}$$

where g is the gap and v is the velocity.

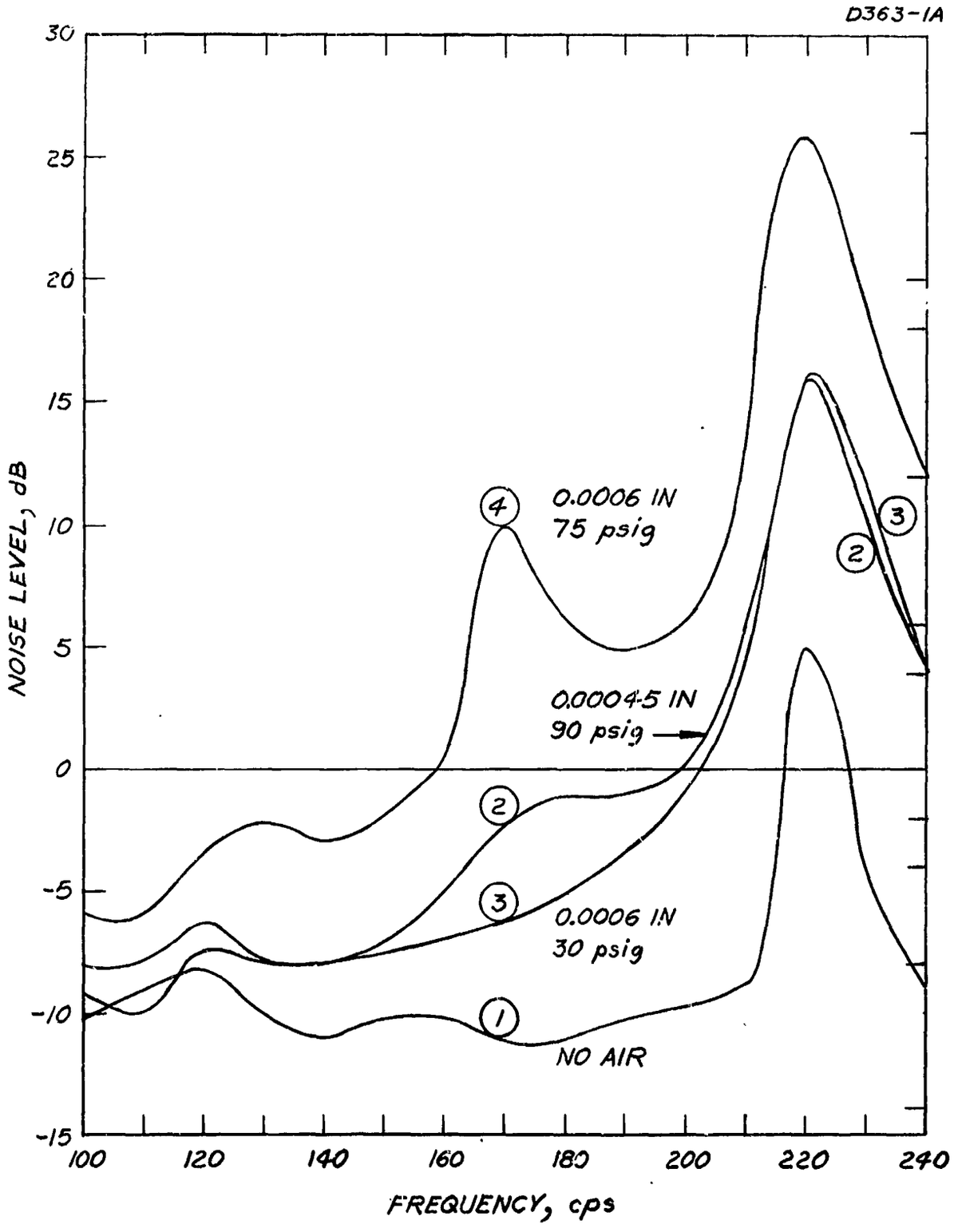

Fig. 44. Air bearing static tests.

The velocity of the air flow is given by

$$\frac{v^2}{2} = \frac{P}{\rho} \ln \frac{P}{P_a} \tag{60}$$

where P is the absolute pressure of the supply source, ρ is the density, and $P_a = 15$ psia is the ambient pressure. If we assume isothermal conditions for the source, then

$$\frac{P}{\rho} = \text{const} = \frac{P_2}{\rho_2} = \frac{P_3}{\rho_3} \tag{61}$$

and the velocity ratio in the two tests are given by

$$\frac{v_2}{v_3} = \left(\frac{\ln P_2/P_a}{\ln P_3/P_a} \right)^{1/2} . \tag{62}$$

For these tests,

$$\begin{aligned} P_2 &= 105 \text{ psia} \qquad P_3 = 45 \text{ psia} \\ g_2 &= 0.00045 \qquad g_3 = 0.0006 \end{aligned} \tag{63}$$

and the mass rate of flow ratio is found to be

$$\frac{\dot{m}_2}{\dot{m}_3} = \frac{0.00045}{0.0006} \left(\frac{\ln 7}{\ln 3} \right)^{1/2} = 1.0 . \tag{64}$$

This would indicate that the noise level is a direct function of the mass rate of flow through the bearing. At the largest noise level (test 4), a second resonant peak is seen at about 170 cps. This is the resonance in the tuning fork mode which, although not as responsive to the vibrational forces as the translational mode, still responds to that portion of the vibrational noise which leaks into the mode because of asymmetries in the sensor structure.

3. Magnetic Bearing

The magnetic bearing which we purchased for the preliminary phases of our program was a single-axis, Beams type suspension.[34] It was constructed by William H. Dancy of the Instrument Development Group, Research Laboratory for the Engineering Sciences, University of Virginia.

The magnetic support provides an inherently frictionless bearing in which the sensor may be rotated with a minimum amount of drive power, as well as providing a high compliance isolation between the sensor and ambient floor vibration. It has a third virtue in that it allows the sensor to rotate about its center of mass rather than forcing rotation about a mechanically fixed axis, thus relaxing the requirements for exact balancing of the sensor and sensor chamber.

a. Equipment Description

The magnetic support system is composed of five separate but interacting subsystems together with the necessary power supplies (see Fig. 45). The major subgroups are the magnetic support solenoid and drive motor assembly, the magnetic support circuit, the current control circuit, the rotor drive circuit, and the speed pickup system. Figure 46 shows the mechanical relationships between the major components of the magnetic support solenoid and drive motor assembly. A detailed description of the circuitry and the operation of the bearing is given in Appendix D.

b. Operating Characteristics

In general, the magnetic bearing and drive performs well and is quite satisfactory for this program. The levitation circuits are slightly tricky in adjustment, but have proved to be capable of stably levitating the 6 lb mass of the sensor chamber and the iron pole cap. The compliance of the magnetic "spring" is very low, so that there is good vibration isolation at the sensor frequency. When the servo loop is properly adjusted, the vertical stability of the support is good, except for a long term drift which requires that the servo gain be adjusted periodically. The pancake motor drive works quite well, although the available torque is necessarily limited by the relatively large air gaps which result from the levitation requirements.

c. Static Noise Tests

After the magnetic bearing was assembled and checked out, a series of noise level tests were made with the same torsion bar mounted cruciform sensor used for the noise tests on the air bearing. The sensor chamber was designed so that the chamber base could be mated securely to the air bearing table with the slip rings pointing up

M 4050

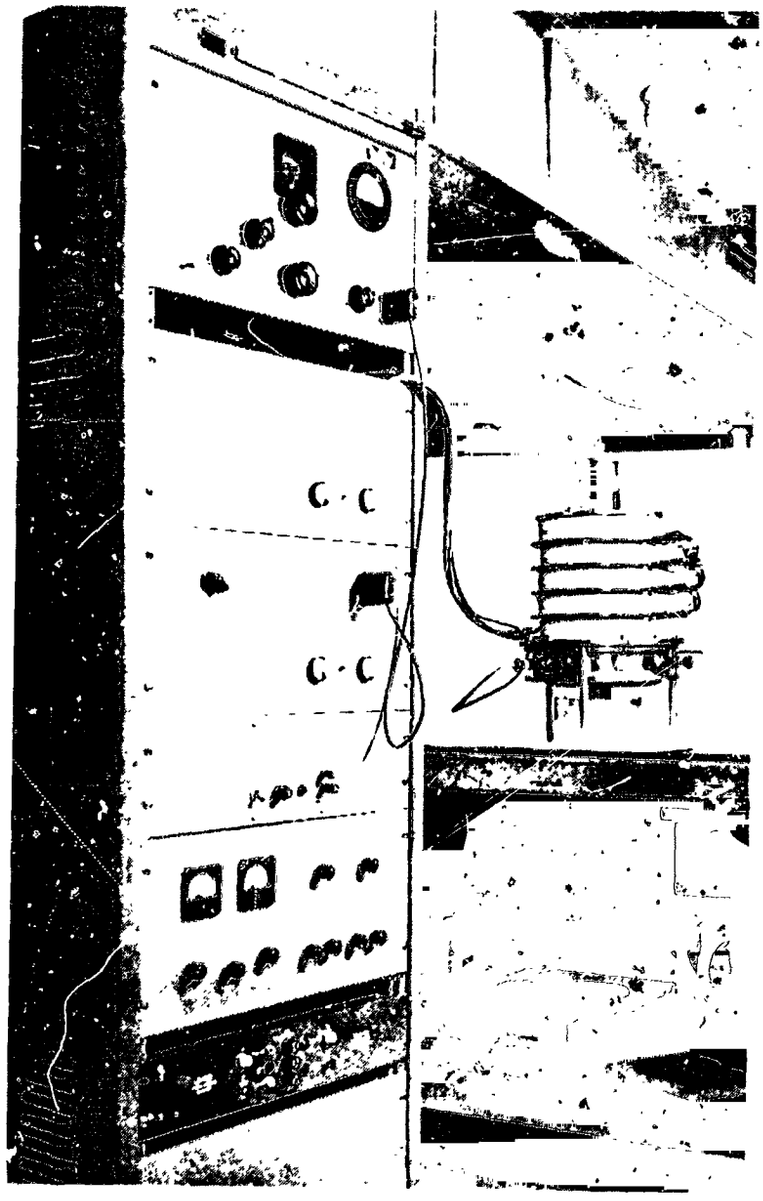

Fig. 45. Magnetic support and drive unit.

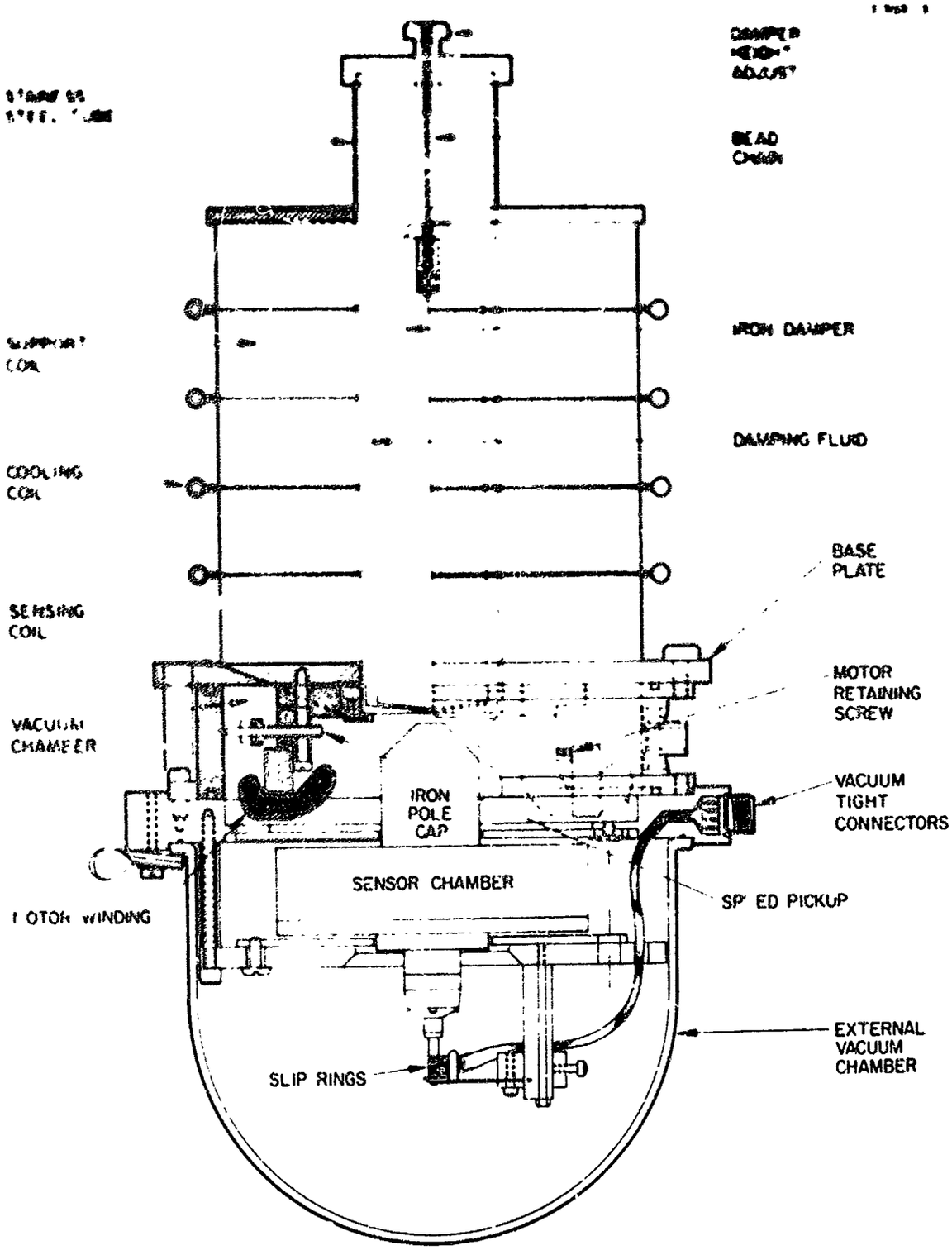

Fig. 46. Layout drawing of magnetic bearing.

[illegible] Fig. 47 [illegible] the magnetic [illegible] with the sleeve position [illegible] Fig. 47. The voltages generated by a transducer on one of the [illegible] are [illegible] of the suspension [illegible] General Radio [illegible] amplifier. No attempt was made in these tests to balance [illegible] or to use the sensor chamber trim-vane phase cancellation [illegible] techniques.

The first noise tests were made with the sensor not levitated in the magnetic support. As can be seen in Fig. 47, the intrinsic noise of the magnetic support is very low, the noise observed seems to be primarily due to ac pickup and vibration since there are definite noise peaks at multiples of 60 cps and the level is dependent upon the support current. The ac hum in the solenoid current is easily measured and was found to range from 0.1 to 10 V for various harmonics of 60 cps at various support currents. This may be suppressed at any desired frequency by means of a twin-tee notch filter between the solenoid and its power supply. However, even without the filtering, the noise level due to this noise source is only a few percent of the expected signal levels and is of minor concern.

When the drive amplifiers are turned on, with no drive signals applied, there is a general noise level increase. This is a result of hash and hum in the drive amplifiers. This noise was eliminated by filtering the outputs of the amplifiers.

d. Synchronous Drive Noise Tests

Tests were made of the contribution of the synchronous drive motor to the noise seen by the sensor. As was to be expected, the drive motor introduces noise resulting from the interaction of the rotating drive field and the remnant magnetic poles in the hysteresis plate. This noise is a direct function of the drive power; for synchronous operation at some subharmonic of the sensor resonant frequency, the noise output at 172 cps can be many millivolts.

However, as can be seen from Fig. 48, the noise induced at these resonant peaks decreases rapidly as the drive power is decreased; if the drive is lowered to a level just sufficient to maintain synchronous rotation, the noise level drops to the level seen under free rotation conditions. This synchronous drive noise was our most troublesome noise source since the sensor operation requires that the sensor be accurately rotated at half the sensor vibration frequency. This noise source was eliminated by the use of the asynchronous drive control.

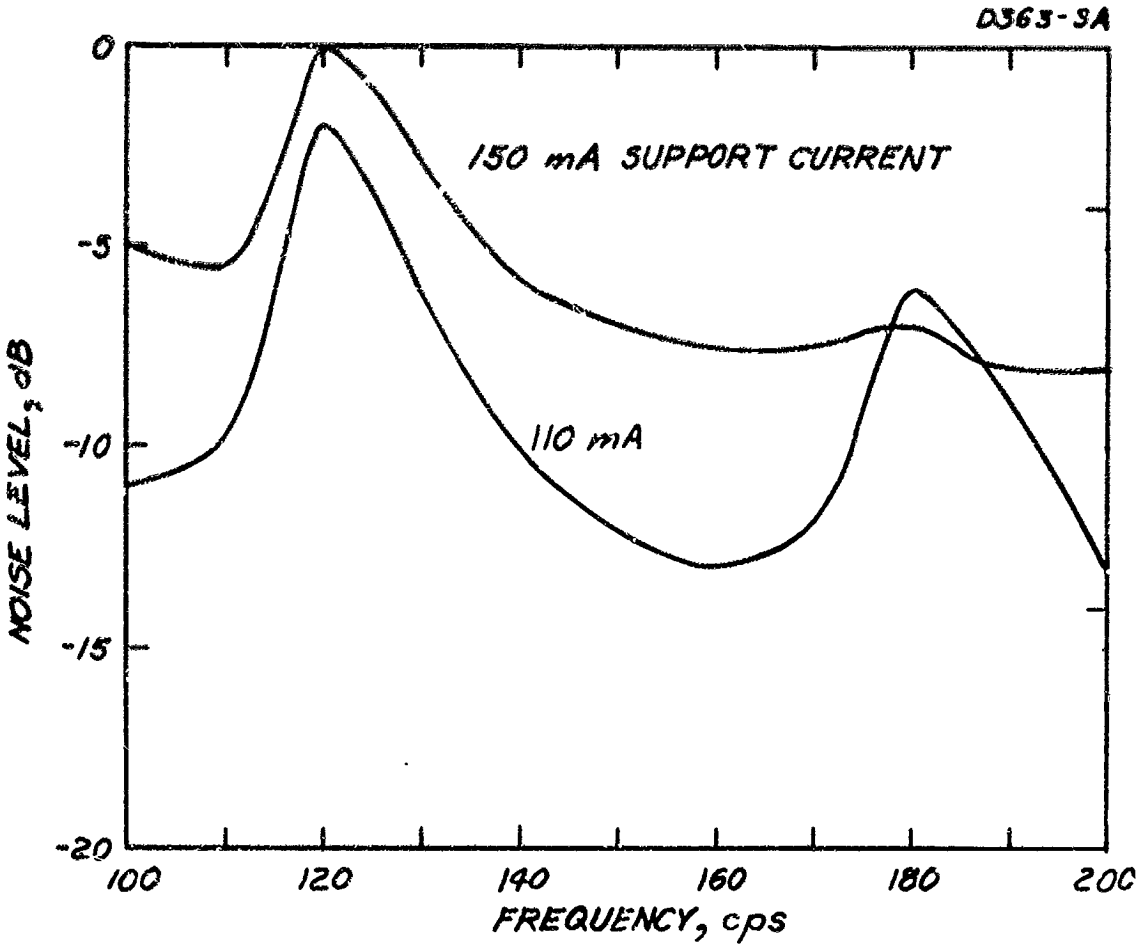

Fig. 47. Static magnetic bearing tests.

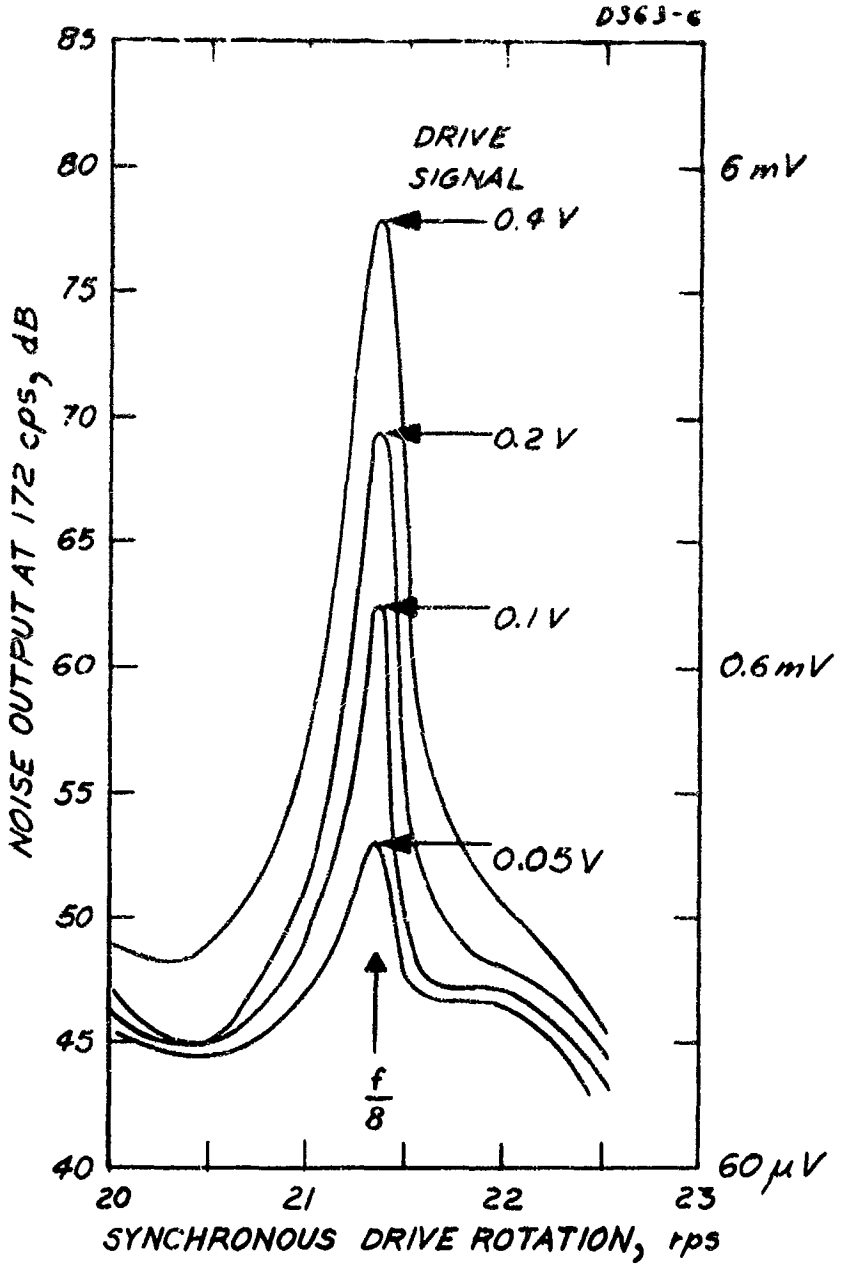

Fig. 48. Noise output as a function of drive signal.

e. Asynchronous Drive

One requirement of our mass sensing study is that the sensor be rotated at one half the tuning fork resonant frequency. Furthermore, the instantaneous position (phase) of the sensor must be known for processing the data. The synchronous drive built into the single-axis magnetic suspension has not been completely satisfactory for our purposes. First, the motor drive frequency is twice the synchronous speed – exactly the sensor output frequency. Thus it is not possible to use frequency discrimination techniques to eliminate electrical pickup from the drive. In addition, there is no control over the oscillation of the rotor between the synchronously rotating poles, other than by varying the drive intensity.

In order to overcome these difficulties, an asynchronous drive system invented by L. R. Miller has been constructed and tested. The important features of this system are:

1. Any frequency higher than the sensor frequency may be used to drive the rotor.

2. The rotor speed may be synchronized with an external frequency.

3. Well damped phase lock is achieved.

The theory of operation can be seen by reference to the block diagram in Fig. 49.

1. A photoelectric pickoff produces one spike per rotor revolution.

2. This spike operates a gate which allows a reference frequency sine wave to be scrutinized.

3. When the spike and reference frequency are synchronous, the voltage level of the reference will be the same each time the gate is opened. This level and its derivative (for damping) are used to control a variable gain amplifier through which the drive frequency passes.

4. If the rotor rotation rate falls behind the reference frequency, the spike position moves down the reference sine wave, sampling a lower level. The lower level increases the drive frequency amplification, causing the rotor to speed up.

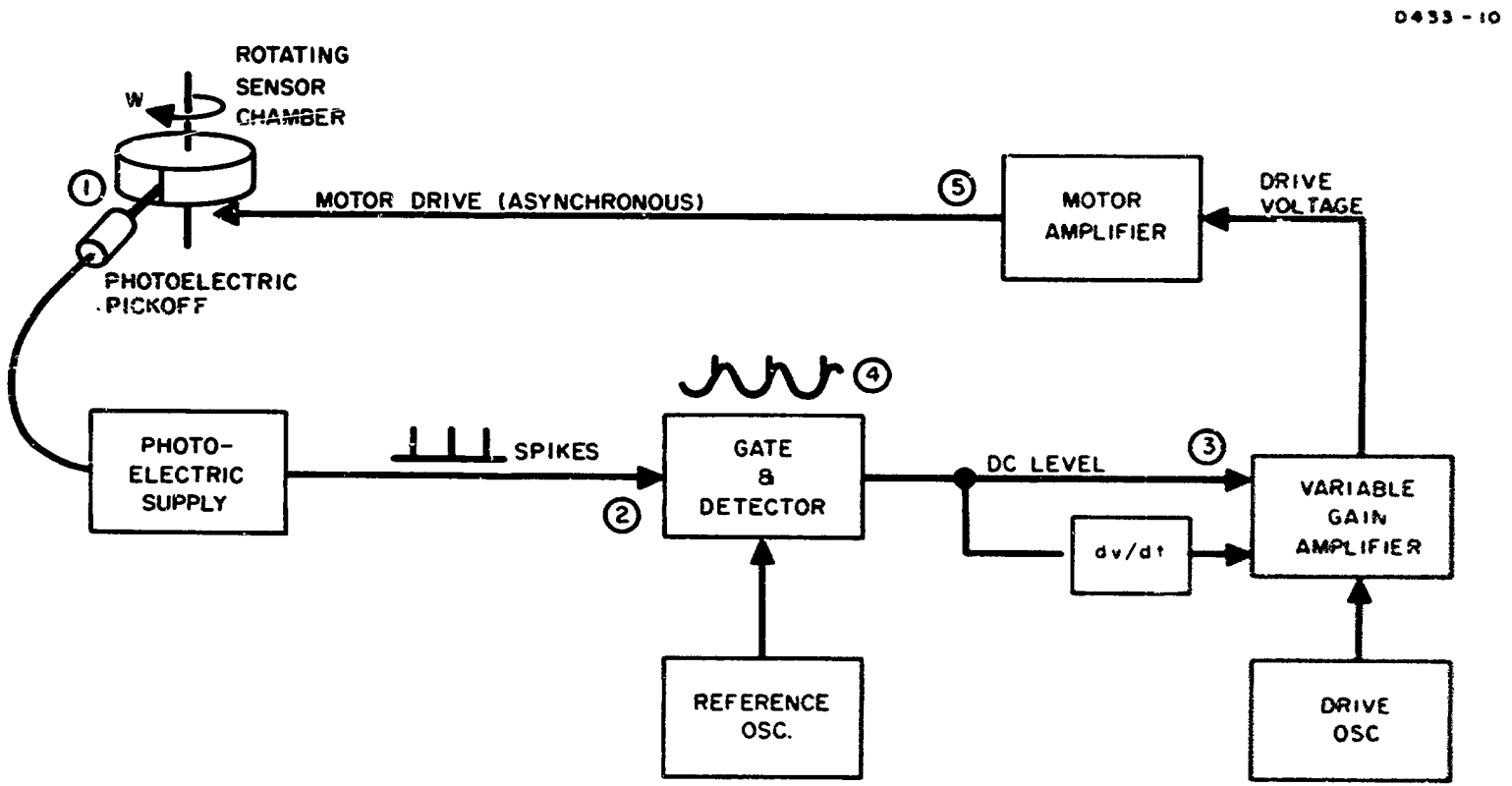

Fig. 49. Block diagram of asynchronous drive.

5 The rotor is thus forced to maintain a fixed position relative to the reference phase and the drive frequency may be any frequency above the reference frequency.

Two of these drive units have been constructed, one for use on the magnetic bearing and the other for the motor on the air bearing They are slightly more complicated to set up and operate than the synchronous drive, but work well The schematic for the electronics is shown in Fig. 50. The circuit is believed to be novel, and a patent disclosure has been submitted to NASA through the Hughes patent office.

4 Comparative Bearing Noise Tests

In both static and dynamic noise tests, the magnetic support seemed to be substantially less noisy than the air bearing support

Figure 51 compares the results of noise measurements made under static conditions with the same sensor. The lowest curve was taken with the sensor chamber suspended from a rubber band to provide isolation from the room vibrations. It is essentially flat with a small peak at the translational mode frequency (220 cps). The next curve was taken with the sensor suspended in the magnetic support. Although there was noise at multiples of 60 cps due to hum harmonics in the solenoid, the noise at 220 cps is actually less than that measured with the rubber band suspension. The highest curve shows the results of the quietest air bearing test. The noise at 220 cps is an order of magnitude higher than that of the magnetic bearing.

Figure 52 compares the results of dynamic tests made with the air bearing and the magnetic bearing under identical conditions. (Free rotation coastdown from 2000 rpm.) The air bearing curve not only has a higher background level, but it also contains many more resonance peaks than the magnetic bearing curve.

In general, the air bearing is 14 dB or more noisier than the magnetic bearing under dynamic as well as static tests. These comparative tests indicate that the magnetic support is, in general, superior to the air bearing support for our purposes.

These preliminary tests and considerations of the potential future use of the sensors indicated that our feasibility model of the gravitational mass sensor required a stable, three-axis magnetic bearing which could be operated in any orientation and which had low magnetic

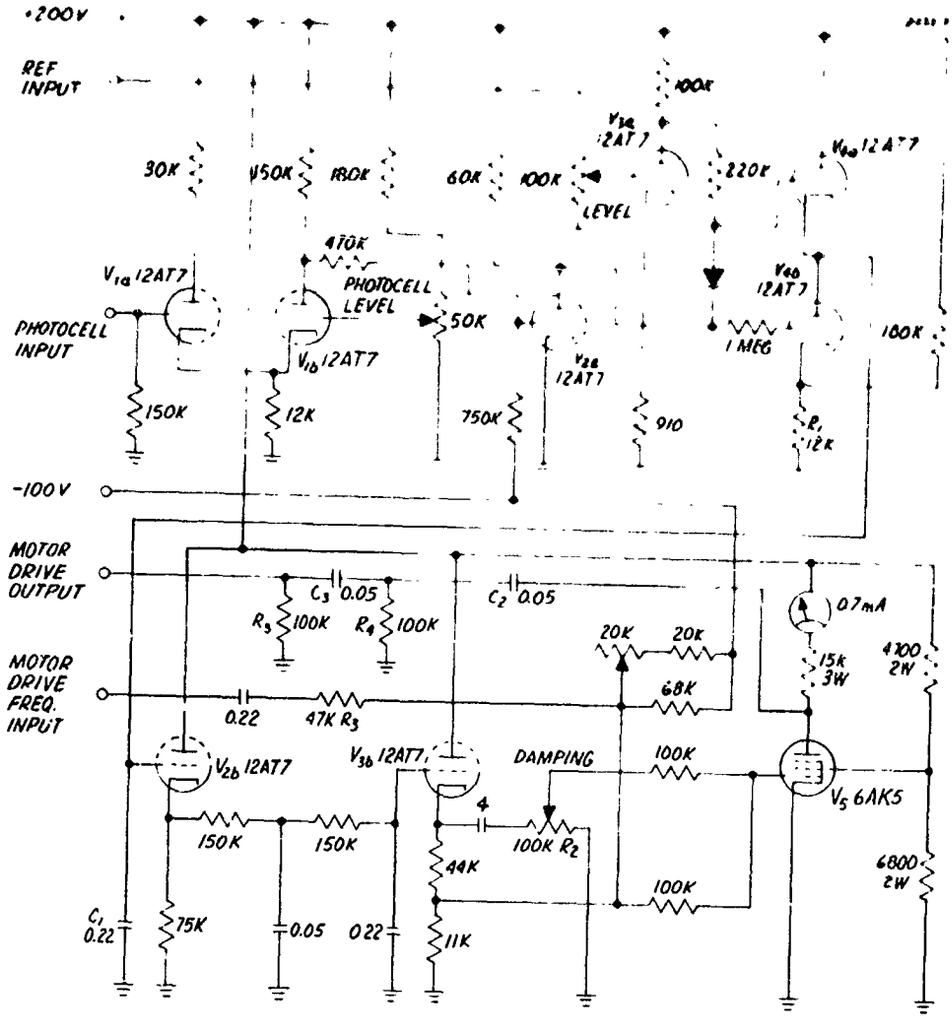

Fig. 50. Schematic of asynchronous drive.

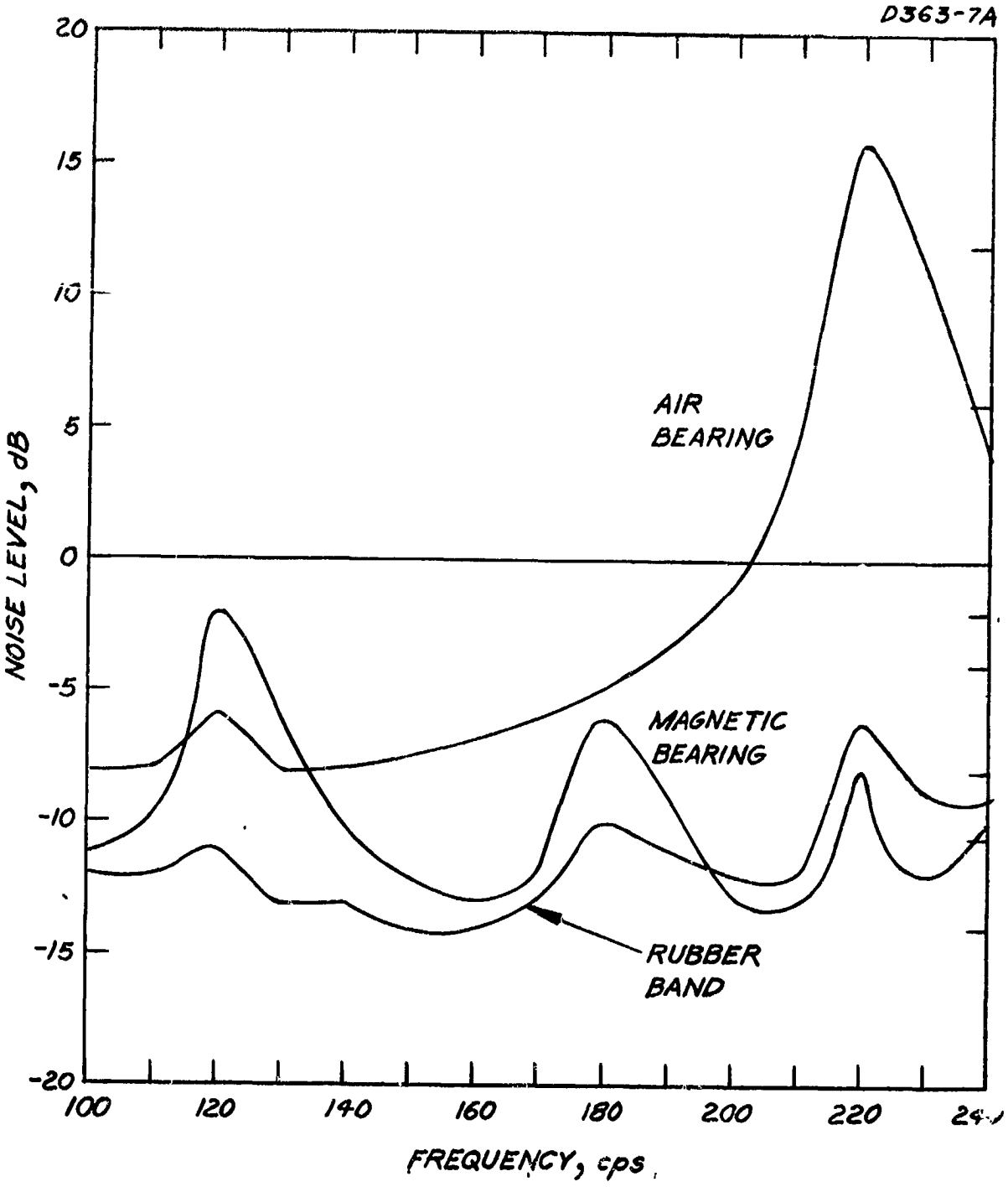

Fig. 51. Comparative static noise tests.

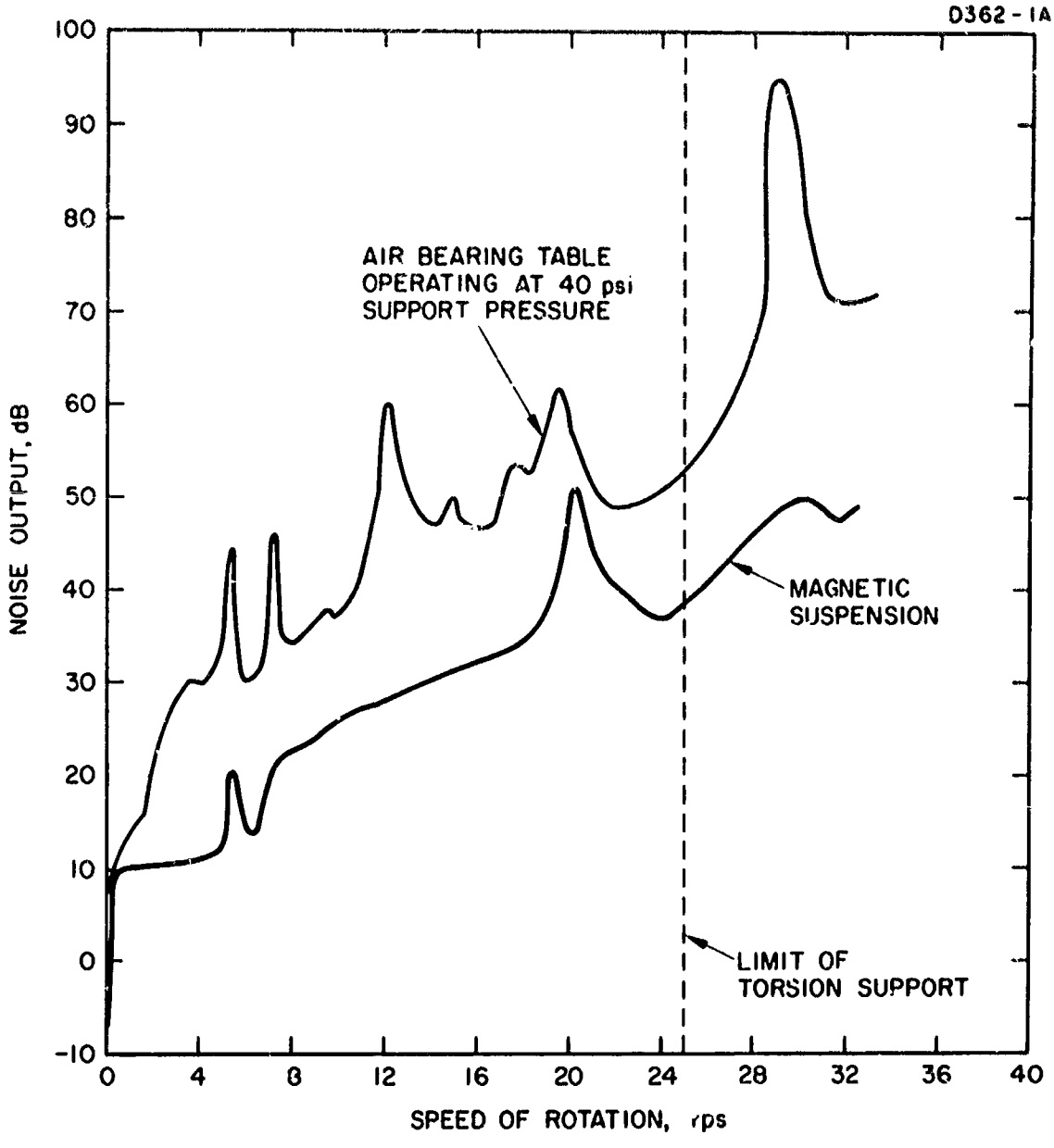

Fig. 52. Comparative dynamic noise tests (coastdown).

flux leakage at the position of the sensor. Arrangements were made with a subcontractor, the Cambridge Thermionic Corp. (CAMBION) in Cambridge, Massachusetts, to construct a well designed three-axis magnetic bearing and drive for use in the feasibility model. After a two month extension time, the subcontractor was able to obtain a stable three-axis bearing; despite another extension, however, the subcontractor was not able to obtain a rotation speed greater than 1500 rpm. Thus, the feasibility model scheduled to be examined during the last third of the contract was never available for study and it was necessary to use the preliminary model for study of noise and instability under rotating conditions.

E. SENSOR ELECTRONICS

The gravitational mass sensors being studied under this contract operate by sensing the gradient of the gravitational force produced by the mass. The presence of the gravitational gradients induces mechanical vibrations in the rotating sensor. The magnitude and phase of these vibrations indicate the strength and direction of the gravitational gradient.

In order for the vibrations to be conveniently observed, they must be converted into electrical signals, amplified, and removed from the rotating sensor. The method of transducing and removing the signals from the sensor is discussed below.

The results of our various design studies and experimental investigations indicate that the present strain transducers, amplifiers, and other electronic components are more than adequate for the purpose of seeing the gravitational gradient signals (see Section II-G).

1. Strain Transducers

The vibrations of the sensor arms are converted to electrical signals by placing strain transducers on the arms. The units used have been Glennite SC-2 ceramic, piezoelectric transducers manufactured by Gulton Industries. These transducers have the advantages of small size (1/2 in. x 1/8 in. x 0.011 in.), high output (0.7×10^5 V/unit strain) and high capacitance (1000 pF). Their disadvantages are a somewhat variable output with temperature and humidity, and a mechanical Q low enough to reduce the Q of the sensor arm to which they are applied.

The piezoelectric strain transducers are calibrated by comparing their output with that of a resistive strain gauge of known gauge factor. The resistive gauge and the piezoelectric transducers are attached with lacquer or Duco cement to a position of identical strain on a bar of metal, and the bar is either struck with a small hammer or driven by an amplified feedback loop to obtain dynamic strains. The strains obtainable in this manner are about 10^{-5} cm/cm. At this level of strain, the resistive gauge, even with high bias currents, has an output of only a few microvolts, while a typical piezoelectric transducer is generating almost a volt. From previous work (see Appendix B) it was known that a calibration obtained at these strain levels was valid at lower strain levels.

Calibrations were carried out using a number of different mechanical resonant structures (including actual sensors) which had frequencies ranging from 100 to 1600 Hz; in all of the tests, the

barium titanate transducers were found to have transducer factors clustered about 0.7×10^5 V/cm/cm. The variation from transducer to transducer was a factor of two or less, depending upon a large number of factors both known (such as bonding material, aging, temperature, etc.) and unknown; it was not possible to obtain repeatable calibrations from day to day even on the same transducer. This transducer calibration problem is felt to represent the largest uncertainty in our knowledge of the absolute sensor output, but at most it is a factor of two.

As part of our research program, an analysis of piezoelectric strain transducer behavior was conducted to determine how good our present transducers are compared with other possible configurations and materials.

The element used for analysis is a piece of piezoelectric material of area A and thickness t strained in the direction shown below. The fundamental piezoelectric relationship is

$$q = d S A \tag{65}$$

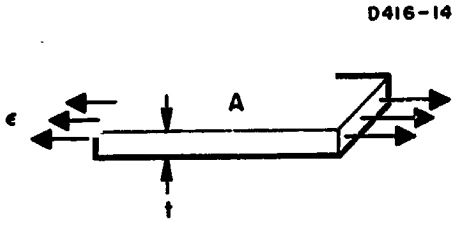

where q is the induced charge, d the piezoelectric constant, and S the stress on a plane perpendicular to A.

To this must be added the stress-strain relationship for the material

$$S = Y \epsilon \tag{66}$$

where ϵ is the strain and Y is Young's modulus.

The capacity-voltage-charge formula is

$$V = q/C \tag{67}$$

and the parallel plate capacity formula is

$$C = K \mathcal{E}_o \frac{A}{t} , \tag{68}$$

where K is the relative dielectric constant and $\mathcal{E}_o$ is the capacitivity of free space.

The above relationships may be combined in several ways to relate voltage to strain.

$$\sigma = \frac{V}{\epsilon} = \frac{d Y A}{C} = \frac{d Y t}{K \mathcal{E}_o} \tag{69}$$

In addition, four other factors must be considered in evaluating a transducer:

1. It must be thin enough to accurately measure the strain on the surface to which it is applied.
2. It should not seriously deteriorate the Q of the vibrating arm.
3. Its capacity should not be too low.
4. Its output should not vary with ambient conditions.

In Table IV, four ceramic materials (made by Gulton) are compared with quartz and our present transducer. Each material is treated as if it were made into a transducer similar to that now in use. An exception is made for quartz, which is assumed to be one-tenth the thickness of the ceramic transducers. This can be done because quartz is easy to work with and such a thickness is quite practical.

TABLE IV

Characteristics of Various Piezoelectric Materials

Material and Thickness t, mm	Piezoelectric Constant d, m/V	Young's Modulus Y, N/m^2	Dielectric Constant κ	Capacitance C pF	Strain-Voltage Ratio, V/unit strain
Present Ceramic (Glennite SC-2) 0.28	(No data available)			~1000	$\sim 0.7 \times 10^5$
Quartz 0.028	2.3×10^{-12}	8.6×10^{10}	4.6	41	1.4×10^5
HD 11 Ceramic 0.28	24×10^{-12}	14.2×10^{10}	600	530	1.7×10^5
HS 21 Ceramic 0.28	62×10^{-12}	11.5×10^{10}	1250	1100	2.0×10^5
HDT 31 Ceramic 0.28	120×10^{-12}	8×10^{10}	1300	1150	2.2×10^5
HST 41 Ceramic 0.28	140×10^{-12}	7.3×10^{10}	1800	1600	1.9×10^5

The important conclusions to be drawn from the data shown in Table IV are as follows:

- There is no immediate advantage to be gained by having new strain transducers made because none of the materials show significant advantages over our present transducer.

- In the future, if higher output is desired, it may be obtained by using HST-41 or HDT-31 in a thicker transducer. Since output is proportional to thickness, the output could be increased by 10 without reducing the capacity below a practical level. The resulting transducer would be quite thick, however, and might cause a bonding and Q problem.

- In the future, if we desire better stability and Q, a quartz transducer could be made with roughly the same output we have now. Each transducer would have a very high output impedance, however, which would require the use of several parallel transducers to bring the impedance down to practical levels.

The voltages obtained from these strain transducers when they are on a sensor are dependent on the detailed sensor design (see Section II-B-6); typically, however, they are in the low microvolt region (a sensor arm motion of 10^{-9} cm produces about 1 μV). When the sensors are calibrated using the dynamic gravitational gradient field generator (see Attachment E) and are stationary, the voltages can easily be measured with commercially available tuned amplifiers such as the Princeton Applied Research HR-8 Lock-In Amplifier, which has a noise level of about 1 nV.

When the sensor is rotating with respect to the laboratory, it is necessary to develop techniques to transmit the voltages to the recording units. A standard slip ring proved to be satisfactory for the initial tests, and they were especially useful during the vibrational mode frequency tests because voltages could be introduced back through the slip rings into the sensor to selectively excite the various modes. No electrical noise was found to be generated by the slip rings during noise tests, but the brushes introduced mechanical vibrational noise.

2. Telemetering Unit

In order to eliminate the mechanical vibrations introduced by the slip rings, an amplifier-transmitter telemetering unit (see Fig. 53) for use with the ultracentrifuge mount was designed and constructed by J. R. Morris. The schematic of the device is shown in Fig. 54.

The input to the amplifier operates in a differential mode and the strain transducers on the sensor are connected in such a manner (see Fig. 55) that the output of the differential input stage is a maximum for the signals from the gravitational gradient sensing mode and a minimum for the signals from other modes and from electromagnetic pickup. The signals from the translational modes are cancelled directly in each pair of transducers because the translational mode excites a positive voltage in the transducer on one arm and a negative voltage in the transducer on the opposite arm. The signals from the torsional mode and from electromagnetic pickup will induce equal voltages in all of the transducer leads, and the differential input will cancel them out.

Each input of the differential input was designed with a 10 MΩ impedance to accommodate the high output impedance of the strain transducer pairs, which is about 0.8 MΩ at 100 Hz. The common mode rejection ratio of the present unit is 23.5. The amplifier has a gain of about 150, and the amplified voltage is then used to frequency modulate the 37 MHz carrier of the transmitter unit by modulating the capacitance of the voltage sensitive Varicaps.

The frequency modulated carrier is detected outside the vacuum chamber by a Hallicrafters SX62B receiver with an over-all gain of 700. The detected video signal is available at the earphone jack for display on an oscilloscope or recorder. The noise in a 5% band at 100 Hz for the entire system, with the sensor connected to the differential input and the entire unit suspended in the magnetic bearing, is 0.15 μV referred to the input. This sensitivity level is more than adequate for the noise tests; the signal-to-noise ratio can be improved further as the sensor noise level decreases by the addition of another stage of gain to the amplifier.

3. Phase Shift Tuned Amplifier

Electronically, the transducers used in this program can be considered as a signal source with a small series output capacitance (typically 1000 pF). This capacitance has a relatively high reactive impedance at the frequencies of interest (1.6 MΩ at 100 Hz). Because of the difficulty in operating at high impedance

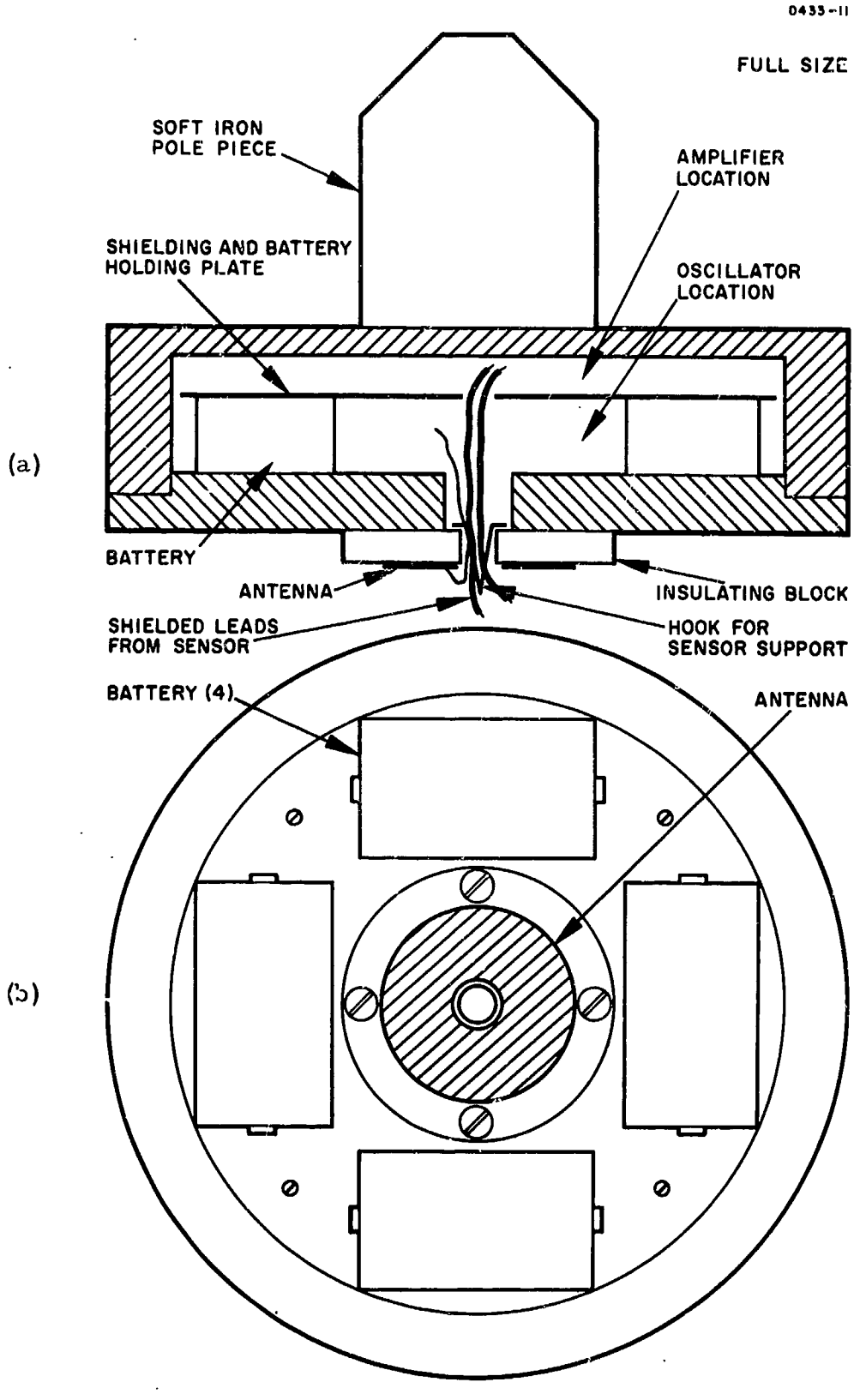

Fig. 53. Telemetering system. (a) Side view. (b) Bottom view.

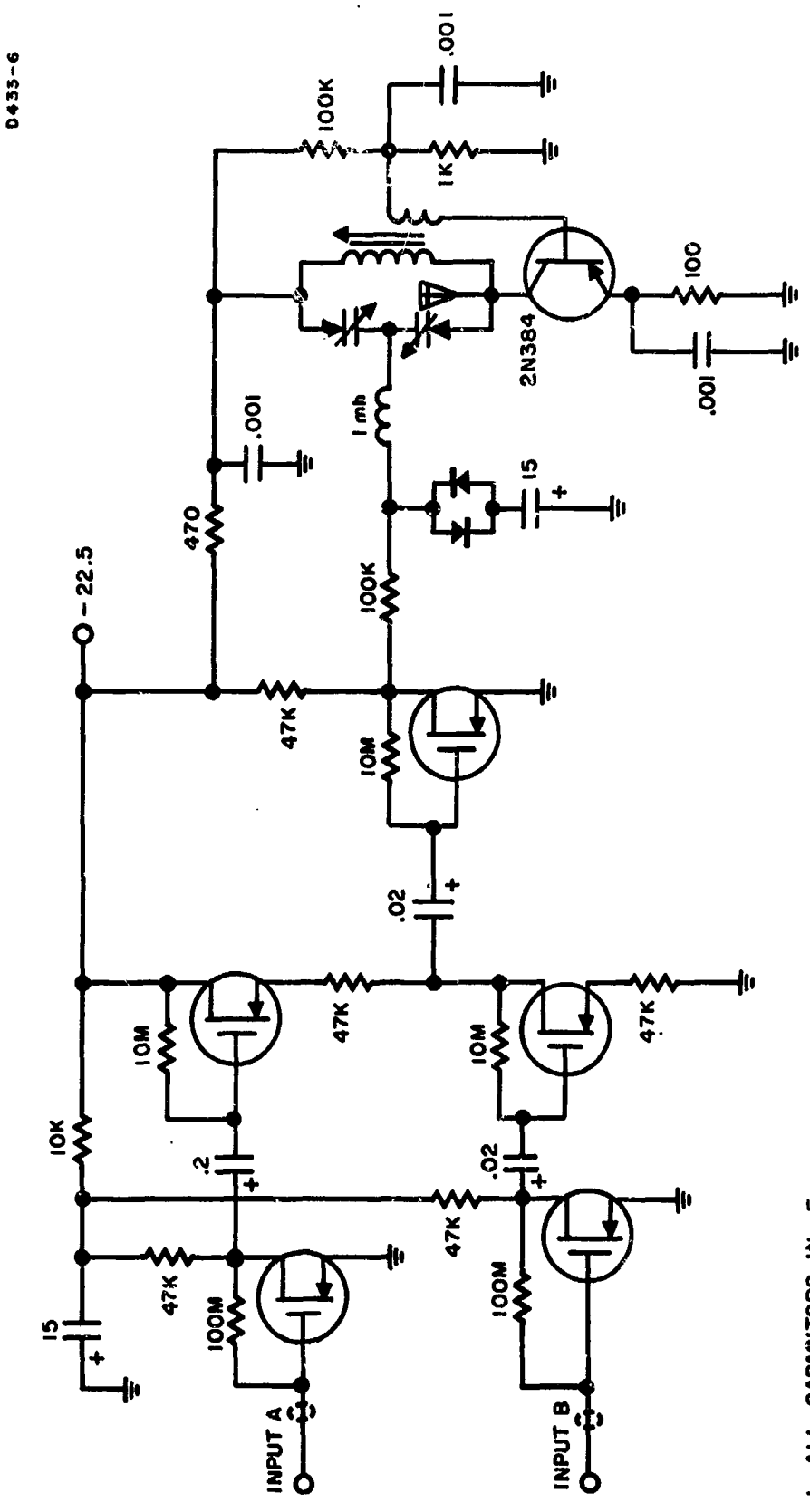

1. ALL CAPACITORS IN uF
2. ALL RESISTORS 1/8 W, 5%
3. ALL MOSFETS 2N3608
4. VARICAPS PC115
5. COIL MILLER 40A226CBI, 1.50-2.75 uh
6. CARRIER FREQ. 36 MHz

Fig. 54. Differential amplifier and FM transmitter.

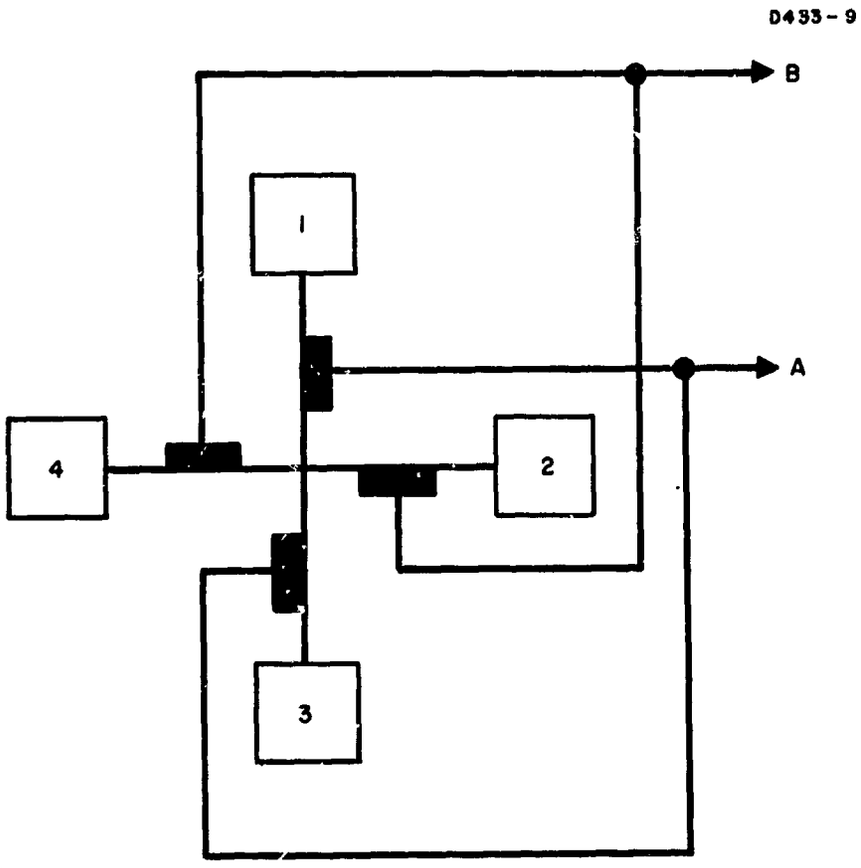

Fig. 55. Gauge connections.

levels, it was thought desirable to develop a method for tuning out the capacitance; however, the small capacitance value and low operating frequencies precluded the use of an inductor because about 2500 H would be needed.

As part of our study of the sensor electronics, a small, simple electronic circuit which behaves as a large inductance was developed by J. R. Morris. A detailed analysis and an experimental description of the circuit behavior are given in Appendix F. The circuit behaves as an inductor for tuning purposes, and it was possible to obtain both strong coupling of the electronics to the sensor structure and a signal gain of 150.

Because the circuit uses active elements and positive feedback, it is sensitive to voltage supply and ambient temperature changes. Because of this problem and because the extra sensitivity was not required for testing the sensor, it has not yet been used on the program.

F. NOISE IN ROTATING SENSORS

Our many tests with rotating and nonrotating sensors have revealed a number of noise sources, which we have investigated. They include

- mechanical vibrations applied to the sensor mount which are generated by drive motors, asymmetric bearings, air turbulence, and other sources inside the sensor bearing and drive, as well as by acoustic and vibrational sources external to the sensor and drive
- differential forces applied directly to the sensor head which arise from coupling of the sensor arms to acoustic noise, turbulence in the residual air of the vacuum chamber, magnetic eddy current forces and light pressure
- pickup in the transducer leads and sensor electronics from electromagnetic coupling to stray electrostatic and magnetostatic fields, and to ac induction fields from the bearings and drive motors.

1. Noise Tests on Rotating Sensors

We made many noise tests of rotating sensors during the contract; only a few of the more pertinent ones are reported here. Most of the early tests indicated either that the bearing we were using was much too noisy or that we had not yet solved the mount instability problem. Some of these preliminary noise comparison tests designed to investigate bearing and drive noise are described in Section II-D.

After techniques were developed to reduce bearing and drive noise, it was possible to measure other sources of noise. The results of this work are reported in this section. In all the tests the magnetic bearing described in Section II-D and Appendix D was used.

a. Adjustable Sensor on Torsion Wire Mount

Our initial method for reading out the sensor voltages used ordinary commercial slip rings. Because the circuits were "dry" and had no bias currents passing through the variable resistance of the rotating contact, no electrical noise was generated by the slip rings. However, as we reduced the other noise sources, the mechanical vibrations produced by the interaction of the brushes against the slip rings became a problem.

A series of noise measurements were taken on a sensor mounted on a 0.020 in. diameter torsion wire inside an evacuated sensor chamber. Three tests were run, the first of which utilized regular slip ring brushes while the sensor chamber was run in air. The second test was identical to the first, except that an external vacuum chamber was added and evacuated in an attempt to cut down windage noise. In the third test, the standard slip ring brushes were replaced with special fine copper wire brushes with low mass and low mechanical coupling. In each case the sensor chamber was brought up to speed and allowed to coast down. The data for these tests are reproduced in Fig. 56.

The data show that the difference between air and vacuum for this configuration is very slight, indicating that windage was not a problem. However, the slip ring brushes were found to be responsible for the large noise peaks at the rotational frequencies corresponding to the lowest translational mode and the gradient sensing mode. Even the low mass brushes appear to introduce some noise, but the peak level is about 30 dB lower and the curve is generally less erratic.

Since slip ring wobble seemed to be the major source of noise, the telemetry unit discussed in Section II-E was constructed and used.

b. Five Inch Sensor on Ultracentrifuge Mount

Because of the mode separation problem which existed when double ended torsion wire mounts for the sensor were used, a thin single ended sensor mount was investigated. This mount consisted of a long rubber band between the sensor and the magnetic bearing rotor (see Fig. 57 and 58). The mount had a low translational natural frequency and was operated far above its translational resonance point in a manner similar to an ultracentrifuge. The mount was not stable unless the rubber band was many inches long; therefore, it was necessary to operate the sensor so that it rotated by itself outside the co-rotating vacuum chamber. The entire apparatus was enclosed in an evacuated, stationary bell jar to prevent external acoustic noise from coupling into the sensor arms.

Signals from opposing pairs of strain gauges in parallel were brought through the fine wire slip rings and fed into the differential input of a Princeton Applied Research HR-8 Lock-In Amplifier. While the sensor was rotating, its output was phase-locked to its rotation position by means of a photoelectric pickoff which observed the sensor's position (see Fig. 58).

The opposing sets of strain transducers were paralleled so that the sensor output in the translational mode would be rejected. Similarly, the paralleled signals from transducers A and C and transducers B and D were handled differentially in order to reject the sensor response in the torsional mode and to reject symmetrical pickup in both channels.

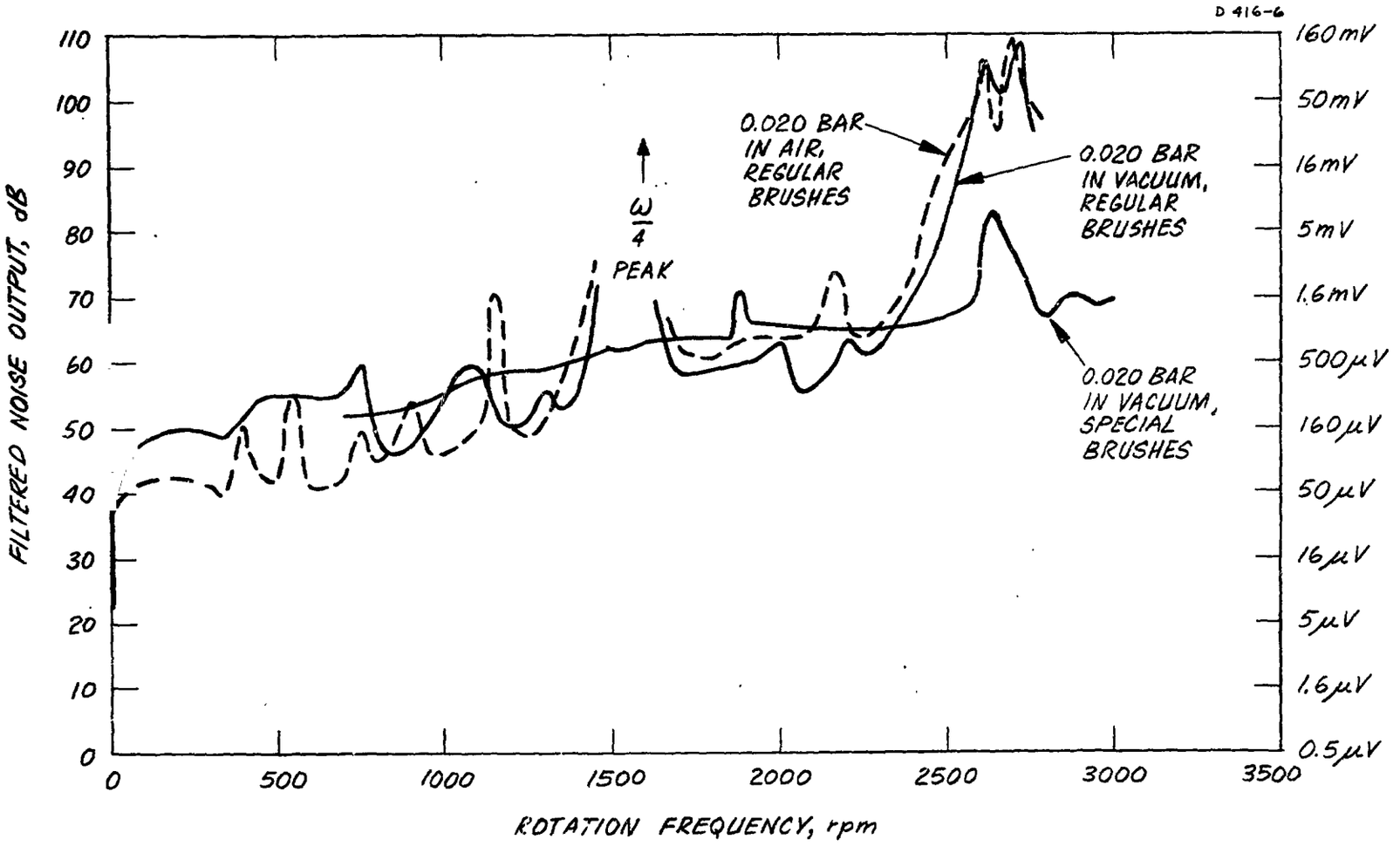

Fig. 56. Noise tests on 90 Hz cruciform on 0.020 in. torsion wire mount.

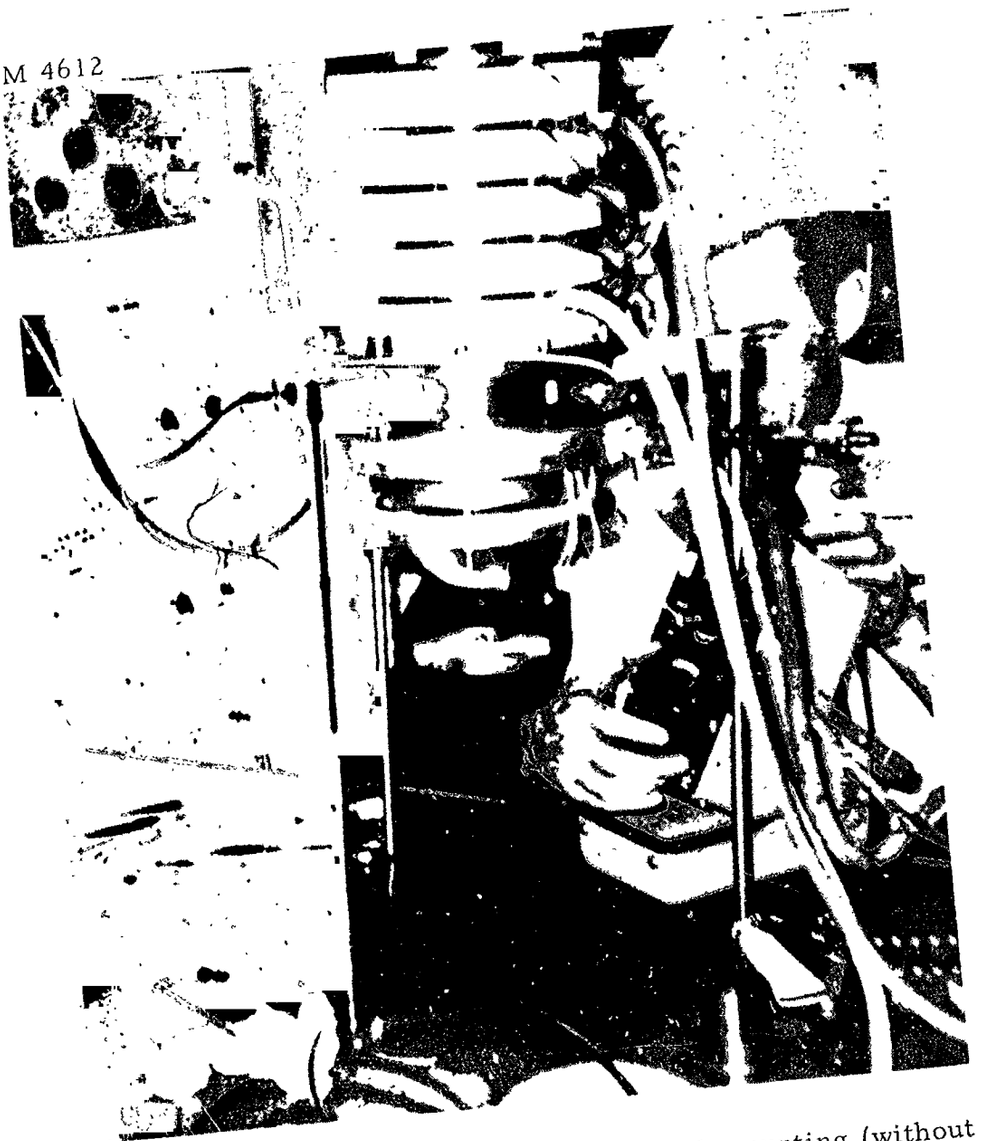

Fig. 57. Sensor rotating on rubber band mounting (without vacuum chamber).

D433-5

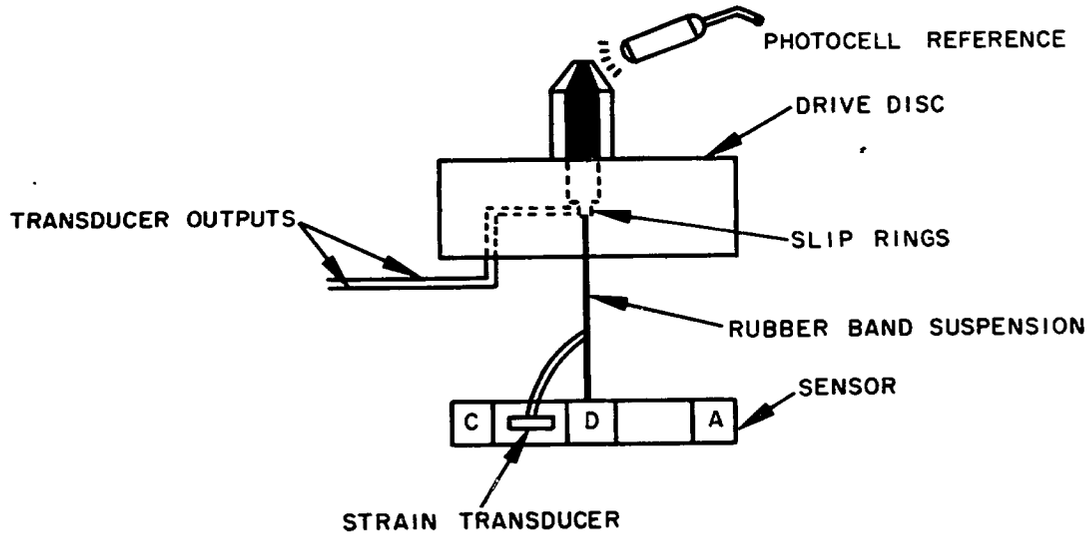

Fig. 58. Rubber band suspension.

Data were taken by running the sensor rotation frequency higher than one half of the translational mode resonant frequency; the drive power was then shut off, and the sensor was allowed to coast down while the output of the sensor was matched against the reference signal generated by the photoelectric pickoff. The resulting noise output data are shown in Fig. 59.

Two peaks can be seen. The peak at 62 rps rotation speed is the response of the translational mode at 124 Hz. The peak at 58.5 rps is the response of the tuning fork or gravitational gradient sensing mode at 117 Hz, and has an amplitude of 70 μV per transducer. The calculated gravitational gradient signal (see Table III in Section II-B-6) is 1.1 μV rms, or approximately 1.5% of this figure.

The sensor was then driven synchronously with minimum drive power, and the rotation speed was adjusted for peak output in the gravity gradient sensing mode. The noise output under low amplitude synchronous drive was the same as that seen during free rotation coastdown, indicating that the vibration and pickup due to the drive motor was negligible compared with the other noise sources.

The vacuum system was then shut off, and pressure was allowed to rise slowly from 0.022 Torr to 0.16 Torr. Noise data were taken at various points in this range. These data are reproduced in Fig. 60. This graph shows the direct relationship between noise level and vacuum level in the vacuum level range examined. We were unable to reduce the pressure level of the system below 0.022 Torr with the equipment available. Although the noise level test data indicated significant noise-pressure dependence, it must be remembered that the sensor head is rotating in the external vacuum chamber without the usual co-rotating sensor vacuum chamber; it is in effect "windmilling" the remaining air molecules about in the chamber.

c. Seven Inch Sensor on Ultracentrifuge Mount

A similar experimental setup was used to measure the noise performance of one of the 7 in. monolithic sensors on an ultracentrifuge suspension (see Fig. 38). In this experiment the rotor with the slip rings shown in Fig. 58 was replaced with the amplifier-transmitter telemetering unit discussed in Section II-E-2. The rotor speed was increased above that necessary to excite the gravitational gradient mode and allowed to coast slowly down through the resonance. The data are shown in Fig. 61. The resonant noise output of the sensor has the same Q as that of the sensor measured by other techniques, and has a peak amplitude of 135 μV. The gravitational gradient signal calculated for this sensor (see Table III in Section II-B-6) is 7 μV, or approximately 5% of this figure. This is the best signal-to-noise performance we could obtain with a rotating sensor during this phase of our work. The noise

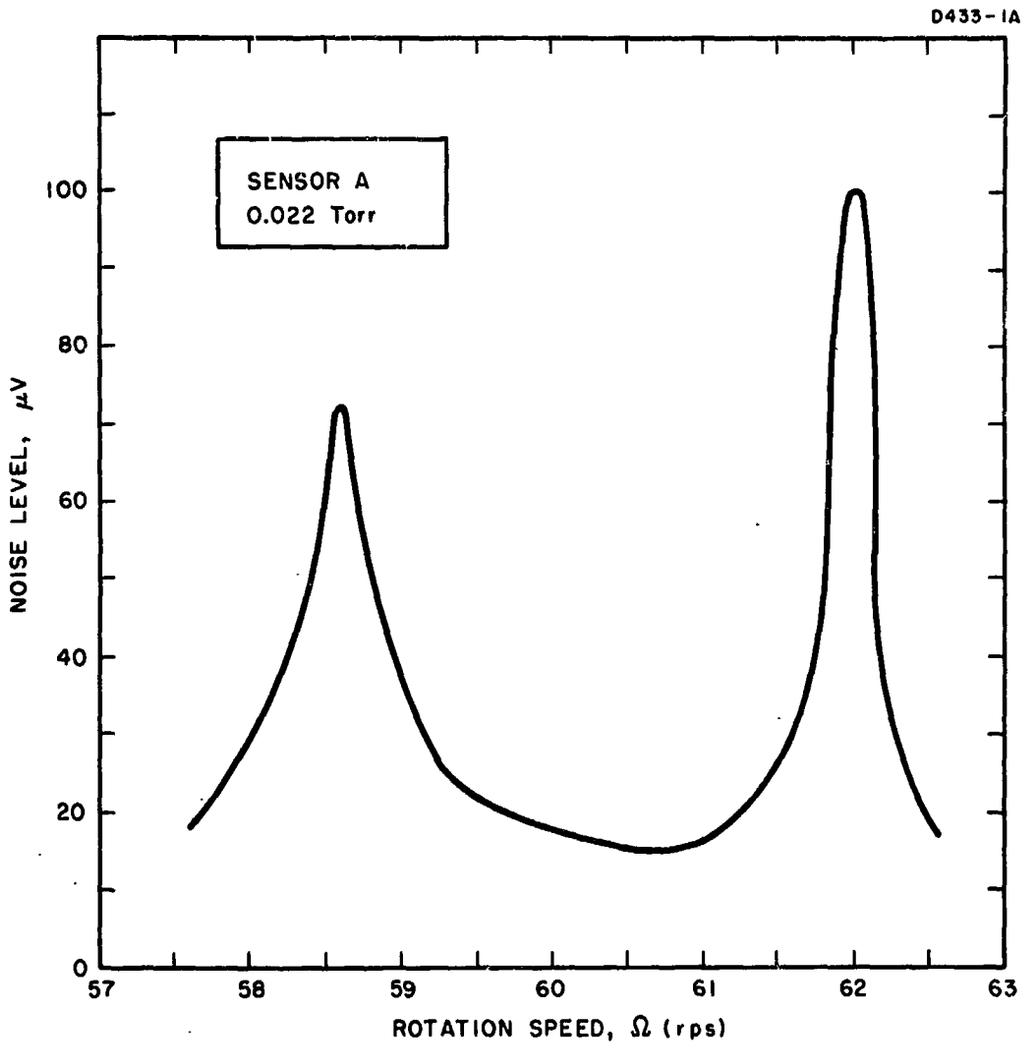

Fig. 59. Noise tests on rubber band suspension.

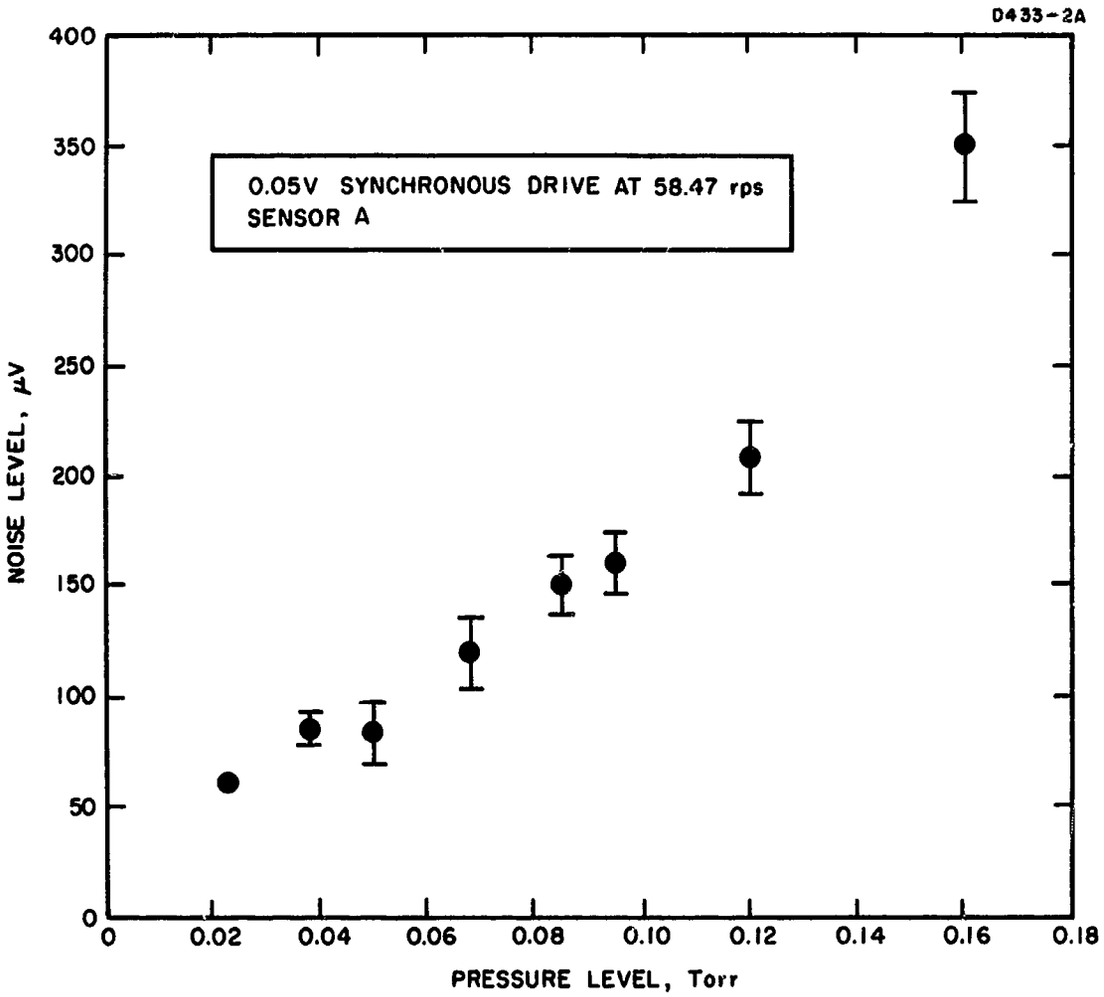

Fig. 60. Pressure dependence of noise.

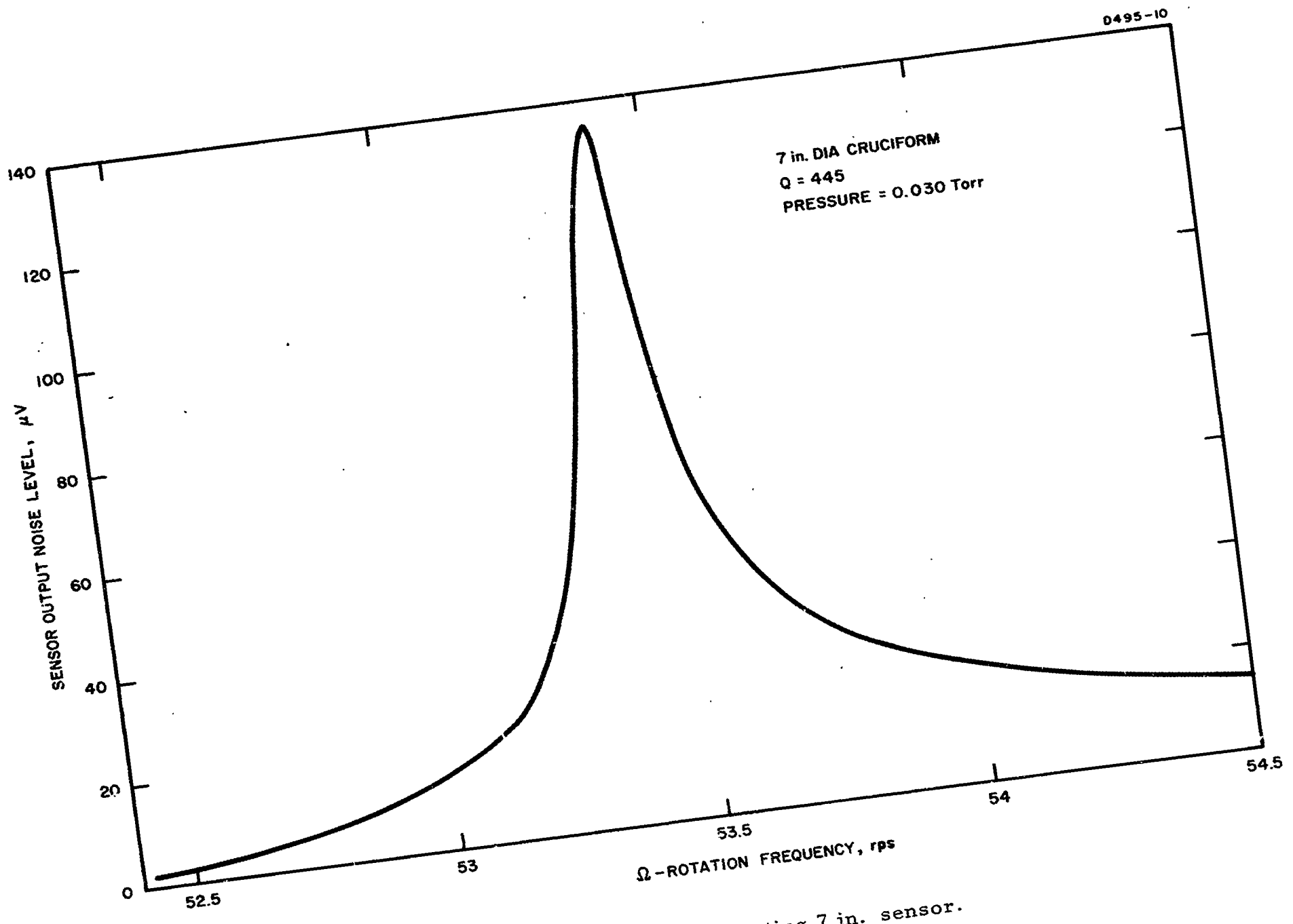

Fig. 61. Noise output of rotating 7 in. sensor.

level appeared to result from a combination of vacuum "turbulence" caused by the sensor rotating through the residual air in the stationary vacuum chamber and eddy current forces exerted on the sensor arms by the stray magnetic fields of the single-axis magnetic bearing.

The effects of light pressure were noticed during the noise tests on this sensor. It was discovered that the output from the sensor varied when the sensor was being observed with the electronic strobe flash. The coupling was so strong that when the amplified and inverted sensor output was used to trigger the strobe flash, the intermittent light output of the flash unit would depress the noise output of the sensor and maintain it at almost zero level.

In order to insure that the observed coupling was not a result of interaction of the strobe electronics with the sensor electronics, other tests were run with a small battery operated flashlight. When the light beam was directed toward the whirling arms, the signals from the sensor would increase by a factor of two or more. The extra voltage output had the resonant frequency and the rise and decay time of the sensor, indicating that the voltages seen were not being generated by a photoelectric effect or other forms of electromagnetic pickup. The effect of turning off the room lights was very slight, probably because the illumination was more even.

The effect of magnetic eddy currents was also investigated during these noise tests. If a large magnet was brought up to the bell jar, a field of about 100 G was generated near the sensor. When this was done, the sensor speed decreased noticeably and the ultracentrifuge mount twisted, indicating a significant amount of drag torque; there was also a large increase in the sensor noise output.

2. Mechanical Noise

A noise source which was of major concern in the program was mechanical vibration noise. Mechanically generated noise effects were observable when we used poor bearings, slip rings, stiff sensor mounts, and/or high synchronous motor drive levels; however, they were found to be negligible compared with other noise sources when the sensor was mounted on a soft suspension with a telemetered output and was rotated on a good (i.e., magnetic) bearing by a drive motor using a phase locked asynchronous drive source.

Quite early in the program it was determined that mechanical vibrational noise applied to the sensor mount would have no effect upon the gradient output of an ideal (symmetric) sensor. However, it was also known that mechanical asymmetries in the construction of the sensor head would allow noise reaching the sensor head through the isolation supports to be reflected into the gradient sensing resonant mode of the cruciform head.

The response of a nonideal sensor-mount system to external vibrational inputs was analyzed so that the effects of mount characteristics and sensor imperfections on the performance of the system could be studied. This work by D. Berman, given in detail in Attachment F, will be summarized here. The analytical model includes the effects of differences in arm lengths, sensing masses, and spring constants; the effects of attaching the mount at a point other than at the center of mass of the sensor head; and the effects of vibrations applied to the mounting structure. The analysis confirmed that the gravitational gradient sensing mode of an ideal sensor responds only to gravitational gradient forces and does not respond to externally applied forces of any kind or magnitude. A nonideal sensor responds to external forces only if they are dynamic vibrations with frequency components at Ω or $3\,\Omega$ (where Ω is the rotational frequency) and does not respond to constant linear accelerations. The response occurs because a portion of the driving forces is coupled into the gravitational gradient sensing mode by the asymmetries of the sensor. This response of the sensor at $2\,\Omega$ to vibrations with a frequency of Ω and $3\,\Omega$ occurs because of the rotating coordinate system of the sensor. A transverse Ω vibration can be treated as a linear combination of a right and left circularly polarized vibration (see Fig. 62(a)). The component rotating in a direction opposite to that of the sensor rotation is rotating at a rate of $2\,\Omega$ in the sensor coordinate system (see Fig. 62(c)); the opposite component is rotating at the same rate as the sensor and therefore is a static force in the frame of reference of the sensor (see Fig. 62(b)).

This result of the analysis is of practical interest and helps to explain the low noise levels seen in the magnetic bearing. Fortunately, bearing vibrations from unbalanced rotors belong to this second (or unobservable) class of Ω motions. This can be seen from Fig. 63, which shows the cross section of a rotating shaft and bearing. Within the bearing, the shaft experiences translational motion as well as spin. If the stabilizing action of the bearing is the same in all directions (as with a magnetic bearing), the translational shaft motion will be circular and in the same direction of rotation as the sensor rotation; therefore, the sensor sees it as a constant force.

The $2\,\Omega$ motions which are generated at the center of the sensor by other types of vibrations give rise to beam deflections at the ends of the sensor arms. If there are asymmetries in the construction of the sensor, the deflections are not equal for all four arms; the differences in the deflection amplitudes is proportional to the asymmetry parameter h. These deflection differences produce sensor vibrations which are identical in mode structure and frequency to the vibrations produced by gravitational gradients; these represent a potential source of noise. The gradient mode amplitude a_g caused by

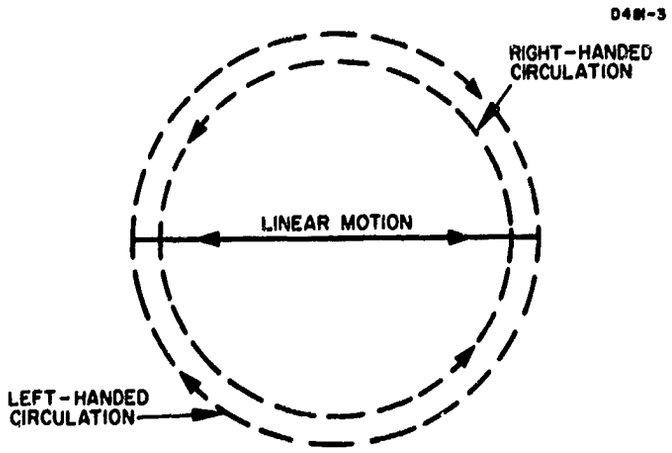

Fig. 62(a).
Translational motion decomposes into right- and left-hand circulation.

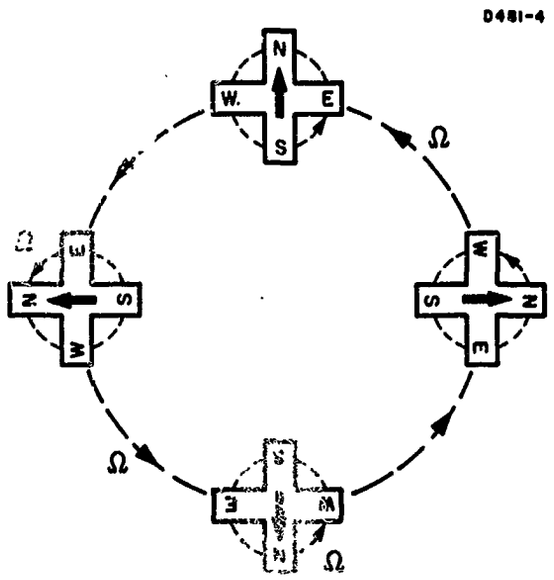

Fig. 62(b).
Positive circulation produces no vibrational effect in rotating reference frame.

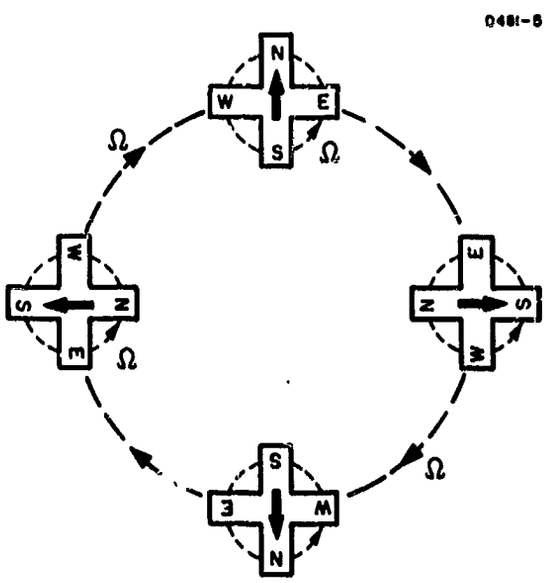

Fig. 62(c)
Negative circulation induces a vibrational mode forcing function at twice the frequency of rotation.

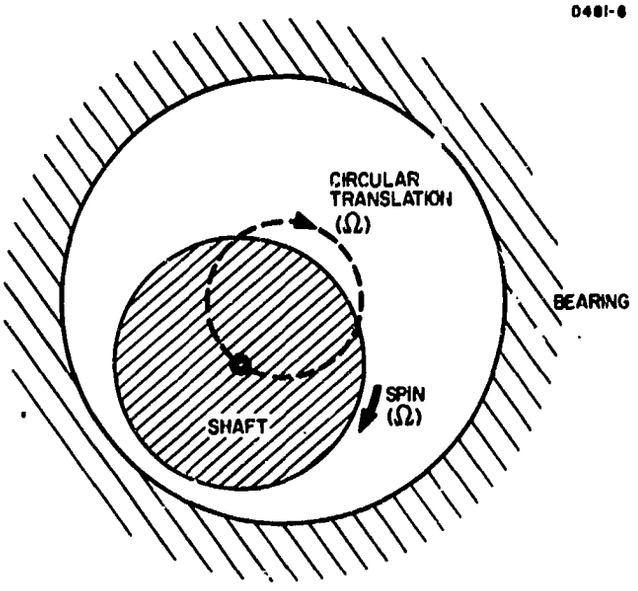

Fig. 63.
Inherent bearing vibrations give rise to positive circulation motions which have no effect on sensor response.

a given linear bearing vibration amplitude X_o was calculated for a sensor with $Q = 100$ as a function of the ratio of the suspension frequency Ω_m to the gradient mode frequency ω_g for various magnitudes of sensor asymmetry h. These data are plotted in Fig. 64.

This curve can be used to determine the isolation characteristics of the present ultracentrifuge mount-sensor system. If we assume a value for the center of mass asymmetry h on the order of 0.1% (0.001 in. center of support displacement), a sensor Q of 400 at 100 Hz and a natural frequency of the ultracentrifuge suspension of 3 Hz, then $\Omega_m/\omega_g = 0.03$; we find that the noise output to disturbance ratio (attenuation factor) of the system is about 10^{-3}.

The noise levels seen in our 7 in., 107 Hz cruciform sensor under rotation (see Fig. 61) were about 20 times the expected gravitational signal calculated in Table III of Section II-B-6. This implies an equivalent arm motion of about 4×10^{-7} cm, or about 40 Å. The attenuation factor of 10^{-3} calculated from the analysis of this mount-sensor system indicates that the amplitude of the negative circulation Ω motion of the rotor in the bearing must be less than 4×10^{-4} cm, or about 8 light wavelengths. Actually, we believe the noise seen in Fig. 61 resulted from a combination of eddy current forces and vacuum "turbulence," and that the mechanical noise of the bearing was substantially below that calculated above.

3. Vacuum Turbulence

It was known from previous experience (see Appendix B) that the coupling of external acoustic noise to the sensor head would be negligible even at the very low signal levels (2 nV) attained during the gravitational calibration experiments (see Attachment E), provided that the sensor was operated in a moderate vacuum (0.010 Torr). Therefore, it did not appear to be neces ary to strive for ultrahigh vacuum capabilities in our bearing and chamber designs. However, as shown in Fig. 60, this vacuum level is not low enough to prevent excitation of the sensor when it is rotated inside a stationary vacuum chamber. The differential rotation of the sensor and chamber walls creates turbulence in the residual air in the chamber, which results in the generation of an appreciable amount of noise. This turbulence noise source can be easily eliminated in future designs by operating at lower pressures or operating the sensor in a corotating vacuum chamber.

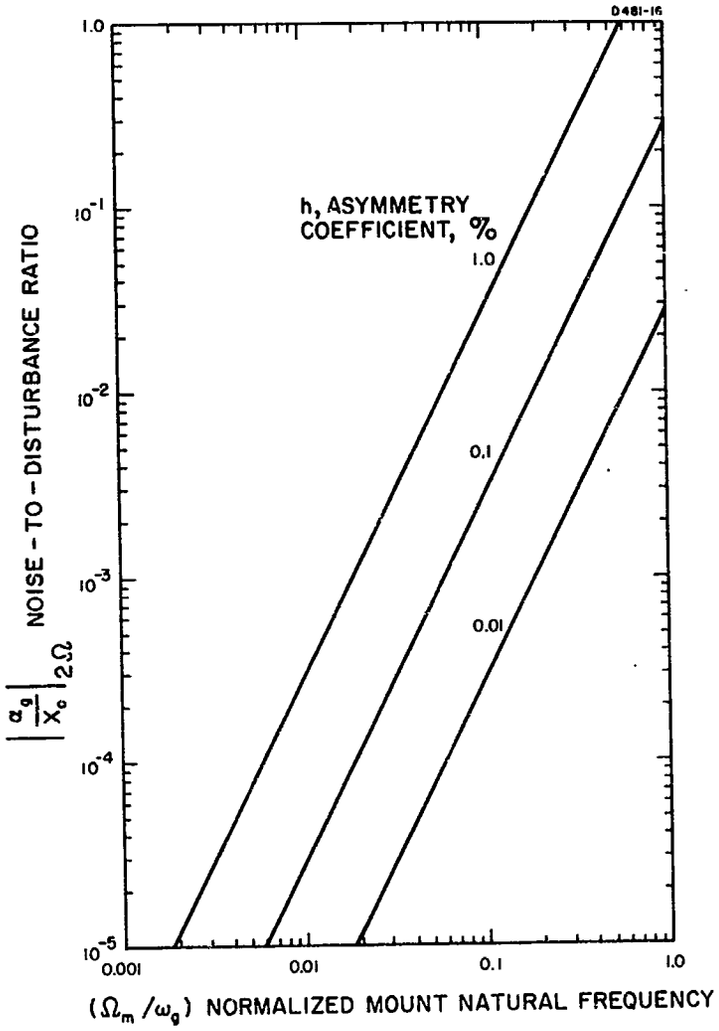

Fig. 64. Gravitational mode response (at gravity-sensing frequency) due to external disturbance of Ω negative circulation.

4. Eddy Current Forces

Eddy current forces can be generated in the sensor itself by the motion of the conductive arms through a static magnetic field. The eddy current force F on a conductor of characteristic dimension ℓ moving at a velocity v through a static magnetic field B is given by

$$F = B^2 \ell^2 v/R \tag{70}$$

where R is the resistance of the path through the conductor. This resistance is difficult to calculate accurately; however, if we assume that the end mass of the sensor has a resistance path of a few centimeters and use the resistivity of aluminum, which is 3×10^{-6} Ω-cm, the path resistance can be estimated at about 3×10^{-6} Ω. With a stray magnetic field of 5 G and a sensor arm velocity of about 2 m/sec at 50 rps, the calculated eddy current force is about 30 dyn, which is many orders of magnitude higher than the calculated gravitational force level of about 0.6×10^{-3} dyn. This calculated force level is a static force; its predominant effect on the sensor is to apply a retarding torque rather than generating noise. However, any asymmetries in the magnetic field would produce dynamically varying forces in the sensor arms at the rotation frequency and its harmonics.

It is not possible to calculate the amount of harmonically generated eddy current noise at the present time because we do not know the asymmetries of the magnetic field in the prototype magnetic bearing. However, it is quite probable that our present noise level in the rotating sensors is caused by this effect; it is obvious that in the future the magnetic suspension will have to be carefully designed to isolate the magnetic flux from the sensor head.

5. Electrostatic Field Pickup

It has been found that rotation of the wire leads on the capacitive strain transducers through an electrostatic field can generate an appreciable amount of electrical pickup. The electrostatic fields observed in our test setups were found to be generated by static charges left on the teflon bumper plates when the apparatus was handled.

The removal of the teflon plates and the use of electrostatic shielding, twisted leads, and differential preamplifiers reduced the noise level from electrostatic pickup well below levels produced by other sources of noise; electrostatic fields do not represent a problem at present.

6. Magnetic Induction Pickup

When the sensor lead wires rotate through a diverging magnetic field, they generate induced currents which will depend to a large extent on the geometry of both the wire loops and the magnetic field.

The induced emf V from magnetic pickup in a wire loop of area A rotating at a speed Ω through a constant magnetic field B perpendicular to the loop is given by

$$V = B A \Omega \sin \Omega t \quad . \tag{71}$$

This output is at the rotation rate, of course; however, if two loops were rotating through an asymmetric field, a portion of this voltage would be proportional to the gradient of the magnetic field and at twice the rotation rate[35] (see Attachment A).

The residual flux level in our prototype magnetic bearing has been measured as approximately 5 G at the position of the rotating sensor; therefore, magnetic induction can be a problem. As a rough estimate, let us assume that the area of the loop in the leads is $0.1\ cm^2$ and that the asymmetries will produce $2\ \Omega$ outputs which are 1% of the $1\ \Omega$ outputs. At a rotation speed of 50 rps, this will give a coherent noise level of approximately 10^{-7} V, although this noise level is not large enough to cause a problem at present, it should be considered later.

This analysis and that on eddy current forces indicate the need for careful control and suppression of asymmetric magnetic flux in the region of the sensor.

7. Drive Motor Noise

Vibrational noise and electromagnetic pickup from the drive fields of the motor represented a potential noise source. However, experience with noise tests on rotating sensors has shown that this is not a major problem. With synchronous drive at high drive levels it was possible to see the effects of the drive fields (see Section II-D-3-d); when the drive voltages were decreased to just that necessary to maintain synchronous rotation, however, the noise level decreased to that seen under free rotation operation. In any case, the use of the phase locked asynchronous drive (see Section II-D-3-e) was found to eliminate all noise from the drive motor.

8. Light Pressure

During some of our noise tests on rotating sensors, it was noticed that sensor responded to light from the strobe flash unit and small flightlights when the beams were directed at one side of the rotating sensor.

The force of light pressure on a reflecting object is given by

$$F = 2P/c \tag{72}$$

where P is the light power and c is the velocity of light. The handbook on the strobe flash unit stated that the unit produced a beam intensity of 1.2×10^6 lm/m^2 at 1 m distance. The experiments were carried out at a distance of approximately 1 ft, or 1/3 m; and since the sensor arm area was about 8 cm^2, the force on the arms is calculated to be about 10^{-2} dyn, or about 20 times the calculated gravitational force.

The agreement of the level of forces obtained in this calculation with the comparative noise voltages observed during the tests and the behavior of the sensor during the various tests with different light sources give strong assurance that the effect observed resulted from light pressure.

These experiments also confirm that the voltage outputs obtained from the sensor during rotation are a true indication of its excitation and that the external vibrational noise sources acting on the sensor during high speed rotation are small enough to allow the measurement of very weak force levels.

Light pressure as a noise problem is completely eliminated when an opaque vacuum chamber is used.

G. GRAVITATIONAL CALIBRATION OF SENSOR

Although our primary goal is to determine methods of rotating the gravitational mass sensor structures without introducing large amounts of noise into the gravity gradient sensing mode, one objective of our work is to learn enough about these structures that we can predict their response to the gravitational gradient field of a mass. The theoretical portion of this work is largely complete and is given in Section II-B and Attachment C.

In order to verify experimentally the theoretical equations and to develop a test system for calibrating the gravitational gradient response of the various mass sensors, we have constructed a generator of dynamic gravitational gradient fields and have measured the response of one of our sensors to these fields.

This work is reported in detail in Attachment E and will not be repeated here. Later tests using the same generator but a more sensitive detector (see Fig. 28) have led to a slight improvement in measured sensitivity over that given in Attachment E. With the more sensitive detector and with a 100 sec integration time, the minimum gravitational gradient field strength measured was 10^{-9} sec $^{-2}$ (1 Eötvös unit, or 3×10^{-4} of the earth's gradient).

This work demonstrates that the sensors and the sensor electronics which we have developed during the research phase of the program have the basic sensitivity to gravitational gradient fields which is required for the presumed future applications and that sensor calibration can be accomplished without requiring a zero g environment.

H. SENSOR APPLICATIONS

Two fairly obvious applications of the gravitational mass sensor will be to measure the masses of the asteroids and the variations in the gravitational field of the moon. However, since the devices respond in different ways to inertial and gravitational forces, they could also conceivably be used as sensors for active attitude control.

1. Asteroid Mass Measurement

The principal scientific goal of the space program is the exploration of the universe, with special emphasis on our solar system. The study of the composition of the asteroids will give us information concerning the origin of the solar system and the formation of the planets. It may also tell us something about the types and amounts of simple organic constituents which were in the primordial cosmic dust, and thus give us clues to the origin of life.

a. The Asteroid Belt

The asteroid belt consists of a large number of small planetoids in solar orbits between Mars and Jupiter. The various orbits have a mean semi-major axis of 2.77 AU, a mean inclination to the ecliptic of 8.6°, and a mean period of 4.6 years.[36] There are ten asteroids with radii greater than 100 km, and over 300 with radii greater than 25 km. The number of asteroids increases with decreasing size, and there are estimated to be over 100,000 with radii greater than 1 km, or as large as a mountain.[37-39] These numbers indicate that it will be desirable to investigate a large number of the asteroids in order to obtain data concerning the average composition. An extensive search will also ensure that we do not overlook any of the asteroids with anomalous features. The space containing these asteroids is a large donut shaped volume containing 10^{26} km^3, so that even the smaller asteroids are separated from each other by hundreds of thousands of kilometers. Therefore, it is not feasible to consider visiting them sequentially with a single probe.

b. Proposed Program

In order to investigate the asteroid belt in an efficient manner, we propose to send a simple probe out to each of the larger asteroids in a 1000 km fly-by to measure as much as possible concerning the composition. The information would then be used to classify the asteroids into groups. Typical asteroids from each group or those with anomalous characteristics would then

be targets for more sophisticated manned or self-controlled vehicles which could rendezvous and land on the asteroid for more detailed investigation.

c. Gravitational Field Measurement

The most important parameter in determining the composition of an asteroid is a measurement of its density. Measurement of the volume can be obtained from photographs during the flyby, and a sensor which measures the mass during the flyby will enable us to obtain the density. The mass measurement technique used in planetary probes cannot be used because the gravitational force field of even the larger asteroids is not strong enough to appreciably affect the trajectory of the probe during flyby.

We propose to measure the mass of the asteroid by measuring the gravitational field of the asteroid with a gravitational mass sensor.

The first models have detected dynamic gravitational gradients of 1×10^{-9} sec^{-2} or 0.0003 of the surface gradient of an asteroid with a 100 sec integration time. The present noise level in the rotating sensors is caused by bearing noise since we must rotate these devices while supporting them in the earth's field. We propose to eliminate the bearing problem and the vehicle gravity gradient problem by attaching the sensor to the vehicle and rotating the entire vehicle. As currently envisioned, the spacecraft would be spin stabilized at 300 to 600 rpm (5 to 10 rps), and the sensor would respond to the presence of a gravitational gradient by vibrating at twice this frequency.

The surface gravitational gradient of an asteroid is a function of its density and falls off as the cube of the ratio of radius to distance:

$$\Gamma = \frac{G M}{R^3} = \frac{4\pi}{3} G \rho \left(\frac{a}{R}\right)^3 , \qquad (73)$$

If we assume an asteroid density of 4×10^3 kg/m^3 (4 g/cm^3), the gravity gradient for the various asteroids at a miss distance of 1000 km is given by Table V.

TABLE V

Gravitational Field of an Asteroid at 1,000 km

Number		Radius km	Mass $\times 10^{17}$ kg	Gravity Gradient $\times 10^{-9}$ sec^{-2} or Eötvös Units
(Ceres)	1	350	6000	44
(Pallas)	1	230	1800	12
(Vesta)	1	190	1000	7.1
	6	~ 140	450	2.7
	25	~ 70	60	0.34
	80	~ 44	15	0.085
	200	~ 28	4	0.024

From Table V we see that the gravitational gradient of an asteroid is easily measured at a flyby distance of 1000 km. The larger asteroids, with gravity gradients of 10^{-8} to 10^{-9} sec^{-2}, could be detected with the present laboratory models. The limit of sensitivity of these rotating sensors is expected to be 10^{-12} to 10^{-13} sec^{-2}, which is adequate for a 10% measurement of the mass of the smaller, more numerous asteroids.

d. Range

In order to interpret the data from the gravitational mass sensor in any absolute manner, it is necessary to know the miss distance R_m. The miss distance can be obtained in a simple manner from the response of the gravitational sensor. For a simple example, the voltage output of the gravitational sensor is a function of the separation distance R which is a function of time

$$V(t) = K\frac{GM}{R^3} = \frac{KGM}{(R_m^2 + v^2t^2)^{3/2}} = \frac{KGM}{R_m^3}\left[1 - \frac{3}{2}\left(\frac{vt}{R_m}\right)^2\right]. \qquad (74)$$

This is a simple two parameter (R_m, M) curve, and a best fit of the data, along with a knowledge of the relative flyby velocity v obtained from orbital parameters, will give both the mass and miss distance.

To determine the ultimate limit on this type of application, we shall assume a thermally limited gravitational mass sensor detecting the gravitational force gradient of the asteroid. The usual thermally limited equation from eq. (16) is

$$\frac{GM\ell\tau}{R^3} = (S/N)^{1/2}(2kT/m)^{1/2} \tag{75}$$

where S/N is the desired signal-to-noise ratio; T, m, and ℓ are the temperature, mass, and length of the sensor; M is the mass of the asteroid; and τ is the integration time. The integration time, however, is not completely independent of the range, since in a flyby the effective integration time must be less than the time of effective interaction of the sensor and asteroid.

$$\tau < \frac{2R}{v} \tag{76}$$

where v is the velocity of the probe and R is the miss distance or effective range. Using (76) our maximum range for a given set of operating parameters is given by

$$R^2 = \frac{GM\ell}{v(S/N)^{1/2}}\left(\frac{2m}{kT}\right)^{1/2} . \tag{77}$$

If we assume a room temperature sensor of effective mass 200 g (1/2 lb), and effective length of 30 cm (1 ft) on a probe with a relative velocity of 5 km/sec, the range in kilometer for a 100 to 1 signal-to-noise ratio is given in Table VI.

TABLE VI

Mass Measurement of Asteroids

Number	Radius km	Mass $\times 10^{17}$ kg	Range For S/N = 100 km	Integration time sec
1 (Ceres)	350	6000	49,000	20,000
1 (Pallas)	250	1800	27,000	11,000
1 (Vesta)	190	1000	20,000	8,000
6	~140	450	13,000	5,000
25	~ 70	60	4,900	2,000
80	~ 44	15	2,400	950
200	~ 28	4	1,300	500

2. Lunar Gravitational Field Measurement

The objective of selenodesy is to determine the values of the coefficients of the spherical harmonics of the lunar gravitational potential:

$$V = \frac{GM}{r}\left[1 + \sum_{n=2}^{\infty}\left(\frac{a}{r}\right)^n \sum_{m=o}^{\infty} P_{nm}(\sin\phi)\left\{C_{nm}\cos m\lambda + S_{nm}\sin m\lambda\right\}\right]. \quad (78)$$

Although it is conceptually possible that data from gravimeters on the surface could be used (as was originally done in geodesy), this technique is not practical for the moon. The method currently preferred involves the detailed analysis of the orbital parameters of a satellite around the body under investigation. This requires highly precise oscillators in the satellite, a highly accurate radio tracking network collecting data over a long time, and sophisticated computer programs.

In the present satellite geodesy programs, this method of obtaining the gravitational potential harmonics has led to the determination of zonal harmonics of odd degree through the ninth, the nonzonal harmonics of all degrees from the second through the eighth, and because of a resonance for m = 13, the sectorial harmonics of thirteenth degree and order.[41] It is expected that a lunar orbiter gravity survey using similar techniques will give comparable accuracy. In theory, this technique can be extended to obtain all higher orders of the gravitational potential; however, the orbital parameter technique has a tendency to smooth out the higher order contributions and the localized features, and it is expected that it will be difficult to obtain the higher order components. Each increase in n will require longer tracking times and more sophisticated computer programs.

However, terms with increasing n correspond to small scale features on or near the lunar surface; although the contribution of these harmonic components to the gravitational potential is quite small, their contribution to the gravitational force gradient at a point above them is a substantial fraction of the gravitational gradient of the whole moon. Of course, these higher order components die out with increasing altitude and increasing n. This leads to the phenomenon that a gravitational force gradient sensor operating in a lunar orbiter at a given altitude will preferentially sense the gravitational force gradient of those harmonic components of the lunar potential which have a wavelength roughly proportional to the altitude of the sensor. The exact response will depend upon the behavior of the amplitude of the harmonic components with increasing n and the depth of the sources of various order.

To illustrate this peaking behavior of the gravitational force gradient, let us examine the gradient which is predicted for higher orders of n if we assume that the strength of the lunar potential components has approximately the same statistical behavior as the earth's potential (which is highly doubtful).

A typical term in the gravitational potential

$$\frac{GM}{r}\left(\frac{a}{r}\right)^n P_{nm}(\sin\phi)\, C_{nm} \cos m\lambda \tag{79}$$

gives rise to a gravitational force gradient of

$$\Gamma = (n+1)(n+2)\frac{GM}{a^3}\left(\frac{a}{r}\right)^{n+3} P_{nm}(\sin\phi)\, C_{nm} \cos m\lambda \,. \quad (80)$$

If we assume that the strength of the components follows the statistical law $S_{nm} \approx C_{nm} \approx 1.3 \times 10^{-6}/n - 1$, and that $(2n + 1)$ terms contribute to the variations with "wavelength" $\lambda = 2\pi a/n$, we obtain an average value for the n^{th} order gradient of

$$\Gamma_{rms} \approx \frac{(n+1)(n+2)(2n+1)^{1/2}}{(n-1)} \left(\frac{a}{a+h}\right)^{n+3} \frac{GM}{a^3}(4\pi)^{1/2} \times 1.3 \times 10^{-6} \text{ sec}^{-2} \quad (81)$$

where Γ_{rms} is the root means square value of gradient per unit frequency range, with frequency measured in cycles per orbital revolution. We have plotted this for a number of different combinations of orbital altitude h and harmonic order n in Fig. 65. The amplitude of these contributions is approximately 10^{-3} to 10^{-4} of the moon's gradient of about 9.3×10^{-7} sec^{-2}. These are average values over the entire orbit for each value of n. A gravity gradient sensor, with a sensitivity of 10^{-9} sec^{-2} in a 10 sec averaging period, would take about 500 data points during each orbit, giving a resultant rms average sensitivity of 5×10^{-11} sec^{-2} per orbit. This is quite adequate for a reasonably accurate measurement of the rms value of the spheroidal harmonics at even 80 km altitude.

The change in the gradient resulting from a specific local anomaly can be quite a bit higher than the rms values over the entire orbit. For example, if we assume an altitude of 50 km, local anomalies (such as a large lunar crater with characteristic dimensions of 50 km) will create a gravitational force gradient of the order of 10^{-7} to 10^{-8} sec^{-2}, which is a variation of a few percent in the gradient of the moon.

The preliminary work indicates that if a gravitational gradient sensor could be made to work in an orbiting satellite, it would prove extremely useful in obtaining the higher order harmonics of the lunar gravitational potential and should give a real time readout of the strength of the local features in the gravitational map.

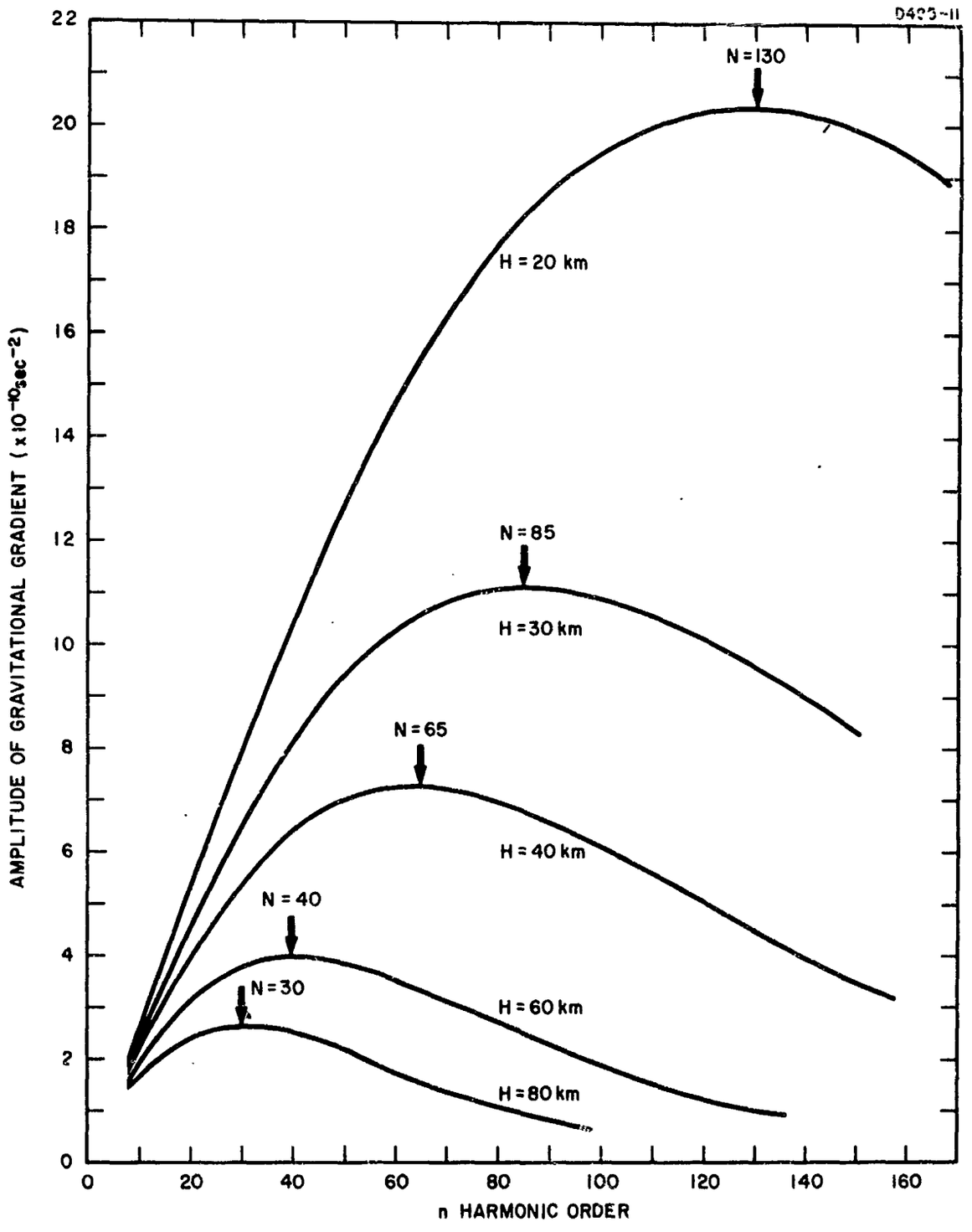

Fig. 65. Lunar gravitational gradient amplitudes.

BLANK

PAGE

SECTION III

CONCLUSIONS

From our research on gravitational mass sensors we can derive the following conclusions regarding the feasibility of using rotating elastic bodies to detect the gravitational gradient field of a mass.

Analysis shows that when an elastic body is rotated in a force field, vibrations at various harmonics of the rotational rate will be induced in the body by the force field and its gradients. The gravitational force gradient will induce vibrations at twice the rotation rate, while inertial accelerations or motions will induce vibrations with a frequency near the rotational frequency. Thus, frequency separation techniques can be used to separate gravitational effects from certain types of inertial effects. Rotational motions have gradients, and certain types of these motions can be confused with the gravitational field: this is common to all gradient sensors, and they will all require some type of space stabilization.

Analysis has shown that radially vibrating structures are not useful for gravitational gradient sensors because they are unstable under rotation.

Analysis and experiments have demonstrated that a tangentially vibrating cruciform can be used to measure the gravitational gradient field. When properly designed and operated, it is not appreciably affected by rotation. Analysis has shown that an ideal cruciform is unaffected by any type of vibration and that only certain restricted types of high frequency vibration affect a nonideal sensor.

Experiments have proved that piezoelectric strain-to-voltage transducers have the necessary sensitivity to measure the very small motions (10^{-9} to 10^{-12} cm) induced in the sensors by the gravitational fields, and that the present amplifiers, telemetering units, detectors, recorders, and other electronic components are more than adequate for the problem of handling the signals.

Experiments with a stationary sensor excited by a dynamic gravitational gradient field generator have demonstrated that a cruciform sensor can measure a gravitational gradient field of 10^{-9} sec^{-2} (1 Eötvös unit).

Experiments have shown that a single axis, Beams type magnetic bearing can rotate the sensors without introducing an appreciable amount of bearing noise of the type which will affect the cruciform sensors.

Experiments have demonstrated that the accelerations exerted on a rotating sensor by all noise sources are less than 4×10^{-7} g's. This measured noise level is caused by the known noise sources of residual air turbulence and magnetic eddy current forces, both of which will be easily eliminated in the next model. There does not seem to be any noise source of appreciable magnitude which cannot be eliminated by careful engineering.

Analysis and experiment indicate a practical device requires that the sensor be operated on some sort of soft mounting structure, either elastic or magnetic.

Experiments have demonstrated that soft mounting structures exist which are stable at the necessary rotation speeds; however, we do not yet understand the behavior of such mounts and have not yet found a completely practical mount structure.

The results of our experimental and theoretical work to date indicate that it is feasible to use a rotating cruciform structure to sense the gravitational gradient field of a mass. They are rugged enough to handle without caging or other precautions, and it is possible to test their operating characteristics and calibrate them with gravitational fields without requiring flight tests.

SECTION IV

RECOMMENDATIONS

It is recommended that further work continue on the development of rotating gravitational gradient sensors. The areas of primary concern which require investigation are

- The development and understanding of sensor mounting structures to find a compact version which will give good mode separation and good noise isolation, and is stable under all conditions of rotation speed and orientation
- The detailed study of the effects of sensor design errors on the coupling of noise into the gravitational gradient sensing mode to determine the critical design parameters and methods for measuring and controlling them
- The design of a stable, driftless, well-engineering, three-axis magnetic suspension with low magnetic flux leakage
- The continued study of noise sources under rotating conditions.

As these efforts are successful in reducing the noise introduced into the sensor, further effort will be required to

- Improve sensor design and sensor electronics to attain greater sensitivity to gravitational gradient fields
- Study the sensor response to gravitational fields to provide better agreement between calculated and measured response.

BLANK PAGE

REFERENCES

1. R. L. Forward, "Mass Detector," Hughes Research Laboratories Internal Report RL-59, 19 March 1962.

2. R. L. Forward, "Gravitational Mass Sensor," Proc. 1963 Symposium on Unconventional Inertial Sensors, Farmingdale, New York, 18-19 November 1963, pp. 36-60; also Hughes Research Laboratories Research Report No. 284A, November 1963.

3. R. L. Forward, "Rotating tensor sensors," Bull. Am. Phys. Soc. 9, 711 (1964).

4. R. L. Forward, "Rotating Gravitational and Inertial Sensors," presented at AIAA Unmanned Spacecraft Meeting, Los Angeles, 1-4 March 1965.

5. C. C. Bell, R. L. Forward, and J. R. Morris, "Mass Detection by Means of Measuring Gravity Gradients," presented at AIAA Second Annual Meeting, San Francisco, Calif., 26-29 July 1965; also AIAA Paper 65-403.

6. J. Weber, "Detection and generation of gravitational waves," Phys. Rev. 117, 306 (1960).

7. J. Weber, General Relativity and Gravitational Waves (Interscience, New York, 1961), Chap. 8.

8. R. L. Forward, D. M. Zipoy, and J. Weber, "Measurement of dynamic gravitational fields," Bull. Am. Phys. Soc. 7, 320 (1962).

9. R. L. Forward, "Detectors for Dynamic Gravitational Fields," unpublished thesis.

10. J. Weber, "Gravitational Waves," in Gravitation and Relativity, H.-Y. Chiu and W. F. Hoffman, Eds. (W. A. Benjamin, Inc., New York, 1964), Chap. 5, p. 100.

11. J. Sinsky and D. Zipoy, "Experimental and Theoretical Research in Gravitation Physics," Final Technical Report on Grant AF AFOSR 409-63, 1965.

12. C. C. Bell, J. R. Morris, J. M. Richardson, and R. L. Forward, "Vibrational Mode Behavior of Rotating Gravitational Gradient Sensors," submitted to J. Spacecraft and Rockets, 1966.

13. D. Berman, "Nonideal Behavior of Rotating Gravitational Mass Sensors," to be submitted to J. Spacecraft and Rockets, 1966.

14. R. L. Forward and L. R. Miller, "Generation and detection of dynamic gravitational gradient fields," Bull. Am. Phys. Soc. 11, 445 (June 1966).

15. R. E. Roberson, "Gravitational torque on a satellite vehicle," J. Franklin Inst. 265, 13 (January 1958).

16. J. C. Crowley, S. S. Kolodkin, and A. M. Schneider, "Some properties of the gravitational field and their possible application to space navigation," IRE Trans. SET-4, 47 (March 1959).

17. M. Streicher, R. Zehr, and R. Arthur, "An Inertial Guidance Technique Usable in Free Fall," Proc. National Aeronautical Electronics Conf., Dayton, May 1959, pp. 768-772.

18. J. J. Carroll and P. M. Savet, "Space Navigation and Exploration by Gravity Difference Detection," IAS paper 59-61, IAS National Summer Meeting, Los Angeles, 16-19 June 1959 (also Aerospace Eng. 18, 44 (July 1959)).

19. R. E. Roberson, "Sensing and Actuating Methods," in "Methods for the Control of Satellites and Space Vehicles," WADD Technical Report 60-643, July 1960, Vol. 1.

20. P. Savet, "Satellite attitude detection and control," Arma Eng. 3, 4 (November 1960).

21. J. W. Diesel, "A New Navigation Concept for Orbital Systems, Spacecraft, and Intercontinental Missiles," Litton Systems, Inc., TM 61-34, November 1961.

22. R. E. Roberson, "Gravity gradient determination of the vertical," ARS J. 31, 1509 (November 1961).

23. P. Savet, "Attitude control of orbiting satellites at high eccentricity," ARS J. 32, 1577 (October 1962).

24. S. Thyssen-Bornemisza, "Gravitational exploration and the principle of equivalence," Geophysics 24, 301 (April 1963).

25. J. W. Diesel, "A new approach to gravitational gradient determination of the vertical," AIAA J. 2, 1189 (July 1964).

26. R. E. Roberson, "Establishment of the Center of Mass and Rotational State of a Space Vehicle by Inertial Techniques," to be published in Proceedings of the XV International Astro. Cong., Warsaw, 1964.

27. L. G. D. Thompson, R. O. Bock, and P. H. Savet, "Gravity Gradient Sensors and Their Applications for Manned Orbital Spacecraft," Third Goddard Memorial Symposium, AAS, Washington, D. C., 19 March 1965.

28. Van Nostrand's Scientific Encyclopedia, 3rd ed. (Van Nostrand, New York, 1958), p. 611.

29. H. P. Kalmus, "A New Gravity Meter," Gravity Research Foundation Fifth Award Essay, New Boston, New Hampshire, 1964.

30. J. V. Fitzgerald, "Resonant Rotational Gravimeter," essay submitted to the Gravity Research Foundation, 1962.

31. J. V. Fitzgerald and F. J. Matusik, "Nonlinear resonance device for measuring uniform force fields," Rev. Sci. Instr. 34, 396 (April 1963).

32. J. P. Den Hartog, Mechanical Vibrations (McGraw-Hill, New York, 1956), pp. 225 ff and 247 ff.

33. V. Chobotov, "Gravity Gradient Excitation of a Rotating Cable-Counterweight Space Station in Orbit," Aerospace Coporation, TD-169 (3530-20)TN-1, AD-297871, 11 January 1963.

34. J. W. Beams, R. D. Boyle, and P. E. Hexner, "Magnetically suspended equilibrium ultracentrifuge," Rev. Sci. Instr. 32, 645 (June 1961).

35. L. R. Miller, "Magnetic gradient sensor," IEEE Trans. Geosci. Elect. GE-3, 10-13 (1965).

36. C. W. Allen, Astrophysical Quantities, 2nd ed. (Athlone Press, University of London, 1963).

37. J. C. Brandt and P. Hodge, Solar System Astrophysics (McGraw-Hill, New York, 1964), Chap. 12.

38. B. M. Middlehurst and C. P. Kuiper, ed., The Moon, Metorites and Comets (University of Chicago Press, Chicago, 1963).

39. F. G. Watson, Between the Planets (Harvard University Press, Cambridge, 1965).

40. M. Kaula, "Determination of the earth's gravitational field," Rev. Geophys. 1, 507 (1963).

41. W. H. Guier and R. R. Newton, "The earth's gravity field as deduced from the Doppler tracking of five satellites," J. Geophys. Res. 70, 4613 (1965).

BLANK PAGE

N65 35767

APPENDIX A

THEORY OF RADIALLY VIBRATING GRAVITATIONAL MASS SENSORS

Because of the instabilities found in the radially vibrating gravitational mass sensors studied in the original papers,[A-1, A-2] it was decided to perform the analysis again in a more general manner to determine whether it was possible to find a stable version of a radially vibrating structure.

A system such as that shown in Fig. A-1 is assumed for the calculations of the operation of a freely falling radially vibrating gravitational mass sensor. The sensor consists of two equal masses M_1 and M_2 connected by massless springs to a central mass M_3. The sensor is rotating in free fall near an object with mass M_4. The springs have an initial length of ℓ_o; under the centrifugal force caused by the sensor rotation they experience an extension e_a. The sensor system then oscillates about this extended position with amplitude $\xi_a(t)$.

In the analysis, we will assume the following:

1. The sensor masses are constrained to vibrate only in the radial direction.

2. The radial vibrations ξ_a are small compared with the length ℓ_o and the centrifugal extensions e_a, and their effect on the gravitational interaction of the sensor masses with the detected mass is negligible.

3. The self gravitation of the three sensor masses is negligible compared with the centrifugal force.

4. In contrast to previous analyses,[A-3, A-5] we will not assume that the rotational frequency is constant, but instead will assume that the angular momentum of the total system, including the object being measured, remains constant.

Under these assumptions, the equations of motion of the four masses are written. These equations are then combined and manipulated into a useful form in polar coordinates. These equations of motion and another equation expressing the conservation of angular momentum are then solved to obtain a pair of equations describing the radial vibrations of each spring. These equations are examined to determine the response of the sensor to the gravitational gradients produced by the mass M_4.

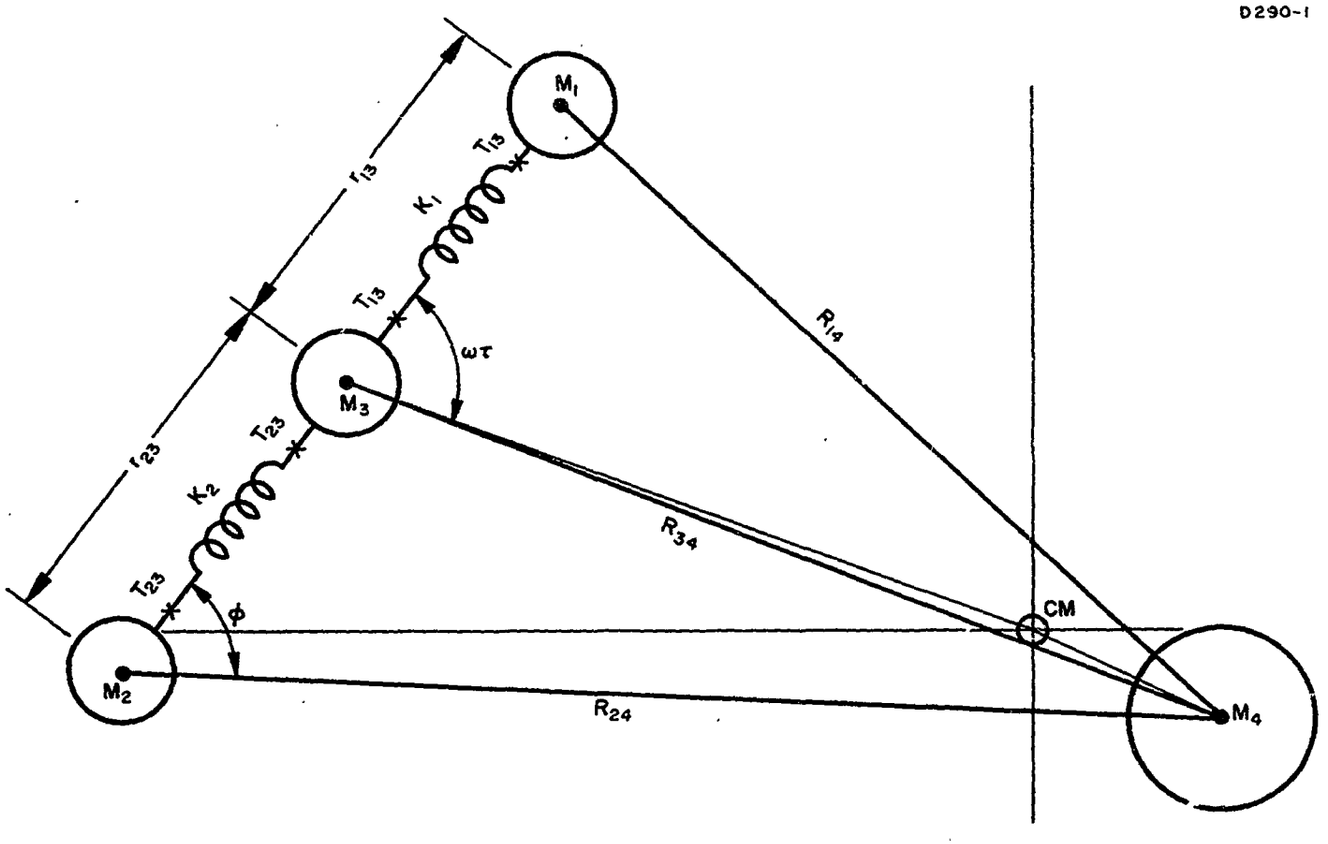

Fig. A-1. Schematic of three mass, two spring, radially vibrating gravitational mass sensor.

It shall be assumed first that the central mass of the sensor is equal to the outer sensor masses; variations in the relative magnitude of this mass will then be discussed.

The equations of motion of the masses shown in Fig. A-1 are as follows:

For Mass 4

$$M_4 \ddot{x}_4 = - \frac{GM_4 M_1}{(R_{14})^2} \frac{x_4 - x_1}{R_{14}} - \frac{GM_4 M_2}{(R_{24})^2} \frac{x_4 - x_2}{R_{24}} - \frac{GM_4 M_3}{(R_{34})^2} \frac{x_4 - x_3}{R_{34}} \qquad \text{(A-1)}$$

$$M_4 \ddot{y}_4 = - \frac{GM_4 M_1}{(R_{14})^2} \frac{y_4 - y_1}{R_{14}} - \frac{GM_4 M_2}{(R_{24})^2} \frac{y_4 - y_2}{(R_{24})} - \frac{GM_4 M_3}{(R_{34})^2} \frac{y_4 - y_3}{R_{34}} \qquad \text{(A-2)}$$

For Mass 1

$$M_1 \ddot{x}_1 = \frac{GM_1 M_4}{(R_{14})^2} \frac{x_4 - x_1}{R_{14}} + T_{13} \frac{x_3 - x_1}{r_{13}} \qquad \text{(A-3)}$$

$$M_1 \ddot{y}_1 = \frac{GM_1 M_4}{(R_{14})^2} \frac{y_4 - y_1}{R_{14}} + T_{13} \frac{y_3 - y_1}{r_{13}} . \qquad \text{(A-4)}$$

For Mass 2

$$M_2 \ddot{x}_2 = \frac{GM_2 M_4}{(R_{24})^2} \frac{x_4 - x_2}{R_{24}} + T_{23} \frac{x_3 - x_2}{r_{23}} \qquad \text{(A-5)}$$

$$M_2 \ddot{y}_2 = \frac{GM_2 M_4}{(R_{24})^2} \frac{y_4 - y_2}{R_{24}} + T_{23} \frac{y_3 - y_2}{r_{23}} . \qquad \text{(A-6)}$$

For Mass 3

$$M_3 \ddot{x}_3 = \frac{GM_4 M_3}{(R_{43})^2} \frac{x_4 - x_3}{R_{43}} - T_{13} \frac{x_3 - x_1}{r_{13}} - T_{23} \frac{x_3 - x_2}{r_{23}} \tag{A-7}$$

$$M_3 \ddot{y}_3 = \frac{GM_4 M_3}{(R_{43})^2} \frac{y_4 - y_3}{R_{43}} - T_{13} \frac{y_3 - y_1}{r_{13}} - T_{23} \frac{y_3 - y_2}{r_{23}} \tag{A-8}$$

where

$$T_{a3} = k_a(e_a + \xi_a) + D \dot{\xi}_a$$

$$r_{a3} = (\ell_o + e_a) + \xi_a \approx \ell_a + \xi_a \quad .$$

We will assume initially that the three sensor masses are equal

$$M_1 = M_2 = M_3 = m$$

and the two springs are identical so that

$$k_1 = k_2 = k$$

$$e_1 = e_2 = e \quad .$$

In addition, the mass being measured is assumed larger than the sensor

$$M_4 = M >> 3m \quad .$$

Subtracting (A-7) from (A-3) and (A-5), and similarly (A-8) from (A-4) and (A-6), and using the above simplifications, we obtain equations expressing the relative motion of the sensor masses:

$$\ddot{x}_1 - \ddot{x}_3 = GM \left[\frac{x_4 - x_1}{(R_{14})^3} - \frac{x_4 - x_3}{(R_{34})^3} \right] + \frac{2T_{13}}{m} \frac{x_3 - x_1}{r_{13}} + \frac{T_{23}}{m} \frac{x_3 - x_2}{r_{23}} \tag{A-9}$$

$$\ddot{x}_2 - \ddot{x}_3 = GM \left[\frac{x_4 - x_2}{(R_{24})^3} - \frac{x_4 - x_3}{(R_{34})^3} \right] + \frac{2T_{23}}{m} \frac{x_3 - x_2}{r_{23}} + \frac{T_{13}}{m} \frac{x_3 - x_1}{r_{13}} \tag{A-10}$$

$$\ddot{y}_1 - \ddot{y}_3 = GM \left[\frac{y_4 - y_1}{(R_{14})^3} - \frac{y_4 - y_3}{(R_{34})^3} \right] + \frac{2T_{13}}{m} \frac{y_3 - y_1}{r_{13}} + \frac{T_{23}}{m} \frac{y_3 - y_2}{r_{23}} \tag{A-11}$$

$$\ddot{y}_2 - \ddot{y}_3 = GM \left[\frac{y_4 - y_2}{(R_{24})^3} - \frac{y_4 - y_3}{(R_{34})^3} \right] + \frac{2T_{23}}{m} \frac{y_3 - y_2}{r_{23}} + \frac{T_{13}}{m} \frac{y_3 - y_1}{r_{13}} \tag{A-12}$$

The gravitational terms which drive this system of equations are very small compared with the inertial terms and the spring tension terms; therefore, we can assume for the gravitational terms that

$$\omega \equiv \text{constant}$$

$$R_{34} = R \equiv \text{constant}$$

$$R_{14}^2 = R^2 + r_{13}^2 - 2\, r_{13} R \cos \omega t$$

$$R_{24}^2 = R^2 + r_{23}^2 + 2\, r_{23} R \cos \omega t$$

$$x_4 - x_1 = R - r_{13} \cos \omega t$$

$$x_4 - x_2 = R + r_{23} \cos \omega t$$

$$x_4 - x_3 = R$$

$$y_4 - y_1 = - r_{13} \sin \omega t$$

$$y_4 - y_2 = + r_{23} \sin \omega t$$

$$y_4 - y_3 = 0 \quad .$$

This is not strictly true, but the differences are of order G^2 and are therefore negligible. We cannot make these kinds of assumptions for the other terms, but instead must use the relations

$$x_1 - x_3 = r_{13} \cos \phi \tag{A-13}$$

$$\ddot{x}_1 - \ddot{x}_3 = \ddot{r}_{13} \cos \phi - (2\dot{r}_{13}\dot{\phi} + r_{13}\ddot{\phi}) \sin \phi - r_{13} \cos \phi\, \dot{\phi}^2 \tag{A-14}$$

$$x_2 - x_3 = - r_{23} \cos \phi \tag{A-15}$$

$$\ddot{x}_2 - \ddot{x}_3 = - \ddot{r}_{23} \cos \phi + (2\dot{r}_{23}\dot{\phi} + r_{23}\ddot{\phi}) \sin \phi + r_{23} \cos \phi\, \dot{\phi}^2 \tag{A-16}$$

$$y_3 - y_1 = - r_{13} \sin \phi \tag{A-17}$$

$$\ddot{y}_1 - \ddot{y}_3 = \ddot{r}_{13} \sin \phi + (2\dot{r}_{13}\dot{\phi} + r_{13}\ddot{\phi}) \cos \phi - r_{13} \dot{\phi}^2 \sin \phi \tag{A-18}$$

$$y_3 - y_2 = r_{23} \sin \phi \tag{A-19}$$

$$\ddot{y}_2 - \ddot{y}_3 = - \ddot{r}_{23} \sin \phi - (2\dot{r}_{23}\dot{\phi} + r_{13}\ddot{\phi}) \cos \phi + r_{13} \dot{\phi}^2 \sin \phi \tag{A-20}$$

(The equations (A-14), (A-16), (A-18), and (A-20) are correct and therefore the rest of the analysis will differ from the similar but simpler analysis in Ref. 1, which contains an error of 2 in its corresponding eqs. (25) and (27).)

If we multiply (A-9) and (A-10) by cos ϕ and add them to (A-11) and (A-12), respectively, multiplied by sin ϕ and then make the above substitutions into the various terms and simplify, we obtain equations representing the radial motion of the spring mass systems of the sensor driven by the gravitational force terms:

$$\ddot{r}_{13} - r_{13}\dot{\phi}^2 + \frac{2T_{13} - T_{23}}{m} = \frac{GM}{R^2} \left[\frac{\cos \omega t - \frac{r_{13}}{R}}{\left[1 + \left(\frac{r_{13}}{R} \right)^2 - 2 \frac{r_{13}}{R} \cos \omega t \right]^{3/2}} - \cos \omega t \right] \tag{A-21}$$

$$\ddot{r}_{23} - r_{23}\dot{\phi}^2 + \frac{2T_{23} - T_{13}}{m} = - \frac{GM}{R^2} \left[\frac{\cos \omega t + \frac{r_{23}}{R}}{\left[1 + \left(\frac{r_{23}}{R} \right)^2 + 2 \frac{r_{23}}{R} \cos \omega t \right]^{3/2}} - \cos \omega t \right] . \tag{A-22}$$

If we then expand the denominator in the gravitational driving terms and keep the largest factors of (r/R) for each term in cos $n\omega t$ we obtain

$$\ddot{r}_{13} - r_{13}\dot{\phi}^2 + \frac{2T_{13} - T_{23}}{m}$$

$$= \frac{GM\, r_{13}}{R^3}\left[\frac{1}{2} + \frac{9}{8}\left(\frac{r_{13}}{R}\right)\cos\omega t + \frac{3}{2}\cos 2\omega t + \frac{15}{8}\left(\frac{r_{13}}{R}\right)\cos 3\omega t + \frac{35}{16}\left(\frac{r_{13}}{R}\right)^2 \cos 4\omega t\right] ; \qquad \text{(A-23)}$$

in a similar manner,

$$\ddot{r}_{23} - r_{23}\dot{\phi}^2 + \frac{2T_{23} - T_{13}}{m}$$

$$= -\frac{GM\, r_{23}}{R^3}\left[-\frac{1}{2} + \frac{9}{8}\left(\frac{r_{23}}{R}\right)\cos\omega t - \frac{3}{2}\cos 2\omega t + \frac{15}{8}\left(\frac{r_{23}}{R}\right)\cos 3\omega t - \frac{35}{16}\left(\frac{r_{23}}{R}\right)^2 \cos 4\omega t\right] . \qquad \text{(A-24)}$$

The usual analysis then proceeds with the assumption that the angular velocity of the sensor is a constant and sets $\dot{\phi}^2 = \omega^2$. However, we have found that if we assume that the total angular momentum of both the sensor and the object under measurement remains constant, the conservation of angular momentum principle (acting through the centrifugal force term $(-r\dot{\phi}^2)$) leads to a modification of the effective spring constant and to additional driving terms of the same order of magnitude as the obvious gravitational terms. Therefore, in order to obtain a correct expression for $-r\dot{\phi}^2$, we start from the law of conservation of angular momentum

$$\text{Ang. Momentum} = \Sigma\, m_i\,(\bar{r}_i \times \bar{P}_i) = 2m\ell^2\omega ; \qquad \text{(A-25)}$$

$$\therefore M_1(x_1\dot{y}_1 - y_1\dot{x}_1) + M_2(x_2\dot{y}_2 - y_2\dot{x}_2) + M_3(x_3\dot{y}_3 - y_3\dot{x}_3)$$

$$+ M_4(x_4\dot{y}_4 - y_4\dot{x}_4) = 2m\ell^2\omega .$$

For this part of the problem it can be assumed that $r_{13} = r_{23} = r$; then

$$x_1 = x_3 + r\cos\phi$$
$$x_2 = x_3 - r\cos\phi$$

$$y_1 = y_3 + r\sin\phi$$
$$y_2 = y_3 - r\sin\phi$$

$$\dot{x}_1 = \dot{x}_3 + \dot{r}\cos\phi - r\sin\phi\,\dot{\phi}$$
$$\dot{x}_2 = \dot{x}_3 - \dot{r}\cos\phi + r\sin\phi\,\dot{\phi}$$

$$\dot{y}_1 = \dot{y}_3 + \dot{r}\sin\phi + r\cos\phi\,\dot{\phi}$$
$$\dot{y}_2 = \dot{y}_3 - \dot{r}\sin\phi - r\cos\phi\,\dot{\phi} \quad .$$

From the center of mass location

$$M_4 x_4 + m(x_1 + x_2 + x_3) = 0 \quad , \qquad \text{(A-26)}$$

but

$$x_1 + x_2 = 2x_3 \qquad \text{(A-27)}$$

$$\therefore\ x_4 = -\frac{3M}{m}x_3 \quad .$$

Similarly,

$$y_4 = -\frac{3M}{m}y_3$$

$$\dot{x}_4 = -\frac{3M}{m}\dot{x}_3$$

$$\dot{y}_4 = -\frac{3M}{m}\dot{y}_3 \quad .$$

Substituting all this into (A-25) and expanding and collecting terms, we obtain an expression for the instantaneous angular velocity of the sensor:

$$r^2\dot{\phi} = \ell^2\omega - \left(\frac{3}{2} + \frac{9m}{2M}\right)\frac{M^2}{9m^2}(x_4\dot{y}_4 - y_4\dot{x}_4) \quad . \tag{A-28}$$

Equation (A-28) shows that the angular velocity $\dot{\phi}$ of the sensor is a function of the motion of the object being measured. Since the sensor is a rotating mass quadrupole rather than a simple gravitating body, we find that the sensor and the mass under measurement do not fall smoothly toward each other. Superimposed on the expected radial acceleration is an oscillating radial motion as well as an oscillating transverse motion. This can be shown by taking the equations of motion for the mass M_4 (eqs. (A-1) and (A-2)), expanding the denominators of the gravitational terms, collecting terms of the same frequency, dropping the higher order terms, and substituting for higher powers of cos $n\omega t$ to obtain

$$\ddot{x}_4 = -\frac{Gm}{R^2}\left[3 + \frac{9}{2}\left(\frac{r}{R}\right)^2\cos 2\omega t - \frac{35}{16}\left(\frac{r}{R}\right)^4\cos 4\omega t\right] ; \tag{A-29}$$

in a similar manner,

$$\ddot{y}_4 = -\frac{Gm}{R^2}\left[-3\left(\frac{r}{R}\right)^2\sin 2\omega t - \frac{135}{8}\left(\frac{r}{R}\right)^4\sin 4\omega t\right] . \tag{A-30}$$

These expressions may be integrated directly if we assume that R, r, and ω are constant, the initial velocity of the mass M_4 is zero, and that the initial position is given by

$$x_4(0) = \frac{3mR}{M + 3m}$$

$$y_4(0) = 0 \quad .$$

When we carry out the integration and examine the angular momentum of the mass M_4, we find that

$$(x_4\dot{y}_4 - y_4\dot{x}_4) \approx x_4(0)\dot{y}_4 = -\frac{3mR}{M+3m}\left(\frac{5Gmr^2}{2R^4}\cos 2\omega t + \frac{35Gmr^4}{32\omega R^6}\cos 4\omega t\right) \tag{A-31}$$

because all other terms are of the order G^2 and are negligible.

Substituting (A-31) into (A-28) and solving for the instantaneous angular velocity $\dot{\phi}$, we obtain

$$\dot{\phi} \approx \frac{\ell^2}{r^2}\omega + \frac{3}{4}\frac{GM}{\omega R^3}\cos 2\omega t + \frac{35}{64}\frac{GM\ell^2}{\omega R^5}\cos 4\omega t \ . \tag{A-32}$$

We may now use this equation to obtain the desired centrifugal force term

$$-r\dot{\phi}^2 = -\frac{\ell^4\omega^2}{r^3} - \frac{3GM\ell}{2R^3}\cos 2\omega t - \frac{35}{32}\frac{GM\ell^3}{R^5}\cos 4\omega t \tag{A-33}$$

where in the gravitational terms we have assumed $r \approx \ell$ and have dropped all other terms in G^2 or $G\xi$. We now see that the centrifugal term is not constant, but contains gravitationally driven ac components that are of the same order of magnitude as the gravitational terms in (A-23) and (A-24).

We now use the fact that the radial extension of each spring consists of an initial length ℓ_o and extension due to the dc component of the centrifugal force e and a time varying vibration ξ_1, e.g.,

$$r_{13} = \ell_o + e + \xi_1 = \ell + \xi_1 \ , \tag{A-34}$$

and the tension in the spring contains not only the reaction to the extension of the spring, but also dissipation, e.g.,

$$T_{13} = k(e + \xi_1) + D\dot{\xi}_1 \ . \tag{A-35}$$

... (A-11), (A-14), and (A-15) in (A-23) and (A-24), we can obtain ... for the radial motion of the springs which are expressed in ... of the time varying vibrations ξ and the initial centrifugal ... of the springs.

$$\ddot{\xi}_1 + \frac{D}{m}(\dot{\xi}_1 - \dot{\xi}_2) + \left(\omega^2 + \frac{2k}{m}\right)\xi_1 - \frac{k}{m}\xi_2 + \frac{k}{m}e - \ell_o\omega^2 - e\omega^2$$

$$\frac{9}{8}\frac{GM\ell^2}{R^4}\cos\omega t$$

$$- 3\frac{GM\ell}{R^3}\cos 2\omega t - \frac{15}{8}\frac{GM\ell^2}{R^4}\cos 3\omega t - \frac{105}{32}\frac{GM\ell^3}{R^5}\cos 4\omega t = 0$$

(A-36)

and

$$\ddot{\xi}_2 + \frac{D}{m}(2\dot{\xi}_2 - \dot{\xi}_1) + \left(3\omega^2 + \frac{2k}{m}\right)\xi_2 - \frac{k}{m}\xi_1$$

$$+\left(\frac{k}{m}e - \ell_o\omega^2 - e\omega^2\right) + \frac{9}{8}\frac{GM\ell^2}{R^4}\cos\omega t - 3\frac{GM\ell}{R^3}\cos 2\omega t$$

$$+ \frac{15}{8}\frac{GM\ell^2}{R^4}\cos 3\omega t - \frac{105}{32}\frac{GM\ell^3}{R^5}\cos 4\omega t = 0 \quad .$$

(A-37)

The equations are valid only if the constant terms are zero

$$\frac{k}{m}e - \ell_o\omega^2 - e\omega^2 = 0 \quad \text{or} \quad e = \frac{\ell_o\omega^2}{\frac{k}{m} - \omega^2} \qquad \text{(A-38)}$$

and this puts a condition on the strength of the spring usable in the sensor for any given rotational frequency. As long as k/m is appreciably greater than ω^2, the initial extension of the spring due to the centrifugal force is

reasonable, if the sensor has a rotational speed greater than the natural static vibrational frequency determined by the spring constant $k = m(2\pi f)^2$. However, the extension given by (A-38) becomes infinite and the sensor flies apart.

These combined equations of motion ((A-36) and (A-37)) then describe the behavior of the sensor as it is driven by the various gravitational terms at the various frequencies. If we wish to sense the driving force at twice the rotational frequency caused by the gravitational force gradient, we pick a spring constant so that excitations of the form

$$\xi_1 \quad A \sin 2\omega t \tag{A-39}$$

$$\xi_2 \quad B \sin 2\omega t \tag{A-40}$$

will predominate. Since under these conditions only the gravitational driving term at $2\omega t$ will be important, the equations of motion (A-36) and (A-37) become

$$\ddot{\xi}_1 + \frac{D}{m}(2\dot{\xi}_1 - \dot{\xi}_2) + \left(3\omega^2 + \frac{2k}{m}\right)\xi_1 - \frac{k}{m}\xi_2 = \frac{3GM\ell}{R^3}\cos 2\omega t \tag{A-41}$$

$$\ddot{\xi}_2 + \frac{D}{m}(2\dot{\xi}_2 - \dot{\xi}_1) + \left(3\omega^2 + \frac{2k}{m}\right)\xi_2 - \frac{k}{m}\xi_1 = \frac{3GM\ell}{R^3}\cos 2\omega t \tag{A-42}$$

where we have assumed that (A-38) holds. If we substitute (A-39) and (A-40) into (A-41) and (A-42), we find that there are two possible values for the spring constant that will cause a resonance at the driving frequency 2ω; these are

$$\frac{k}{m} = \omega^2 \qquad \text{(symmetric oscillation)}$$

$$\frac{k}{m} = \frac{1}{3}\omega^2 \qquad \text{(antisymmetric oscillation)} .$$

They are not at $k/m = (2\omega)^2$, as would be expected from a naive analysis, since the centrifugal force term and conservation of momentum conditions create an effective restoring force in addition to the restoring force of the spring.

Unfortunately, however, the two allowable spring constants that would permit resonance at 2ω in a rotating sensor frame of reference are too weak to allow (A-38) to be satisfied, and the sensor will fly apart.

If we wish to sense the driving force at three times the rotational frequency resulting from the gradient of the gravitational force gradient, we find that it is possible to pick the spring constant as either

$$\frac{k}{m} = 2\omega^2 \quad \text{(antisymmetric)}$$

or

$$\frac{k}{m} = 6\omega^2 \quad \text{(symmetric)} \ .$$

These correspond to an initial extension of the spring of (eq. (A-38))

$$e = \frac{\ell_o \omega^2}{\frac{k}{m} - \omega^2} = \frac{\ell_o}{2}$$

and

$$e = \frac{\ell_o}{5} \ ,$$

which are large but not unreasonable for a coil spring. Since the gravitational driving forces at 3ω in (A-36) and (A-37) are antisymmetric, the proper choice for the spring constant is $k/m = 2\omega^2$. At this frequency the resonant vibrations of the springs will have the form

$$\xi_1' = -\xi_2 = \frac{5}{24} \frac{GM\ell^2 Q}{\omega^2 R^4} \sin 3\omega t$$

where

$$Q \quad \frac{(3\omega)m}{D} \quad .$$

Similarly, to detect the fourth gradient of the gravitational potential which produces symmetric driving forces at 4ω, we choose our spring constant as

$$\frac{k}{m} \quad 13\,\omega^2 \qquad \frac{\ell_o}{12}$$

and the solutions of the equations of motion are

$$\xi_1 \quad \xi_2 \quad \frac{35}{128}\,\frac{GM\ell^3 Q}{\omega^2 R^5}\,\sin 4\omega t$$

where

$$Q \quad \frac{(4\omega)m}{D} \quad .$$

It may be noted that if the central sensor mass were to go to zero, only symmetric response would be possible since

$$\xi_1 \equiv \xi_2$$

and we find that only even gradients of the gravitational potential can be measured with a two mass, one spring sensor in free fall. However, as a previous analysis has shown, the sensor cannot be used to measure the second order gradient because of the infinite extension predicted by (A-38).

If the analysis is repeated with the central sensor mass of 10 times the outer sensor masses, we find that for response at ωt

$$\frac{k}{m} = -\,2\,\omega^2$$

$$\frac{k}{m} = -\,\frac{5}{3}\,\omega^2$$

for response at $2\omega t$

$$\frac{k}{m} = \omega^2$$

$$\frac{k}{m} = \frac{5}{6}\omega^2$$

for response at $3\omega t$

$$\frac{k}{m} = 6\omega^2$$

$$\frac{k}{m} = 5\omega^2$$

and for response at $4\omega t$

$$\frac{k}{m} = 13\omega^2$$

$$\frac{k}{m} = \frac{65}{6}\omega^2 \quad .$$

It may now be seen that the response to the frequency component at $2\omega t$ is controlled by $\omega^2 = k/m$, regardless of the size of the central sensor mass; if this value of ω^2 is substituted into (A-38) the value of e becomes infinite (i.e., the spring is stretched beyond its distortion point).

Therefore the 3ω or 4ω responses must be observed in this type of sensor in order to obtain gravity gradient data. Thus, in general, it does not seem possible to measure the gravitational force gradient which introduces forces at 2ω with a radially vibrating sensor of this design.

REFERENCES

A-1. R. L. Forward, "Mass Detector," Hughes Research Laboratories Internal Report RL-59, 19 March 1962.

A-2. R. L. Forward, "Gravitational Mass Sensor," Proc. 1963 Symposium on Unconventional Inertial Sensors, Farmingdale, New York, 18-19 November 1963, pp. 36-60; also Hughes Research Laboratories Research Report No. 284A, November 1963.

A-3. J. W. Diesel, "A New Navigation Concept for Orbital Systems, Spacecraft, and Intercontinental Missiles," Litton Systems, Inc., TM 61-34, November 1961.

A-4. J. W. Diesel, "A new approach to gravitational gradient determination of the vertical," AIAA J. 2, 1189 (July 1964).

A-5. V. Chobotov, "Gravity Gradient Excitation of a Rotating Cable-Counterweight Space Station in Orbit," Aerospace Corporation TD-169 (3530-20)TN-1, AD-297871, 11 January 1963.

N66 36768

APPENDIX B

GRAVITATIONAL RADIATION DETECTORS

A major question which is often raised concerning the engineering feasibility of our work on gravitational mass sensors is based on the supposed difficulty of measuring the very small forces or motions that would be induced in the sensors by the gravitational gradient field. This appendix briefly describes the research on gravitational radiation antennas which has been in progress since 1959 at the University of Maryland, and has led to the development of piezoelectric transducer techniques for measuring motions as small as 3×10^{-14} cm or, equivalently, for detecting dynamic gravitational gradients as small as 3×10^{-13} sec^{-2}.

Experimentally oriented research on gravitational radiation generators and detectors has been in progress at the University of Maryland under the direction of Prof. J. Weber. The present emphasis is on the construction, test, and operation of a gravitational radiation detector to be used as a crude gravitational telescope to sense gravitational radiation from astronomical objects.

1. Gravitational Radiation

According to the Einstein theory of gravity, the general theory of relativity, gravitational phenomena should propagate at the velocity of light. The gravitational forces are predicted to be transverse to the direction of propagation, as are the electromagnetic forces in radio waves, however, the gravitational forces are not vector forces, but are differential forces which do not cause a net motion of a mass as they pass (see Fig. B-1). Instead they cause tensions and compressions in an elastic mass, or differential motion between two masses. Gravitational radiation is therefore a propagating gravitational gradient wave, and gravitational radiation antennas are dynamic gravitational gradient detectors. Thus, techniques developed to improve the sensitivity of gravitational radiation antennas can be directly applied to gravitational gradient sensors.

2. Generation and Detection of Gravitational Waves

It has been known since the early work of Einstein that gravitational radiation would be emitted by a rotating or oscillating mass quadrupole such as a rotating rod, a binary star system, or a vibrating mass. There was some doubt, however, that the gravitational radiation could be observed, since theoretically, according to the principle of equivalence, any

D403-3A

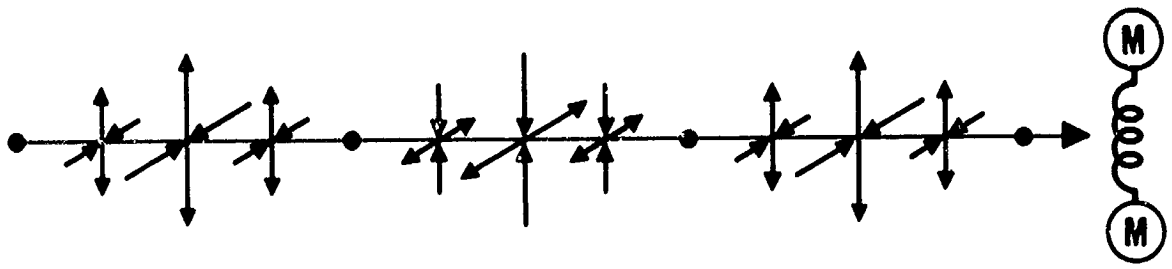

Fig. B-1. Schematic representation of gravitational radiation.

gravitational effect caused by the radiation could be transformed away by a coordinate transformation. However, gravitational radiation consists of gravitational gradient fields or tensor type forces, and the principle of equivalence pertains only to vector forces. In 1960, Prof. Weber published a paper[B-1] showing in a rigorous manner that a mass quadrupole consisting of two masses connected by a spring will interact with certain components of the gravitational radiation field and extract energy from the field. The work on constructing an experimental model of a gravitational antenna was started in 1960 by Prof. J. Weber, Prof. D. M. Zipoy, and R. L. Forward.[B-2 – B-5] A generator of dynamic gravitational fields to calibrate the antenna was constructed by J. Sinsky under the direction of Pro. Zipoy and is now being used to calibrate the response of the antenna to dynamic gravitational gradient fields.[B-6] After the calibration, the antenna will be used to take a twelve month data run to search for gravitational radiation coming from astronomical objects.

3. Gravitational Radiation Antenna[B-4]

The gravitational radiation detector configuration resulting from the preliminary research work is a cylinder of aluminum 2 ft in diameter and 5 ft long, with a weight of 1267 kg (see Fig. B-2). The cylinder is suspended from an overhead crossbar with high strength steel wire wrapped around the center, which is the nodal plane of the first longitudinal vibrational mode. The mode has a resonant frequency of 1657 Hz and a Q of approximately 200,000. As the gravitational fields interact with the antenna, it is alternately compressed and expanded in the longitudinal direction, setting up oscillations in the mode which increase in amplitude because of the acoustic resonance. To prevent seismic vibrations from exciting the longitudinal mode of the cylinder, the ends of the supporting crossbar were supported by two acoustic filter stacks. The filter stacks in turn were supported by a small wheeled cart on tracks, which allowed the apparatus to be assembled outside before being rolled into a vacuum tank which acted as a vibrational and electrical noise barrier. To detect the resonant response of the aluminum cylinder a ring of X-cut quartz transducers (see Fig. B-3 and B-4) were glued near the center of the cylinder where the strains are a maximum.

The output of these piezoelectric transducers was carefully calibrated against standard resistive strain gauges and were found to have a transducer factor of 7.0×10^4 V/unit strain. Because of the relative insensitivity (10^{-5}) of the resistive type gauge, these measurements had to be taken at high dynamic strain levels (10^{-5} cm/cm). In order to insure that this calibration was valid for lower levels of strain, the voltage output of the transducers was monitored as a function of time as the acoustic resonant response of the aluminum rod decayed exponentially. The voltage output of the strain transducers also decayed exponentially,

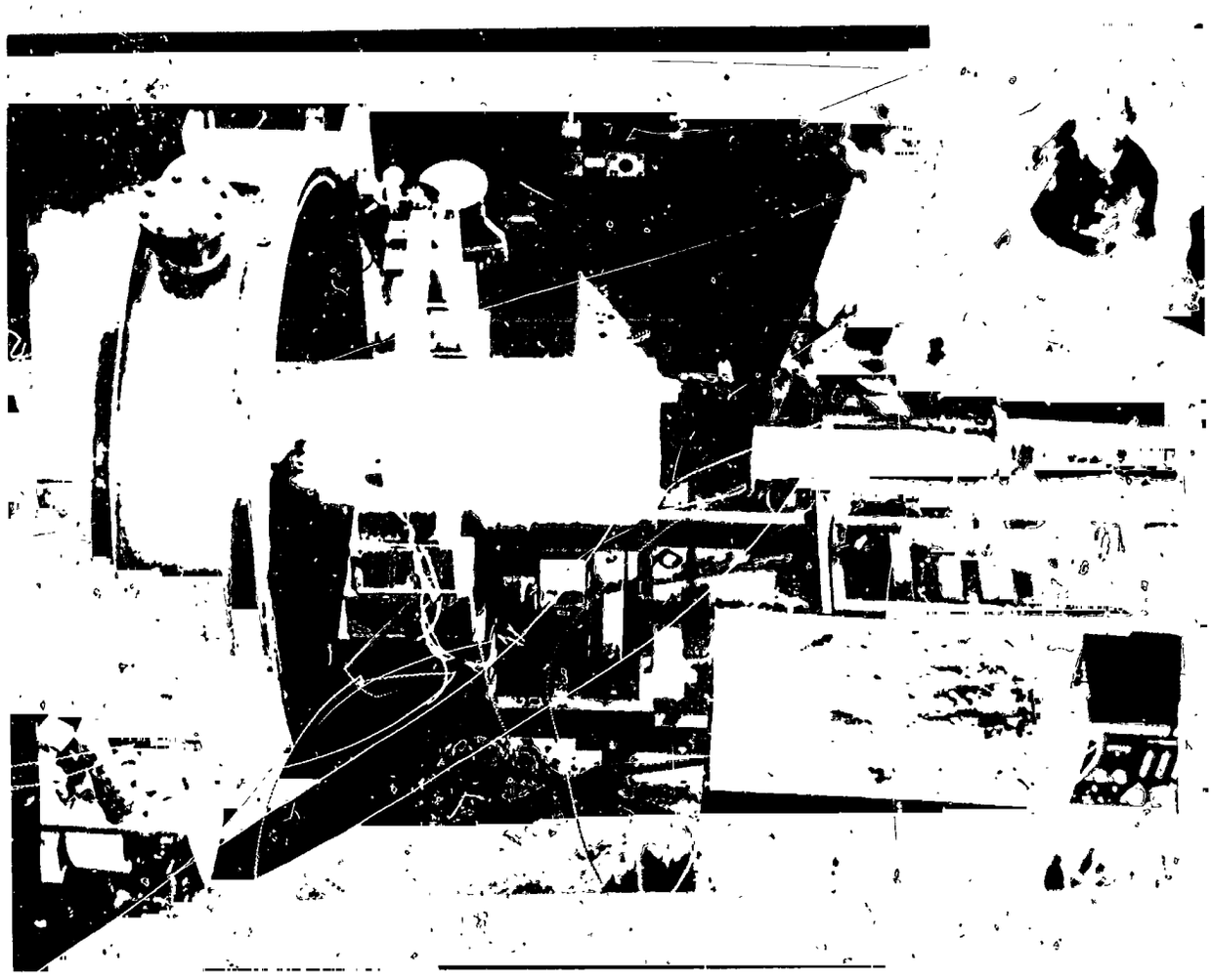

Fig. B-2 Gravitational radiation detector (large bar) and induction field generator (small bar)

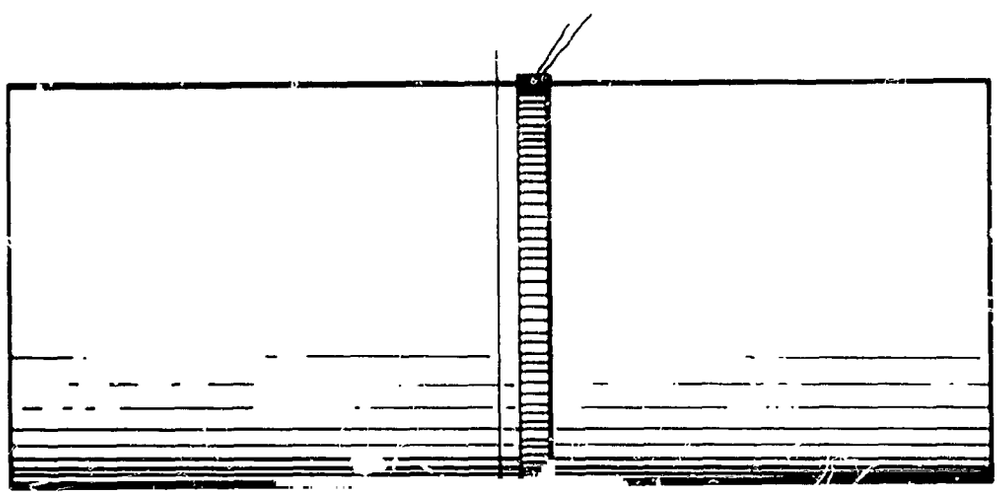

Fig. B-3. Detail showing placement of transducers.

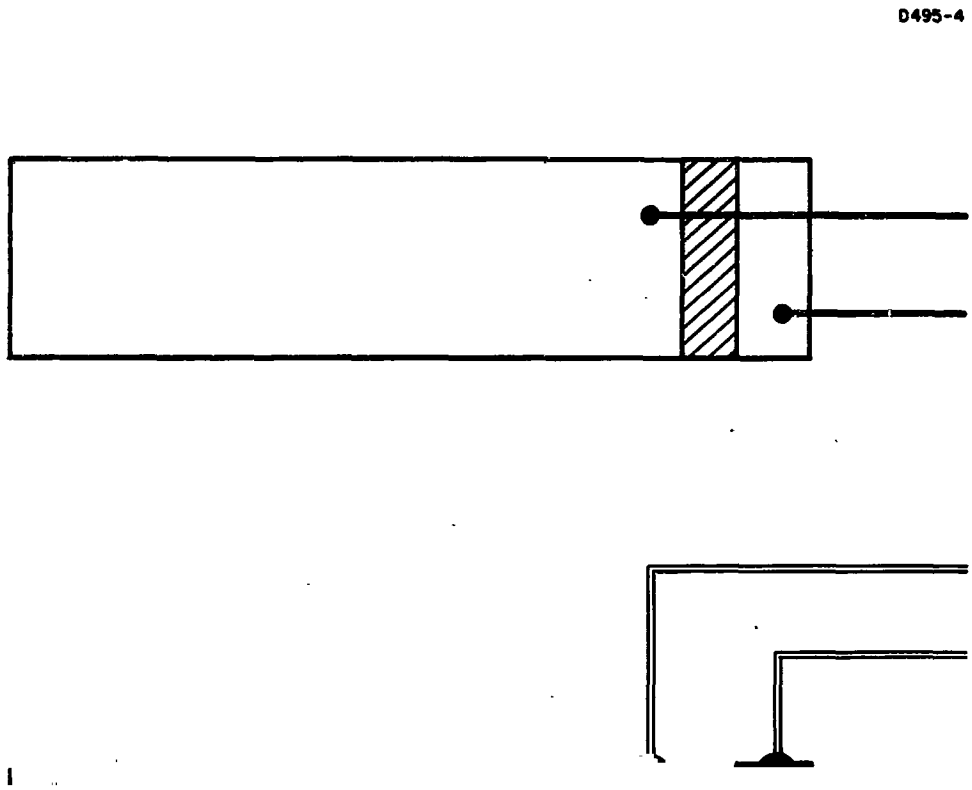

Fig. B-4. Quartz strain transducer.

showing a constant decrement over the entire range of measurement, indicating that the calibration obtained at the high end is valid at the lower end (see Fig. B-5). The strain being measured at the low end is about 7×10^{-11} cm/cm, which implies a total displacement over the length (2.5 cm) of the strain transducers of 1.6×10^{-10} cm (1.6×10^{-2} Å). This level of motion is already past any possible discontinuity in the operating characteristics which might be expected as a result of atomic granularity; thus we can feel confident in extrapolating the calibrated response characteristics of the quartz strain transducers down into the region of picostrains and below.

Since the piezoelectric transducers have a capacitance associated with them, for the lowest noise performance it is necessary to resonate out the capacitance with an inductance, so that the antenna is matched to the preamplifier. For best match, the Q of the electronic circuitry should be the same as the Q of the detector. For the research at the University of Maryland, the detector Q was 200,000 and the inductance used is a 1 H superconducting inductance with a similar Q. For our work on gravitational mass sensors, the sensor Q is chosen to be about 100 so that the response time of the sensor is not too long. Ordinary inductances will therefore serve for matching purposes.

4. Antenna Noise Level

With the antenna matched to the preamplifier and with the acoustic, seismic, and electrical filters in place, it was found possible to reduce the noise input to the antenna to the point where its sensitivity was limited only by its own internal thermal noise. Since the electronics are tuned to the motions of the first longitudinal vibrational mode of the cylinder and do not sense the motions of the other modes, the thermal noise energy detected is just the single kT of energy associated with that normal mode according to the equipartition theorem. This very small amount of energy (4×10^{-21} J) is distributed over 1267 kg of matter; therefore, the resultant motions associated with this energy are extremely small, 3×10^{-14} cm, or 0.1 of the diameter of a nucleus. Of course, the ends of the cylinder are moving more than this since it is vibrating in 10^{25} normal modes at one time; the electronic circuitry, however, by using frequency selection techniques, is able to look at only one of the 10^{25} normal modes.

The thermal noise limit for the gravitational radiation antenna is much lower than the noise limit for the gravitational mass sensors because of the much larger mass used in the antenna. The gravitational mass sensors therefore will need proportionately less shielding in order to attain thermal noise limited sensitivity.

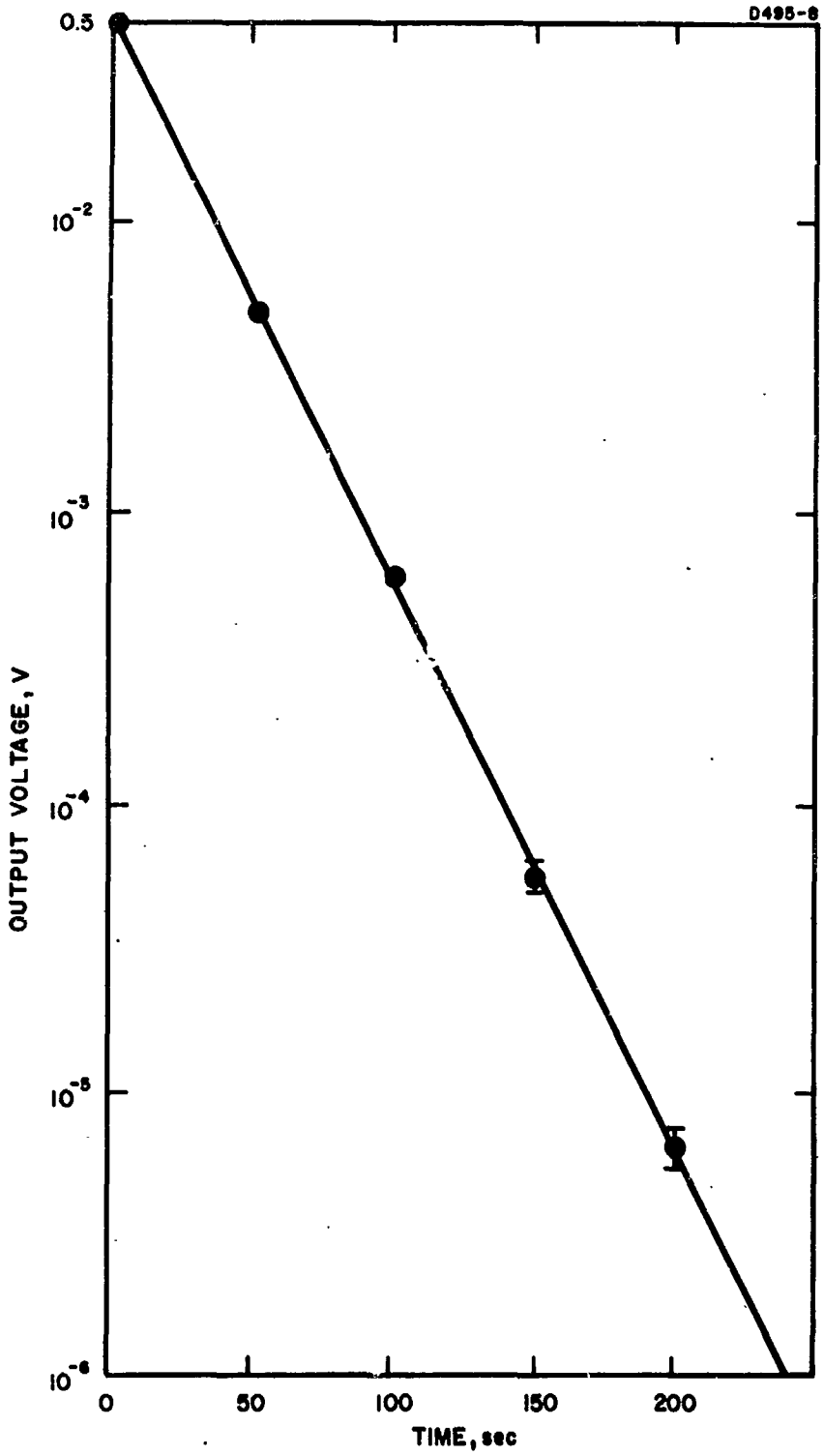

Fig. B-5. Transducer output sensing decaying strains.

5. Gravitational Antenna Calibration[B-6]

In order to calibrate the gravitational response of the gravitational radiation antenna, a generator of dynamic Newtonian gravitational fields was constructed. The generator consists of an aluminum cylinder, of the same length (5 ft) and therefore the same resonant frequency (1657 Hz) as the antenna, but of smaller diameter (8 in.) for easier handling (see Fig. B-2).

This cylinder was also supported on a wire harness in its own vacuum chamber. A number of large barium titanate strain transducers were placed at the center and were driven with a high power oscillator-amplifier combination to make the ends of the generator vibrate with an amplitude of about 10^{-2} cm. This mass motion of the ends of the generator causes an ac gravitational field to be generated at the position of the antenna. This very weak gravitational signal can be seen over the internal noise of the detector, and measurements at various separation distances and angles have verified that the observed interaction is gravitational in origin.

The dynamic gravitational gradient field which would give an equivalent amount of gravitational coupling would have a strength of 3×10^{-13} sec^{-2}, or three to four orders of magnitude lower than that needed in the gravitational mass sensor for accurate geophysical measurements.

BLANK
PAGE

REFERENCES

B-1. J. Weber, "Detection and generation of gravitational waves," Phys. Rev. 117, 306 (1960).

B-2. J. Weber, General Relativity and Gravitational Waves (Interscience, New York, 1961), Chap. 8.

B-3. R. L. Forward, D. M. Zipoy, and J. Weber, "Measurement of dynamic gravitational fields," Bull. Am. Phys. Soc. 7, 320 (1962).

B-4. R. L. Forward, "Detectors for Dynamic Gravitational Fields," unpublished thesis.

B-5. J. Weber, "Gravitational Waves," in Gravitation and Relativity, H.-Y. Chiu and W. F. Hoffman, Eds. (W. A. Benjamin, Inc., New York, 1964), Chap. 5, p. 100.

B-6. J. Sinsky and D. Zipoy, "Experimental and Theoretical Research in Gravitational Physics," Final Technical Report on Grant AF AFOSR 409-63, 1965.

N66 36769

APPENDIX C

AIR BEARING ANALYSIS

Because of the vertical vibrations found in the air bearing constructed for us, it was decided to analyze the behavior of this type of system to determine the changes which would be necessary to eliminate this source of high frequency noise.

In order to make the analysis tractable, the simplified structure shown in Fig. C-1 was used as the model, and the following assumptions were made.

1. All expansion processes were isothermal
2. There is no pressure drop across the spotface area (point 1)
3. All frictional losses are negligible.

From conservation of momentum applied to expanding gases the pressure-velocity relationship in the tube at point 1 is

$$\frac{v_1^2}{2} = \frac{P_2}{\rho_2} \ln \frac{P_o}{P_1} \tag{C-1}$$

and the pressure-velocity relationship in gap g is

$$\frac{v^2}{2} - \frac{v_1^2}{2} = \frac{P_2}{\rho_2} \ln \frac{P_1 r_1}{Pr} \quad . \tag{C-2}$$

The equation for the conservation of mass ratio of flow in the gap is

$$\rho A v = \rho_1 A_1 v_1 \tag{C-3}$$

where A is the cross-sectional area of the air path or

$$v = v_1 \frac{\rho_1}{\rho} \frac{r_1}{r} \quad . \tag{C-4}$$

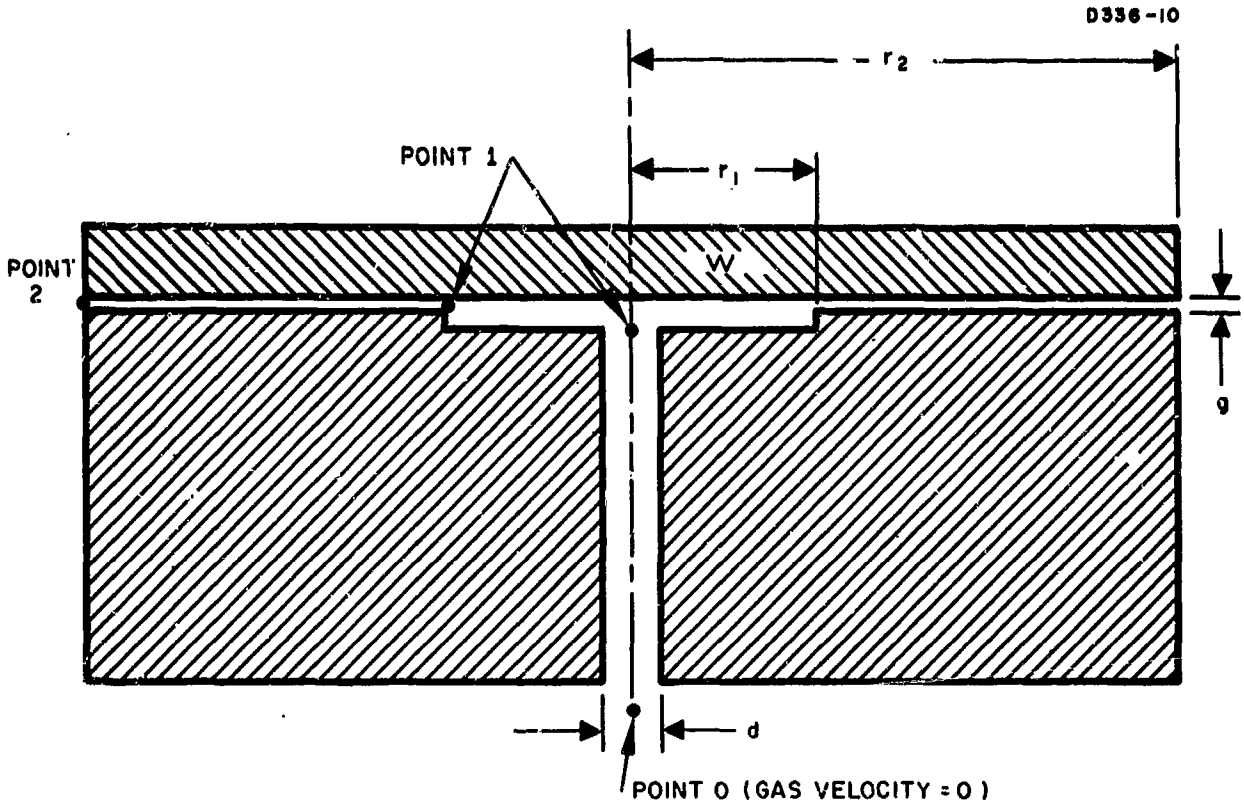

Fig. C-1. Air bearing table schematic.

If we combine (C-1), (C-2), and (C-4) using the gas law for isothermal expansion that

$$\frac{P}{\rho} \equiv \text{constant} = \frac{P_2}{\rho_2} \quad , \tag{C-5}$$

we obtain

$$\left(\frac{P_1 r_1}{Pr}\right)^2 \ln \frac{P_o}{P_1} = \ln \frac{P_o r_1}{Pr} \tag{C-6}$$

or

$$P_1^2 \ln \frac{P_o}{P_1} = P^2 \left(\frac{r}{r_1}\right)^2 \ln \frac{P_o r_1}{Pr} \quad . \tag{C-7}$$

If we use the known atmospheric conditions at point 2

$$P_1^2 \ln \frac{P_o}{P_1} = P_2^2 \left(\frac{r_2}{r_1}\right)^2 \ln \frac{P_o r_1}{P_2 r_2} \tag{C-8}$$

to solve for P_1, we observe that this equation is satisfied by two values of P_1 for each value of P_o except where

$$\frac{d}{dP_1}\left[P_1^2 \ln \frac{P_o}{P_1}\right] = 0 \quad . \tag{C-9}$$

In performing this differentiation we find

$$2 \ln \frac{P_o}{P_1} = 1 \tag{C-10}$$

or

$$\frac{P_o}{P_1} = 1.65 \quad . \tag{C-11}$$

If we substitute this value into (C-6) we obtain

$$\left(\frac{P_1 r_1}{Pr}\right)^2 = 2 \ln \frac{P_1 r_1}{Pr} + 1 \qquad \text{(C-12)}$$

or

$$\left(\frac{P_1 r_1}{Pr}\right)^2 - 2 \ln \frac{P_1 r_1}{Pr} = 1 \quad . \qquad \text{(C-13)}$$

However, this is only true when

$$Pr = P_1 r_1 \quad . \qquad \text{(C-14)}$$

Therefore, in gap g the product Pr is constant and

$$P_1 r_1 = Pr = P_2 r_2 \quad , \qquad \text{(C-15)}$$

or (using (C-11)),

$$\frac{r_1}{r_2} = \frac{1.65 P_2}{P_o} \quad . \qquad \text{(C-16)}$$

The following summarizes the above portion of the analysis.

In order to obtain a truly stable air bearing support the pressures across the support pads should be constant and single valued. If the system is subjected to external pressures of P_o and P_2 the internal pressure is made single valued by giving the ratio r_1/r_2 the value provided by (C-16). Note also that (from (C-2) and (C-15))

$$\frac{v^2}{2} - \frac{v_1^2}{2} = 0 \quad ,$$

or the air velocity anywhere in the gap is constant. In order to determine the actual value of P_o required, we equate the upward force produced by the air pressure in the gap to the weight supported by the pad.

$$F = \pi r_1^2 P_1 + \int_1^2 2\pi r P dr - \pi r_2^2 P_2 \qquad \text{(C-17)}$$

$$F = 2\pi \int_1^2 P r dr + \pi(P_1 r_1^2 - P_2 r_2^2) \quad . \qquad \text{(C-18)}$$

However, from (C-15) we know that

$$Pr = P_2 r_2 \; ; \qquad \text{(C-15)}$$

therefore,

$$F = 2\pi P_2 r_2 [r_2 - r_1] + \pi P_2 r_2 [r_1 - r_2] \; , \qquad \text{(C-19)}$$

and, by combining terms,

$$F = \pi P_2 r_2^2 \left[1 - \frac{r_1}{r_2}\right] . \qquad \text{(C-20)}$$

However, from (C-16) we know that

$$\frac{r_1}{r_2} = \frac{1.65\, P_2}{P_o} \; ; \qquad \text{(C-16)}$$

therefore,

$$F = \pi P_2 r_2^2 \left[1 - \frac{1.65\, P_2}{P_o}\right] = W \qquad \text{(C-21)}$$

or, the desired operating pressure is

$$P_o = \frac{1.65\, \pi P_2^2 r_2^2}{\pi P_2 r_2^2 - W} \quad . \qquad \text{(C-22)}$$

In calculating for the sensor design we use (C-16) and (C-22) and environmental conditions as follows:

$$W = 4.74 \text{ lb}$$

$$r_2 = 0.375 \text{ in.}$$

$$P_2 = 14.7 \text{ psia} \quad .$$

We can solve for P_o and r_1

$$P_o = 90 \text{ psia} \qquad \text{(C-23)}$$

$$r_1 = 1.65 \frac{P_2}{P_o} r_2$$

$$= 0.101 \text{ in.} \qquad \text{(C-24)}$$

A new spud, or air bearing stator, was constructed with different dimensions based on the above analysis;

BLANK PAGE

N66 36770

APPENDIX D

MAGNETIC BEARING AND DRIVE

In response to a request from Hughes Research Laboratories, the Instrumentation Development Group of the Research Laboratories for the Engineering Sciences, University of Virginia, developed and constructed a magnetic support system capable of supporting a composite rotor having a weight in excess of 5 lb. The system also includes a drive system capable of accelerating the rotor up to angular speeds in excess of 1000 rps when the rotating components are enclosed in a vacuum tight chamber maintained at a pressure not exceeding 50 μ Hg. The initial design specifications for the system are included in Research Laboratories for the Engineering Sciences Proposal No. IDG-HRL-1-64U.

The magnetic support system is composed of five separate but interacting subsystems together with the necessary power supplies (see Fig. D-1). The major subgroups are (1) the magnetic support solenoid and drive motor assembly, (2) the magnetic support circuit, (3) the current control circuit, (4) the rotor drive circuit, and (5) the speed pickup system. Figure D-2 shows the mechanical relationships between the major components of the magnetic support solenoid and drive motor assembly.

Figure D-3 is a block diagram of the magnetic support circuit along with the various circuit interconnections required for normal operation. Each of the major components is discussed separately.

1. Magnetic Support Solenoid

The magnetic support solenoid is made up of five individual self-supporting coils wound from No. 24 Phelps-Dodge Bondeze No. 3 magnetic wire. Each coil contains approximately 5000 turns of wire, has a resistance of about 165Ω, and an inductance of about 2.5 H when measured individually with the iron core removed. Four copper cooling plates, slotted to minimize eddy currents, have been provided to facilitate adequate cooling when the coils are operated continuously at their maximum design current of 0.5 A. Either gas or liquid cooling will provide sufficient heat transfer from the coils. Since the individual plates may be considered as one-turn windings which are magnetically coupled to the main support solenoid, they must not be electrically interconnected nor may they be directly connected to the periphery of the brass plate at the base of the coil. A 50,000 Ω, 10 W resistor has been permanently connected across the coil stack to limit the voltage peaks in the coil caused by rapid changes in the coil current such as that resulting from accidental failure of the power supply.

M 4050

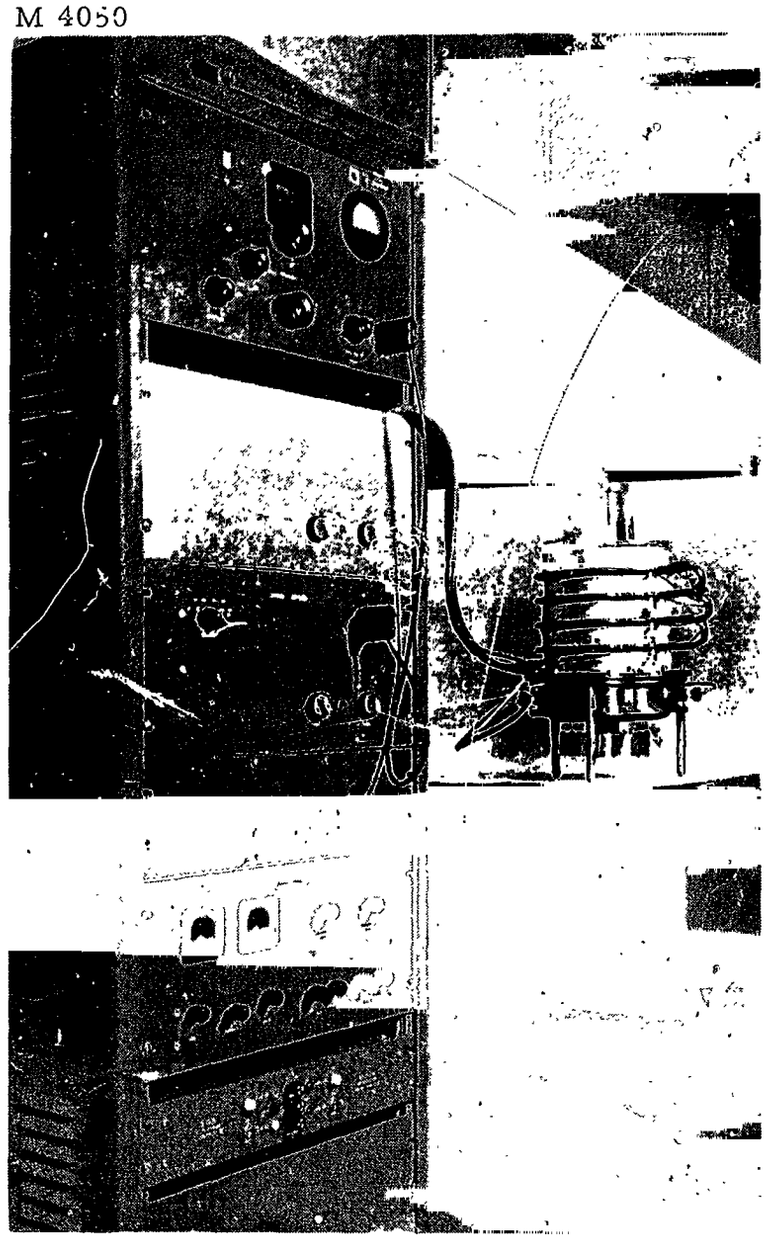

Fig. D-1. Magnetic support and drive unit.

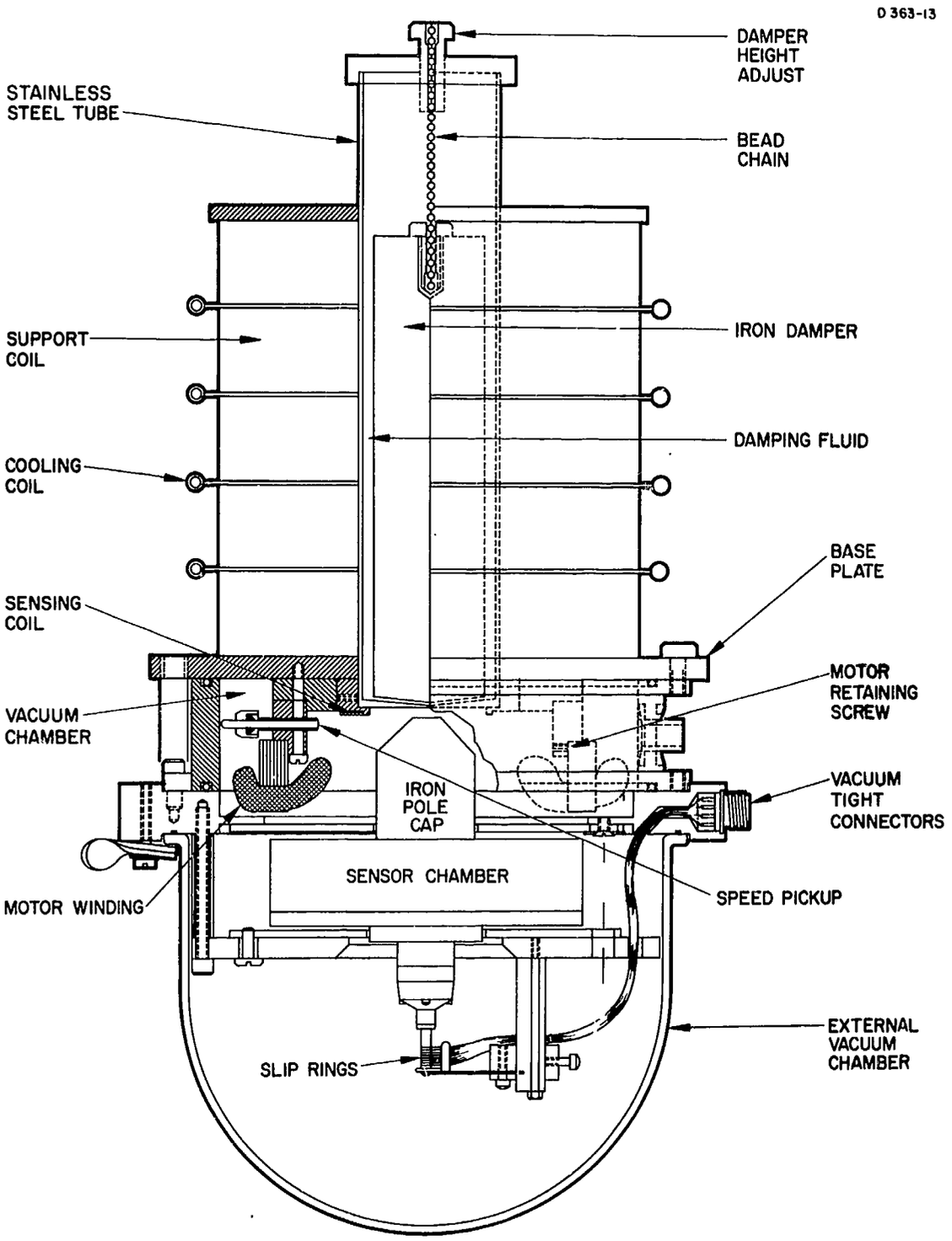

Fig. D-2. Layout drawing of magnetic bearing.

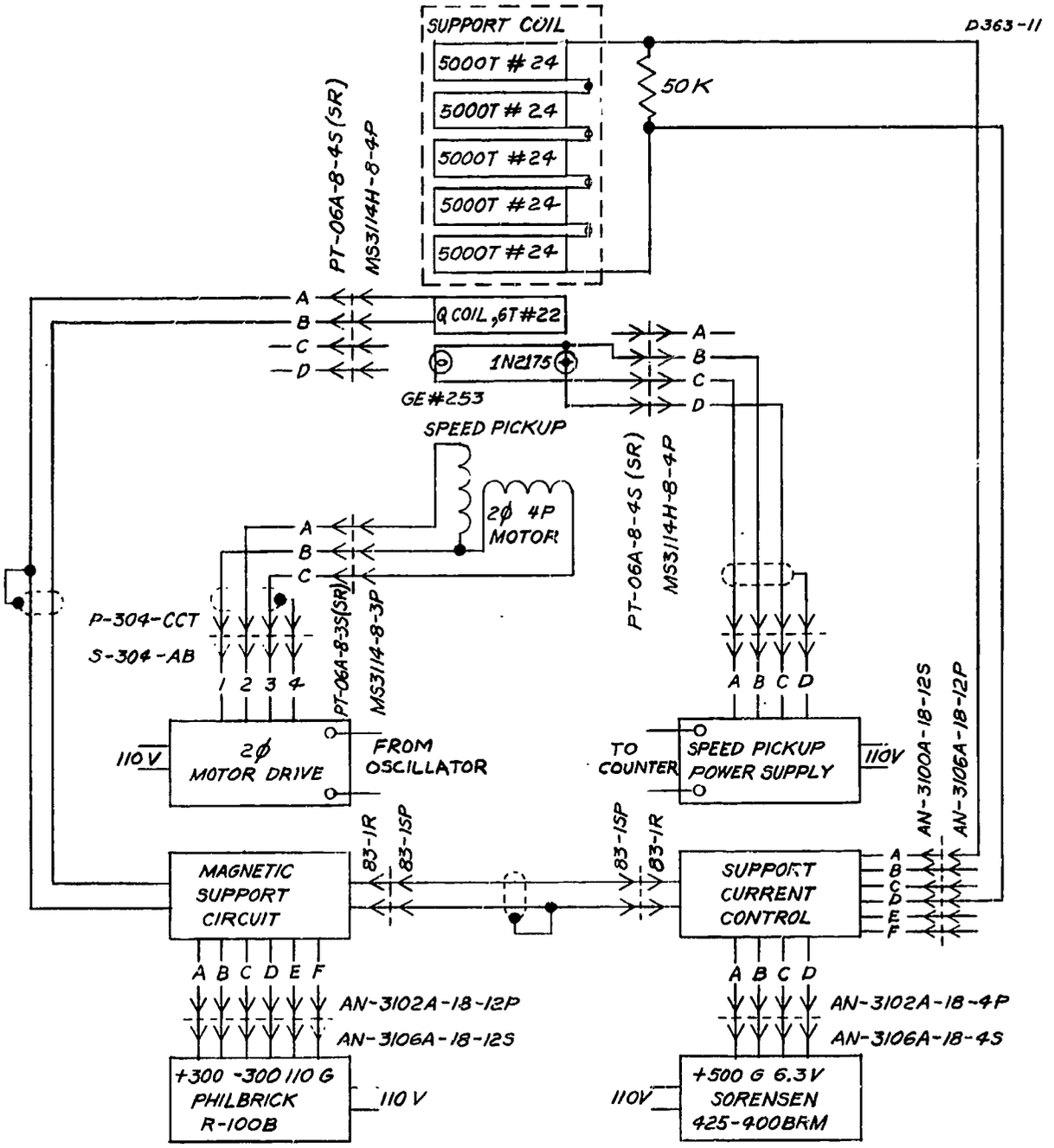

Fig. D-3. Magnetic support system interconnection diagram.

The main support coils surround a thin wall, nonmagnetic stainless steel tube which serves to hold the coils in position and which also serves as a support for the iron damper. This tube is silver soldered to the brass base plate to provide a gas tight seal. A thin diaphragm of nonmagnetic stainless steel silver soldered across the lower end of the tube completes the seal to the rotor chamber.

A soft iron core, supported in the center of the stainless steel tube on a short section of bead chain, provides a means of introducing the required lateral damping to the rotating system. The clearance between the lower end of the iron damper and the stainless steel diaphragm should be adjusted to about 1/32 in. for satisfactory operation with the test rotor furnished with the apparatus. Other rotors may require different clearance adjustments.

2. Magnetic Support Circuit

The magnetic support circuit consists of a rotor position sensing circuit, two dc amplifiers, and an associated power supply. Figure D-4 shows the elements included in this circuit. The position sensing coil, which can be seen in Figure D-5, is a tuned-plate, tuned-grid radio frequency oscillator coupled to an infinite impedance detector. The plate tank circuit consists of about one-half of a 2 in. length of Barker-Williamson No. 3105 coil stock and a 140 pF variable capacitor. The grid tank circuit consists of a six-turn, spiral wound coil made from No. 22 magnet wire, the distributed capacitance of an 8 ft length of RG-62U coaxial cable and a 140 pF variable capacitor. Satisfactory operation is achieved when both of these circuits are resonant at a frequency of about 5 Mc. Since the circuits are not inductively coupled, an adjustable feed back network consisting of the second half of the Barker-Williamson No. 3105 inductor and a 30 pF variable capacitor has been provided to facilitate adjustment of the rf oscillator output. The envelope of the oscillator voltage is detected by the infinite impedance detector and an error voltage proportional to the oscillator voltage is developed across the cathode resistor of the detector. All components of the rf system have been rigidly mounted to minimize spurious signals arising from thermal and microphonic effects.

The normal operating level of the infinite impedance detector cathode is at about +90 V with respect to ground. A 5651 voltage reference tube connected to the cathode of the detector stage provides the necessary dc coupling to transform the error voltage, without significant attenuation or phase shift, to a suitable level for application to the error signal amplifier.

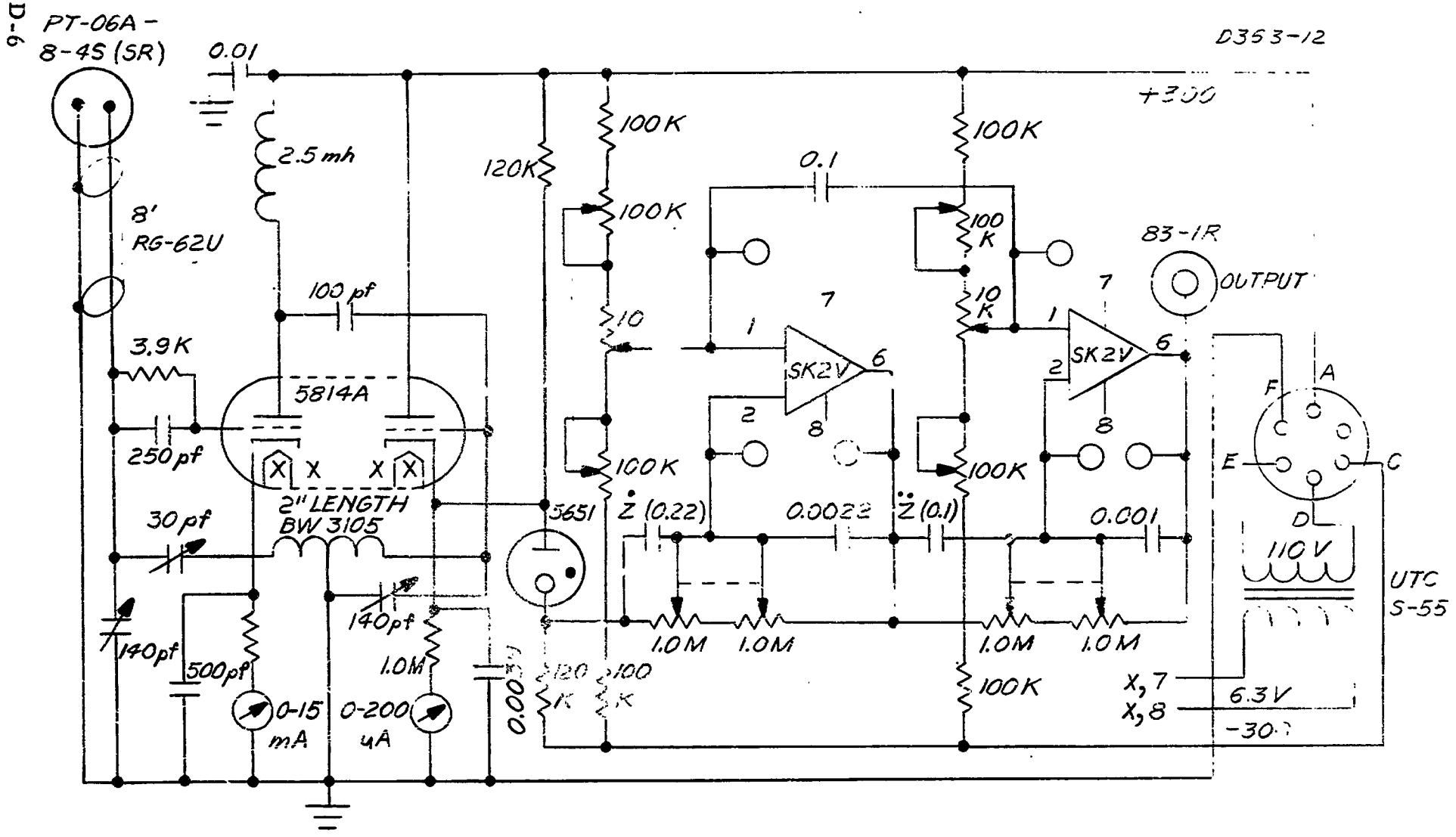

Fig. D-4. Magnetic support circuit.

M 4052

Fig. D-5. View of underside of assembly showing drive motor and position sensing coil.

The error amplifier is made up of two Philbrick Model SK2V operational amplifiers and the related bias and gain adjustment potentiometers. Two sets of bias and gain controls have been provided to facilitate rapid adjustment of the support system when rotors other than the test rotor are installed.

Since the magnetic support system is inherently friction free, some form of vertical damping must be introduce in order to achieve stable support. The required damping is introduced electronically through the use of derivative signals generated by selected resistor-capacitor networks located in the input circuits of the operational amplifiers. Both first and second derivative circuits have been provided for ease of adjustment. Stable operation of the test rotor is achieved with an 0.2 μF first derivative capacitor and an 0.1 μF second derivative capacitor.

Test points have been provided on the rear of the magnetic support chassis to permit ready monitoring of each of the six active terminals of the two SK2V operational amplifiers. Power for operation of the error detector and the two operational amplifiers is furnished by a Philbrick R-100B dual voltage power supply.

3. Current Control Circuit

Figure D-6 shows the circuit diagram for the magnetic support current control circuit. A parallel-connected bank of five 6550 vacuum tubes which are, in turn, connected in series with the main support solenoid and the +500 V power supply accepts error signals from the magnetic support circuit and provides the necessary regulation of the current passing through the support solenoid. A Sorensen model 425-400BRM regulated power supply furnishes the +500 V excitation for the current control circuit.

4. Rotor Drive Circuit

Torque for rotation of the magnetically suspended rotor is supplied by a two-phase, four-pole electric motor that is mounted in coaxial alignment with the main support field (see Fig. D-6). The stator of this motor has been designed so that an axially directed, four-pole rotating field is obtained when the stator is excited from a two-phase power source. Optimum rotor torque with a minimum of magnetic support reaction is obtained when the motor armature measures about 6 in. diameter and is fabricated from 0.025 in. thick steel spring stock. The motor stator has been mounted above the rotor of the magnetic support assembly in order to provide maximum access to the space below the suspended rotor. The unit will function equally well with the motor and driving plate mounted below the rotating assembly.

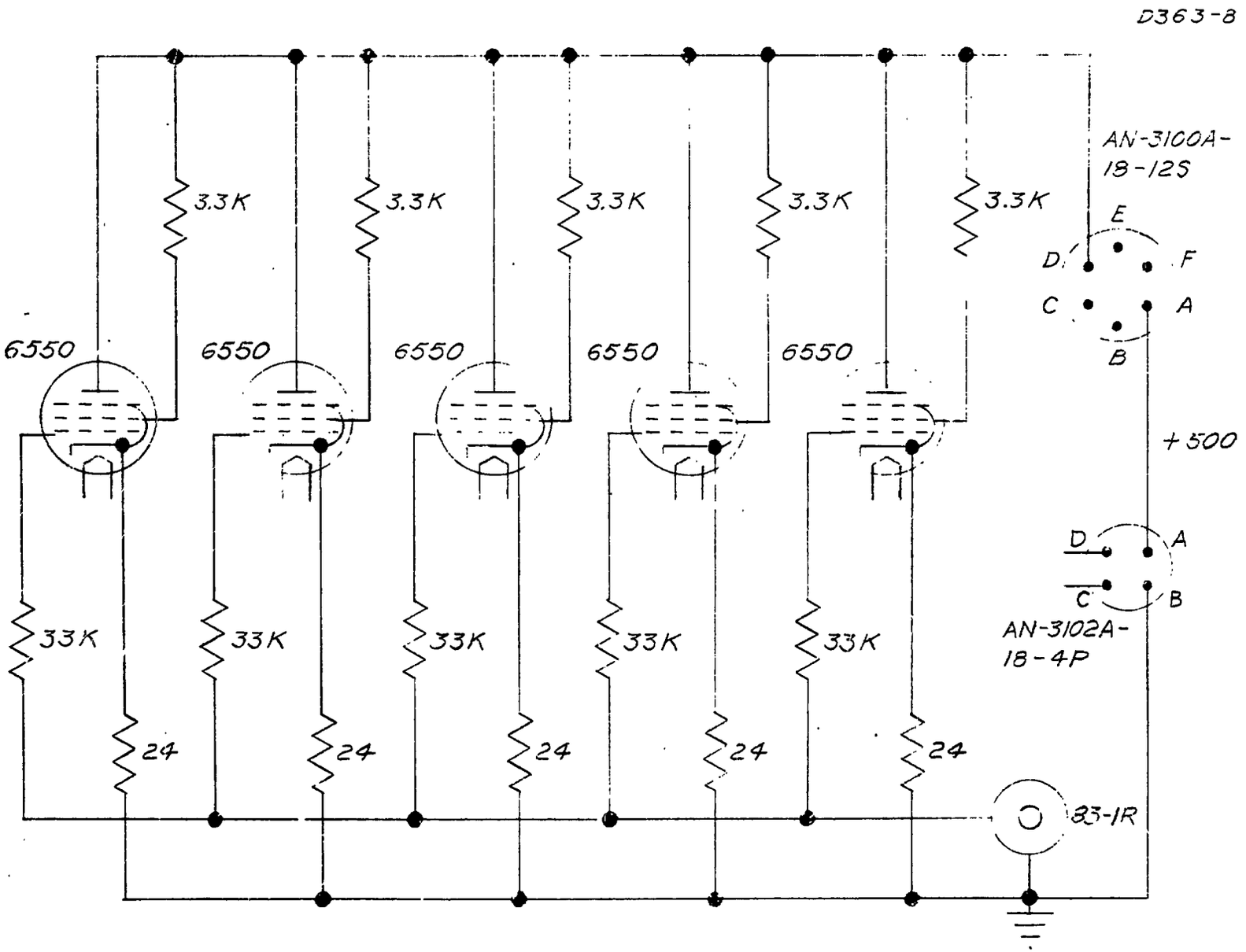

Fig. D-6. Support current control.

Two-phase power for operation of the drive motor is supplied by two Bell Sound model No. BA-75 audio amplifiers. Figure D-7 shows the circuit diagram for the motor drive power supply. An amplifier input filter has been supplied which will apply two signals of equal amplitude but having a phase difference of approximately 90° to the input terminals of the two BA-75 amplifiers when a single phase, sine wave signal is applied to the input of the filter unit. A single switch controls the two sections of the input filter and the impedance matching networks at the output of the amplifiers. Four positions on the frequency selection switch cover amplifier input frequency ranges of 50 to 150, 150 to 500, 500 to 1500, and 1500 to 5000 cps, respectively. Optimum drive torque will be obtained if these frequency ranges are observed. With the amplifier gain controls placed in the maximum clockwise position, a 1 V rms input signal applied to the input terminals will supply ample rotor driving torque. Larger signals may be used as long as they remain within the limits of operation of the power amplifier units.

The drive motor will perform equally well as an induction or a synchronous unit. Larger synchronous torques may be developed by selecting an armature design incorporating shaped salient poles. The armature furnished with the test rotor is one example of a salient pole synchronous armature having good induction armature properties. Because of the strong interaction between the supporting field and the rotating field generated by the motor, it is recommended that the transistion between different positions on the filter switch and the transition between induction and synchronous motor operation be accomplished at low input power levels.

5. Speed Pickup System

A rotational speed monitoring system has been incorporated in the magnetic support assembly. A General Electric type 253 prefocused lamp mounted above the motor assembly illuminates a small area of the rotor surface. A Texas Instruments 1N2175 photoduodiode, also mounted above the motor assembly, collects light reflected from the rotor surface. If half of the periphery of the iron pole piece on the top of the rotor is covered with a flat black coating, the output of the photoduodiode approximates a square wave having a fundamental frequency equal to the angular speed of the supported rotor. Power for the operation of both the lamp and the photoduodiode is supplied by the power supply shown in Fig. D-8.

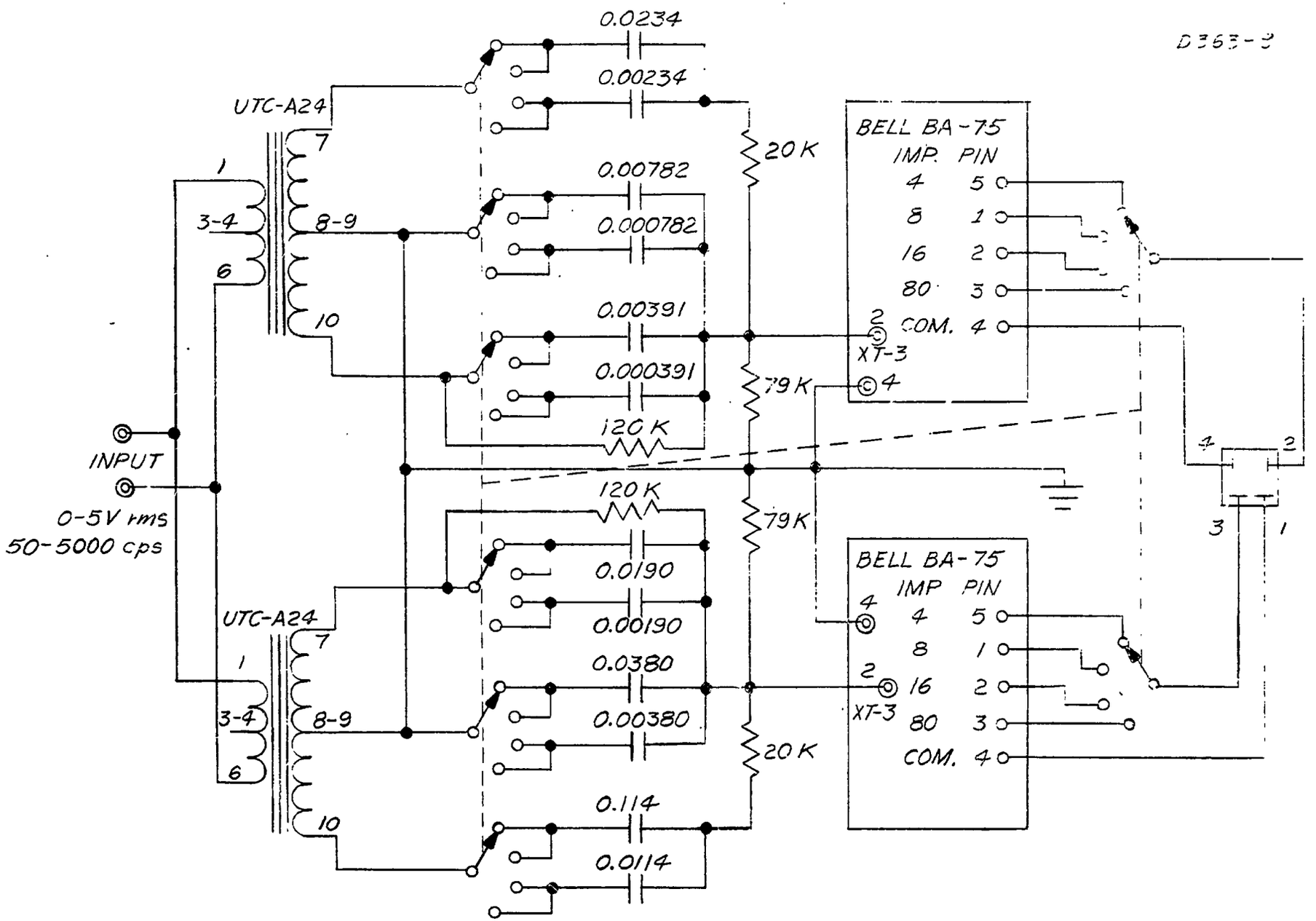

Fig. D-7. Two-phase motor drive.

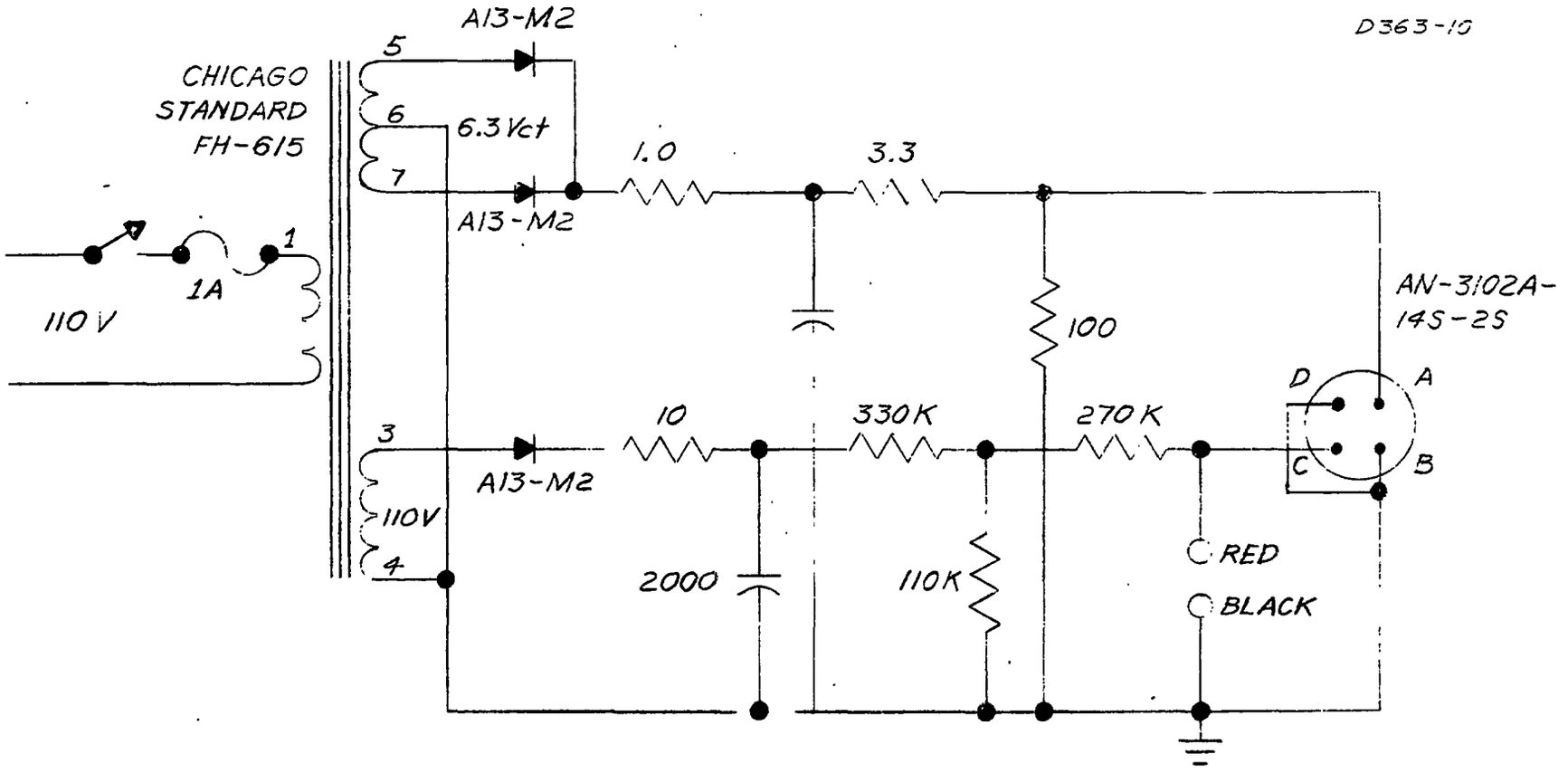

Fig. D-8. Speed pickup power supply.

BLANK PAGE

N66 36771

APPENDIX E

FOUR SPRING MOUNT ANALYSIS (2-D)

Figure E-1 shows the geometric arrangement for the four-spring mount. The rotating platform is driven at constant angular speed Ω. The sensor is coupled to the platform by the four springs indicated. The springs are attached to the sensor at positions 1, 2, 3, and 4 and to the platform at A, B, C, and D. Hence, the sensor is pulled into circular motion by the rotation of the platform.

The forces on the sensor from the springs are most easily expressed with respect to the platform as a frame of reference. Hence, we establish the rotating coordinate system x-y fixed to the platform (with origin at the center). Since the sensor is a rigid body, a third coordinate θ is required. The coordinates x and y locate the sensor center of gravity with respect to the platform, and θ describes the "twist" relative to the rotating frame.

The equation for translational motion in the rotating frame is:

$$M \frac{d^2}{dt^2} \vec{r} = \vec{F} - M\vec{\Omega} \times (\vec{\Omega} \times \vec{r}) - 2M\vec{\Omega} \times \frac{d\vec{r}}{dt} \qquad \text{(E-1)}$$

where:

$\vec{r} = x\hat{i} + y\hat{j} + z\hat{k}$

$\hat{i}, \hat{j}, \hat{k} \equiv$ unit vectors in rotating frame

$\vec{\Omega} \equiv \Omega \hat{z}$

$M \equiv$ sensor mass

$\vec{F} \equiv$ total forces, expressed in $\hat{i}, \hat{j}$.

The second term on the right hand side of (E-1) is the centrifugal term, and may be readily evaluated for the x-y system:

$$M\vec{\Omega} \times (\vec{\Omega} \times \vec{r}) = -(M\Omega^2 x)\hat{i} - (M\Omega^2 y)\hat{j} \quad . \qquad \text{(E-2)}$$

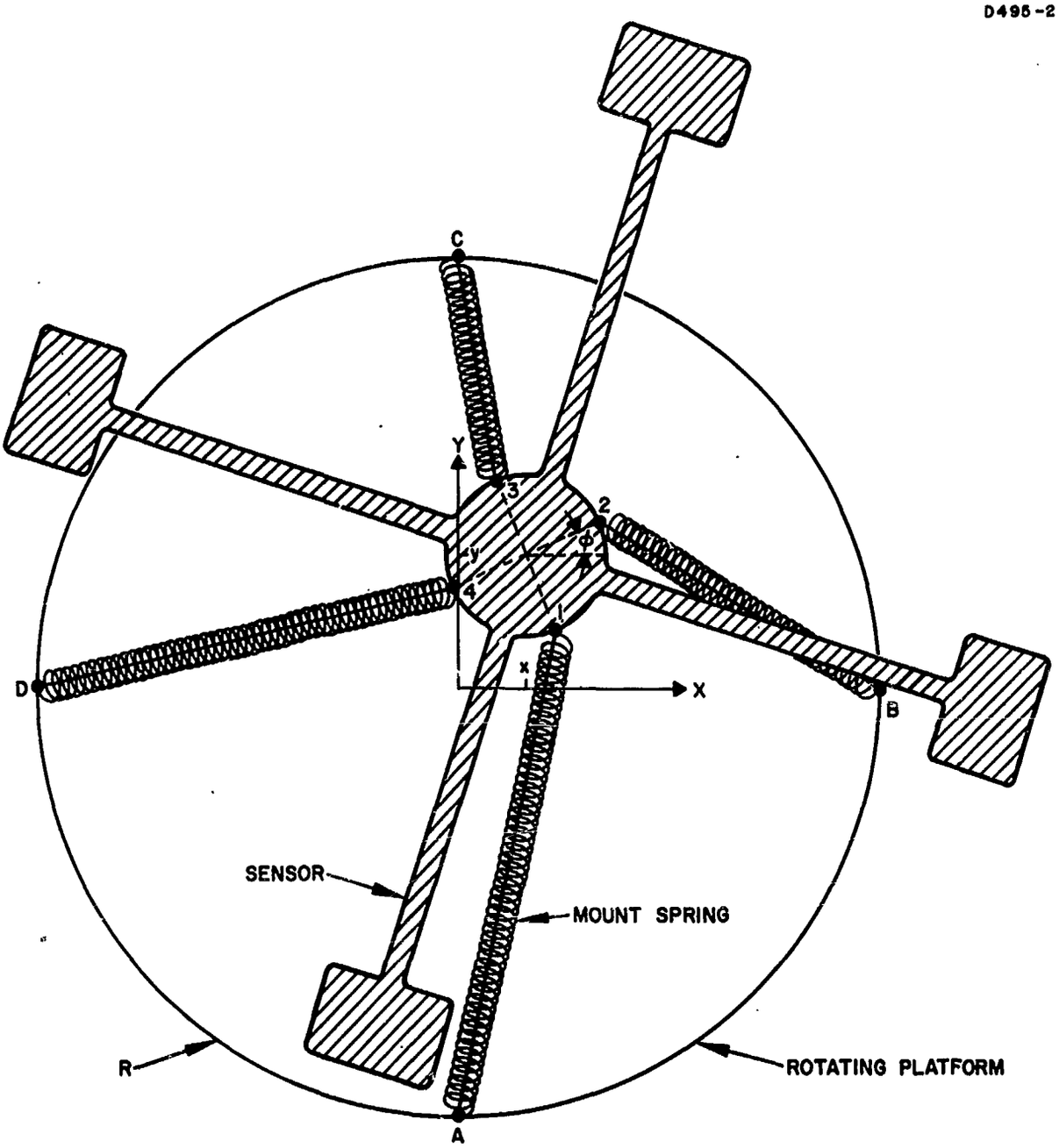

Fig. E-1. Model of four-spring mounted rotating gravitational mass sensor.

The last term is the Coriolis force, evaluated as follows:

$$2\,M\vec{\Omega} \times \frac{d\vec{r}}{dt} = +2\,M\Omega\dot{y}\hat{i} - 2\,M\Omega\dot{x}\hat{j} \quad . \tag{E-3}$$

Equating the $\hat{i}$-components of (E-1) and using (E-2) and (E-3) produces the equation for x:

$$\ddot{x} - \Omega^2 x - 2\Omega\dot{y} = \frac{F_x}{M} \quad . \tag{E-4}$$

Similarly, equating the $\hat{j}$-vector components of (E-1) and using (E-2) and (E-3) produces the equation for j:

$$\ddot{y} - \Omega^2 y + 2\Omega\dot{x} = \frac{F_y}{M} \quad . \tag{E-5}$$

It remains to write the expression for F_x and F_y, the spring force on the sensor in the rotating coordinates. In general, the force will be a function of x, y, and θ, and therefore a third differential equation will be required for θ. However, we shall show that for small θ this dependence is negligible.

The F_x, F_y forces are simply the sum of the x, y components of the restoring force of four stretched springs. Hence, we must calculate the stretched length H_i of the four springs such that

$$F_x = -k \sum_i^4 (H_i - H_o)\cos\alpha_i \tag{E-6}$$

$$F_y = -k \sum_i^4 (H_i - H_o)\sin\alpha_i$$

where

$H_o \equiv$ unstretched length of springs

$k \equiv$ spring constant

$\alpha \equiv$ angle which springs make with x-axis .

Figure E-2 shows the evaluation of the force H_i from geometric consideration. The results are, for a typical x, y, θ position,

$$
\begin{aligned}
H_1 &= [(R + y - a\cos\theta)^2 + (x + a\sin\theta)^2]^{1/2} \\
H_2 &= [(R - x - a\cos\theta)^2 + (y + a\sin\theta)^2]^{1/2} \\
H_3 &= [(R - y - a\cos\theta)^2 + (x - a\sin\theta)^2]^{1/2} \\
H_4 &= [(R + x - a\cos\theta)^2 + (y - a\sin\theta)^2]^{1/2} \quad .
\end{aligned}
\tag{E-7}
$$

In the above, R is the distance from the center of the rotating platform to the position of spring attachment on the platform; a is the radius of attachment on the sensor. Thus, (R - a) is the spring length when $x = y = \theta = 0$.

We now make four convenient definitions which will aid the expansion of (E-7):

$$
\begin{aligned}
z^2 &\equiv R^2 + a^2 - 2Ra\cos\theta \qquad & X &\equiv x\cos\theta + y\sin\theta \\
w^2 &\equiv x^2 + y^2 + z^2 & Y &\equiv x\sin\theta + y\cos\theta \quad .
\end{aligned}
\tag{E-8}
$$

Using the definitions in (E-8), eq. (E-7) takes the form

$$
\begin{aligned}
H_1 &= [w^2 + 2(Ry - aY)]^{1/2} \\
H_2 &= [w^2 - 2(Rx - aX)]^{1/2} \\
H_3 &= [w^2 - 2(Ry - aY)]^{1/2} \\
H_4 &= [w^2 + 2(Rx - aX)]^{1/2} \quad .
\end{aligned}
\tag{E-9}
$$

At this point we introduce an assumption that will limit the results of the analysis to small displacements of the sensor, e.g.,

$$
w^2 >> 2(Ry - aY) \quad . \tag{E-10}
$$

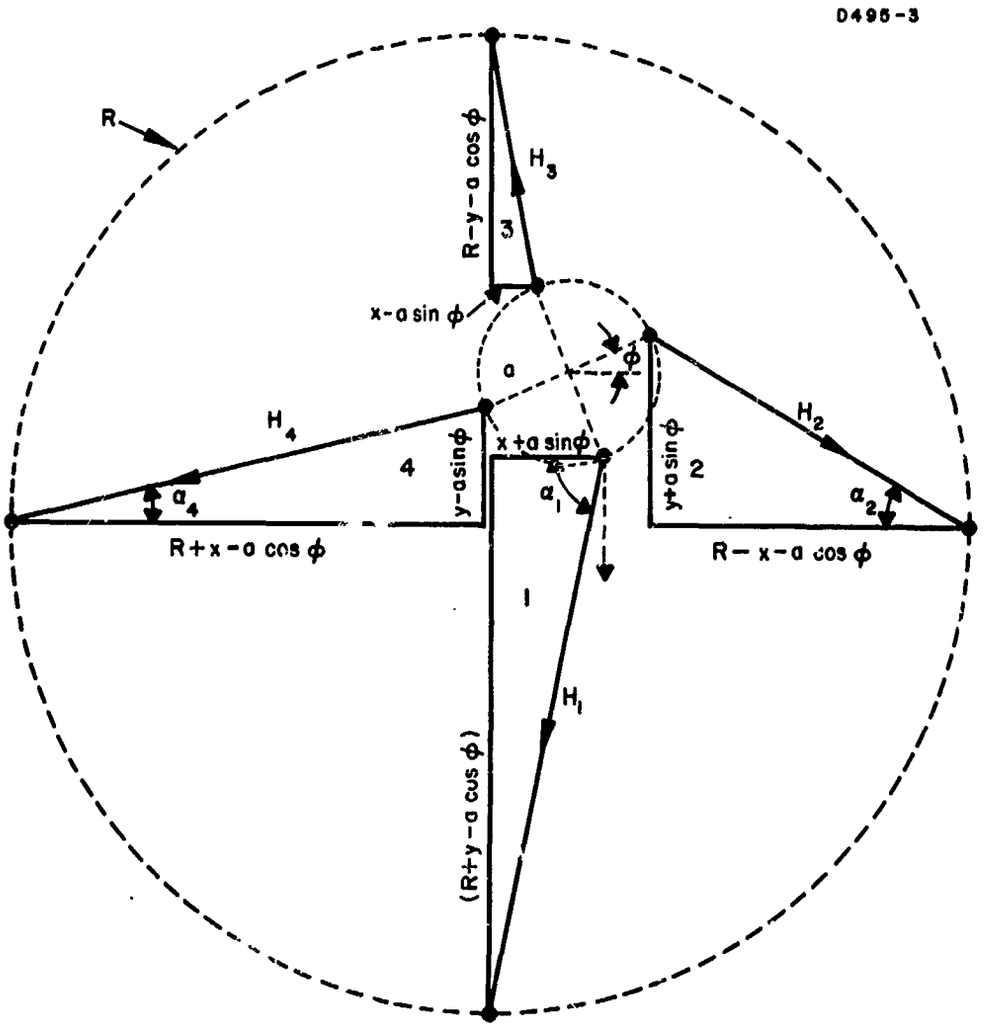

Fig. E-2. Vector diagram of restoring spring forces on sensor (four-spring mount).

The square root operation indicated in (E-9) may then be approximated as follows:

$$\begin{aligned} H_1 &= (w^2 + Ry - aY)/w \\ H_2 &= (w^2 - Rx + aX)/w \\ H_3 &= (w^2 - Ry + aY)/w \\ H_4 &= (w^2 + Rx - aX)/w \quad . \end{aligned} \tag{E-11}$$

The final term to evaluate in (E-6) is $\cos \alpha_i$. These terms are obtained by inspection of Fig. E-2:

$$\begin{aligned} \cos \alpha_1 &= + (x + a \sin\theta)/H_1 \\ \cos \alpha_2 &= - (R - x - a \cos\theta)/H_2 \\ \cos \alpha_3 &= (x - a \sin\theta)/H_3 \\ \cos \alpha_4 &= (R + x - a \cos\theta)/H_4 \quad . \end{aligned} \tag{E-12}$$

The net restoring spring force (x-component) is now available by direct substitution of (E-11) and (E-12) into (E-6). The algebra will not be given; the result is

$$F_x = - 4 kx \left| 1 - \frac{H_o}{w^3} \left(w^2 - \frac{1}{2} z^2 \right) \right| \quad . \tag{E-13}$$

Thus, the net restoring spring force is something less than four times the x-displacement times the spring constant (unless H_o, the unstretched length, $= 0$).

Returning to (E-8), we note that for small θ,

$$z \approx R - z \equiv z_o \quad . \tag{E-14}$$

Using (E-14) and (E-8) to expand (E-13),

$$F_x = -4kx\left[1 - \frac{H_o}{(x^2 + y^2 + z_o^2)^{3/2}}\left(x^2 + y^2 + \frac{1}{2}z_o^2\right)\right]. \qquad \text{(E-15)}$$

This is the expression for the x-component of the net restoring force of the four-springs for any position x, y in the rotating force (for small θ, x, y). Equation (E-15) demonstrates that over the x-y range of interest, the restoring force may be considered linear. Typical values of z_o are several centimeters, while the range of interest of x, y is below 1 mm. Hence x^2, $y^2 << z_o^2$, and (E-15) becomes

$$F_x = -4kx\left[1 - \frac{H_o}{2z_o}\right]. \qquad \text{(E-16)}$$

Equation (E-16) demonstrates a linear spring force, with effective spring constant:

$$k' = 4k\left[1 - \frac{H_o}{2z_o}\right]. \qquad \text{(E-17)}$$

Typical values for H_o and z_o are

$$H_o \approx 2 \text{ cm}$$

$$z_o \approx 3 \text{ cm},$$

such that

$$\frac{k'}{k} = 4\left[1 - \frac{(2)}{(2)(3)}\right] = 2.67.$$

The effective spring constant is thus much larger than the single spring constant.

To determine the validity of the assumption of linear spring force, the exact value of spring constant was calculated over a range to values for x and y assuming $\theta = 0$. Equation (E-9) was used so that no limit was imposed on the range of x and y. The results of the calculations are shown in Fig. E-3. It is noted that for x, y < 1 mm, the assumption of constant k' is good indeed.

So far, (E-16) expresses only the static spring restoring force. However, we know that there is a dynamic contribution to the total spring force: terms which are proportional to the velocity and higher derivatives. We consider here simply a velocity-dependent damping term, such that the expression for total spring force becomes

$$\begin{aligned} F_x &= - k'x - D\dot{x} \\ F_y &= - k'y - D\dot{y} \quad . \end{aligned} \tag{E-18}$$

We may now return to the equations of motion ((E-4) and (E-5)) with this information.

Using (E-18), eqs. (E-4) and (E-5) become

$$\ddot{x} + (\Omega_m^2 - \Omega^2)\, x - 2\Omega\dot{y} + \frac{\Omega_m}{Q}\,\dot{x} = 0 \tag{E-19}$$

$$\ddot{y} + (\Omega_m^2 - \Omega^2)\, y + 2\Omega\dot{x} + \frac{\Omega_m}{Q}\,\dot{y} = 0 \tag{E-20}$$

where

$$Q \equiv \text{inverse damping coefficient} = \frac{M\Omega_m}{D}$$

$$\Omega_m \equiv \sqrt{k'/M} \quad .$$

Solution of (E-19) and (E-20) now proceeds. Let

$$x = e^{\omega t} \quad ; \tag{E-21}$$

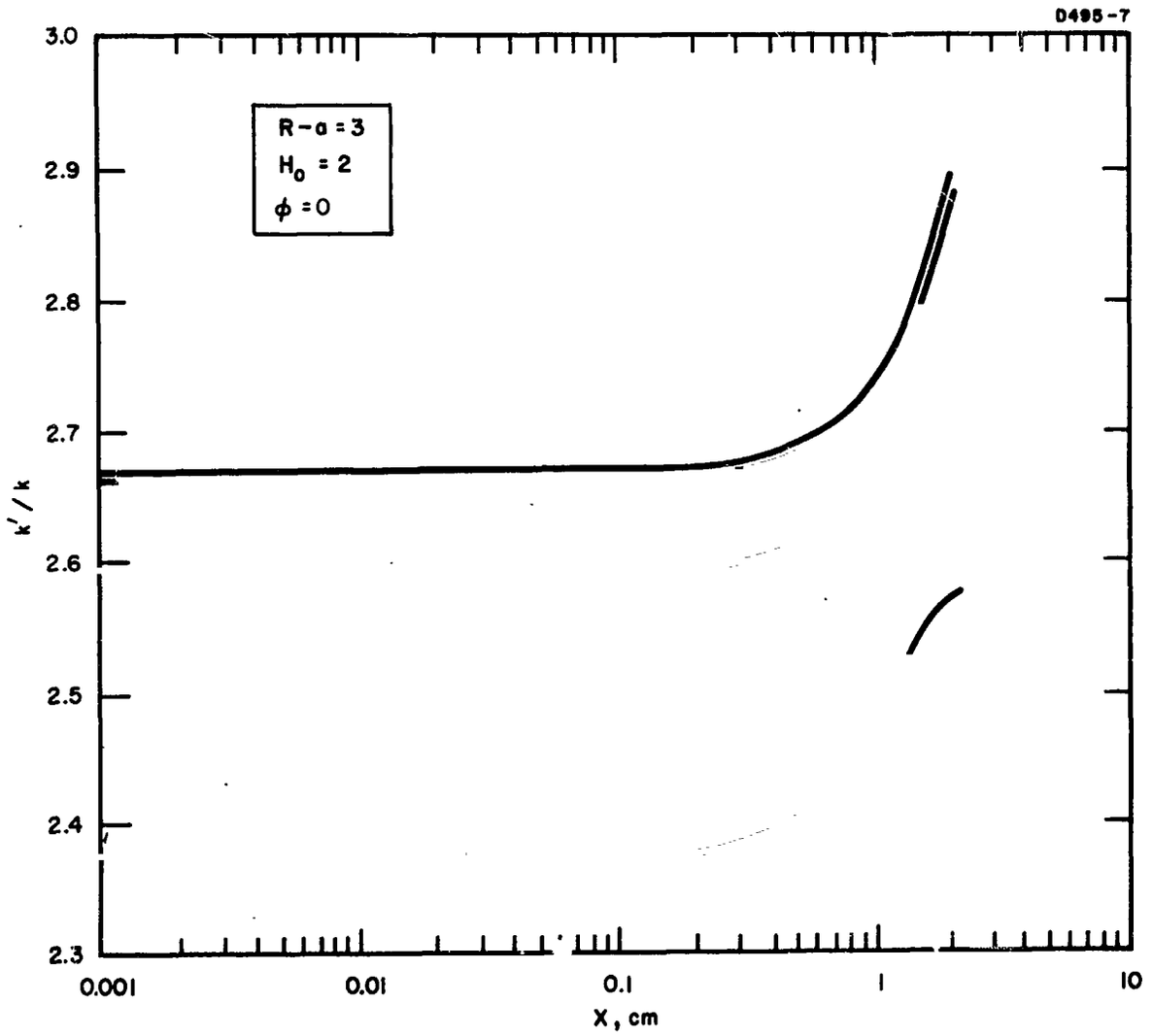

Fig. E-3. Effective spring constant of four-spring sensor mount.

then

$$\dot{x} = \omega e^{\omega t}, \quad \ddot{x} = \omega^2 e^{\omega t} \quad . \tag{E-22}$$

Substitution into (E-19) yields

$$\dot{y} = \frac{1}{2\Omega} \left[\omega^2 + (\Omega_m^2 - \Omega^2) + \frac{\omega \Omega_m}{Q} \right] e^{\omega t} \tag{E-23}$$

such that

$$y = \frac{1}{2\Omega\omega} \left[\omega^2 + (\Omega_m^2 - \Omega^2) + \frac{\omega \Omega_m}{Q} \right] e^{\omega t} \quad , \tag{E-24}$$

which, substituted into (E-20) yields

$$\omega^2 + (\Omega_m^2 - \Omega^2) + \frac{\Omega_m}{Q} \omega = \pm 2i\Omega\omega \quad . \tag{E-25}$$

This produces two equations:

$$\begin{aligned} \omega^2 + \left(\frac{\Omega_m}{Q} + 2i\Omega \right) \omega + (\Omega_m^2 - \Omega^2) = 0 \\ \omega^2 + \left(\frac{\Omega_m}{Q} - 2i\Omega \right) \omega + (\Omega_m^2 - \Omega^2) = 0 \end{aligned} \quad . \tag{E-26}$$

Each of the above equations produces two complex roots (a total of four):

$$\begin{aligned} \omega_1, \omega_2 &= -\left(\frac{\Omega_m}{2Q} + i\Omega \right) \pm \left[\left(\frac{\Omega_m}{2Q} + i\Omega \right)^2 - (\Omega_m^2 - \Omega^2) \right]^{1/2} \\ \omega_3, \omega_4 &= -\left(\frac{\Omega_m}{2Q} - i\Omega \right) \pm \left[\left(\frac{\Omega_m}{2Q} - i\Omega \right)^2 - (\Omega_m^2 - \Omega^2) \right]^{1/2} \end{aligned} \quad . \tag{E-27}$$

For $1/4Q^2 << 1$, the above reduce to the following simplified form:

$$\omega_1, \omega_2 = -\left(\frac{\Omega_m}{2Q} + i\Omega\right) \pm \left[-\Omega_m + i\frac{\Omega}{Q}\right]^{1/2}$$

$$\omega_3, \omega_4 = -\left(\frac{\Omega_m}{2Q} - i\Omega\right) \pm \left[-\Omega_m - i\frac{\Omega}{Q}\right]^{1/2} . \qquad \text{(E-28)}$$

Obtaining the indicated complex roots results in the following solutions for the ω's:

$$\omega_1 = \frac{1}{2Q}(\Omega - \Omega_m) + i(\Omega_m - \Omega)$$

$$\omega_2 = -\frac{1}{2Q}(\Omega + \Omega_m) - i(\Omega_m + \Omega) \qquad \text{(E-29)}$$

$$\omega_3 = -\frac{1}{2Q}(\Omega + \Omega_m) + i(\Omega_m + \Omega)$$

$$\omega_4 = \frac{1}{2Q}(\Omega - \Omega_m) - i(\Omega_m - \Omega) .$$

The time-dependent solution to (E-19) and (E-20) follows immediately:

$$x, y = A_1 e^{(\Omega - \Omega_m)t/2Q} \cos[(\Omega_m - \Omega)t + \beta_1] + A_2 e^{-(\Omega + \Omega_m)t/2Q} \cos[(\Omega_m + \Omega)t + \beta_2]. \qquad \text{(E-30)}$$

The constants $A_1, A_2, \beta_1, \beta_2$ depend on initial conditions.

Equation (E-30) demonstrates potential instability. If $\Omega > \Omega_m$, the amplitude of the first term in (E-30) grows in time. This condition occurs when the centrifugal force resulting from rotation becomes larger than the restoring spring force. The sensor then would not remain centered, but would have a tendency to fly out.

These mathematical results indicate that the instability occurs when the rotational frequency is just slightly larger than the effective four-spring natural frequency. However, experimental evidence indicates that the mount is stable for rotational speeds of several times the natural frequency. The apparent lack of correlation between (E-30) and the experimental results is possibly explained by one of the following hypotheses.

1. The dynamic nature of the spring restoring force is not as defined by (E-18). In other words, the damping is not a simple velocity dependent term.

2. The initial conditions of (E-30) are such that $A_1 = 0$. This implies that the unstable mode is not exited, even though it exists.

3. The time constant $(2Q/\Omega - \Omega_m)$ is very large. Thus, an apparently stable situation might actually prove to be unstable in a longer period of time.

It seems that more work is required to correlate the four-spring mount with analysis. For one thing, the dynamic nature of the restoring force should be investigated further. The assumption of velocity-dependent damping was somewhat arbitrary.

BLANK PAGE

N66 36772

APPENDIX F

PHASE SHIFT TUNED AMPLIFIER

The mechanical vibrations of interest on this program are detected by means of piezoelectric strain transducers. The transducers used have a high voltage output ($> 10^5$ V/unit strain), but they also have a characteristic small series output capacity (typically 1000 pF). Because the vibrations of interest are extremely small, and signal-to-noise problems are of paramount importance, it is desirable to tune out the capacity rather than work into high impedance. The low capacity value and low frequencies of interest (typically 100 cps) preclude the use of an inductor, however. A small, simple circuit which behaves as an inductor is needed. The phase shift tuned amplifier fulfills these requirements.

Figure F-1 shows the amplifier circuit. It is identical to the conventional phase shift oscillator circuit except that it has an input, and its gain is adjusted so that it is not quite sufficient for oscillation.

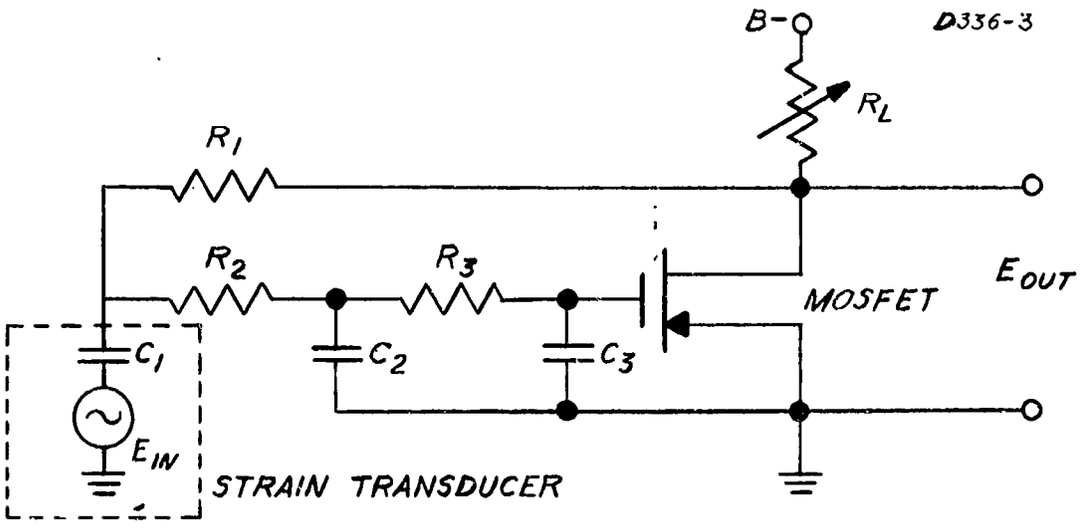

Fig. F-1. Generalized phase shift tuned amplifier.

The MOSFET (Metal Oxide Silicon Field Effect Transistor) is ideal for this circuit because it has essentially infinite input resistance ($>10^{15}\ \Omega$) and operates with a forward bias equal to its drain (collector) voltage.

The complete relationship between input and output is:

$$\frac{E_{out}}{E_{in}} = \frac{-AsC_1R_1}{s^3C_1C_2C_3R_1R_2R_3 + s^2(C_1C_2R_1R_2 + C_2C_3R_2R_3 + C_1C_3R_1R_3 + C_2C_3R_1R_3 + C_1C_3R_1R_2) + s(C_1R_1 + C_2R_2 + C_3R_3 + C_2R_1 + C_3R_1 + C_3R_2) + A + 1} \qquad \text{(F-1)}$$

where $s = j\omega$ and A is the gain of the MOSFET transistor.

This equation is considerably simplified if we let $R_1 = R$, $R_2 = NR$, $R_3 = N^2R$, and $C_1 = C$, $C_2 = C/N$, $C_3 = C/N^2$.

Then,

$$\frac{E_{out}}{E_{in}} = \frac{-AsCR}{(sCR)^3 + [3 + (2/N)](sCR)^2 + [3 + (2/N) + (1/N^2)](sCR) + A + 1} \qquad \text{(F-2)}$$

(See Fig. F-2.)

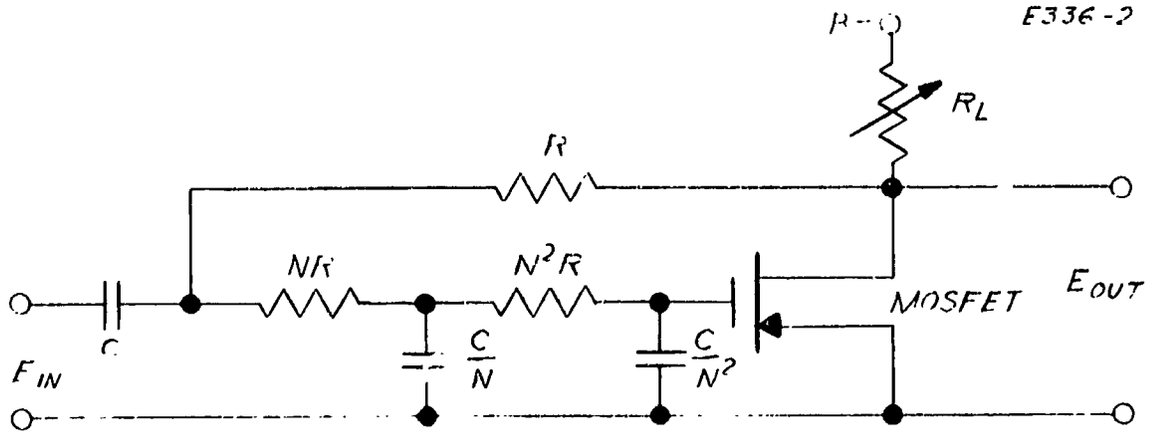

Fig. F-2. Optimized phase shift tuned amplifier.

For this circuit, resonance will occur at

$$\omega = \frac{\sqrt{3 + (2/N) + (1/N^2)}}{CR} \qquad \text{(F-3)}$$

when the MOSFET transistor gain is adjusted to

$$A = 8 + \frac{12}{N} + \frac{7}{N^2} + \frac{2}{N^3} \quad . \qquad \text{(F-4)}$$

Although the resonance denominator of (F-2) is fairly complicated, the calculated and observed resonance of the circuit for high N and high gain consists of a simple resonance shape that is almost indistinguishable from a typical LC resonance curve of the same amplitude and Q.

In order to develop expressions for an equivalent resonance frequency and Q for the phase shift tuned amplifier, we will let N be very large; then

$$\frac{E_{out}}{E_{in}} = \frac{-AsCR}{(sCR+1)^3 + A} \quad . \qquad \text{(F-5)}$$

This relationship may be rearranged as follows*:

$$\frac{E_{out}}{E_{in}} = \frac{AQ}{\left[j\frac{\omega}{\omega_o}\left(1 - A^{1/3} + A^{2/3}\right)^{1/2} + 1 + A^{1/3}\right]\left[1 - A^{1/3} + A^{2/3}\right]^{1/2}}$$

$$\div \left[1 + jQ\left(\frac{\omega_o}{\omega} - \frac{\omega}{\omega_o}\right)\right] \qquad \text{(F-6)}$$

where

$$Q = \frac{\left(1 - A^{1/3} + A^{2/3}\right)^{1/2}}{2 - A^{1/3}} \qquad \text{(F-7)}$$

$$\omega_o = \frac{\left(1 - A^{1/3} + A^{2/3}\right)^{1/2}}{RC} \quad . \qquad \text{(F-8)}$$

Note that the Q of the circuit resonance becomes very large as the gain of the MOSFET transistor A approaches 8. For gains higher than 8 the amplifier becomes an oscillator. Since we will normally be operating at high Q's, we can assume that $A \cong 8$, and the above equations become

$$Q \cong \frac{\sqrt{3}}{2 - A^{1/3}} \qquad \text{(F-9)}$$

$$\omega_o \cong \frac{\sqrt{3}}{RC} \qquad \text{(F-10)}$$

*Suggested by T. R. O'Meara, Hughes Research Laboratories, Malibu, Calif.

Note that for high Q, the slight dependence of the resonant frequency ω_o on the gain disappears.

At resonance, where $\omega = \omega_o$ and for a Q greater than 25, the circuit gain (eq. F-6) and the imput impedance simplify to

$$\frac{E_{out}}{E_{in}} \cong 1\ \frac{1}{3}\ Q \angle 150^\circ \qquad \text{(F-11)}$$

$$Z_{in} \cong \frac{R\sqrt{3}}{2Q} \angle 0^\circ \qquad \text{(F-12)}$$

These circuit parameters are to be compared with the equivalent LC circuit parameters (see Fig. F-3), which are

$$Q = \frac{\omega_o L}{R_L} \qquad \text{(F-13)}$$

$$\omega_o = \frac{1}{\sqrt{LC}} \qquad \text{(F-14)}$$

$$\frac{E_{out}}{E_{in}} \cong Q \angle 90^\circ \qquad \text{(F-15)}$$

$$Z_{in} = R_L \angle 0^\circ \qquad \text{(F-16)}$$

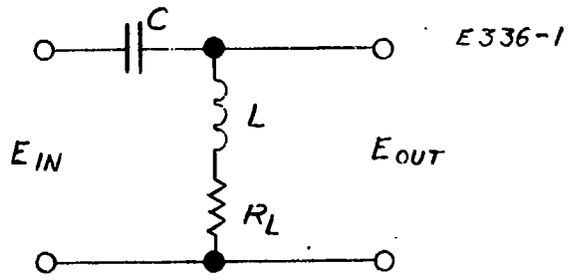

Fig. F-3. Equivalent LC circuit.

The input capacitance C is the capacitance of the strain transducer.

Although the circuit has been analyzed for the ideal case, the formulas describe the general circuit behavior and are useful for high values of N. The circuit will work for any value of N; if N is small, however, the gain necessary for a high Q may be more than the MOSFET can deliver.

Because of the high input resistance of MOSFET's, the value of R_3 is limited only by the MOSFET input capacity (typically 8 pF).

To verify the analytical study experimentally, a circuit with variable resistors was connected to a cruciform mass sensor. One strain transducer was used as a control. Another transducer was connected alternately to the tuned amplifier circuit and to an oscilloscope. The mechanical resonant frequency of the sensor was found by exciting the sensor acoustically and peaking the monitor transducer output. The output transducer indicated 1 mV peak-to-peak on the oscilloscope at resonance.

The output transducer was then coupled into the test circuit. The gain and RC time constants were adjusted to reduce the monitor transducer output by 3 dB. Since the acoustic excitation was not changed, this indicates that a significant portion of the stored vibrational energy was being extracted from the sensor. The output of the test circuit was measured to be 150 mV.

The experiment showed high effective gain (150 for one transistor) and strong coupling between mechanical and electrical resonant circuits.

ATTACHMENTS

The following six attachments are copies of papers generated during the work on the contract. They are reprinted here in their original format. In addition to these six papers, a condensed version of Quarterly Progress Report No. 1 was submitted to the 1965 Essay Competition of the Gravity Research Foundation, New Boston, New Hampshire. The essay received the fourth award of $150.

N66 36773

ATTACHMENT A

ROTATING TENSOR SENSORS

The following paper was presented at the American Physical Society Winter Meeting, Berkeley, California, 21-23 December 1964. The abstract was published in the Bulletin of the American Physical Society, volume 9, page 711 (December 1964).

BLANK
PAGE

ROTATING TENSOR SENSORS[†]

Robert L. Forward
Member of the Technical Staff
Hughes Research Laboratories
Malibu, California

36773

ABSTRACT[1]

We have been investigating a novel class of differential force sensors which utilize the rotational properties of tensors in order to separate the effects of forces from the effects of the gradients of the forces. The basic co· ·pt is that tensors of n^{th} rank, when examined in the rotating reference frame of a sensor, will be found to produce time-varying signals that are at n times the rotational frequency of the sensor. Two applications, namely a gravitational mass sensor and a magnetic gradient sensor, are discussed. Work has started on a research model of the gravitational mass sensor.[*] It is theoretically capable of distinguishing the gravitational effects of a nearby mass from the inertial effects of acceleration and rotation. The magnetic gradient sensor, recently constructed and tested, consists of two opposed coils attached to opposite sides of a rotating shaft and operates in such a manner that any gradient in a magnetic field produces currents at a frequency twice the rotation speed, while mechanical imbalances come out at the rotation frequency.

Author

[†] Presented at the American Physical Society Winter Meeting, Berkeley, California, 21-23 December 1964.

[*] The gravitational mass sensor work is supported by NASA Contract NASW-1035.

DIFFERENTIATION OF GRAVITATIONAL AND INERTIAL EFFECTS

For the problem of measuring the mass of an asteroid at a distance[2] or a planet's gravitational field structure when both the body and the sensor are in free fall, and for the problem of determining the attitude of a spacecraft in orbit around the earth,[3-10] it is necessary to find ways to distinguish the inertial effects of acceleration and rotation of the spacecraft from the gravitational effects from massive nearby objects.

Although it is generally assumed that it is impossible to distinguish between gravitational and inertial effects (Einstein's Principle of Equivalence), these effects do have different tensor characteristics.[11] The inertial field created by acceleration is a uniform vector field and has no gradients, while the inertial field created by rotation has a uniform cylindrically symmetric tensor gradient but none of higher order. The gravitational field created by a mass is highly nonuniform with essentially no limit to the number of higher order gradients. These differences make it theoretically possible to measure independently gravitation, rotation, and acceleration effects; to do so, some form of differential force sensor with tensor response characteristics must be used.

The differential force sensors usually discussed in the literature[2-10] consist of spaced pairs of low level accelerometers with opposed outputs. However, a very good accelerometer is only capable of a linearity of one part in 10^5, and the outputs of two accelerometers cannot be matched to even this degree of accuracy. Thus, it has not been possible to make differential force sensors whose outputs could be combined to cancel out the acceleration terms in order to obtain the rotation and gravitation terms.

The most promising technique is a dynamic one.[2, 9] By rotation of specially designed differential force sensors, the static spatial variations of the fields can be transformed into temporal variations in the sensor. Because of the rotational properties of tensors the various inertial and gravitational effects come out at different frequencies.[2]

The basic concept is that forces are vectors (tensors of first rank), the gradients of forces are tensors of second rank, and higher order gradients are higher rank tensors. In general, the components of a tensor of n^{th} rank, when examined in the rotating reference frame of a sensor, will be found to have time-varying coefficients that are at n times the rotational frequency of the sensor.[1]

GRAVITATIONAL MASS SENSOR

The basic gravitational sensor configuration being studied at Hughes[11, 12] consists of a mass-spring system with one or more vibrational modes. The system is then rotated at some subharmonic of the vibrational mode. If there is a nonuniform gravitational field present, the differential forces on the sensor resulting from the gradients of the gravitational field will excite the vibrational modes of the sensor structure. In the schematic of Fig. 1, the gradient of the gravitational field excites vibrations at twice the rotation frequency of the sensor. The most promising sensor configuration is that shown in Fig. 2. It consists of four masses on the end of four transversely vibrating arms. The gradient of the gravitational field causes differential torques on the arms. As the sensor rotates, the direction of the applied torque varies at a frequency which is twice the rotation frequency of the sensor.

The readout of the sensor vibrations is accomplished by sensing the dynamic strains in the sensor arms with barium titanate strain transducers which have a "gauge factor" of about 10^5 volts per unit

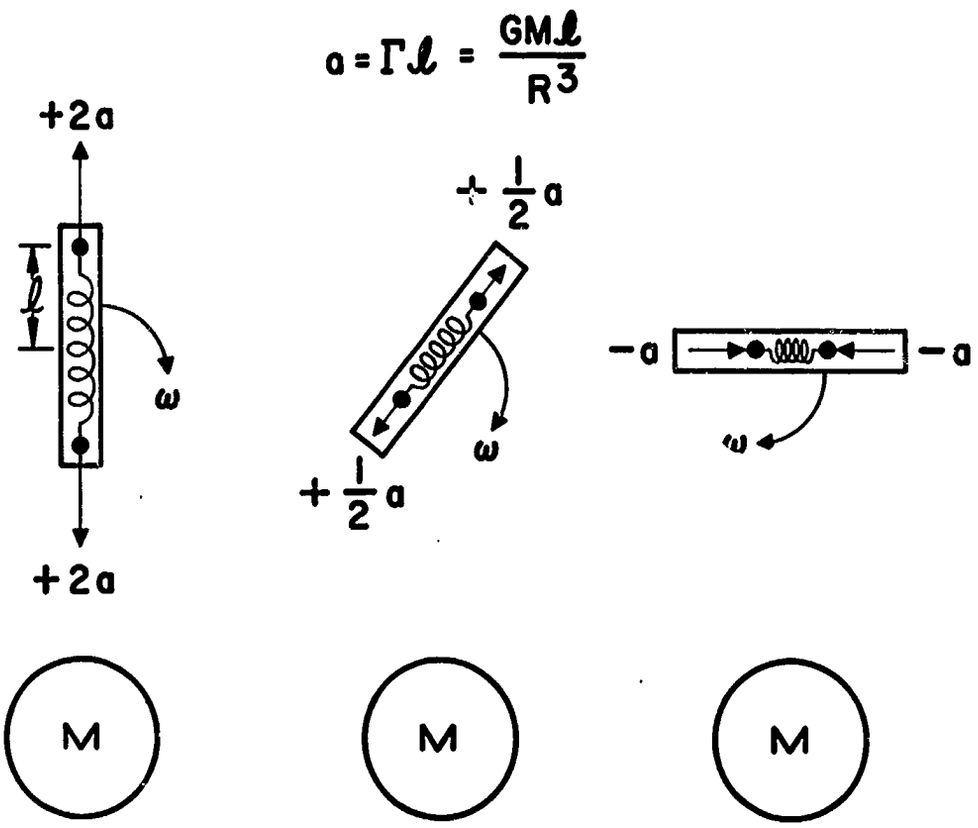

Fig. 1. Response of rotating gradient sensor to gravity gradients.

M 3615

Fig. 2. Five-inch diameter cruciform gravitational mass sensor

strain [illegible]. An assumption of a narrow band [illegible] over [illegible] and amplifier means that dynamic strains of [illegible] can be detected. For typical sensor structures (1 m. in diameter) and integration times of a few seconds, this strain level corresponds to detecting the gravitational gradient anomaly (10^{-9} sec^{-2}) from a small object some 1 km away. (The gravitational gradient of the earth at its surface is about 10^{-6} sec^{-2}.)

Because of its different response to gravitational and inertial effects, this sensor can be used to measure the mass of an object at a distance even when the sensor is being disturbed by drag effects or other nongravitational forces. If present research is successful, this type of sensor should be more rugged and sensitive than accelerometers, gyros, and gravity meters. These sensors could be used for inertial guidance and attitude control, for airborne gravity surveys for oil, satellite-borne gravity surveys of the moon and planets, and for mass measurement of asteroids at miss distances up to 10,000 km. However, background clutter from distant geophysical objects and nearby natural objects makes it doubtful that it will have a substantial military usefulness for detection of man-made objects on the earth. (A 10 g bug at 1 m has the same gravitational gradient as a 100 ton tank at 100 m.)

MAGNETIC GRADIENT SENSOR

In geology, magnetic measurements are often the basis for determining the location of ferromagnetic ores. The gradients of the magnetic field are usually more significant than the magnetic field itself in this application because they reflect more strongly the local sources of magnetic field. In practice, this gradient is determined indirectly either by forming the difference of magnetic field readings at neighboring points or by electrically taking the difference in output of two adjacent magnetic field sensors. The first of these methods, however, greatly magnifies small errors in the original readings

because of instrumental drift or diurnal variations, and the second is subject to large errors arising from a possible slight imbalance of output of the two sensors in the presence of a strong constant magnetic field.

The same design philosophy employed for the gravitational sensor was used in the construction and test of a magnetic gradient sensor which measures directly the gradients of a static magnetic field and which is not subject to interference by large constant magnetic fields or by large-scale diurnal variations.[13] The sensor consists of two small coils of wire attached tangentially to opposite sides of a common shaft and rotated by a synchronous motor. (See Fig. 3.) The coils are opposed and the sensor operates in such a manner that any gradient in a magnetic field will cause currents at a frequency twice the rotation speed, while any instrumental imbalances cause currents at the rotation frequency. Because the spurious signals are easily filtered out from the desired signals, the performance of the relatively unsophisticated device is quite interesting.[13] A magnetic field of 50 gamma from a large coil is easily seen even in the presence of the 50,000 gamma earth field because the earth's gradient is much smaller. The sensor is presently limited in sensitivity to about 1 gamma/cm by the magnetic gradient background clutter in the laboratory.

The magnetic gradient sensor will be useful in geophysical prospecting if the present sensing coils are replaced with nuclear or flux gate type sensors and a little effort is applied to proper engineering design. The magnetic sensor is not applicable in space, where the gradients are small, and it has only a moderate applicability to detection 'at a distance' because of the $1/R^4$ characteristic.

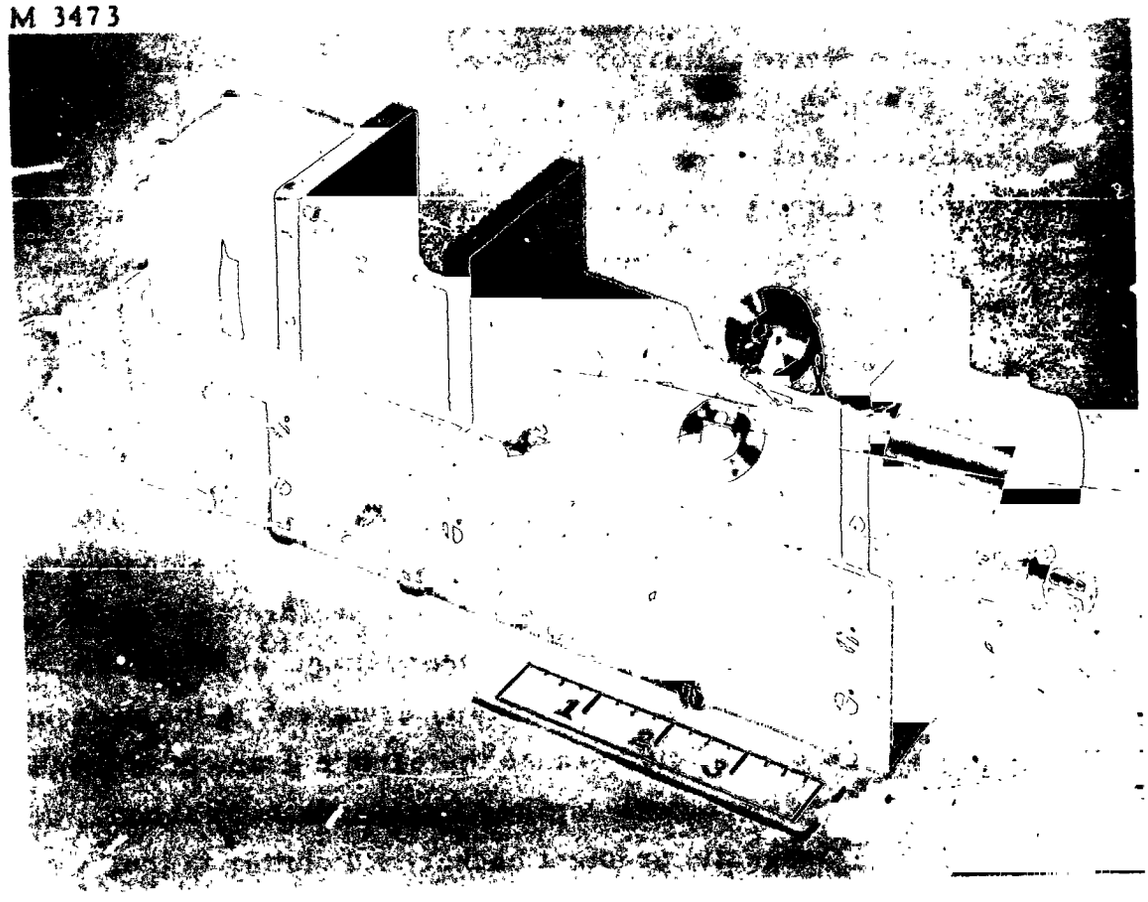

Fig. 3. Flip coil magnetic gradient sensor.

REFERENCES

1. R. L. Forward, "Rotating Tensor Sensors," Bull. Am. Phys. Soc. 9, 711 (1964).

2. R. L. Forward, "Gravitational Mass Sensor," Proc. Symp. on Unconventional Inertial Sensors (Farmingdale, N.Y., 1963), pp. 36-60.

3. J. C. Crowley, S. S. Kolodkin, and A. M. Schneider, "Some properties of the gravitational field and their possible application to space navigation," IRE Trans. SET-4, 47-54 (1959).

4. M. Streicher, R. Zehr, and R. Arthur, "An Inertial Guidance Technique Usable in Free Fall," Proc. Nat. Aero. Elec. Conf. (Dayton, Ohio, 1959), pp. 768-772.

5. J. J. Carroll and P. M. Savet, "Space navigation and exploration by gravity difference detection," IAS Paper 59-61, IAS National Summer Meeting, Los Angeles, 1959; also Aerospace Eng. 18, 44-47 (1959).

6. R. E. Roberson, "Methods for the Control of Satellites and Space Vehicles, Vol. I, Sensing and Actuating Mechanisms," WADD Tech. Rpt. 60-643 (1960).

7. R. E. Roberson, "Gravity gradient determination of the vertical," ARS J. 31, 1509-1515 (1961).

8. P. Savet, "Attitude control of orbiting satellites at high eccentricity," ARS J. 32, 1577-1582 (1962).

9. J. W. Diesel, "A new approach to gravitational gradient determination of the vertical," AIAA J. 2, 1189-1196 (1964).

10. R. E. Roberson, "Establishment of the Center of Mass and Rotational State of a Space Vehicle by Inertial Techniques," Proc. XV Inter. Astro. Cong., Warsaw, 1964 (to be published).

11. R. L. Forward, "Rotating Gravitational and Inertial Sensors," to be presented at the AIAA Unmanned Spacecraft Meeting, Los Angeles, 1-4 March 1965.

12. R. L. Forward, "Measurement of Static Force Field Gradients," U. S. Patent Application 372,866, filed 5 June 1964.

13. L. R. Miller, "Magnetic Gradient Sensor," Hughes Research Laboratories Research Report RR-319 (September 1964); to be published in IEEE Trans. on Geophysical Electronics.

N66 36774

ATTACHMENT B

ROTATING GRAVITATIONAL AND INERTIAL SENSORS

The following paper was published in the Proceedings of the AIAA Unmanned Spacecraft Meeting, Los Angeles, California, 1-4 March 1965, pp. 346-351.

BLANK

PAGE

ROTATING GRAVITATIONAL AND INERTIAL SENSORS

Robert L. Forward

Member of the Technical Staff
Theoretical Studies Department
Hughes Research Laboratories, Malibu, California

Abstract

The tensor characteristics of the inertial fields created by acceleration and rotation and the gravitational fields created by masses are discussed. Although it is generally assumed that it is impossible to distinguish between gravitational and inertial effects (Einstein's Principle of Equivalence), these effects do have different, detectable tensor characteristics. The inertial field created by acceleration is a uniform vector field and has no gradients, while the inertial field created by rotation has a uniform cylindrically symmetric tensor gradient but none of higher order. The gravitational field created by a mass is highly non-uniform with essentially no limit to the number of higher order gradients. These differences make it theoretically possible to measure independently gravitation, rotation, and acceleration effects; to do so, some form of differential force sensor with tensor response characteristics must be used. The standard technique is static, using differential accelerometers to sense the spatial gradient characteristics of the fields. A more promising technique is dynamic; by rotation of the differential sensor, the static spatial variations are transformed into temporal variations with various frequency components. It is then possible to distinguish between the various fields by frequency filtering.

Introduction

In order to measure the mass of an object at a distance[1] when both the object and the sensor are in free fall, and in order to determine the attitude of an unmanned spacecraft in orbit around the earth,[2-10] it is necessary to distinguish the inertial effects of the spacecraft's acceleration and rotation from the gravitational effects of massive nearby objects. The standard method[2-8, 10] of separating the various effects involves the use of differential accelerometers to sense the spatial gradient characteristics of the various fields. By the proper combination of the various accelerometer outputs, it is theoretically possible to attain the desired separation. However, the accelerometers available to date have not had the necessary sensitivity or linearity to make such a differential sensor practical. A more promising method is a dynamic technique, which, by rotation of a rugged differential sensor,[1, 9, 11] transforms the static spatial variations of the various fields into temporal variations with various frequencies. It is then possible to distinguish between the various fields by frequency filtering.

Acceleration Inertial Field

The linear acceleration of a vehicle of mass m from an applied force F creates a uniform inertial field in the frame of reference of the vehicle which has purely vector properties and no spatial gradients (see Fig. 1):

$$a_i = \frac{1}{m} F_i . \qquad (1)$$

The accelerating force field can be detected by any force or acceleration measuring device, such as an accelerometer.

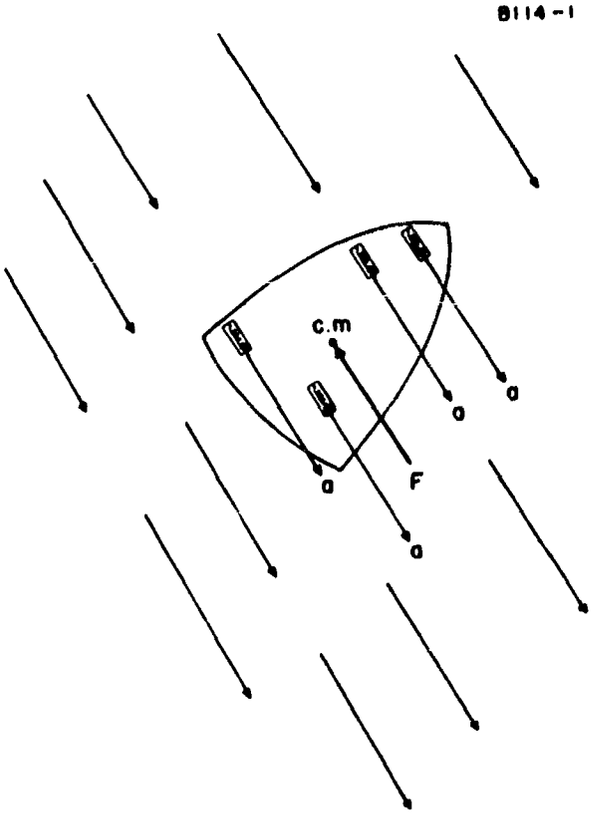

Fig. 1. The uniform inertial reaction acceleration field created by a force on a body.

Rotation Inertial Field

If the vehicle using the sensor is rotating, the rotation sets up a cylindrically symmetric inertial field (see Fig. 2).

$$a_j = \Omega^2 d_j \qquad (2)$$

where Ω is the angular velocity and d is the position vector from the axis of rotation. (For purposes of clarity, we have chosen the rotation axis

along the z axis.) This acceleration field not only has a radial gradient resulting from the change in the magnitude of the acceleration vector with a change in radius, but also a tangential gradient due to the change in direction of the acceleration vector with a change in angle.

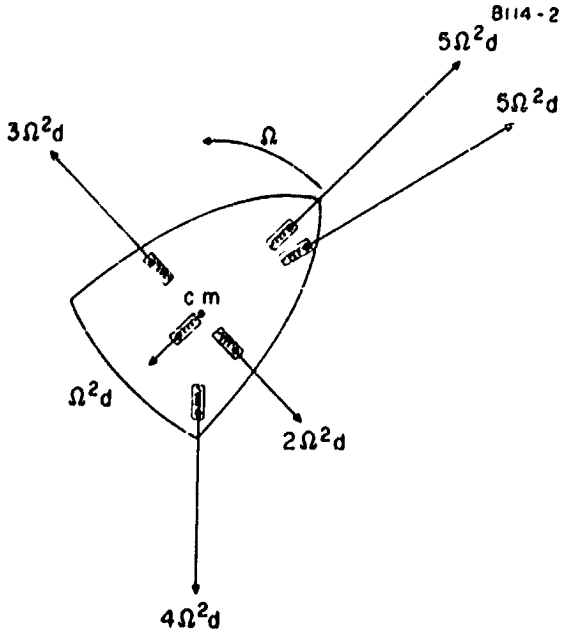

Fig. 2. The radially increasing, cylindrically symmetric, inertial reaction acceleration field created by a rotation of a body.

The resultant acceleration gradient field is a tensor field and is unusual in that it is zero in the direction of the rotation axis and has a value of Ω^2 in the directions at right angles to the rotation axis.

$$R_{ij} = \nabla_i a_j = \begin{pmatrix} \Omega^2 & 0 & 0 \\ 0 & \Omega^2 & 0 \\ 0 & 0 & 0 \end{pmatrix} . \qquad (3)$$

This gradient is constant and has no higher order gradients.

Gravitational Field

According to Newton's law of gravitation, a mass M characteristically sets up a field in the space around it which interacts with other masses. If a small test mass m is placed at a distance R from the mass M, it is found that the system has a potential energy given by

$$\phi = - \frac{GMm}{R} \qquad (4)$$

where $G = 6.67 \times 10^{-11}$ $m^3/kg\ sec^2$. Strictly speaking, the above formula applies only to a spherically symmetric mass, but the concept can be extended to more complicated distributions of mass simply by adding the contributions of each part of the distribution. The gravitational potential is not directly measurable since the point of zero reference can be changed arbitrarily.

Gravitational Force

The gradient of the potential is the gravitational force field. Since the inertial mass and the gravitational mass are the same for all bodies, the gravitational force field is equivalent to a gravitational acceleration field.

$$a_k = \frac{1}{m} F_k = - \frac{1}{m} \nabla_k \phi = - \frac{GM}{R^2} \qquad (5)$$

This accelerating force field can be detected by any force or acceleration measuring device such as an accelerometer or gravity meter, provided that the center of mass of the sensing device and the object being sensed are not in free fall (see Fig. 3).

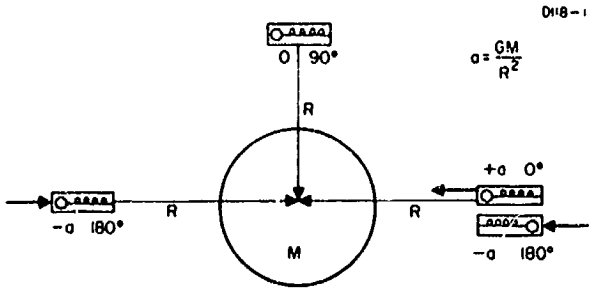

Fig. 3. Accelerometer reading as a function of relative orientation to attracting mass.

Gravitational Force Gradient

If the object being measured is in free fall with respect to the sensor, the only measurable components of the gravitational field are the gravitational force gradients which comprise a symmetric tensor.

$$\Gamma_{ij} = \nabla_i \nabla_j \frac{\phi}{m} \approx \frac{GM}{R^3} . \qquad (6)$$

The gravitational force gradient field of an object can be measured by a gradiometer. The usual gradiometer consists of two accelerometers on the ends of a rod of length ℓ. In this type, the tension, compression, or torque due to the gradient will cause the accelerometers to indicate an acceleration given by

$$a_i = \sum_{j=1}^{3} \Gamma_{ij} \ell_j \qquad (7)$$

where we have assumed that the rod is lying in the $\pm j$ direction and the accelerometers are oriented in the $\pm i$ direction (see Fig. 4).

Higher Order Gradients

Unlike the rotational inertial field which has a uniform force gradient and therefore has no higher order gradients, there is essentially no limit to the number of higher gravitational gradients that can be measured, provided the sensor is close enough and the object under investigation is massive

enough that the interaction overcomes the sensor noise. These higher order gradients are complicated tensors of high rank and sophisticated techniques and sensors may be able to obtain a great deal of information from them. Basically, they have the form,

$$T_{ab\ldots n} = \frac{1}{m} \frac{\partial^n \phi}{\partial x^a \partial x^b \ldots \partial x^n} = \frac{GM}{R^n} \qquad (8)$$

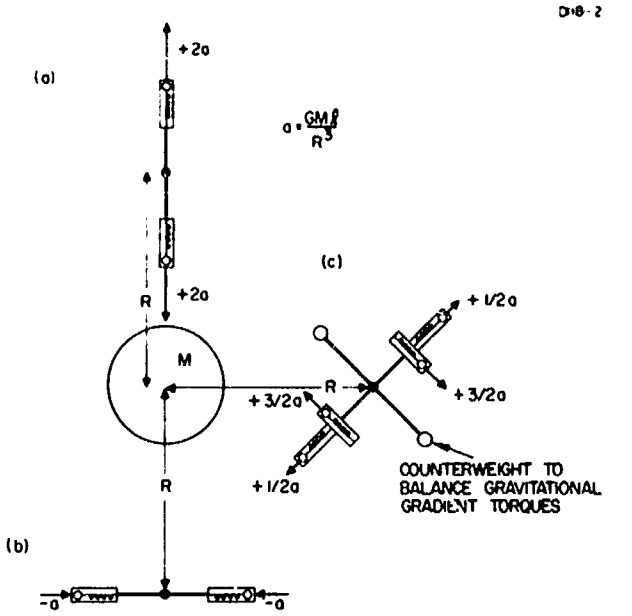

Fig. 4. Types of gravitational gradients and sensor configurations. (a) Case showing radial tension; (b) case showing tangential compression; (c) more general case showing tension and torque.

Differential Force Sensors

The published literature[1-10] has long shown that a differential force measuring device can be used to distinguish between gravitational and inertial effects. These devices are usable in free fall and can determine, without outside reference, whether they are in free fall in deep space or in orbit around a planet. If they are in orbit, they can also determine the plane of the orbit, the direction of the local vertical with respect to the planet, and, if the mass of the planet is known, the radial distance to the planet. Conversely, in deep space, they can measure the mass of an asteroid or other massive object if the distance and direction to the object are known.[1]

However, the problem has always been academic, because none of the differential accelerometers produced to date have the physical ability to measure the very weak gravitational gradient forces in the presence of the unavoidable and much larger acceleration and rotation forces. A very good accelerometer is only capable of a linearity of one part in 10^5, and the output of two accelerometers cannot be matched to even this degree of accuracy. Thus, it has not been possible to make differential accelerometers whose outputs could be added to cancel out the force terms in order to obtain the rotation and gravitational terms.

We have proposed a new type of differential accelerometer[1] which is able to separate out the effects of acceleration, rotation, or gravitational by frequency filtering techniques. Its operation is based on the rotational properties of tensors.

Rotational Properties of Tensors

A scalar is a tensor of zero rank. At any given point in space it can be expressed by a single number which is independent of the coordinate system in which it is measured.

$$A = a \qquad (9)$$

A scalar can exhibit time varying properties only by changing its magnitude with time.

A vector is a tensor of first rank. At any given point in space it can be expressed by three numbers which are its components along the axes of some coordinate system defined at that point.

$$A_i = (a_1, a_2, a_3) \ . \qquad (10)$$

A vector cannot only change its magnitude with time, but it also can change its direction by rotation. The rotation is expressed mathematically by a matrix of second rank. For example, if the vector is rotating about the z axis at the angular rate ω, the effect of the rotation $\phi = \omega t$ at any time t is given by

$$S_{ij} = \begin{pmatrix} \cos \omega t & \sin \omega t & 0 \\ -\sin \omega t & \cos \omega t & 0 \\ 0 & 0 & 1 \end{pmatrix} . \qquad (11)$$

If a vector is originally lying along the x axis of a coordinate system and either the coordinate system or the vector is rotating about the z axis, the components of the vector expressed in terms of the coordinate axes are given by

$$A_i = \sum_{j=1}^{3} S_{ij} A_j = \begin{pmatrix} a_x \cos \omega t \\ -a_x \sin \omega t \\ 0 \end{pmatrix} . \qquad (12)$$

Notice that the new representation of the vector has sinusoidally time-varying components with a frequency that is equal to the relative rotation of the vector and the coordinate system.

What is usually called a tensor is actually a tensor of second rank. At any given point in space it can be expressed by nine numbers which are dependent upon the coordinate system in which they are defined:

$$A_{ij} = \begin{pmatrix} a_{11} & a_{12} & a_{13} \\ a_{21} & a_{22} & a_{23} \\ a_{31} & a_{32} & a_{33} \end{pmatrix} . \qquad (13)$$

A tensor cannot only change its magnitude with time, but it can also change its direction by rotation.

The rotation of a tensor is handled more radically by the formula

$$A_{ab} = \sum_{i=1}^{3} \sum_{j=1}^{3} S_{ai} S_{bj} A_{ij} \qquad (14)$$

For a general tensor subjected to a rotation about the z axis, the form of the rotated tensor is a fairly complicated one. The nine components are:

$$\begin{aligned}
a'_{11} &= a_{11}\cos^2\omega t + a_{22}\sin^2\omega t + (a_{12}+a_{21})\sin\omega t\cos\omega t \\
a'_{12} &= a_{12}\cos^2\omega t - a_{21}\sin^2\omega t + (a_{22}-a_{11})\sin\omega t\cos\omega t \\
a'_{13} &= a_{13}\cos\omega t + a_{23}\sin\omega t \\
a'_{21} &= a_{21}\cos^2\omega t - a_{12}\sin^2\omega t + (a_{22}-a_{11})\sin\omega t\cos\omega t \\
a'_{22} &= a_{22}\cos^2\omega t + a_{11}\sin^2\omega t - (a_{12}+a_{21})\sin\omega t\cos\omega t \\
a'_{23} &= a_{23}\cos\omega t - a_{13}\sin\omega t \\
a'_{31} &= a_{31}\cos\omega t + a_{32}\sin\omega t \\
a'_{32} &= a_{32}\cos\omega t - a_{31}\sin\omega t \\
a'_{33} &= a_{33} \; .
\end{aligned} \qquad (15)$$

Because of the double application of the rotation matrix we now have products of $\sin\omega t$ and $\cos\omega t$ in some of the components of the rotated tensor. It is well known that these can be reduced to combinations of constant terms and terms in $\cos 2\omega t$ and $\sin 2\omega t$. Thus, in general, a rotating tensor of second rank has sinusoidally time-varying components which have a frequency twice the relative rotational frequency of the tensor and the coordinate system.

The tensors of higher rank rotate by the general rule

$$A_{ab\cdots e} = \sum_{h=1}^{3} \sum_{i=1}^{3} \cdots \sum_{n=1}^{3} S_{ah} S_{bi} \cdots S_{en} A_{hi\cdots n} \qquad (16)$$

and, in general, a tensor of n^{th} rank will have time-varying coefficients that are at n times the rotational frequency.

To give some specific physical examples, let us assume that we define a coordinate system with three orthogonal pairs of differential accelerometers. Then the force gradient due to the gravitational field of a mass M at a distance R along the x axis is given by:

$$\Gamma_{ij} = \frac{GM}{R^3}\begin{pmatrix} 2 & 0 & 0 \\ 0 & -1 & 0 \\ 0 & 0 & -1 \end{pmatrix}. \qquad (17)$$

Now, if we rotate the mass in the x-y plane around the differential accelerometer (to eliminate temporarily the problem of centrifugal forces), the resulting gradient in the reference frame of the differential accelerometer is

$$\Gamma_{kl} = \frac{GM}{R^3}\begin{pmatrix} \frac{1}{2} + \frac{3}{2}\cos 2\omega t & -\frac{3}{2}\sin 2\omega t & 0 \\ -\frac{3}{2}\sin 2\omega t & \frac{1}{2} - \frac{3}{2}\cos 2\omega t & 0 \\ 0 & 0 & -1 \end{pmatrix} \qquad (18)$$

Force gradients can thus be distinguished by their frequency behavior in a rotating reference frame. The existence of the doubled frequency in the components of a gradient makes sense physically, since a gradient can be represented by a double headed arrow; if it is turned through 180°, the new orientation is identical to the one at 0° The gradient sensors shown in Fig. 4 also have this property. If we had rotated the sensor instead of rotating the mass, the rotation would have created the inertial gradient

$$R_{ij}(z) = \begin{pmatrix} \omega^2 & 0 & 0 \\ 0 & \omega^2 & 0 \\ 0 & 0 & 0 \end{pmatrix}. \qquad (19)$$

In this gradient, $a_{11} = a_{22}$; when we substitute this back into the general expression (15) for the form of the rotated tensor, we find that there are no time-varying components to the rotated tensor. Thus, although the rotation of the sensor about the z axis creates a force gradient, the gradient is constant in the x-y plane and time varying components do not occur. This means that a differential accelerometer rotating about its z axis can distinguish gravitational gradients from rotational gradients in the x-y plane by the frequency difference between the two gradients.

However, if the differential accelerometer is slowly precessing about some other axis, e.g., at a rate Ω about the y axis, there will exist a rotational gradient given by

$$R_{ij}(y) = \begin{pmatrix} \Omega^2 & 0 & 0 \\ 0 & 0 & 0 \\ 0 & 0 & \Omega^2 \end{pmatrix}. \qquad (20)$$

This gradient does not have the degeneracy exhibited by the gradient due to rotation about the z axis in that $a_{11} \neq a_{22}$, and therefore it will have time-varying components when viewed in the rotating reference frame of the rotating sensor.

In order to separate the gravitational effects from all the rotational effects by frequency discrimination, we utilize the fact that there are no higher order gradients to the rotational force field, whereas the gravitational force field has an unlimited number of higher order gradients.

To measure these higher order gradients, complicated sensor with multiplicated lengths and differential pairs of differential accelerometers should be used. However, if a first order gradient

sensor (such as a differential accelerometer with a long length) is used these higher order gradients show up as nonlinear perturbations of the gravitational force gradient field. These perturbations have periodic variations with the orientation of the sensor that permit them to be singled out.

Rotating Nonuniform Gradient Sensor

As a simplified example of a sensor that can can be used to detect either acceleration, rotation, or gravitation by frequency selection, let us assume the configuration shown in Fig. 5. Here we have an accelerometer* at the end of a rod of length ℓ rotating around a fixed point at a distance r from the center of mass of the using vehicle. The rod ℓ is forced to move at a constant angular velocity ω. The vehicle is subject to forces F and has a residual inertial rotation Ω_z ($<<\omega$) about the z axis and a residual rotation Ω_x ($<<\omega$) about the x axis. A nearby mass M is in the x-y plane at a distance R from the center of the sensor.

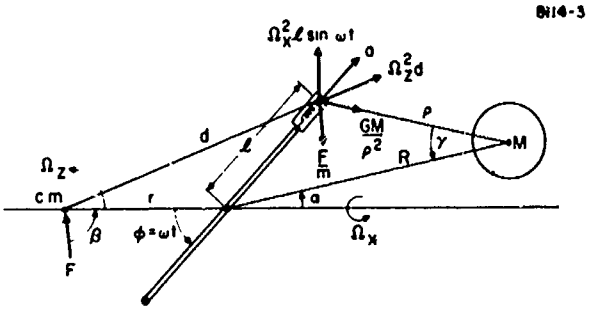

Fig. 5. Effect of gravitational and inertial fields on rotating sensor.

The accelerometer will now respond to all these effects. The inertial linear acceleration reaction of the mass in the accelerometer will be directed opposite to the force F and will have the amplitude $a = F/m$, where m is the mass of the using vehicle. The inertial rotation reaction of the mass in the accelerometer will have three components: one with amplitude $\omega^2 \ell$ directed radially outward from the axis of rotation of the sensor, one with amplitude $\Omega_z^2 d = \Omega_z^2 (r^2 + \ell^2 + 2r\ell \cos \omega t)^{1/2}$ radially outward from the z axis through the center of mass of the vehicle, and one of amplitude $\Omega_x^2 \ell \sin \omega t$ directed outward from the x axis. The gravitation reaction of the mass in the accelerometer will have the amplitude GM/ρ^2 and will be in the direction of the gravitating mass. However, the accelerometer responds only to the components which are along its sensitive axis, and this sensitive axis is rotating due to the rotation of the rod. Thus the rotation of an accelerometer on the end of the rod not only changes the amplitude of the various forces by changing the effective length of the sensor with time, but the rotation also changes the directional response of the sensor to these time-varying amplitudes.

Because of all these forces the acceleration read by the accelerometer at the end of the rod will vary with the angle of rotation in a complicated manner.

$$a = \frac{F}{m} \cos(\omega t + \beta) + \Omega_z^2 d \cos \omega t + \omega^2 \ell + \frac{GM}{\rho^2} \cos(\omega t + \gamma - \alpha) + \Omega_x^2 \ell \sin^2 \omega t \,. \tag{21}$$

The primary effect results from the directional sensitivity of the accelerometer to the various accelerations, but the effects that interest us arise from the change in the gravitational force with angle, distance, and time. If we simplify the inertial terms and keep all the components, and expand the gravitational term, but keep only the highest order terms of each frequency component, we obtain

$$\begin{aligned} a = {} & \omega^2 \ell + \frac{1}{2} \Omega_x^2 \ell + \Omega_z^2 \ell + \frac{GM}{R^2} \left[\frac{1}{2} \frac{\ell}{R} \right] \\ & - \frac{F}{m} \cos(\omega t + \beta) - \Omega_z^2 r \cos \omega t + \frac{GM}{R^2} [\cos(\omega t - \alpha)] \\ & - \frac{1}{2} \Omega_x^2 \ell \cos 2\omega t + \frac{GM}{R^2} \left[\frac{3}{2} \frac{\ell}{R} \cos 2(\omega t - \alpha) \right] \\ & + \frac{GM}{R^2} \left[\frac{15}{8} \left(\frac{\ell}{R} \right)^2 \cos 3(\omega t - \alpha) \right] \\ & + \frac{GM}{R^2} \left[\frac{35}{16} \left(\frac{\ell}{R} \right)^3 \cos 4(\omega t - \alpha) \right] \end{aligned} \tag{22}$$

(In free fall, the odd harmonics of the gravitational interaction will drop out.)

Now, if we design the accelerometer at the end of the rotating rod so that it is not highly damped, but instead is tuned to some harmonic of the rotational frequency, the sensor will respond preferentially to one of the frequency components of (22).

If the accelerometer were tuned to 3ω, it would see only the gravitational term even in the presence of the usually much larger rotational and acceleration terms. If it were tuned to 2ω, it would see the terms due to the rotations at right angles to the z axis (assuming that the gravitational gradient is weaker). Other sensors rotating about the other axes would enable all of the rotational components to be measured without the interference of the usually much larger force term. If it were tuned to ω, it would see the term due to the forces on the using vehicle (assuming that the rotational and gravitational effects are weaker). Again, other sensors rotating about other axes would enable all the components of the force vector to be determined.

Summary

By using rotating force sensors, it is possible to sense the difference in the tensor characteristics of gravitational and inertial fields by

*An accelerometer is being used in this example for clarity of the analysis. A real accelerometer would be saturated by the rotation necessary to accomplish the desired frequency separation. More practical rotating sensors are described in Refs. 1, 9, and 11.

frequency filtering. The application of this basic principle to instrument design should lead to the development of rugged, sensitive devices for use on unmanned spacecraft for attitude control, on lunar orbiters to measure the mass distribution of the moon, and on deep space probes to measure the mass of the asteroids.

References

1. R. L. Forward, "Gravitational Mass Sensor," Proc. Symp. on Unconventional Inertial Sensors (Farmingdale, N. Y., 1963), pp. 36-60.

2. R. E. Roberson, "Gravitational torque on a satellite vehicle " J. Franklin Inst. 265, 13-22 (1958).

3. J. C. Crowley, S. S. Kolodkin, and A. M. Schneider, "Some properties of the gravitational field and their possible application to space navigation," IRE Trans. SET-4, 47-54 (1959).

4. M. Streicher, R. Zehr, and R. Arthur, "An Inertial Guidance Technique Usable in Free Fall," Proc. Nat. Aero. Elec. Conf. (Dayton, Ohio, 1959), pp. 768-772.

5. J. J. Carroll and P. M. Savet, "Space navigation and exploration by gravity difference detection," IAS Paper 59-61, IAS National Summer Meeting, Los Angeles, 1959; also Aerospace Eng. 18, 44-47 (1959).

6. R. E. Roberson, "Methods for the Control of Satellites and Space Vehicles, Vol. I, Sensing and Actuating Mechanisms," WADD Tech. Rpt. 60-643 (1960).

7. R. E. Roberson, "Gravity gradient determination of the vertical," ARS J. 31, 1509-1515 (1961).

8. P. Savet, "Attitude control of orbiting satellites at high eccentricity," ARS J. 32, 1577-1582 (1962).

9. J. W. Diesel, "A new approach to gravitational gradient determination of the vertical," AIAA J. 2, 1189-1196 (1964).

10. R. E. Roberson, "Establishment of the Center of Mass and Rotational State of a Space Vehicle by Inertial Techniques," Proc. XV Inter. Astro. Cong., Warsaw, 1964 (to be published).

11. R. L. Forward, "Rotating Tensor Sensors," Bull. Am. Phys. Soc. 9, 711 (1964).

BLANK PAGE

N66 36775

ATTACHMENT C

MASS DETECTION BY MEANS OF MEASURING GRAVITY GRADIENTS

The following paper was presented at the AIAA Second Annual Meeting, San Fracisco, California, 26-29 July 1965. It is available as AIAA Paper No. 65-403.

BLANK
PAGE

MASS DETECTION BY MEANS OF MEASURING GRAVITY GRADIENTS*

by

Curtis C. Bell
Robert L. Forward
J. Roger Morris

Members of the Technical Staff
Theoretical Studies Department
Hughes Research Laboratories
Malibu, California

Introduction

Up to the present time, the methods for measuring the local gravitational fields of the earth have been limited to readings obtained by precise gravity meters placed at various locations on the earth's surface. The disadvantages of this method are obvious: the necessity for frequent equipment calibration, long test setup time and inaccessibility of certain localities for measurement.

It would be desirable to take such measurements from rapidly moving vehicles, such as aircraft or spacecraft, but the unavoidable vehicle motions create accelerations and rotations which tend to mask the desired gravitational interaction. The present method of measurement is also quite useless if measurements of the gravitational field of bodies in outer space (moon, asteroids, etc.) are desired, because the gravity meter and the measured body would be in free fall with respect to each other and the gravitational force is exactly counterbalanced by the inertial reactions of the spacecraft. It is therefore desirable to find ways to distinguish the inertial effects of acceleration and rotation of the vehicle from the gravitational effects from massive nearby objects.

The characteristics of the above differ primarily in their gradient fields. The inertial field created by acceleration is a uniform vector field and has no gradients, while the inertial field created by rotation has a uniform, cylindrically symmetric tensor gradient, but none of higher order. The gravitational field created by a mass is highly nonuniform with essentially no limit to the number of higher order gradients. These differences make it theoretically possible to measure independently gravitation, rotation

*Work supported by NASA Contract NASw-1035

and acceleration effects; to do so, some form of differential force sensor with tensor response characteristics must be used.

It has been known[1-11*] that such sensors could be constructed by using spaced pairs of low level accelerometers with opposed outputs. However, a very good accelerometer is only capable of a linearity of one part in 10^5, and the outputs of two accelerometers cannot be matched to even this degree of accuracy. Thus, it has not been possible to make differential force sensors whose outputs could be combined to cancel out the acceleration terms in order to obtain the rotation and gravitation terms.

The problem therefore lies in measuring the gradients and differentiating between them. This problem can be solved if we consider the tensor characteristics of these forces and gradients. Forces are vectors (tensors of first rank), the gradients of forces are tensors of second rank, and higher order gradients are higher rank tensors. Our basic concept is that when the components of a tensor of n^{th} rank are examined in the reference frame of a sensor which is rotating at a constant angular frequency ω, they will be found to have time-varying coefficients at n times the rotational frequency of the sensor ($n\omega$).[1]

This implies that if a sensor is made in the form of a rotating multipole spring-mass system with a resonant frequency at one of the higher values of the $n\omega$ gravity tensor components, it will be insensitive to all force fields except those caused by gravitational attraction between the sensor and another mass.[1,2,9,11] In addition, if the signal from such a sensor is filtered and amplified, a reading may be obtained which is directly proportional to the gravitational gradient of the mass to be measured. If this proportionality constant and the distance from the sensor to the object are known, the mass of the object may be easily computed.[2]

Two similar classes of sensors operating on the above basic principle which use radially vibrating structures have been analyzed as to their response (Figs. 1 and 2). Analysis has shown that if the spring constants of either of these two systems are adjusted to resonate at twice the rotation frequency, the extension of the spring becomes infinite,[2] because of the centrifugal forces acting on the outer masses.

A more promising type of sensor, therefore, is one which the restoring spring forces are perpendicular to the centrifugal forces acting on the outer masses. A sensor of this type is shown in Fig. 3. The arms of this sensor are constrained to vibrate in the

*Superscript numbers refer to the list of numbered references which appears at the end of this paper.

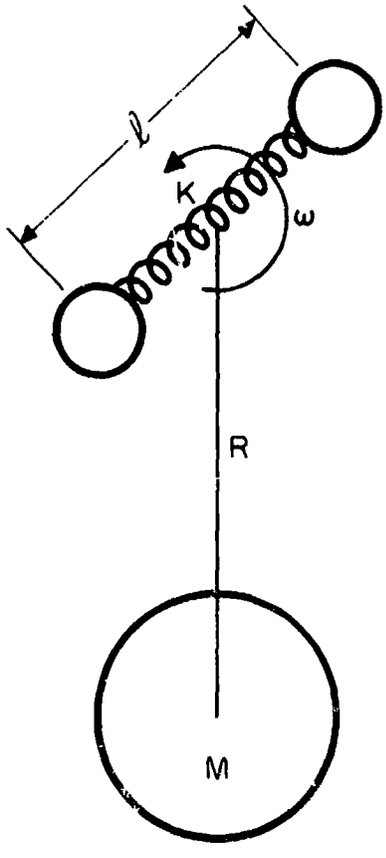

Fig. 1.

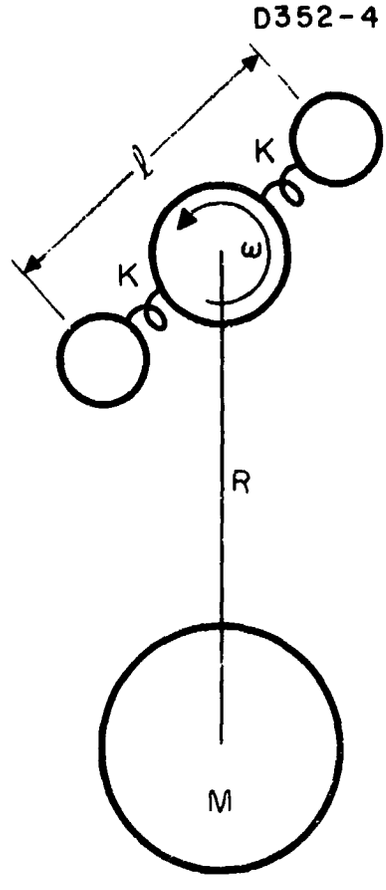

Fig. 2.

Radially vibrating mass sensors.

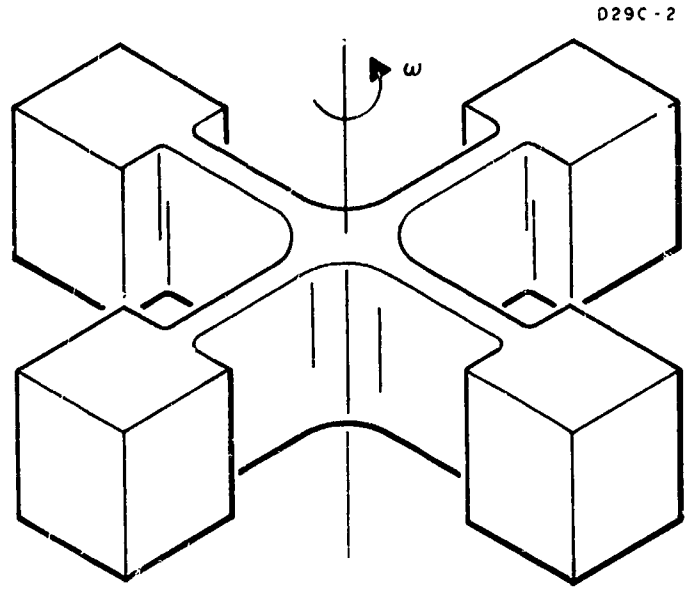

Fig. 3. Cruciform mass sensor.

plane of rotation and in a tangential direction. The arm stiffness in the radial direction may therefore be adjusted well above the critical point.

We analyze, below, the operation of this type of sensor, and show that it responds to the gravitational force gradient but does not respond to vibrations and accelerations.

In the general case, the forces acting upon and within the sensor are as follows:

1. Gravitational forces F_g, which are between the sensor and the sensed mass, are applied to all the masses in the sensor

2. Centrifugal forces F_c, which are caused by the rotation of the sensor, act on the outer sensor masses

3. Vibrational forces F_v, which are passed through or generated by the rotational drive mechanism, are applied to the central hub of the sensor

4. Beam forces F_b, which result from the elastic properties of the arms, cause coupling between the central hub and the outer masses

5. Tuning fork spring forces F_k, which are the result of the elastic properties of the radius from one arm to an adjoining arm, cause coupling between the outer masses.

Gravitational Force Input

If the sensor is rotating in the vicinity of a large mass as shown in Fig. 4, there will be gravitational forces between each mass of the sensor and the large mass, which has a magnitude

$$F_{gi} = \frac{G M_i M_5}{R_i^2} \tag{1}$$

where

F_{gi} ≡ total gravitational force for each sensor mass; i = (1, 2, 3, 4, and 6)

M_i ≡ mass of each sensor portion evaluated

M_5 ≡ sensed mass

R_i ≡ distance between M_5 and M_i

G ≡ universal gravitational constant = $6.670 \times 10^{-8} (cm^2/gm^2)$ dyne.

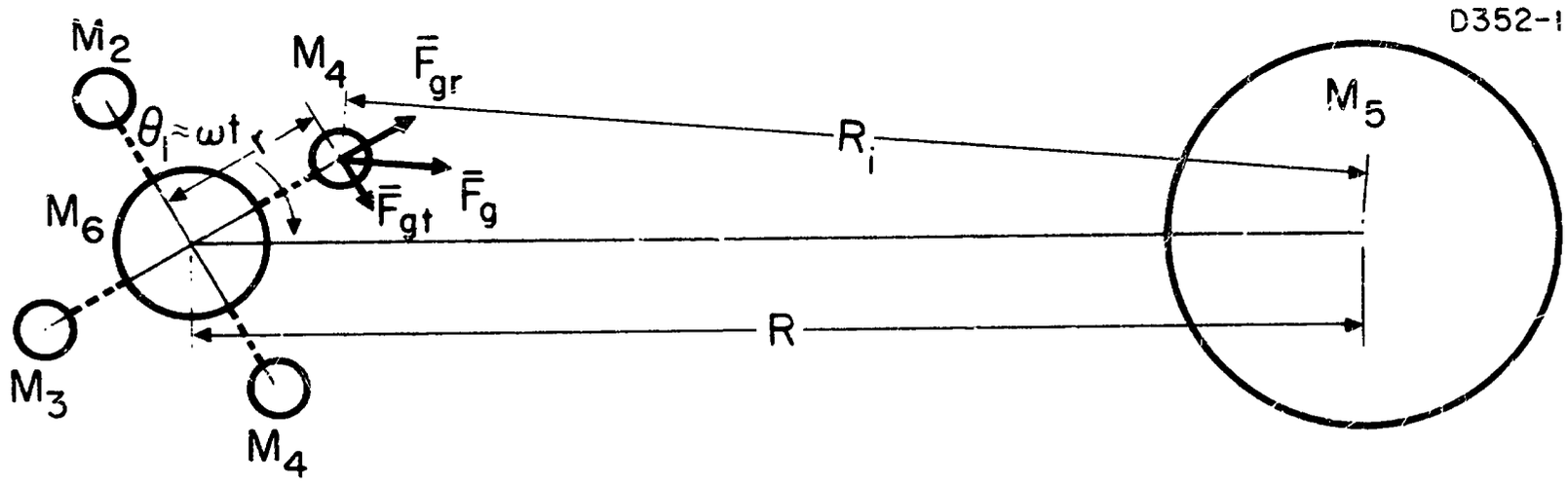

Fig. 4. Operating mass sensor.

The portion of this force which acts upon the cantilever spring is the tangential portion which is evaluated for mass[1] as follows:

$$F_{gt1} = - \frac{F_1 R \sin \theta_1}{R_1} \tag{2}$$

or

$$F_{gt1} = - \frac{G M_1 M_5 R \sin \theta_1}{R_1^3} \tag{3}$$

Since any variation of the rotation speed from ω due to gravitational forces will appear as a G^2 perturbation on the force, θ_1 can be approximated by ωt. ($\omega \equiv$ rotational angular velocity.) Therefore,

$$F_{gt1} \approx - \frac{G M_1 M_5 R \sin \omega t}{R_1^3} \tag{4}$$

where

$$\left(\frac{1}{R_1}\right)^3 = \frac{1}{(R^2 + r^2 - 2Rr \cos \omega t)^{3/2}} \tag{5}$$

If (5) is now expanded binomially, the higher power sine and cosine terms are replaced by their corresponding multiple angle identities, all terms of like frequency are collected, and only the terms with the lowest power of r/R are kept in each frequency, eq. (4) becomes

$$F_{gt1} = - \frac{G M_1 M_5}{R^2} \left[\sin \omega t + \frac{3}{2}\left(\frac{r}{R}\right) \sin 2\omega t + \frac{15}{8}\left(\frac{r}{R}\right)^2 \sin 3\omega t + \frac{35}{16}\left(\frac{r}{R}\right)^3 \sin 4\omega t \right]. \tag{6}$$

In a similar manner, the tangential forces on each of the other three arms can be evaluated by comparing their phase relationships with those of the forces on arm 1 ($\theta_2 \approx \omega t + \pi/2$, etc.), so that

$$F_{gt2} = -\frac{G M_2 M_5}{R^2}\left[\cos \omega t - \frac{3}{2}\left(\frac{r}{R}\right)\sin 2\omega t - \frac{15}{8}\left(\frac{r}{R}\right)^2 \cos 3\omega t + \frac{35}{16}\left(\frac{r}{R}\right)^3 \sin 4\omega t\right] \quad (7)$$

$$F_{gt3} = -\frac{G M_3 M_5}{R^2}\left[-\sin \omega t + \frac{3}{2}\left(\frac{r}{R}\right)\sin 2\omega t - \frac{15}{8}\left(\frac{r}{R}\right)^2 \sin 3\omega t + \frac{35}{16}\left(\frac{r}{R}\right)^3 \sin 4\omega t\right] \quad (8)$$

and

$$F_{gt4} = -\frac{G M_4 M_5}{R^2}\left[-\cos \omega t - \frac{3}{2}\left(\frac{r}{R}\right)\sin 2\omega t + \frac{15}{8}\left(\frac{r}{R}\right)^2 \cos 3\omega t + \frac{35}{16}\left(\frac{r}{R}\right)^3 \sin 4\omega t\right] \quad (9)$$

Centrifugal Force Input

The centrifugal force generated by rotation of the outer masses has a value

$$F_c = M_i r\omega^2 \quad (10)$$

and a direction outward from the center of rotation.

If the arm is allowed to vibrate, a portion of this force will be resolved into a component perpendicular to the arm at the outer mass, as shown in Fig. 5. In this figure, ϕ_1 is the angle through which M_1 has rotated from a reference which rotates with the sensor at ω, and ϕ_6 is the angular displacement of M_6 from its similar rotating reference.

The tangential component of the centrifugal force is given by

$$F_{ct1} = -F_c \sin(\phi_1 - \phi_6) \quad , \quad (11)$$

but since ϕ_1 and ϕ_6 are small angles, this reduces to

$$F_{ct1} \approx F_c(\phi_1 - \phi_6) = -M_i r\omega^2(\phi_6 - \phi_1) \quad . \quad (12)$$

The centrifugal force is therefore seen to act as an effective restoring force in addition to the spring restoring force of the arms. This effect was observed in our first experimental model (see Fig. 6) in which the resonant vibrational frequency of 190 cps shifted to 200 cps when the sensor was rotated at 6000 rpm.

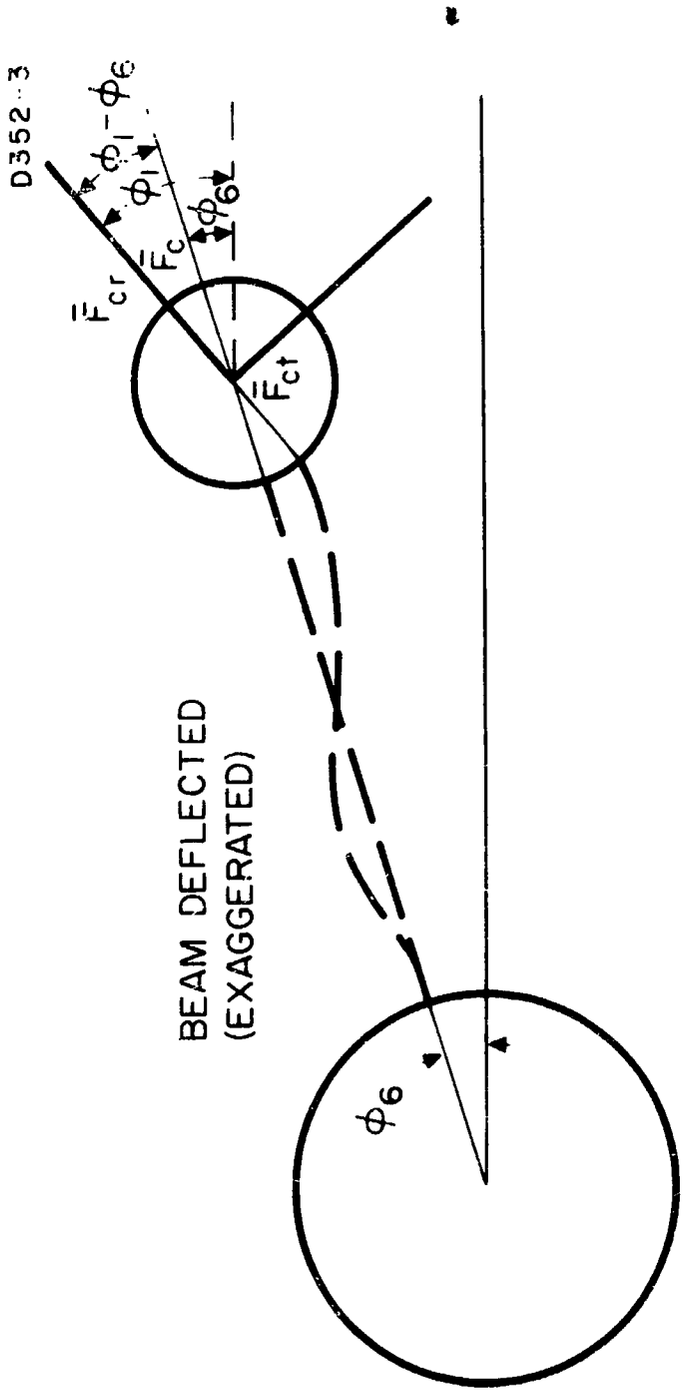

Fig. 5. Centrifugal force resolution.

M 3615

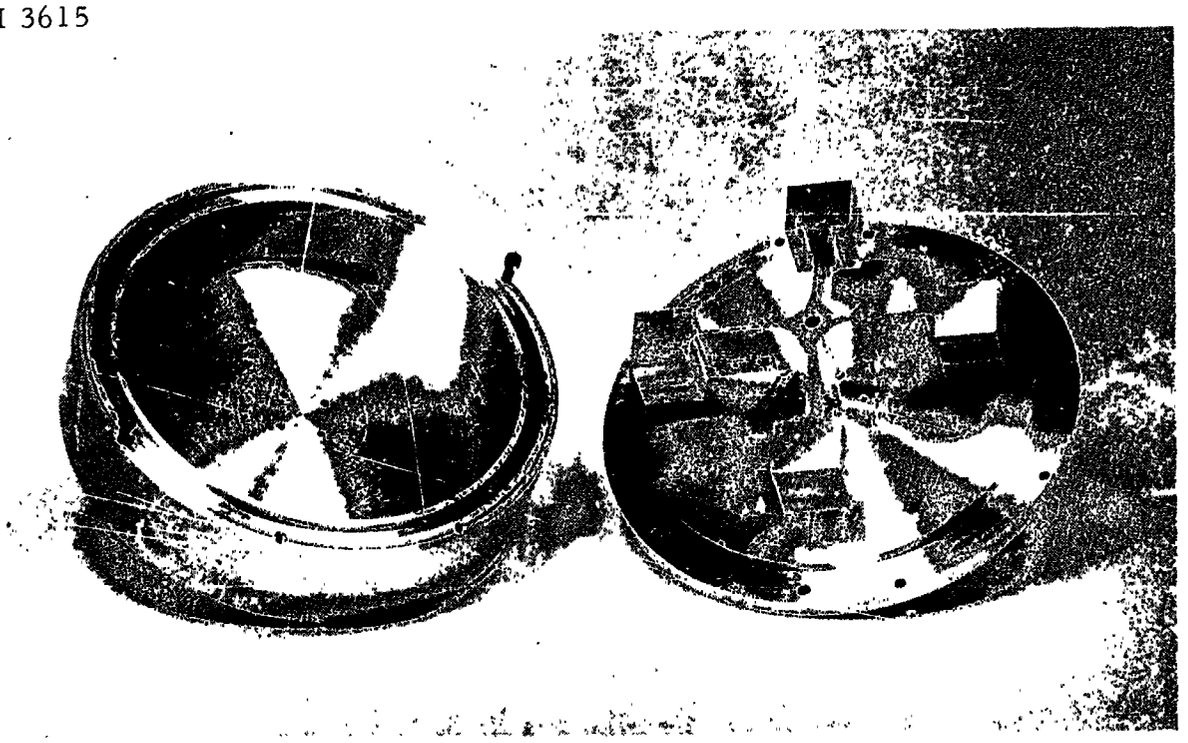

Fig. 6. Cruciform gravitational mass sensor.

Vibration Input

In addition to the support forces which act on the sensor through the hub and which occur primarily at low frequencies and will not affect the vibrational modes of the sensor, there will be other, higher frequency, forces and torques from various sources either outside the sensor or in the rotational mechanism. These forces can be represented by sinusoids of various frequencies, amplitudes, and directions

$$F_v(x) = (A_j \sin \omega_j t + B_j \cos \omega_j t)\hat{e}_x \tag{13}$$

$$F_v(y) = (C_j \sin \omega_j t + D_j \cos \omega_j t)\hat{e}_y \tag{14}$$

where $F_v(x)$ and $F_v(y)$ are the vibratory forces and $\hat{e}_x$ and $\hat{e}_y$ are the unit vectors in the x and y directions, respectively.

For any time t, the forces being seen by the sensor in its frame of reference (which is rotating at ω) are given by

$$F_v(1) = F_v(x) \cos \omega t + F_v(y) \sin \omega t \tag{15}$$

$$F_v(2) = F_v(y) \cos \omega t - F_v(x) \sin \omega t \tag{16}$$

where $F_v(1)$ and $F_v(2)$ are the forces in the direction of arm 1 and arm 2, respectively. These forces, along with the torques applied by the outer sensor masses through the arms, will act as driving functions for the equations of motion of the central hub. (See Fig. 7.)

$$(M_6 + M_1 + M_3)\ddot{x}_6 = V_{A2} - V_{A4} + F_v(1) + \text{damping forces} \tag{17}$$

$$(M_6 + M_2 + M_4)\ddot{y}_6 = V_{A3} - V_{A1} + F_v(2) + \text{damping forces} \tag{18}$$

$$J_6 \ddot{\phi}_6 = \sum_{i=1}^{4} M_{Ai} - \sum_{i=1}^{4} V_{Ai} \tag{19}$$

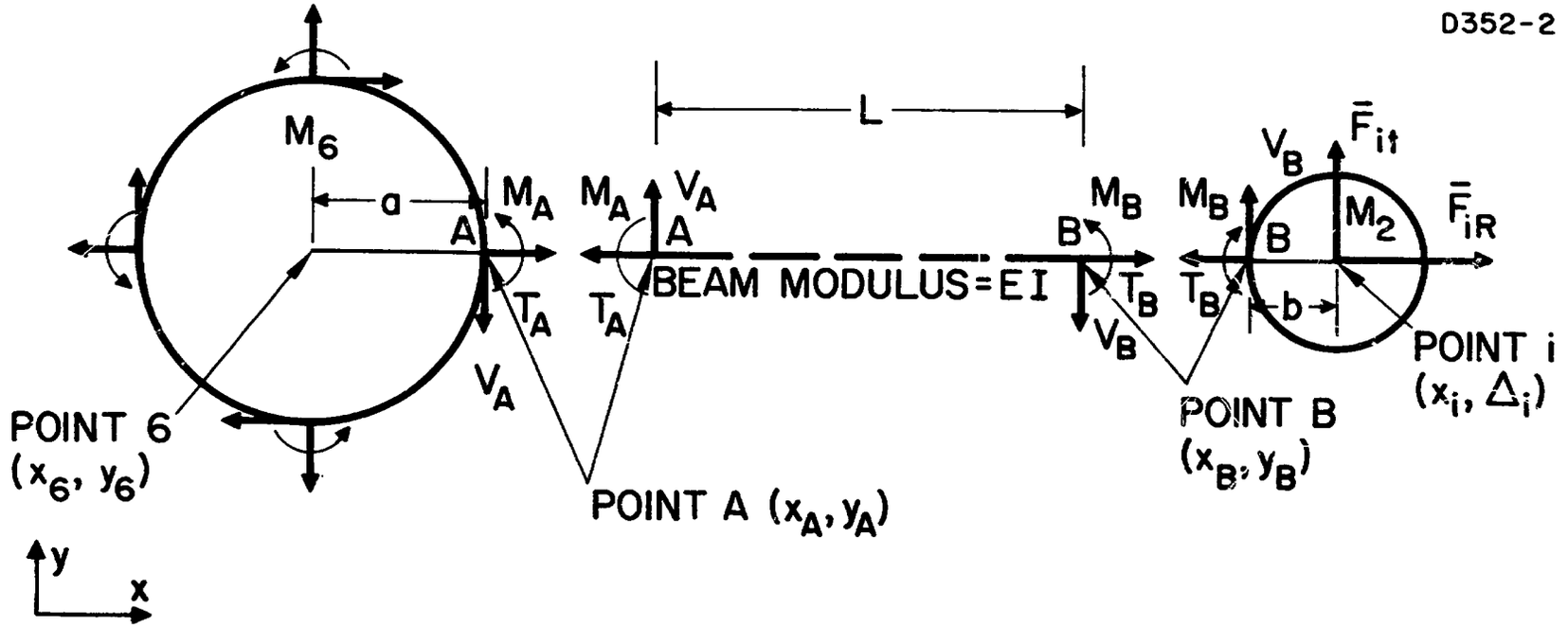

Fig. 7. Sensor free body diagram.

where

V_{Ai} ≡ shear force in arm i at point A

M_{Ai} ≡ moment (bending) force in arm i at point A

J_6 ≡ polar moment of inertia about center of mass of M_6.

In general, these equations are to be solved simultaneously for x_6, y_6, and ϕ_6, along with the equations of motion of the outer masses, (38) through (41), since the general behavior of the outer masses depends upon the motion of the central mass and the motion of the central mass depends in turn on the motion of the outer masses through V_A and M_A. However, we will proceed to show that there exists a mode of vibration of the outer masses which is independent of the motion of the central mass and yet responds to the gravitational force gradient. Since the vibrational noise F_v enters the sensor only through the motions of the central mass (eqs. (17) and (18)), this vibrational mode can be used to sense the gravitational field of a mass even when the sensor is undergoing high frequency inertial accelerations.

Sensor Response

The response of the sensor may be evaluated by considering the free body diagrams shown in Figs. 5 and 6.

Newton's laws applied to mass 1 give rise to the equations of motion:

$$M_1 \ddot{\Delta}_1 = V_B + F_{gt1} - F_{ct1} \tag{20}$$

$$J_1 \ddot{\phi}_1 = -V_B b - M_B \tag{21}$$

where

Δ_1 ≡ deflection of arm 1 in tangential CCW direction

V_B ≡ shear force in arm at point B

J_1 ≡ polar moment of inertia about CM of mass 1

b ≡ radius of mass 1

M_B ≡ moment (bending) forces in arm 1 at point B.

To simplify the solution, it will be assumed that the inertial rotation force on mass 1 is much less than the moments due to the arm $\left|J_1 \ddot{\phi}_1\right| \ll \left|M_B\right|$, so that

$$M_B = -V_B b \tag{22}$$

Past analysis has shown that this condition actually exists physically in any geometry which might be considered.

The beam reactions at Point A can be determined from statics.

$$V_A = V_B \tag{23}$$

$$T_A = T_B \tag{24}$$

$$M_A = M_B - V_B L \tag{25}$$

where T is the tension in the bar. The value of the bending moment at any point x in the beam (where x = 0 at point A) is

$$M(x) = M_A + V_B x = V_B x - V_B(L + b) \quad . \tag{26}$$

The slope of the beam is obtained by integration

$$\theta = \frac{1}{EI} \int M(x)dx + \theta_A \tag{27}$$

where E is Young's modulus and I is the moment of inertia of the cross-sectional area of the arm. Therefore,

$$\theta(x) = \frac{V_B}{EI} \left[\frac{x^2}{2} - (L + b)x \right] + \phi_6 \quad , \tag{28}$$

and at point B we have the boundary condition that

$$\phi(B) = \phi_1 = -\frac{V_B}{EI}\left(\frac{L^2}{2} - bL\right) + \phi_6 \tag{29}$$

so that

$$\phi = -\frac{V_B}{EI}\left(\frac{L^2}{2} - bL\right) \tag{30}$$

The deflection of the beam is obtained through a second integration

$$y = \int \phi(x)\, dx \tag{31}$$

therefore,

$$y(x) = \frac{V_B}{EI}\left[\frac{x^3}{6} - (L + b)\frac{x^2}{2}\right] + \phi_6 x + y(A) \tag{32}$$

and at $x = L$

$$y(L) = -\frac{V_B}{EI}\left(\frac{L^3}{3} + \frac{bL^2}{2}\right) + \phi_6(L + a) + y_6 \tag{33}$$

where

$y_6 \equiv$ y coordinate of the center of mass of M_6

$a \equiv$ radius of M_6.

However, the location of the center of mass of M_1 is given by

$$A_1 = y(L) + \phi_1 b \tag{34}$$

and, by substituting in eq. (33), we obtain

$$\Delta_1 = - \frac{V_B}{EI} \left[\frac{L^3}{3} + bL^2 + b^2 L \right] + (b + L + a)\phi_6 + y_6 \tag{35}$$

or

$$V_B = - \frac{EI}{L^3} \left[\frac{1}{3} + \frac{b}{L} + \frac{b^2}{L^2} \right]^{-1} (\Delta_1 - y_6 - \phi_6 r) \tag{36}$$

where r is as shown in Fig. 4. This may now be incorporated into the equation of motion along with the equations for the centrifugal force and gravity force terms. This results in

$$M_1 \ddot{\Delta}_1 + (1 + C)(B) \frac{EI}{L^3} (\Delta_1 - y_6 - \phi_6 r) + D(\dot{\Delta}_1 - \dot{y}_6 - \dot{\phi}_6 r) = F_{gt1} \tag{37}$$

where

$C \equiv$ centrifugal force factor $= M_1 r \omega^2 / EI[L^2/2 + bL]$

$B \equiv$ geometry fact $[1/3 + b/L + (b/L)^2]^{-1}$

$D \equiv$ damping coefficient of arm

$F_{gt1} \equiv$ tangential gravitational force on mass 1 as given in eq. (6).

The motion of each arm is coupled to the motion of the two adjoining arms by tension and compression stresses which are transmitted through the radii connecting the adjoining arms. This coupling effect will modify eq. (37) for M_1 as follows:

$$M_1 \ddot{\Delta}_1 + D[\dot{\Delta}_1 - \dot{y}_6 - \dot{\phi}_6 r - J(\dot{\Delta}_2 + \dot{\Delta}_4)]$$

$$+ (1 + C)(B) \frac{EI}{L^3} [\Delta_1 - y_6 - \phi_6 r - J(\Delta_2 + \Delta_4)] = F_{gt1} \tag{38}$$

where

$J \equiv$ positive coupling coefficient.

Similarly,

$$M_2 \ddot{\Delta}_2 + D[\dot{\Delta}_2 + \dot{x}_6 - \dot{\phi}_6 r - J(\dot{\Delta}_3 + \dot{\Delta}_1)]$$

$$+ (1 + C)(B) \frac{EI}{L^3} [\Delta_2 + x_6 - \phi_6 r - J(\Delta_3 + \Delta_1)] = F_{gt2} \tag{39}$$

$$M_3 \ddot{\Delta}_3 + D[\dot{\Delta}_3 + \dot{y}_6 - \dot{\phi}_6 r - J(\dot{\Delta}_2 + \dot{\Delta}_4)]$$

$$+ (1 + C)(B) \frac{EI}{L^3} [\Delta_3 + y_6 - \phi_6 r - J(\Delta_2 + \Delta_4)] = F_{gt3} \tag{40}$$

and

$$M_4 \ddot{\Delta}_4 + D[\dot{\Delta}_4 - \dot{x}_6 - \dot{\phi}_6 r - J(\dot{\Delta}_3 + \dot{\Delta}_1)]$$

$$+ (1 + C)(B) \frac{EI}{L^3} [\Delta_4 - x_6 - \phi_6 r - J(\Delta_3 + \Delta_1)] = F_{gt4} \tag{41}$$

Equations (38) through (41) describe the individual motions of the four arms. However, the mode of vibration which interests us is the dual tuning fork mode. The equation for this mode is obtained by taking these four equations and adding and subtracting them as follows: eq. (38) - (39) + (40) - (41), to obtain the relation

$$\ddot{\Delta} + \frac{D}{M} (1 + 2J)\dot{\Delta} + \frac{k}{M} \Delta = - \frac{3G M_5 r}{2R^3} \sin 2\omega t \tag{42}$$

where $\Delta = 1/4(\Delta_1 - \Delta_2 + \Delta_3 - \Delta_4)$ is defined as the amplitude of the mode vibration, $k = B(1 + C)(EI/L^3)(1 + 2J)$ is the effective spring constant, and we have assumed that $M_1 = M_2 = M_3 = M_4 = M$.

Note that the equation for this mode of vibration is driven only by the gravitational gradient forces at 2ω; all of the other gravitational forces have been cancelled out. More important is the fact that the equation is also found to be independent of x_6, y_6, or ϕ_6; it therefore is independent of external inertial or vibrational forces or torques on the sensor which must necessarily act through motions of the central hub.

The above equation (42), however, assumes that the masses and the lengths of the arms are identical and that the sensor and the sensor readout devices are completely symmetric. If the sensor is not symmetric, a small portion of the vibrational forces which are allowed to reach the sensor hub will leak into the sensing mode. In practice, of course, one cannot attain exact balance or prevent some vibrations from reaching the sensor hub. The amount and type of vibrations which do penetrate to a great extent will depend on the exact type of support bearing, rotational drive mechanism, and vibrational isolation mechanisms used.

Our experimental work is primarily directed toward an empirical determination of the noise characteristics of bearings and drives, the effectiveness of vibration isolation mechanisms, and the degree of attainability of sensor symmetry in order to find a configuration which will effectively isolate the sensor vibrational mode from all ac forces except those due to the gravitational force gradient. The detailed results of this work should be available next year.

If such isolation can be achieved, then (42) allows us to calculate the sensitivity of the sensor to the gravitational gradient. The value of the sensor amplitude Δ at resonance is given by

$$\Delta = \frac{3}{2} \frac{GM_5}{R^3} \, r \, \frac{Q}{(2\omega)^2} \cos 2\omega t \tag{43}$$

where

$$Q = 2\omega M/D(1 + 2J)$$

$$2\omega = (k/M)^{1/2}$$

and GM_5/R^3 is the gravitational gradient of the mass M_5 at the distance R from the sensor.

Output Calculation

We will now use eq. (43) to calculate the output to be expected from the sensor currently in use on the experimental program (see Fig. 6). These aluminum cruciform sensors are about 4.5 in. in over-all size, the arms are about 1.5 in. long, 0.75 in. wide and 0.050 in. thick with a 0.75 in. cube at the end for extra mass. The sensors have a resonance at about 170 cps with a Q of about 170 and are rotated at 6000 rpm ($\omega = 170\,\pi$ rad/sec).

If this sensor is operated in the gravitational gradient of the earth, then $3GM_E/2R^3 = 2.3 \times 10^{-6}$ sec^{-2} and the amplitude of the sensor mode given by (43) is found to be $\Delta = 5.8 \times 10^{-10}$ in. The readout of the sensor vibrations in our apparatus is accomplished by sensing the dynamic strains in the sensor arms with piezoelectric barium titanate strain transducers which have a "gauge factor" of 10^5 V per unit strain. The dynamic strain ϵ in the arms corresponding to the mode vibration amplitude Δ is given by the relation

$$\epsilon = \frac{\sigma}{E} = \frac{M_A c}{EI} = 0.06\,\mu\Delta = 3.6 \times 10^{-11}\ \frac{\text{in.}}{\text{in.}} \qquad (44)$$

where

$\sigma \equiv$ stress in the arm

$c \equiv$ arm half thickness.

Other sensor designs which will increase the dynamic strain to vibrational amplitude ratio by varying the length to thickness ratio of the arms are being considered.

The voltage output from the strain transducers corresponding to this level of strain is approximately 4 μV. Since this is a narrow-band signal at 170 cps, it is easily measured with a low noise tuned amplifier such as the General Radio Tuned Amplifier 1232A, which has an equivalent input noise voltage of 50 nV.

Conclusions

An ideal cruciform-shaped system of masses and springs using piezoelectric strain transducers for readout (see Fig. 6) has the basic ability to measure the gravitational force gradient of a massive object and yet is insensitive to inertial vibrations induced through the support and drive mechanism.

Our experimental program to develop a practical device capable of realizing this ideal performance has demonstrated the basic structural integrity of the sensor under rotation. This program now is concerned primarily with the investigation of the noise characteristics of a number of bearings, supports, and drives and the construction of various sensor designs. These designs will be tested to determine whether it is possible to find a structure combining these components which will sufficiently isolate the sensing vibrational mode of the device from external inertial vibration noise so that the signal induced by the gravitational force gradient field can be seen.

REFERENCES

1. R.L. Forward, "Rotating tensor sensors," Bull. Am. Phys. Soc. 9, 711 (1964)

2. R.L. Forward, "Gravitational Mass Sensor," Proc. Symp. on Unconventional Inertial Sensors (Farmingdale, N.Y., 1963), pp. 36-60.

3. J.C. Crowley, S.S. Kolodkin, and A.M. Schneider, "Some properties of the gravitational field and their possible application to space navigation," IRE Trans. SET-4, 47-54 (1959).

4. M. Streicher, R. Zehr, and R. Arthur, "An Inertial Guidance Technique Usable in Free Fall," Proc. Nat. Aero. Elec. Conf. (Dayton, Ohio, 1959), pp. 768-772.

5. J.J. Carroll and P.M. Savet, "Space navigation and exploration by gravity difference detection," IAS Paper 59-61, IAS National Summer Meeting, Los Angeles, 1959; also Aerospace Eng. 18, 44-47 (1959).

6. R.E. Roberson, "Methods for the Control of Satellites and Space Vehicles Vol. I, Sensing and Actuating Mechanisms," WADD Tech. Rpt. 60-643 (1960).

7. R.E. Roberson, "Gravity gradient determination of the vertical," ARS J. 31, 1509-1515 (1961).

8. P. Savet, "Attitude control of orbiting satellites at high eccentricity," ARS J. 32, 1577-1582 (1962).

9. J.W. Diesel, "A new approach to gravitational gradient determination of the vertical," AIAA J. 2, 1189-1196 (1964).

10. R.E. Roberson, "Establishment of the Center of Mass and Rotational State of a Space Vehicle by Inertial Techniques," Proc. XV Inter. Astro. Cong., Warsaw, 1964 (to be published).

11. R.L. Forward, "Rotating Gravitational and Inertial Sensors," presented at the AIAA Unmanned Spacecraft Meeting, Los Angeles, 1-4 March 1965.

BLANK PAGE

N66 36776

ATTACHMENT D

VIBRATIONAL MODE BEHAVIOR OF ROTATING GRAVITATIONAL GRADIENT SENSORS

The following paper has been submitted to the AIAA for publication in the Journal of Spacecraft and Rockets.

BLANK

PAGE

Vibrational Mode Behavior of Rotating Gravitational Gradient Sensors*

by

Curtis C. Bell,** J. Roger Morris,† John M. Richardson,‡ and Robert L. Forward***

Hughes Aircraft Company

ABSTRACT

36776

We are engaged in a program to design and construct a feasibility model of a gravitational mass sensor that uses a rotating resonant elastic system to detect the gravitational force gradient fields of the mass. As part of this program, we have carried out a detailed analysis of the vibrational mode behavior of a rotating cruciform shaped spring-mass system supported on a spring mount. The behavior of the sensor modes as a function of the design parameters and the rotation speed agrees well with data obtained from actual sensors used in the experimental portion of the work. This theory can aid in the design of optimum sensors and sensor mount structures.

Author

---

*The work reported herein was supported by the National Aeronautics and Space Administration under Contract NASW-1035.

**Member of the Technical Staff, Guidance Equipment Department, Culver City, California.

***Senior Member of the Technical Staff, Theoretical Studies Department, Hughes Research Laboratories, Malibu, California.

†Member of the Technical Staff, Control and Support Equipment Department, Culver City, California.

‡Head, Theoretical Studies Department, Hughes Research Laboratories, Malibu, California.

PROGRAM OBJECTIVES

The ultimate objective of our work on gravitational mass sensors is to develop a small, lightweight, rugged gravitational gradient sensor to be used on lunar orbiters to measure the mass distribution of the moon and on deep space probes to measure the mass of the asteroids. The possible applications,[1,2] the basic concepts,[2-10,14] and the theoretical limitations[11,12] have been investigated in earlier papers. The purpose of the present research program is to develop and refine experimental techniques for measuring gravitational and inertial fields using rotating elastic systems, and to develop a more complete understanding of these types of sensors so that accurate predictions of sensor behavior can be made which are based on practical system configurations and measured device sensitivity.

SUMMARY OF PRIOR WORK

The most promising form of gravitational mass sensor has been found to be a cruciform shaped spring-mass system. A number of different cruciform sensor heads (see, e.g., Fig. 1) have been designed and studied experimentally. They have all demonstrated a basic structural stability under high rotation speed. Effort is now concentrated on reducing the effects of bearing noise on the sensor modes.

A continuing theoretical study of the transversely vibrating cruciform sensor structure is under way. The model used for the analyses consists of a central mass connected to the using vehicle through an elastic mount, four equal sensing masses on transversely vibrating arms, and a sensed mass. The analysis is quite complicated because of the multiplicity of masses and springs, the nonuniform character of the gravitational field, and the requirement that the restoring forces on the sensor arms include the centrifugal force as well as the spring constant of the arms. The results of these analyses[2,11,12] indicate that there is a particular mode of vibration of the sensor — the tuning form mode (see Fig. 2(a)) — which is at a frequency which differs from that

M 3615

Fig. 1. Five-inch diameter cruciform gravitational mass sensor.

of the other modes, responds to the presence of a gravitational force gradient field when rotated at half of its vibrational frequency and yet does not respond to inertial forces.[12]

Readout of the very small (10^{-10} in.) vibrations expected is accomplished by means of piezoelectric strain transducers attached to the transversely vibrating arms of the cruciform. These barium titanate transducers have a gauge factor of 10^5 V/unit strain and have been used in previous work[13] to measure motions down to 10^{-14} in. Prior analysis has indicated[12] that this gauge sensitivity will yield gravity gradient produced signals of the order of a few microvolts. Since this is a narrow-band signal at 100 Hz, it is easily measured with a low noise tuned amplifier, such as the General Radio Tuned Amplifier 1232A, which has an equivalent input noise voltage of 50 nV.

STATEMENT OF PROBLEM

A major problem with cruciform gravitational mass sensors lies in maintaining adequate frequency separation between the various vibration sensitive resonant modes of the sensor system and the gradient sensing mode of the cruciform sensing head. If this frequency separation can be maintained, it will then be possible to use narrow band amplifiers to separate the gravitationally driven sensor response from the inertially driven responses.

In earlier work,[12] it was found that if the sensor has a small central mass and is well isolated from other masses by suspension from a weak spring, the gravity gradient sensing mode is the lowest in frequency and is well separated from the rest of the vibrational modes. However, when rotation of the sensor is attempted while using a mount with a weak spring constant, it is not possible to rotate the sensor up to the desired operating speed because the mount cannot resist the centrifugal forces. When the mount stiffness is increased so that it can resist the centrifugal force, two new translational modes formed by

the spring constant of the mount and the total mass of the sensor become important. These modes cause the two translational modes in the sensor head to shift upward, helping to solve the mode separation problem. However, under rotation, the translational modes split; at the desired rotational speed, they become close enough to the gradient sensing mode to make frequency selection techniques difficult.

In an attempt to understand this behavior, an analysis of vibrational mode behavior under rotation was undertaken. This analysis was then compared with the experimental data.

THEORY OF ROTATING CRUCIFORM SENSORS

As a result of earlier theoretical and experimental work,[11, 12] it has long been known that the cruciform shaped gravitational mass sensors have four primary oscillation modes which involve the spring constant of the bending arms. These are the gradient sensing or tuning fork mode (Fig. 2(a)), a torsional mode (Fig. 2(b)) and two translational modes (Fig. 2(c)). In addition, there are higher order harmonics of these four basic modes as well as other modes of oscillation involving other elastic properties of the cruciform, such as the torsional or longitudinal spring constants. These higher order modes, as well as the torsional mode, are usually at much higher frequencies than the gradient sensing mode and the two translational modes; they cause relatively little difficulty since they can be easily filtered out.

Since we wished to investigate the vibrational mode behavior of this class of sensors in as rigorous a manner as possible, the model used was not that of one of the actual sensors, but was chosen to be as general as possible while still retaining the important features of the actual sensors. The model (Fig. 3) assumes a central mass M and four smaller masses m at the ends of four arms of length a ; these arms are pivoted at a distance b from the center of the sensor. The central mass is assumed to be attached to a rotating axis through an axially symmetric spring of spring constant K. (The model shows four

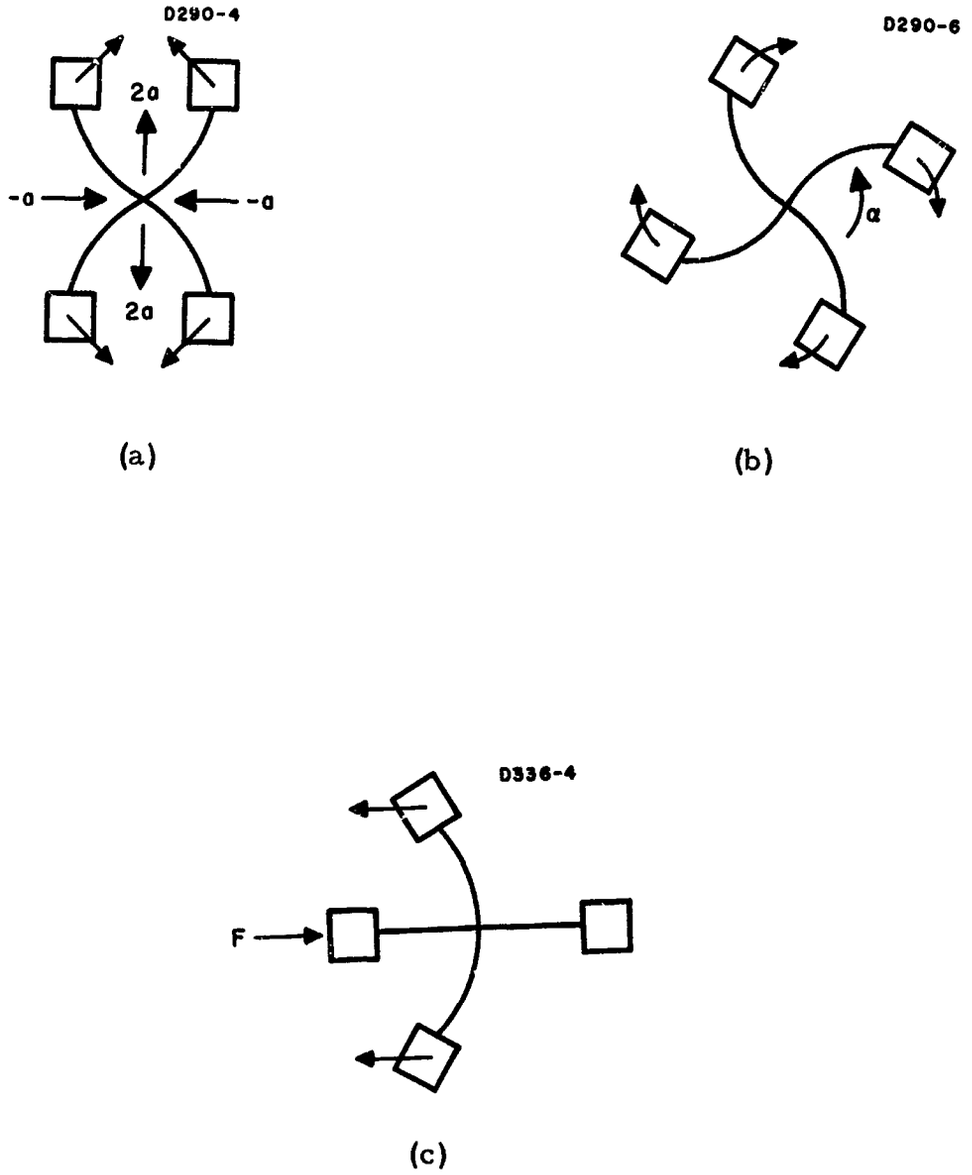

Fig. 2. Sensor vibrational modes

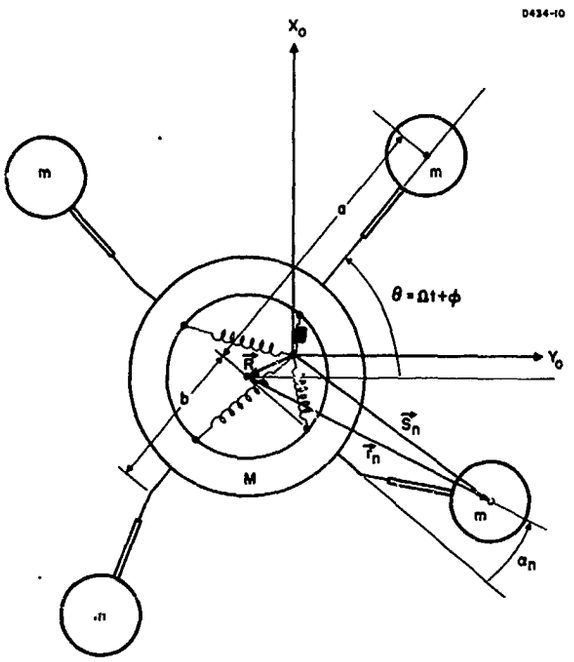

Fig. 3. Model of rotating cruciform sensor on spring mount.

coil springs; the experiment used a flexible shaft.) To simplify the analysis the axis was assumed to remain fixed in position at the origin of the inertial reference frame, while rotating at a constant angular frequency of Ω. The central mass M, since it is attached to the rotating axis through springs, is not constrained to the origin but its center of mass is in general at the position $\vec{R}$ and its speed of rotation varies about Ω by a small amount $\dot{\phi}$ due to the interaction with the vibrating arms. The masses at the ends of the arms participate in the general rotation of the sensor and also can vibrate through a small angle α_n with respect to the rotating reference frame.

The kinetic energy of the system is given by the general formula

$$T = \frac{1}{2} M \dot{\vec{R}}^2 + \frac{1}{2} m \sum_{n=1}^{4} \dot{\vec{s}}_n^2 + \frac{1}{2} I \dot{\theta}^2 \qquad (1)$$

where $\vec{R}$ is the position of the central mass, $\vec{s}_n$ is the position of the n^{th} end mass, I is the moment of inertia of the central mass, and $\dot{\theta} = \Omega + \dot{\phi}$ is its instantaneous angular velocity. We have assumed that the moment of inertia of the end masses is small enough to be neglected.

The potential energy of the system is in the springs of the vibrating arms and the mount

$$V = \frac{1}{2} k a^2 \sum_{n=1}^{4} \alpha_n^2 + \frac{1}{2} K \vec{R}^2 \qquad (2)$$

where k is the effective spring constant of the arms, K is the effective spring constant of the mount, and α_n is the angular deflection of the n^{th} arm. Using these equations, the Lagrangian of the system is therefore

$$L = T - V = \frac{1}{2} M \dot{\vec{R}}^2 + \frac{1}{2} m \sum_{n=1}^{4} \dot{\vec{s}}_n^2$$

$$+ \frac{1}{2} I \dot{\theta}^2 - \frac{1}{2} ka^2 \sum_{n=1}^{4} \alpha_n^2 - \frac{1}{2} K \vec{R}^2 . \qquad (3)$$

For our particular system, the position of the n^{th} arm is given by

$$\vec{s}_n = \vec{R} + \vec{r}_n ; \qquad (4)$$

substituting this into (3) we obtain the Lagrangian in terms of the central mass motion $\vec{R}$ and rotation $\dot{\theta}$, and the relative motion $\vec{r}_n$ and angular deflection α_n of the arms

$$L = \frac{1}{2} (M + 4m) \dot{\vec{R}}^2 + m \dot{\vec{R}} \sum_{n=1}^{4} \dot{\vec{r}}_n + \frac{1}{2} m \sum_{n=1}^{4} \dot{\vec{r}}_n^2$$

$$+ \frac{1}{2} I \dot{\theta}^2 - \frac{1}{2} ka^2 \sum_{n=1}^{4} \alpha_n^2 - \frac{1}{2} K \vec{R}^2 . \qquad (5)$$

This form of the Lagrangian is still not suitable for our purposes, since both $\vec{r}_n$ and $\vec{R}$ are a function of the rotation of the sensor θ as well as the motions of the sensor α_n and x.

The motion of the center of mass of the central mass is given by

$$\vec{R} = (x \cos \theta - y \sin \theta) \vec{1}_x + (x \sin \theta + y \cos \theta) \vec{1}_y \qquad (6)$$

where $\theta = \Omega t + \phi$ is the instantaneous rotation of the central mass and $\vec{1}_x$ and $\vec{1}_y$ are unit vectors.

To first order in x and ϕ, the velocity of the center of mass is given by

$$\dot{\vec{R}} = [(\dot{x} - \Omega y)\cos\Omega t - (\dot{y} + \Omega x)\sin\Omega t]\,\vec{1}_x + [(\dot{x} - \Omega y)\sin\Omega t + (\dot{y} + \Omega x)\cos\Omega t]\,\vec{1}_y \tag{7}$$

and the square of the velocity by

$$\dot{\vec{R}}^2 = \dot{x}^2 + \dot{y}^2 + 2\Omega(x\dot{y} - \dot{x}y) + \Omega^2(x^2 + y^2) = (\dot{x} - \Omega y)^2 + (\dot{y} + \Omega x)^2 \tag{8}$$

where we have assumed that $\theta \approx \Omega t$ and that products of order $x^2\phi$ and $\phi^2 x$ are negligible.

The position of the n^{th} end mass is given by

$$\vec{r}_n = r_n\left[\vec{1}_x \cos\left(\theta + \frac{n\pi}{2} + \alpha_n\right) + \vec{1}_y \sin\left(\theta + \frac{n\pi}{2} + \alpha_n\right)\right] \tag{9}$$

where the absolute value of the effective length of the sensor arm is given by

$$r_n = a\left(1 - \frac{1}{2}\,\frac{b}{a-b}\,\alpha_n^2\right) \equiv a - \frac{1}{2}\,aB\alpha_n^2 \tag{10}$$

where a is the nominal length of the arm and b is the distance from the effective pivot point of the arm to the center of the sensor. $B = \frac{b}{a-b}$ is chosen so that $B = 0$ and $r_n = a$ when the arm is pivoted at the center of rotation ($b \approx 0$) and B and r_n become indeterminant when the arm is pivoted at the end ($b \approx a$).

The calculation of $\Sigma\dot{\vec{r}}_n$ and $\Sigma\dot{\vec{r}}_n^2$ in terms of θ and α_n is straightforward but tedious. For the sum of the arm velocities we obtain

$$\frac{1}{a}\sum_{n=1}^{4}\dot{\vec{r}}_n = [(\dot{a}_3 - \dot{a}_1) - \Omega(a_4 - a_2)]\,[\vec{1}_x \cos\Omega t + \vec{1}_y \sin\Omega t]$$

$$- [(\dot{a}_4 - \dot{a}_2) + \Omega(a_3 - a_1)]\,[\vec{1}_x \sin\Omega t + \vec{1}_y \cos\Omega t] \qquad (11)$$

where we kept only terms of first order in a and ϕ, since we will later be multiplying (11) by the center of mass velocity (7). For the relative energy of the arms alone, we obtain

$$\frac{m}{2}\sum_{n=1}^{4}\dot{\vec{r}}_n^{\,2} = 2ma^2\dot{\theta}^2 + ma^2\dot{\theta}\sum_{n=1}^{4}\dot{a}_n$$

$$+ \frac{1}{2}ma^2\sum_{n=1}^{4}\dot{a}_n^{\,2} - \frac{1}{2}ma^2 B\Omega^2\sum_{n=1}^{4}a_n^{\,2} \qquad (12)$$

where we have kept terms of second order in a and ϕ.

Combining (7), (8), (11), and (12) into (5), we obtain the Lagrangian in terms of the motions and rotation of the central mass and the relative angular displacement of the arms

$$L = \frac{1}{2}(M + 4m)[(\dot{x} - \Omega y)^2 + (\dot{y} + \Omega x)^2] + ma\Big\{(\dot{x} - \Omega y)[(\dot{a}_3 - \dot{a}_1) - \Omega(a_4 - a_2)]$$

$$+ (\dot{y} + \Omega x)[(\dot{a}_4 - \dot{a}_2) + \Omega(a_3 - a_1)]\Big\} + \frac{1}{2}(I + 4ma^2)\dot{\theta}^2 + ma^2\dot{\theta}\sum_{n=1}^{4}\dot{a}_n$$

$$+ \frac{1}{2}ma^2\sum_{n=1}^{4}\dot{a}_n^{\,2} - \frac{1}{2}(ka^2 + ma^2 B\Omega^2)\sum_{n=1}^{4}a_n^{\,2} - \frac{1}{2}K(x^2 + y^2)$$

(13)

where we have neglected terms of third order in x, y, a_n, and ϕ.

This form of the Lagrangian contains the description of the behavior of the sensor in terms of the angular displacement α_n of each one of the arms. However, since we are interested in the behavior of the vibrational modes of the sensor, it will simplify things if we express the Lagrangian in terms of the equivalent displacement of the vibrational modes. Each mode of vibration corresponds to a particular combination of arm phase and amplitude. The four primary modes of interest are the gravity gradient sensing mode (see Fig. 2(a))

$$A_g = \frac{a}{2} (\alpha_1 - \alpha_2 + \alpha_3 - \alpha_4) \ , \tag{14}$$

the torsional mode (see Fig. 2(b))

$$A_t = \frac{a}{2} (\alpha_1 + \alpha_2 + \alpha_3 + \alpha_4) \ , \tag{15}$$

and the two orthogonal translational modes (see Fig. 2(c))

$$A_+ = \frac{a}{\sqrt{2}} (\alpha_3 - \alpha_1) \tag{16}$$

$$A_- = \frac{a}{\sqrt{2}} (\alpha_4 - \alpha_2) \ . \tag{17}$$

The two translational modes can also be expressed in terms of right and left handed circulating translational modes which are complex combinations of the orthogonal modes

$$A_r = \frac{1}{\sqrt{2}} (A_+ + iA_-) = \frac{a}{2} (-\alpha_1 - i\alpha_2 + \alpha_3 + i\alpha_4) \tag{18}$$

$$A_\ell = \frac{1}{\sqrt{2}} (A_+ - iA_-) = \frac{a}{2} (-\alpha_1 + i\alpha_2 + \alpha_3 - i\alpha_4) \tag{19}$$

where the complex number i indicates a 90^{o} phase lag in the response of the arm vibrating in that particular mode.

It is obvious from inspection that

$$a^2 \sum_{n=1}^{4} \alpha_n^{\,2} = a^2(\alpha_1^{\,2} + \alpha_2^{\,2} + \alpha_3^{\,2} + \alpha_4^{\,2}) = A_g^{\,2} + A_t^{\,2} + A_+^{\,2} + A_-^{\,2}$$

$$= A_g^{\,2} + A_t^{\,2} + A_r^{\,2} + A_\ell^{\,2} \qquad (20)$$

and that

$$a \sum_{n=1}^{4} \dot{\alpha}_n = 2\,\dot{A}_t \qquad (21)$$

so that the Lagrangian (13) in terms of the amplitudes of the normal mode vibrations is given by:

$$L = \frac{(M + 4m)}{2m}\left[(\dot{x} - \Omega y)^2 + (\dot{y} + \Omega x)^2\right] + \sqrt{2}(\dot{x} - \Omega y)[\dot{A}_+ - \Omega A_-]$$

$$+ \sqrt{2}(\dot{y} + \Omega x)[\dot{A}_- + \Omega A_+] + \frac{1}{2}\left(\frac{I + 4ma^2}{m}\right)\dot{\theta}^2 + 2a\dot{\theta}\dot{A}_t$$

$$+ \frac{1}{2}(\dot{A}_g^{\,2} + \dot{A}_t^{\,2} + \dot{A}_+^{\,2} + \dot{A}_-^{\,2}) - \frac{1}{2}\left(\frac{k}{m} + B\Omega^2\right)(A_g^{\,2} + A_t^{\,2} + A_+^{\,2} + A_-^{\,2})$$

$$- \frac{K}{2m}(x^2 + y^2) \quad . \qquad (22)$$

We now define the following constants as:
the gradient sensing mode frequency

$$\omega_g^{\,2} = \frac{k'}{m} = \frac{k}{m} + B\Omega^2 \quad , \qquad (23)$$

the reduced mass of the sensor in the translational mode

$$\mu = \frac{M + 4m}{2m} , \tag{24}$$

and the mount translational frequency

$$\Omega_m^2 = \frac{K}{M + 4m} . \tag{25}$$

Substituting into the Lagrangian and rearranging, we obtain

$$L = \mu[\dot{x}^2 + \dot{y}^2 + 2\Omega(x\dot{y} - y\dot{x}) + (\Omega^2 - \Omega_m^2)(x^2 + y^2)] + \sqrt{2}(\dot{x} - \Omega y)(\dot{A}_+ - \Omega A_-)$$

$$+ \sqrt{2}(\dot{y} + \Omega x)(\dot{A}_- + \Omega A_+) + \frac{1}{2}\left(\frac{I + 4ma^2}{m}\right)\dot{\theta}^2 + 2a\ddot{\theta}\dot{A}_t$$

$$+ \frac{1}{2}(\dot{A}_g^2 + \dot{A}_t^2 + \dot{A}_+^2 + \dot{A}_-^2) - \frac{1}{2}\omega_g^2(A_g^2 + A_t^2 + A_+^2 + A_-^2) \tag{26}$$

The equation of motion for the gravity gradient sensing mode is given by

$$\frac{d}{dt}\frac{\partial L}{\partial \dot{A}_g} - \frac{\partial L}{\partial A_g} = 0 = \ddot{A}_g + \omega_g^2 A_g \tag{27}$$

which has the solution

$$A_g = Ae^{i\omega_g t} \tag{28}$$

where the frequency of the resonant mode is given by the spring constant k and mass of the arms as modified by the centrifugal rotation

$$\omega_g^2 = \frac{k}{m} + B\Omega^2 \quad . \tag{29}$$

We note here that the frequency of this mode is not constant but shifts upward under rotation. This effect is borne out by the experimental results and is due to the increase in the effective spring constant from the centrifugal force acting on the sensor arms as gravity on a pendulum. However, the centrifugal force does not simulate gravity exactly since it is not a uniform field but extends radially outward. If the pivot point of the arm were at the center of rotation (b = 0), the frequency of the mode would be independent of the rotational speed, since the mass on the end of the arm would not see any variation in the centrifugal potential as the arm vibrated.

The equation of motion for the torsional mode is given by

$$\frac{d}{dt}\frac{\partial L}{\partial \dot{A}_t} - \frac{\partial L}{\partial A_t} = 0 = 2a\ddot{\theta} + \ddot{A}_t + \omega_g^2 A_t = 0 \tag{30}$$

where we eliminate the term containing the variation in sensor rotation speed $\ddot{\theta} = \ddot{\phi}$ by taking

$$\frac{d}{dt}\frac{\partial L}{\partial \dot{\theta}} - \frac{\partial L}{\partial \theta} = 0 = \left(\frac{I + 4ma^2}{m}\right)\ddot{\theta} + 2a\ddot{A}_t \tag{31}$$

or

$$\ddot{\theta} = -\frac{2ma}{I + 4ma^2}\ddot{A}_t \tag{32}$$

Substituting (32) into (30), we obtain

$$\left[1 - \left(\frac{4ma^2}{I + 4ma^2}\right)\right] \ddot{A}_t + \omega_g^2 A_t = 0 \quad . \tag{33}$$

When we solve this equation, we find that the natural frequency of the torsional mode is related to the gradient sensing mode frequency by

$$\omega_t^2 = \left(\frac{I + 4ma^2}{I}\right) \omega_g^2 \quad . \tag{34}$$

Here we note that the torsional mode frequency starts off higher than the gradient sensing mode frequency, provided the moment of inertia I of the central mass is not too large, and increases with rotation speed in the same manner. This behavior is borne out by the experimental results. An isolated sensor usually has a sufficiently small central mass that the torsional mode frequency is considerably higher than the gradient sensing mode frequency and rises with increasing rotation speed. However, if the sensor is firmly attached to a large sensor chamber, the torsional mode frequency shifts down toward the gradient sensing mode frequency.

The equations of motion for the four translational modes cannot be solved independently since they interact with each other. The four equations are

$$\frac{d}{dt}\frac{\partial L}{\partial \dot{x}} - \frac{\partial L}{\partial x} = 2\mu \left[\ddot{x} - 2\Omega\dot{y} - (\Omega^2 - \Omega_m^2)\, x\right]$$

$$+ \sqrt{2}\left[\ddot{A}_+ - 2\Omega A_- - \Omega^2 \dot{A}_+\right] = 0 \tag{35}$$

$$\frac{d}{dt}\frac{\partial L}{\partial \dot{y}} - \frac{\partial L}{\partial y} = 2\mu\left[\ddot{y} + 2\Omega\dot{x} - (\Omega^2 - \Omega_m{}^2)\, y\right]$$

$$+ \sqrt{2}\left[\ddot{A}_- + 2\Omega\dot{A}_+ - \Omega^2 A_-\right] = 0 \qquad (36)$$

$$\frac{d}{dt}\frac{\partial L}{\partial \dot{A}_+} - \frac{\partial L}{\partial A_+} = \sqrt{2}\left[\ddot{x} - 2\Omega\dot{y} - \Omega^2 x\right] + \ddot{A}_+ + \omega_g{}^2 A_+ = 0 \qquad (37)$$

$$\frac{d}{dt}\frac{\partial L}{\partial \dot{A}_-} - \frac{\partial L}{\partial A_-} = \sqrt{2}\left[\ddot{y} + 2\Omega\dot{x} - \Omega^2 y\right] + \ddot{A}_- + \omega_g{}^2 A_- = 0 \qquad (38)$$

We now define a right and left handed circularly polarized mode for the translational modes of the mount

$$R = \frac{1}{\sqrt{2}}(x + iy) \qquad (39)$$

$$L = \frac{1}{\sqrt{2}}(x - iy) \qquad (40)$$

along with the right and left handed modes for the sensor

$$A_r = \frac{1}{\sqrt{2}}(A_+ + iA_-) \qquad (41)$$

$$A_\ell = \frac{1}{\sqrt{2}}(A_+ - iA_-)\ . \qquad (42)$$

These can then be used to express eqs. (35) to (38) in an equivalent form

$$2\mu\left[\ddot{R} + 2i\Omega\dot{R} - (\Omega^2 - \Omega_m^2)\,R\right] + \sqrt{2}\left[\ddot{A}_r + 2i\Omega\dot{A}_r - \Omega^2 A_r\right] = 0 \qquad (43)$$

$$2\mu\left[\ddot{L} - 2i\Omega\dot{L} - (\Omega^2 - \Omega_m^2)\,L\right] + \sqrt{2}\left[\ddot{A}_\ell - 2i\Omega\dot{A}_\ell - \Omega^2 A_\ell\right] = 0 \qquad (44)$$

$$\ddot{A}_r + \omega_g^2 A_r + \sqrt{2}\left[\ddot{R} + 2i\Omega\dot{R} - \Omega^2 R\right] = 0 \qquad (45)$$

$$\ddot{A}_\ell + \omega_g^2 A_\ell + \sqrt{2}\left[\ddot{L} - 2i\Omega\dot{L} - \Omega^2 L\right] = 0 \qquad (46)$$

Notice that instead of all four mode amplitudes appearing in each equation indicating coupling between all four modes as they did in eqs. (35) to (38), we now find that the right handed circularly polarized mount mode interacts only with the right handed sensor mode and similarly for the two left handed modes.

The equations now only have to be solved in pairs, and the only difference between the two pairs of equations is the direction of rotation $\pm\Omega$.

Assuming solutions of the form

$$A_r = A e^{\pm i\omega t} \qquad (47)$$

$$R = R e^{\pm i\omega t} \qquad (48)$$

and using them in (43) and (45) we obtain a pair of equations

$$(\omega_g^2 - \omega^2)\,A - \sqrt{2}\left[\omega^2 \pm 2\omega\Omega + \Omega^2\right] R = 0 \qquad (49)$$

$$+2\mu\left[\omega^2 \pm 2\omega\Omega + \Omega^2 - \Omega_m^2\right] R + \sqrt{2}\,(\omega^2 \pm 2\omega\Omega + \Omega^2)\,A = 0 \qquad (50)$$

Rearranging (49)

$$A = \sqrt{2}\,\frac{(\omega \pm \Omega)^2}{(\omega_g^2 - \omega^2)}\,R \qquad (51)$$

and substituting it into (50), we obtain

$$2\mu\left[(\omega \pm \Omega)^2 - \Omega_m{}^2\right] R + 2\,\frac{(\omega \pm \Omega)^4}{(\omega_g{}^2 - \omega^2)}\,R = 0 \qquad (52)$$

or

$$(\omega \pm \Omega)^4 + \mu(\omega_g{}^2 - \omega^2)\left[(\omega \pm \Omega)^2 - \Omega_m{}^2\right] = 0 \qquad (53)$$

The four solutions to this fourth order equation in ω then tell us the vibrational frequencies of the four translational modes as a function of the rotation rate Ω, the mass ratio of the sensor masses $\mu = \frac{M + 4m}{2m}$, the basic mount frequency $\Omega_m{}^2 = \frac{K}{M + 4m}$, and the frequency of the gradient sensing mode ω_g. Since the gradient sensing mode frequency is also a function of rotation speed we can either express the dependence directly

$$(\omega \pm \Omega)^4 + \frac{M + 4m}{2m}\left(\frac{k}{m} + B\Omega^2 - \omega^2\right)\left[(\omega \pm \Omega)^2 - \frac{K}{M + 4m}\right] = 0 \qquad (53a)$$

or can normalize it out by taking the ratio of all the frequencies with respect to the gradient sensing mode frequency

$$\left(\frac{\omega}{\omega_g} \pm \frac{\Omega}{\omega_g}\right)^4 + \mu\left[1 - \frac{\omega^2}{\omega_g{}^2}\right]\left[\left(\frac{\omega}{\omega_g} \pm \frac{\Omega}{\omega_g}\right)^2 - \frac{\Omega_m{}^2}{\omega_g{}^2}\right] = 0\,. \qquad (53b)$$

In general it is necessary to use a computer to find the solutions to (53); however, under certain simplified conditions the equation reduces in order and can be solved.

EXAMINATION OF BEHAVIOR OF NORMAL MODE FREQUENCIES

In order to examine the behavior of the four translational mode frequencies, a series of plots of mode response frequencies ω as a function of rotation speed Ω was made for various values of the mount frequency Ω_m. These plots were all made using the normalized equation (53b).

The first plot (Fig. 4) shows the resonance behavior of a sensor on a very weak mount ($\Omega_m \approx 0$). For the case where the central mass of the sensor is negligible ($M \ll m$), the sensor translational modes start at $\omega_\pm = \sqrt{2}\ \omega_g$ and then split as the sensor starts rotating. When the rotation speed is at the desired operating point ($2\Omega = \omega_g$), the two sensor translational modes are at

$$\omega = \frac{1}{2} (\sqrt{10} \pm 1)\ \omega_g \tag{54}$$

or

$$\omega_+ = 2.081\ \omega_g \tag{55a}$$

$$M \ll m\ .$$

$$\omega_- = 1.081\ \omega_g \tag{55b}$$

If the mass of the central hub is increased so that $M = m$, the sensor translational mode starts out at $\omega_\pm = 1.29\ \omega_g$ and again splits under rotation in the same manner. At the desired operating speed the two frequencies are

$$\omega_+ = 1.728\ \omega_g \tag{56a}$$

$$M = m$$

$$\omega_- = 1.062\ \omega_g \tag{56b}$$

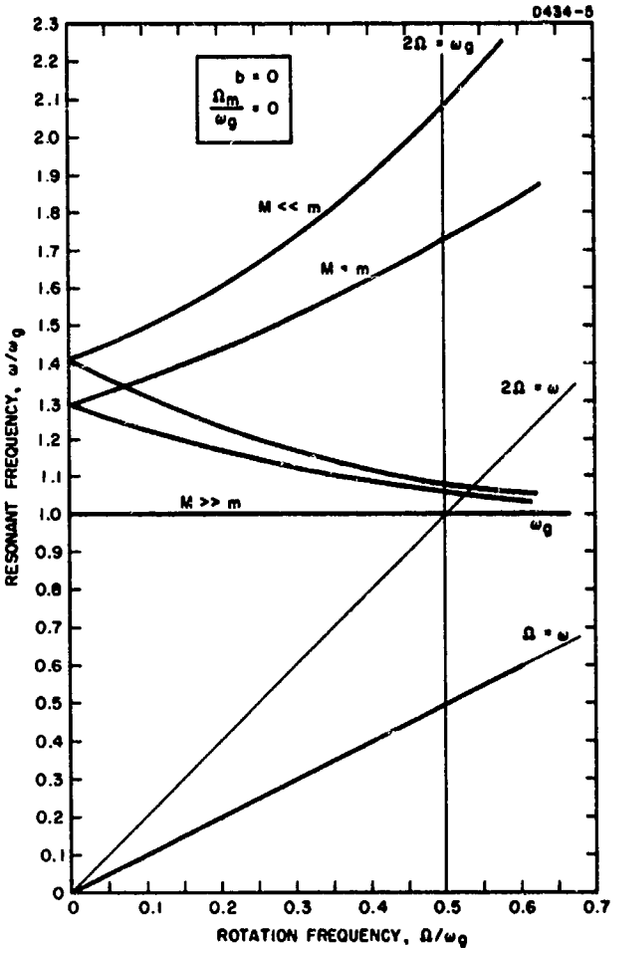

Fig. 4. Predicted translational mode splitting ($\Omega_m = 0$).

For a large centr .l mass $M \gg m$, the sensor translational modes start out at

$$\omega_{\pm} = \omega_g \qquad M \gg m \tag{57}$$

and do not split under rotation.

From this set of curves we see that it is desirable to keep the central mass of the sensor as small as possible. In this manner we can obtain a higher degree of frequency separation between the gravity gradient sensing mode at ω_g and the vibration sensitive translational modes. As a practical matter it is difficult to make the central mass smaller than the arm masses, and in most of our sensors $M \approx m$. Because of this we assumed $M = m$ for the rest of our curves.

The next four graphs (Figs. 5 through 8) show the effect of increasing the frequency or stiffness of the mount. As the basic mount frequency is increased, the sensor translational modes are pushed upward away from the gravity gradient sensing mode, thus helping in the effort to maintain adequate frequency separation.

However, if the basic mount frequency is made higher, we find that when the mount resonance splits under rotation, the higher mode becomes very close to the gradient sensing mode at the desired operating speed ($\Omega = \frac{1}{2}\omega_g$).

Since our sensors are designed to be rotated at a rate which is half of the gradient sensing mode vibration frequency, we also calculated solutions to eq. (53b) assuming that $\Omega = \frac{1}{2}\omega_g$, but varying the mass ratio and the basic mount frequency Ω_m. These are plotted in Fig. 9. From these curves we see that changing the mass ratio does not aid appreciably in the problem of obtaining frequency separation, and that an optimum value for the basic mount frequency is around $\Omega_m = 0.5\,\omega_g$. From Figs. 6, 7, and 9, however, we see that for a mount at $\Omega_m = 0.5\,\omega_g$, the lower mount vibrational mode has a resonance at zero frequency for speeds of $\Omega = \frac{1}{2}\omega_g$, which is a possible point of instability. The best choice for a mount frequency would seem to be $\Omega_m = 0.55\,\omega_g$.

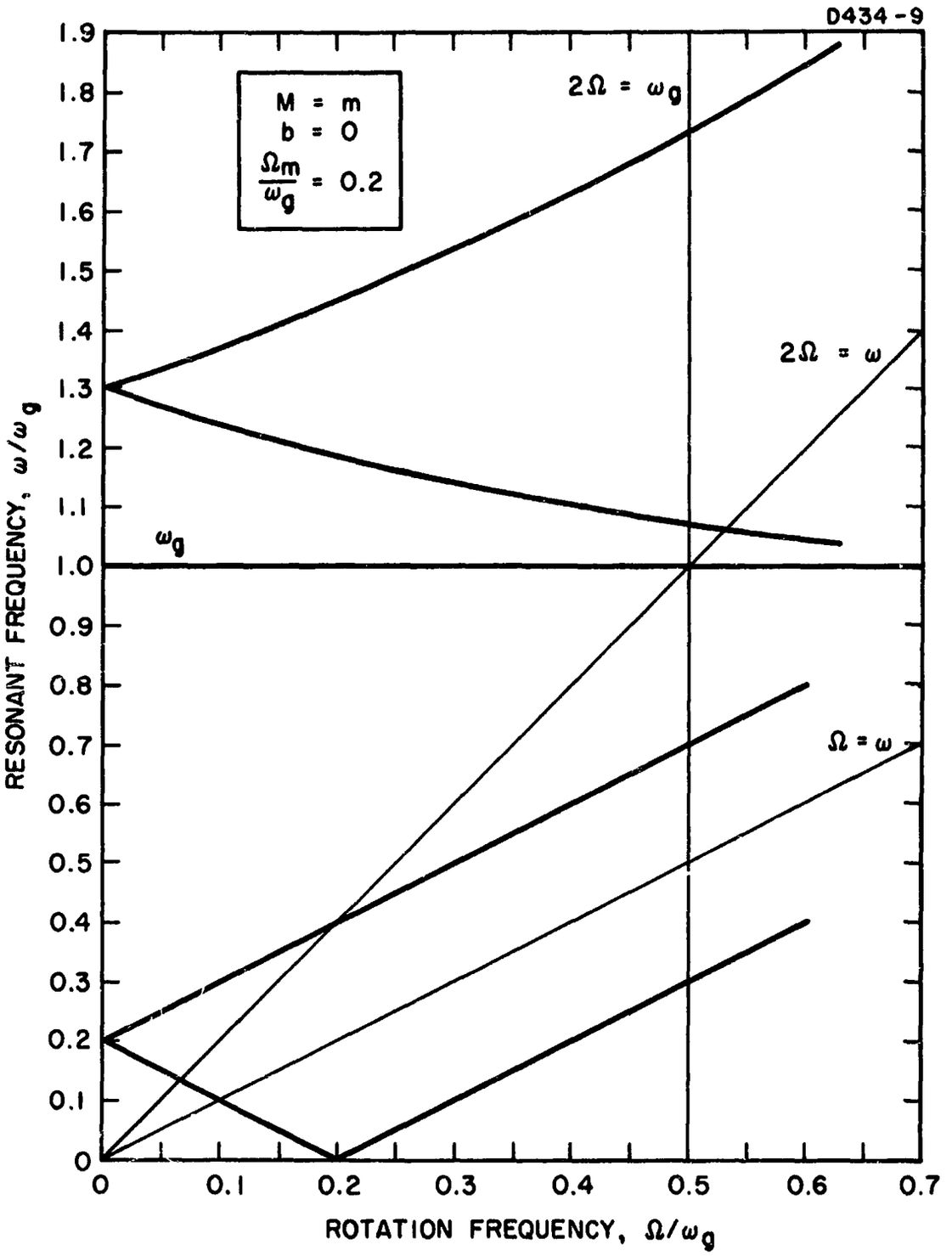

Fig. 5. Predicted translational mode splitting ($\Omega_m = 0.2\ \omega_g$).

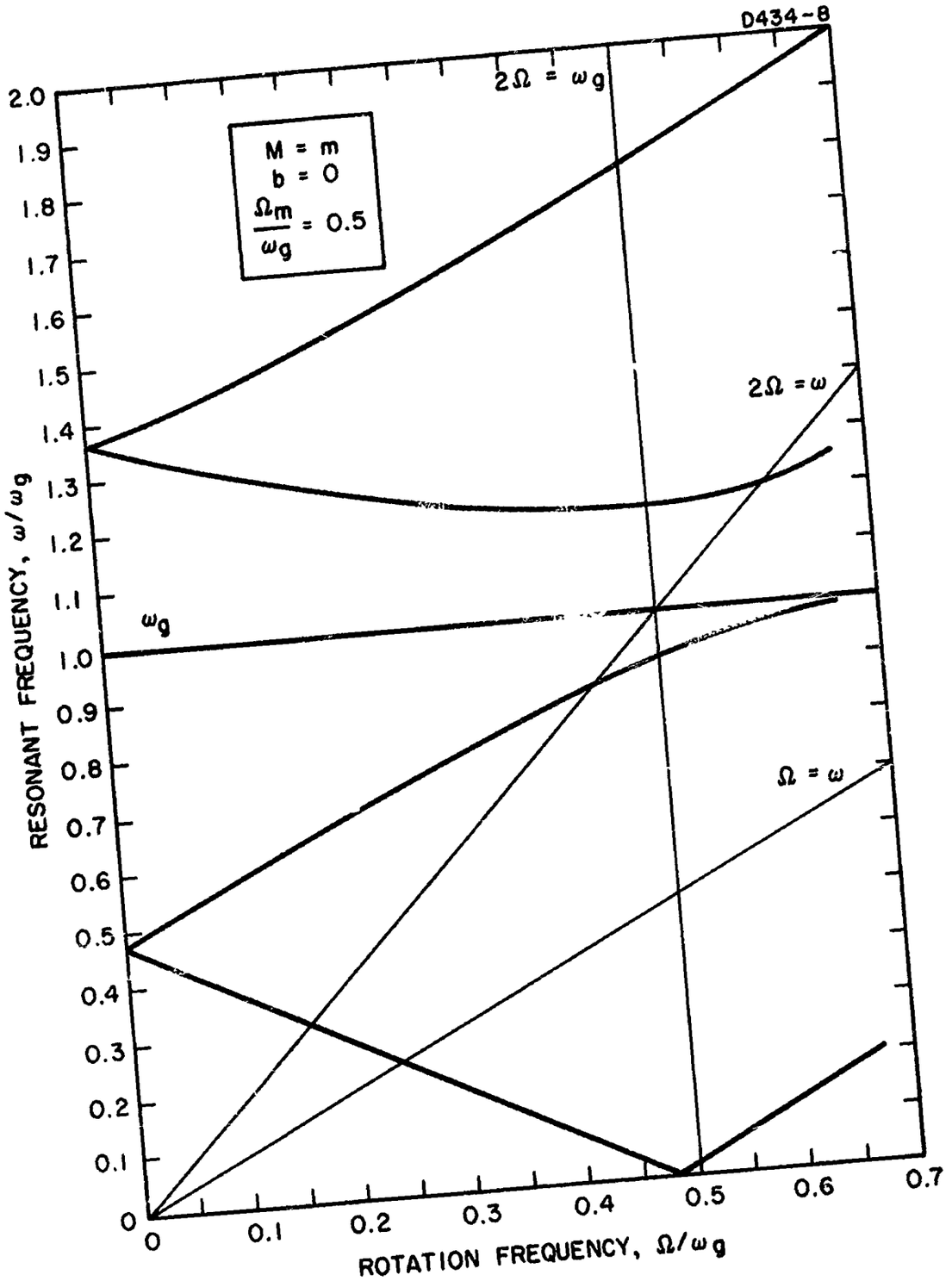

Fig. 6. Predicted translational mode splitting ($\Omega_m = 0.5\ \omega_g$).

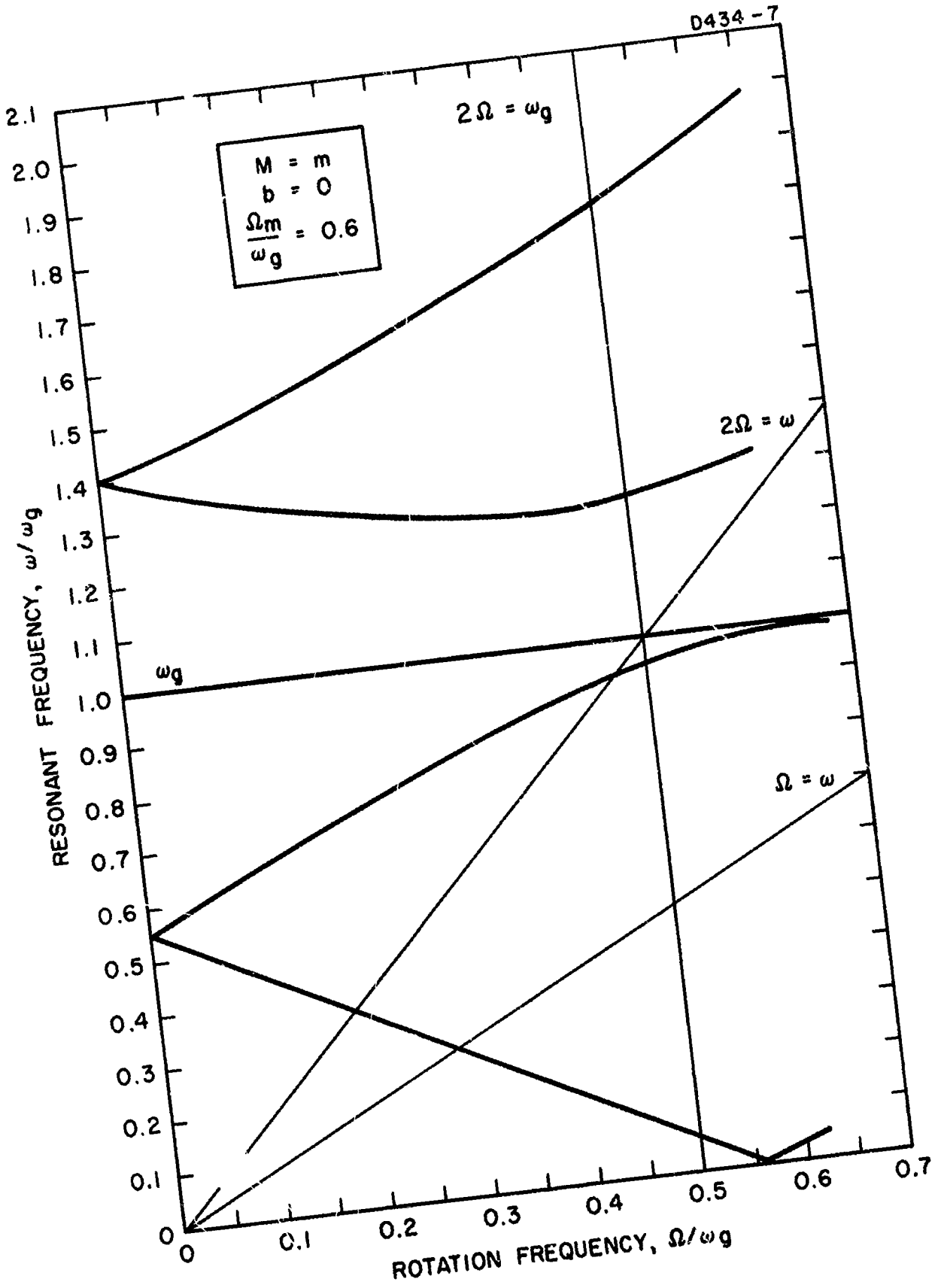

Fig. 7. Predicted translational mode splitting ($\Omega_m = 0.6\ \omega_g$).

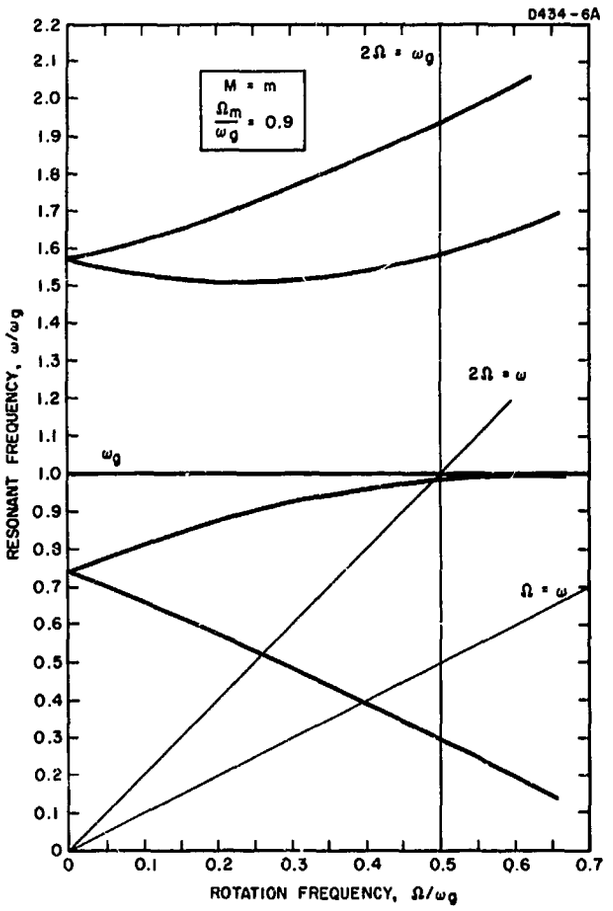

Fig. 8. Predicted translational mode splitting ($\Omega_m = 0.9\ \omega_g$).

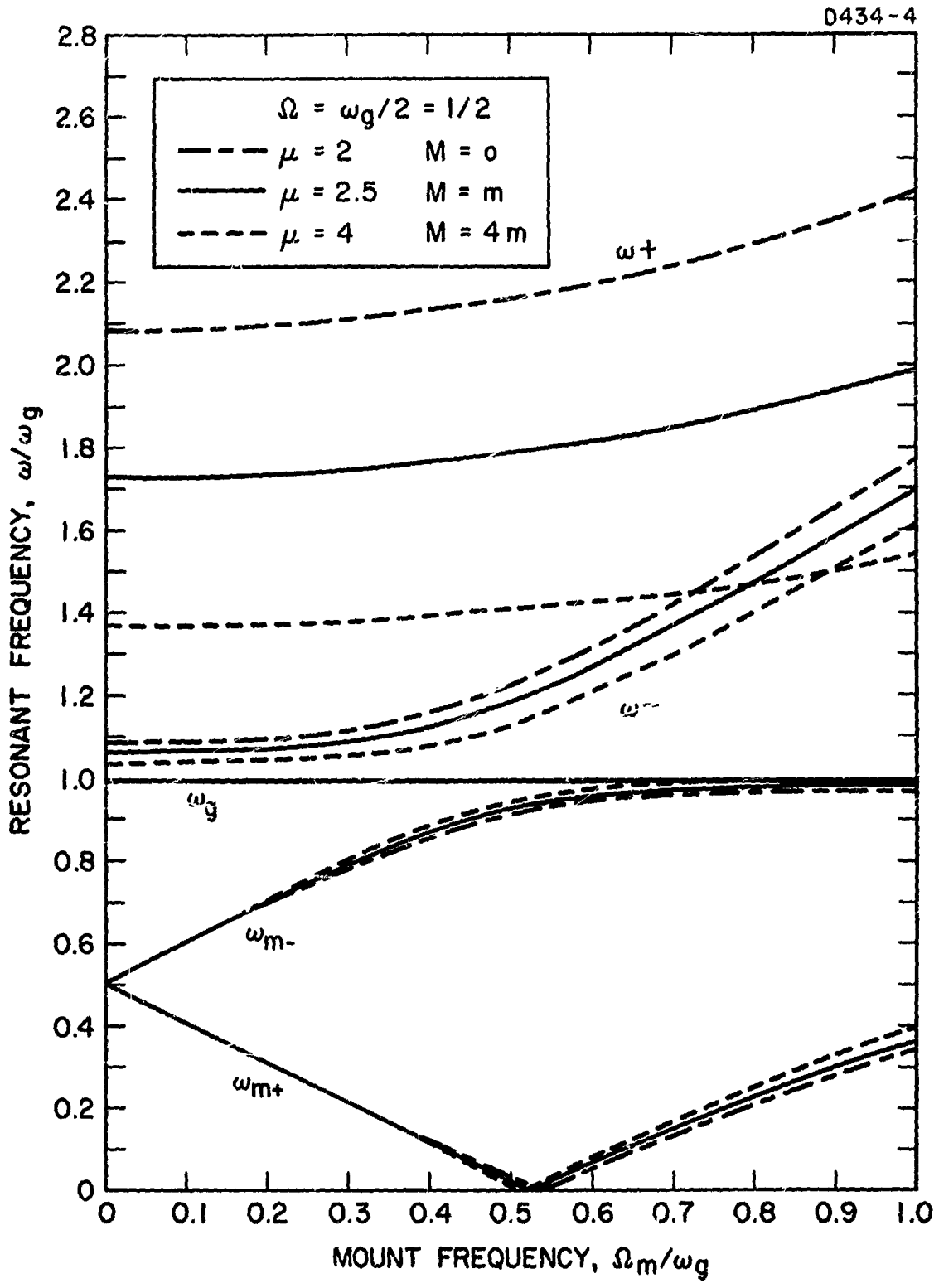

Fig. 9. Predicted translational mode splitting ($\Omega = 1/2\ \omega_g$).

The basic mount frequency is that which would be measured if the sensor arms were held fixed. The actual measured frequency is a little lower than this because of the interaction between the sensor modes and the mount modes.

COMPARISON OF THEORY AND EXPERIMENT

Data on sensor mode frequencies have been taken on various sensors during the experimental work on our program, and in general the theory agrees well with the data.

Sensor – Mount Interaction At $\Omega = 0$

If we assume that the sensor and mount are not rotating ($\Omega = 0$), then (53b) simplifies somewhat to become

$$\left(\frac{\omega}{\omega_g}\right)^4 + \mu\left[1 - \left(\frac{\omega}{\omega_g}\right)^2\right]\left[\frac{\omega^2}{\omega_g^2} - \frac{\Omega_m^2}{\omega_g^2}\right] = 0 . \qquad (58)$$

When this is plotted for $\mu = 3.07$ ($M = 2.15m$) we obtain the curves shown in Fig. 10. The light lines $\omega_\pm$ and Ω_m indicate what the sensor translational modes and the mount translational modes would do if they did not interact with each other.

One of our sensors had been tested with a large number of possible mounts (see Fig. 11). The frequency data from these tests were normalized and are plotted as the points in Fig. 10. The agreement of the theory with the experiment is excellent. This curve can be used to determine the basic mount frequency when the three resonant frequencies of the interacting system are known, and will aid in the optimum mount design.

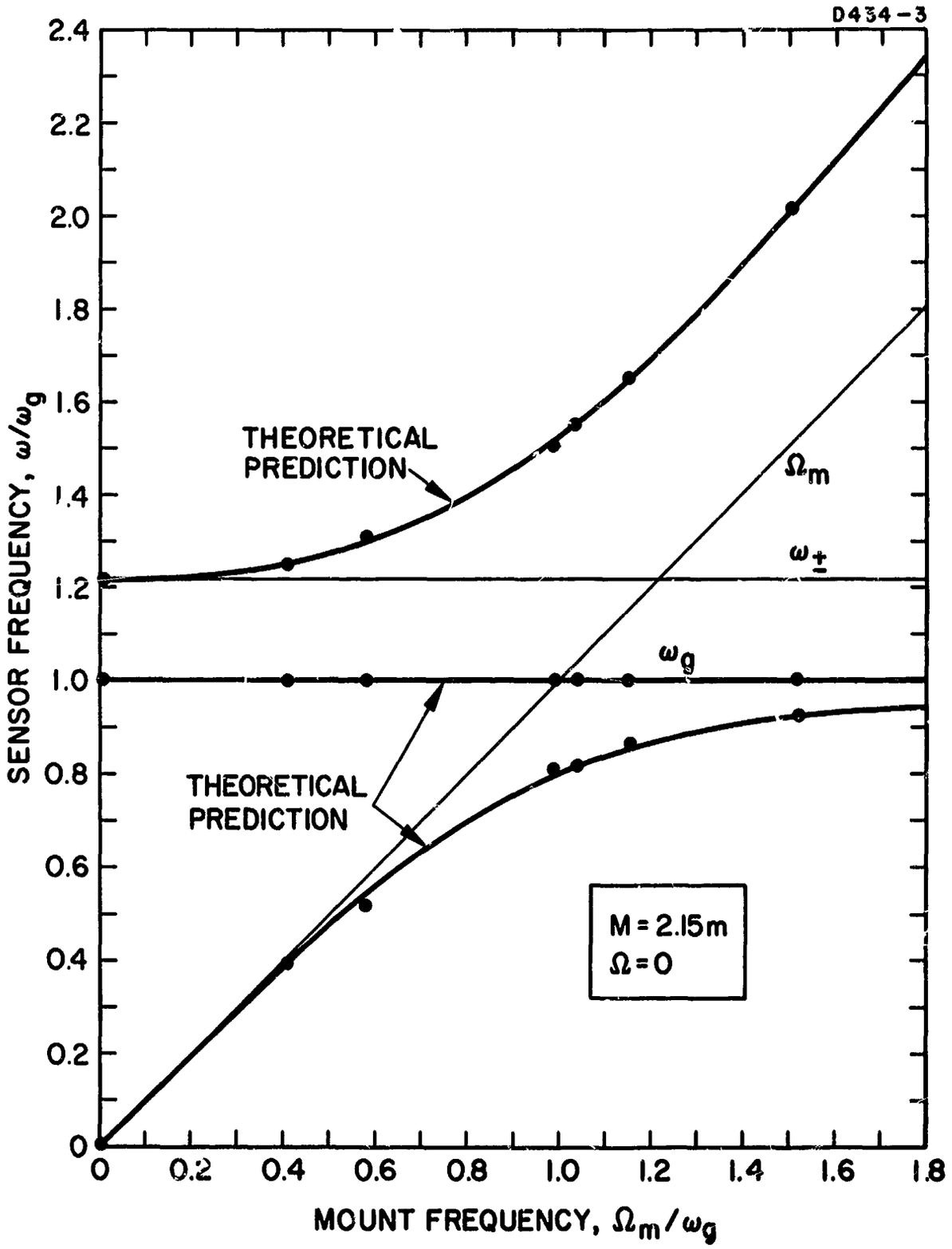

Fig. 10. Mount-sensor interaction (nonrotating).

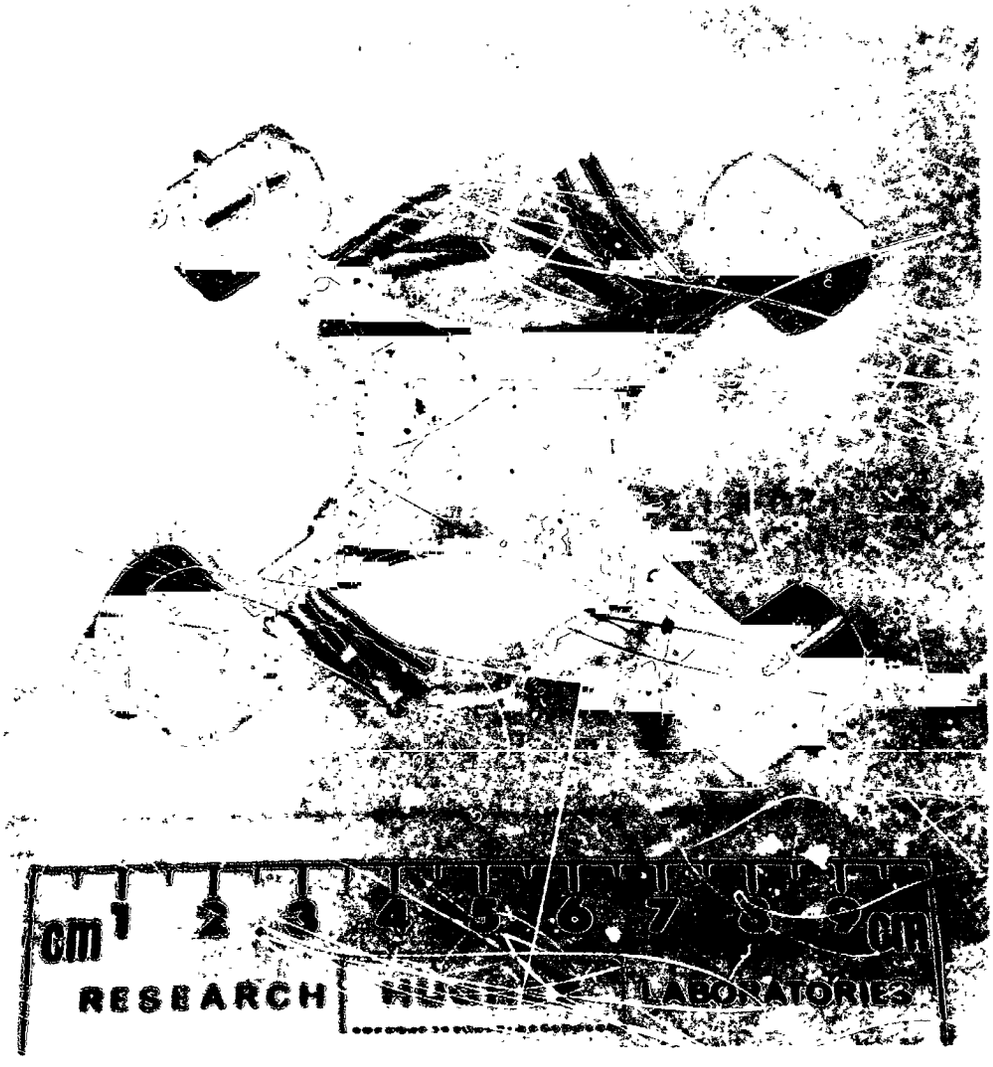

Fig. 11. Ag table sensor.

Rotating Sensor on Soft Mount

A very nice set of sensor resonant frequency data had been taken on a rotating cruciform hanging from a rubber band (see Fig. 12). The rubber band had a very low natural frequency, and therefore $\Omega_m \approx 0$. There was an instability at low rotation rates, but after this was passed through and the sensor rotated above the resonance point, it was very stable. The data are plotted in Fig. 13. Four points from the data (large points) were then used to determine the four sensor parameters $\frac{k}{m}$, B, $\frac{I + 4ma^2}{I}$ and, $\mu = \frac{M + 4m}{2m}$.

These parameters were then used in the three equations

$$\omega_g^2 = \frac{k}{m} + B\Omega^2 \tag{59}$$

$$\omega_t^2 = \left(\frac{I + 4ma^2}{I}\right)\left(\frac{k}{m} + B\Omega^2\right) \tag{60}$$

$$(\omega_\pm \pm \Omega)^2 + \mu\left(\frac{k}{m} + B\Omega^2 - \omega_\pm^2\right) = 0 \tag{61}$$

to obtain the theoretical curves. The agreement with the data is excellent. The highest set of data seems to be the upper half of a split torsional mode. It is believed to result from the effect of the moment of inertia of the arm masses which was neglected in the theoretical calculations.

Rotating Sensor on Hard Mount

Only one set of frequency data is available for a rotating sensor on a fairly rigid mount. The mounting structure used was a wire attached to the sensor at the center and held at the ends by the lid and base of a sensor vacuum chamber (see Fig. 14). The data are shown in Fig. 15. The two translational modes of the sensor and the two translational modes of the mount were not the same at zero rotation speed.

Fig. 12. Sensor rotating on rubber band suspension under magnetic bearing.

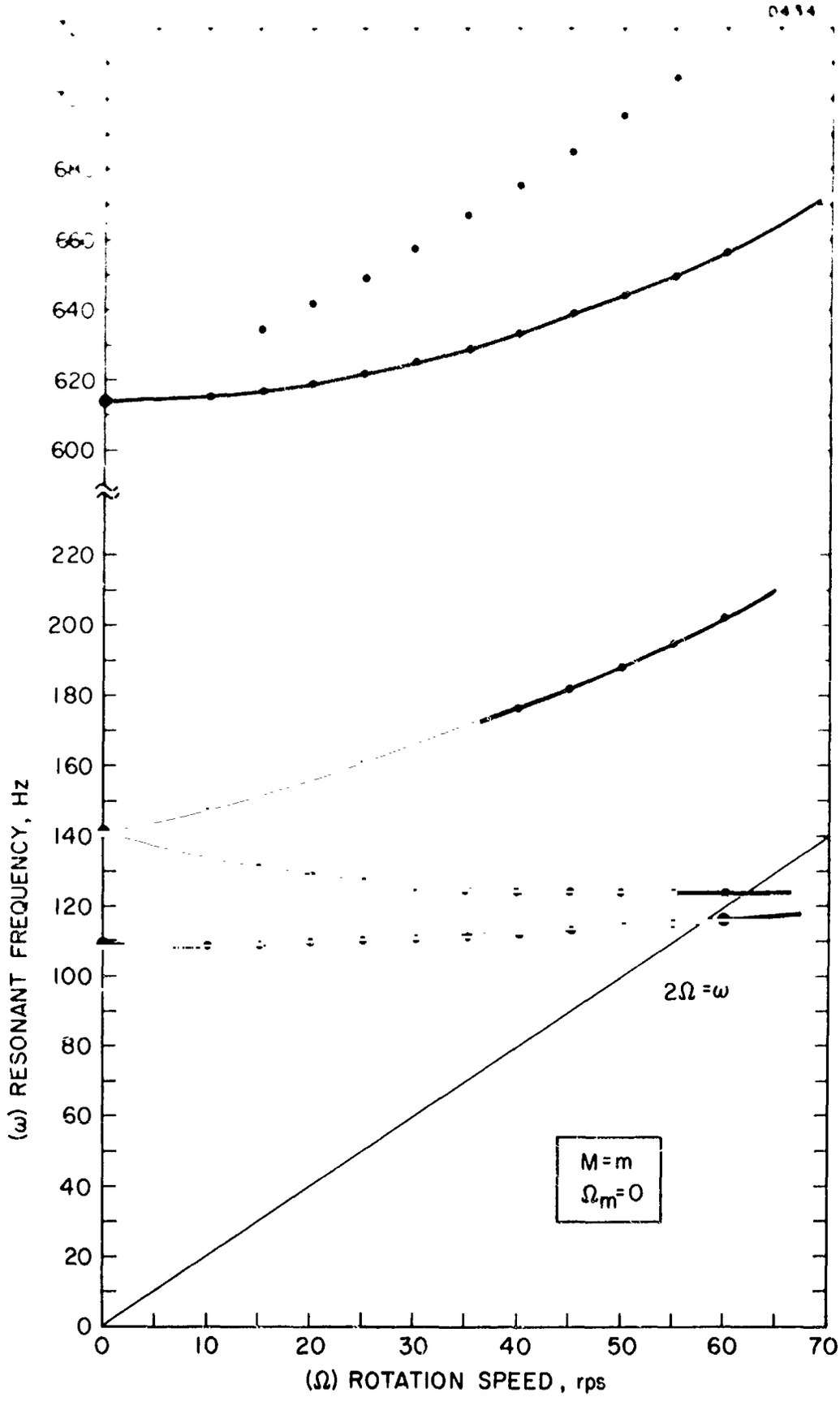

Fig. 13. Rotating sensor system resonant modes on soft mount.

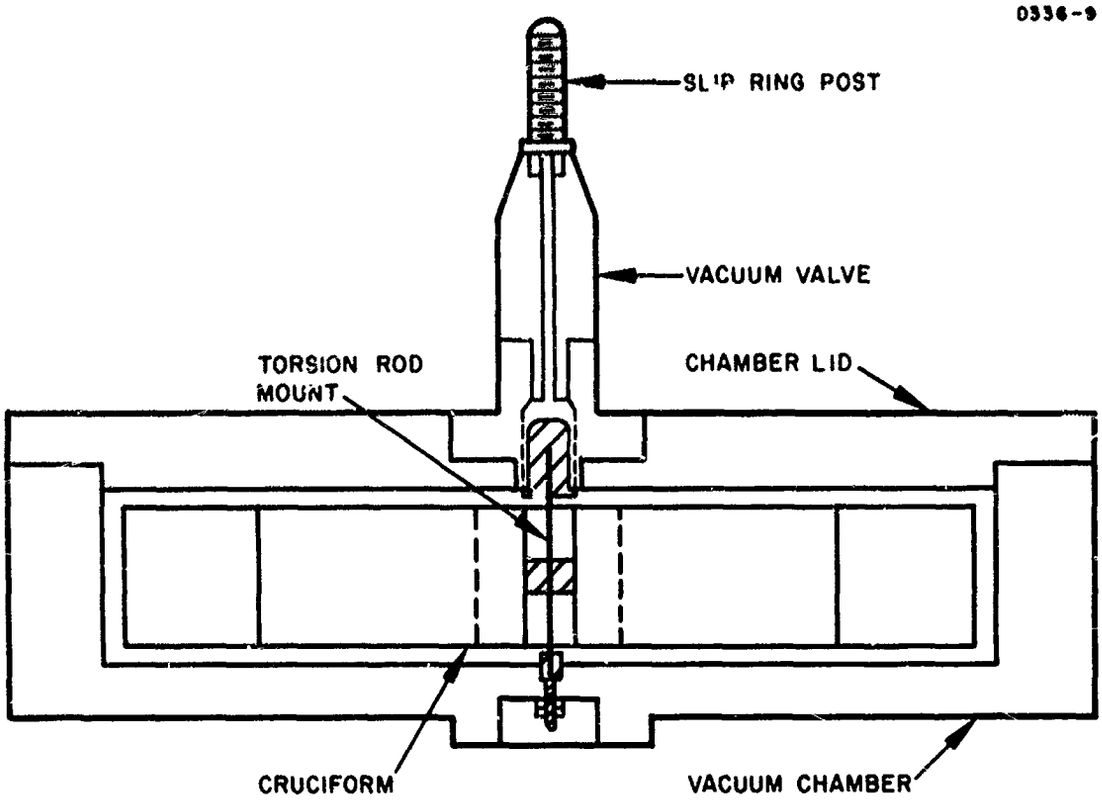

Fig. 14. Cruciform sensor on torsion wire mount.

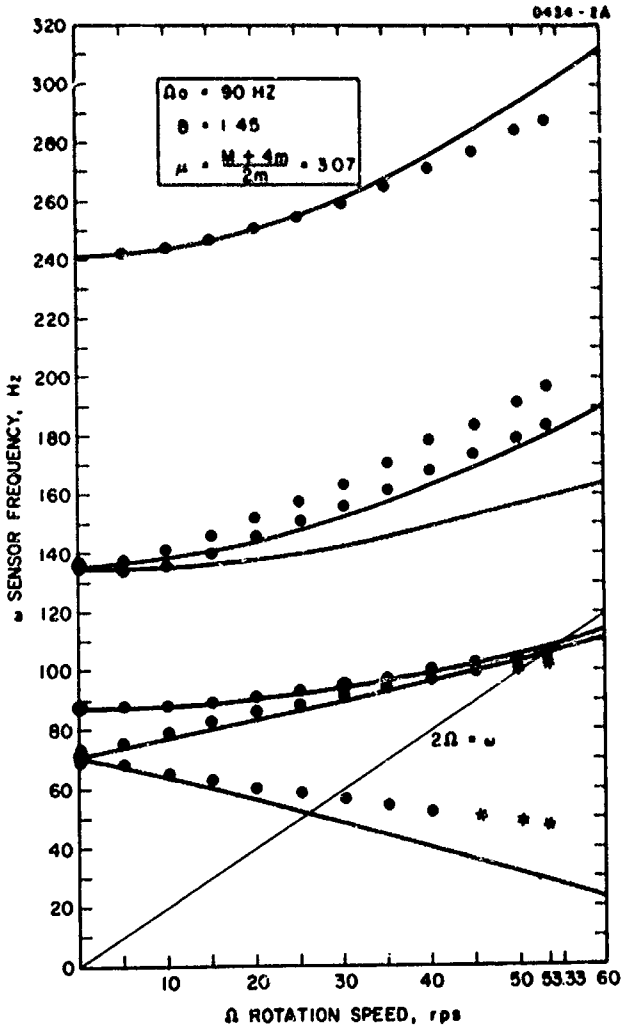

Fig. 15. Rotating sensor resonant modes on hard mount.

This indicates that the sensor had a considerable asymmetry in construction.

This time five points were taken in order to determine the sensor parameters and the mount frequency. These parameters were then used in (59), (60), and (53) to obtain the theoretical curves.

Although the theoretical curves have the same general behavior as the actual measured data, the fit is nowhere near as good as in Fig. 10 and 13. It is believed that this results primarily because the torsion wire is not a linear spring, but its spring constant depends upon the tension in the wire and the tension was increasing during rotation because of the centrifugal force acting on the unbalance in the sensor.

CONCLUSIONS

We have developed a mathematical model of a rotating, spring mounted, cruciform gravitational gradient sensor and have obtained equations describing the behavior of the normal mode frequencies of the system as a function of the system parameters and the rotation speed. These equations agree well with the data from actual sensors and can be used to aid in the design of optimum mount-sensor structures. The theory and experiment indicate that it is possible to operate a sensor at the desired rotation speed of one-half of the gradient sensing mode frequency and still maintain adequate frequency separation between the vibration sensitive translational modes and the gradient sensing mode.

ACKNOWLEDGMENT

The authors wish to acknowledge the patient and precise mechanical dexterity of Donald D. Boswell which enabled us to attain a high degree of accuracy on the experimental portion of this work.

REFERENCES

1. R. L. Forward, "Rotating tensor sensors," Bull. Am. Phys. Soc. 9, 711 (1964).

2. R. L. Forward, "Gravitational Mass Sensor," Proc. Symp. on Unconventional Inertial Sensors (Farmingdale, N. Y., 1963), pp. 36-60.

3 J. C. Crowley, S. S. Kolodkin, and A. M. Schneider, "Some properties of the gravitational field and their possible application to space navigation," IRE Trans. SET-4, 47-54 (1959).

4. M. Streicher, R. Zehr, and K. Arthur, "An Inertial Guidance Technique Usable in Free Fall," Proc. Nat. Aero. Elec. Conf. (Dayton, Ohio, 1959), pp. 768-772.

5. J. J. Carroll and P. M. Savet, "Space navigation and exploration by gravity difference detection," IAS Paper 59-61, IAS National Summer Meeting, Los Angeles, 1959; also Aerospace Eng. 18, 44-47 (1959).

6. R. E. Roberson, "Methods for the Control of Satellites and Space Vehicles, Vol. 1, Sensing and Actuating Mechanisms," WADD Tech. Rpt. 60-643 (1960).

7. R. E. Roberson, "Gravity gradient determination of the vertical," ARS J. 31, 1509-1515 (1961).

8. P. Savet, "Attitude control of orbiting satellites at high eccentricity," ARS J. 32, 1577-1582 (1962).

9. J. W. Diesel, "A new approach to gravitational gradient determination of the vertical," AIAA J. 2, 1189-1196 (1964).

10. R. E. Roberson, "Establishment of the Center of Mass and Rotational State of a Space Vehicle by Inertial Techniques," Proc. XV Inter. Astro. Cong., Warsaw, 1964.

11. R. L. Forward, "Rotating Gravitational and Inertial Sensors," presented at the AIAA Unmanned Spacecraft Meeting, Los Angeles, 1-4 March 1965.

12. C. C. Bell, R. L. Forward and J. R. Morris, "Mass Detection by Means of Measuring Gravity Gradients," presented at AIAA Second Annual Meeting, San Francisco, Calif., 26-29 July 1965.

13. R. L. Forward, D. M. Zipoy, and J. Weber, "Measurement of dynamic gravitational fields," Bull. APS 7, 320 (1962).

14. L. G. D. Thompson, R. O. Bock and P. H. Savet, "Gravity gradient sensors and their applications for manned orbital spacecraft", Third Goddard Memorial Symposium, AAS, Washington, D. C., 19 March 1965.

N... 6777

ATTACHMENT E

GENERATION AND DETECTION OF DYNAMIC GRAVITATIONAL GRADIENT FIELDS

The following paper was presented at the American Physical Society Meeting at Minneapolis, Minnesota, 20-22 June 1966. It was also submitted to the 1966 Essay Competition of the Gravity Research Foundation, New Boston, New Hampshire, and will be submitted to one of the journals of the American Physical Society in coordination with a similar paper being prepared by J. Sinsky, J. Weber, D. M. Zipoy, and R. L. Forward of the University of Maryland.

BLANK

PAGE

Generation and Detection of Dynamic Gravitational Gradient Fields*†

Robert L. Forward and Larry R. Miller†
Hughes Research Laboratories
Malibu, California

36717

ABSTRACT

We have constructed a generator of dynamic Newtonian gravitational force gradient fields and used it as a signal generator to calibrate the response of the gravitational gradient detectors being developed in our research work on gravitational mass sensors. The gravitational gradient field generator is a flat aluminum cylinder 14 cm in diameter, with four holes than can be filled with slugs of different density to create a rotating mass quadrupole moment. The generator is mounted on an air bearing supported motor and rotated at a nominal speed of 44 rps (2640 rpm). Because of the bisymmetric mass distribution, the dynamic gravitational gradient fields generated have a frequency of 88 Hz, or twice the rotation frequency. The detector is a 12 cm diameter cruciform shaped structure which responds to 88 Hz gravitational gradient forces. The small (10^{-11} cm) motions induced in the detector arms are sensed by piezoelectric strain transducers attached to the arms near the point of maximum strain. A simple vacuum

HGJ 1106

*Work partially supported by NASA contract NASW-1035.

†Presently on leave of absence on a Hughes Undergraduate Fellowship at California Institute of Technology, Pasadena, California.

‡Submitted as an essay to the Gravity Research Foundation, New Boston, N. H., 1966.

system, an iron shield plate, and spring mounts suffice for acoustic and magnetic isolation since most of the nongravitational noises were generated at 44 Hz, the rotation frequency, rather than at 88 Hz, the gravitational gradient frequency. Data taken with four different mass distributions varying from 0 to 1000 gm and separation distances varying from 4.8 to 12 cm agree well with the theory, indicating negligible nongravitational coupling. The minimum dynamic gravitational gradient field observed during this test was 6×10^{-9} sec^{-2} or 0.002 of the earth's gradient. The equivalent acceleration exerted on the sensor arms by this field was 3×10^{-11} g's.

INTRODUCTION

We are engaged in a program to design, construct, and test a research model of a gravitational mass sensor which can measure the mass of an object at a distance by using a rotating system of masses and springs (see Fig. 1) to detect the gravitational force gradient field of the object.[1,2] The ultimate objective of our work is to develop a small, rugged sensor to be used on spinning lunar orbiters to measure the mass distribution of the moon and on spinning deep space probes to measure the mass of the asteroids.

Our primary goal in this research project is to develop methods of rotating the gravitational mass sensor structures without introducing large amounts of noise into the gravitational gradient sensing mode, so that we can demonstrate the required degree of sensitivity in the laboratory without requiring flight tests to prove engineering feasibility. At present, we have demonstrated that we can measure accelerations down to 2×10^{-7} g's while operating in a 450 g rotational environment and a 1 g gravitational environment. The force level due to the earth's gravitational gradient is one order of magnitude below this. The noise

M 3615

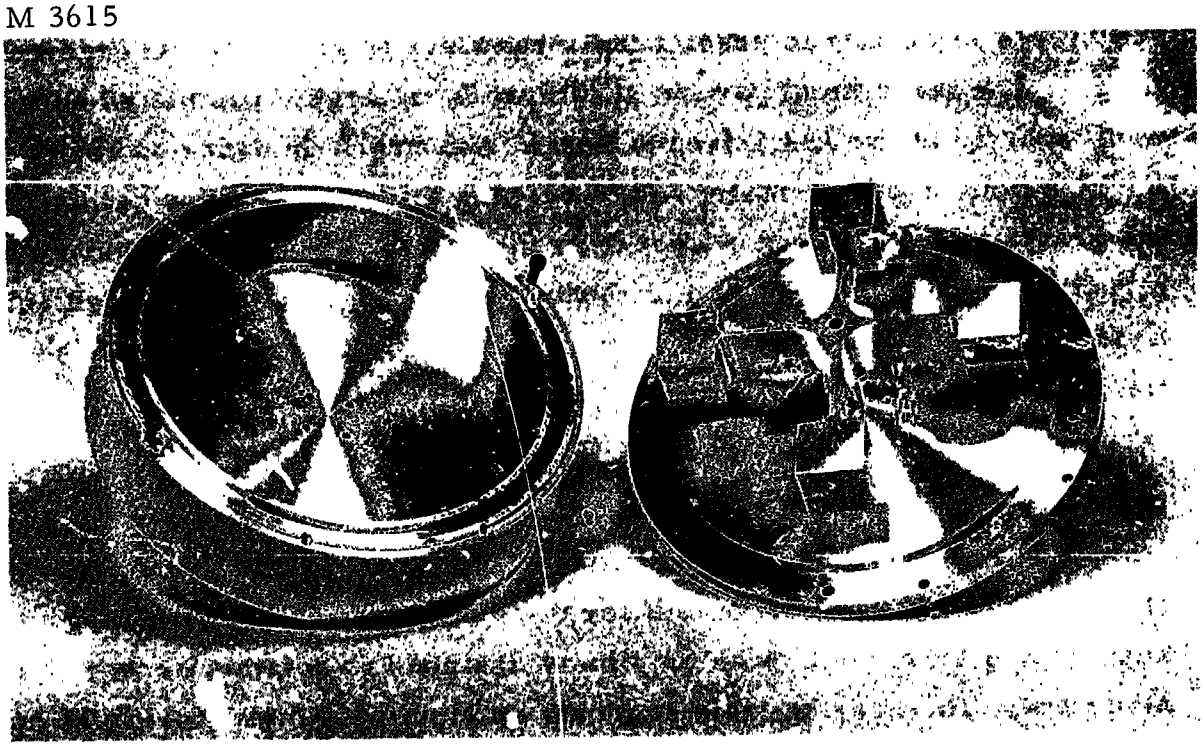

Fig. 1. Five-inch diameter cruciform gravitational mass sensor.

problems are not fundamental and work is continuing on methods for lowering the noise level to the point where gravitational gradients from laboratory masses can be seen.

A concurrent objective of our work is to learn enough about these structures to be able to predict their response to gravitational gradient fields. The theoretical portion of this work is largely completed and was reported at the AIAA Second Annual Meeting.[3] In order to verify the equations experimentally and to develop a test system for calibrating the gravitational gradient response of the various sensors, we have constructed a generator of dynamic Newtonian gravitational force gradient fields and have measured the response of one of our sensors to these fields.

DYNAMIC GRAVITATIONAL GRADIENT FIELD GENERATOR

The generator of the dynamic gravitational gradient fields is shown in Fig. 2. The drive unit for the generator is an air bearing support and drive which was originally designed to rotate a sensor structure. The bearing table supports an aluminum mass holder 14 cm in diameter with four holes, 5.0 cm in diameter and 3.5 cm deep, on a radius of 4.0 cm. Opposite pairs of holes can be filled with either aluminum, brass, or tungsten slugs which slip fit into the holes. The various pairs of mass slugs were trimmed so that static and dynamic balance of the generator was achieved even though the mass holder has a mass quadrupole moment. When balanced, the motor-generator combination is silent under all combinations of speed and mass quadrupole loading, except for a slight, high frequency hiss of the support air passing through the bearing. The motor can be operated in either a synchronous drive mode or a phase locked asynchronous mode. The readout of the generator rotation speed and phase is obtained through a photoelectric pickoff which detects paint marks on the rotor. This photoelectric signal is used as the reference signal for a lock-in amplifier, and in the asynchronous mode can also be used to supply pulses for the asynchronous drive controller.

M4181

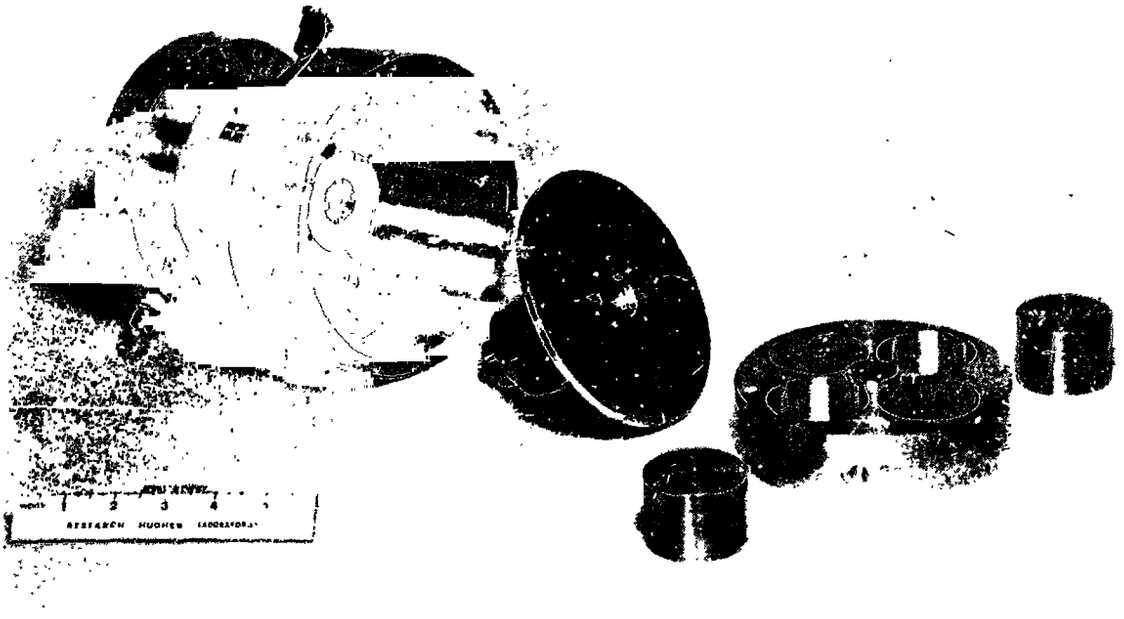

Fig. 2. Dynamic gravitational gradient field generator.

The masses of the various slugs used are

Tungsten	1212.0 g
Brass	606.0 g
Aluminum	200.0 g

If four aluminum slugs are used, the generator has no mass quadrupole moment. The maximum mass quadrupole moment of 3.8×10^4 g-cm^2 is obtained when two tungsten slugs are used and the other two holes are left empty. When the opposing pair of holes is filled, the effective mass is just the mass difference. The various combinations possible with our present setup are listed below.

Holes 1 and 3	Holes 2 and 4	Effective Mass, g
Tungsten	Empty	1212.0
Tungsten	Aluminum	1012.0
Tungsten	Brass	606.0
Brass	Empty	606.0
Brass	Aluminum	406.0
Aluminum	Empty	200.0
Aluminum	Aluminum	0.0

The generator rotates at a nominal speed of 44 rps (2640 rpm); because of the bilateral or tensorial character of the mass quadrupole generators, the ac gravitational gradient fields generated are at 88 Hz, or twice the rotation frequency. (See Appendix.)

DETECTOR

The detector used in this first test was one of our adjustable sensors (see Fig. 3). The sensing masses of the detector are 20 gm brass weights attached to the sensor arms by a screw-clamp arrangement. The weights have an eccentric cam arrangement which allows for

M 4131

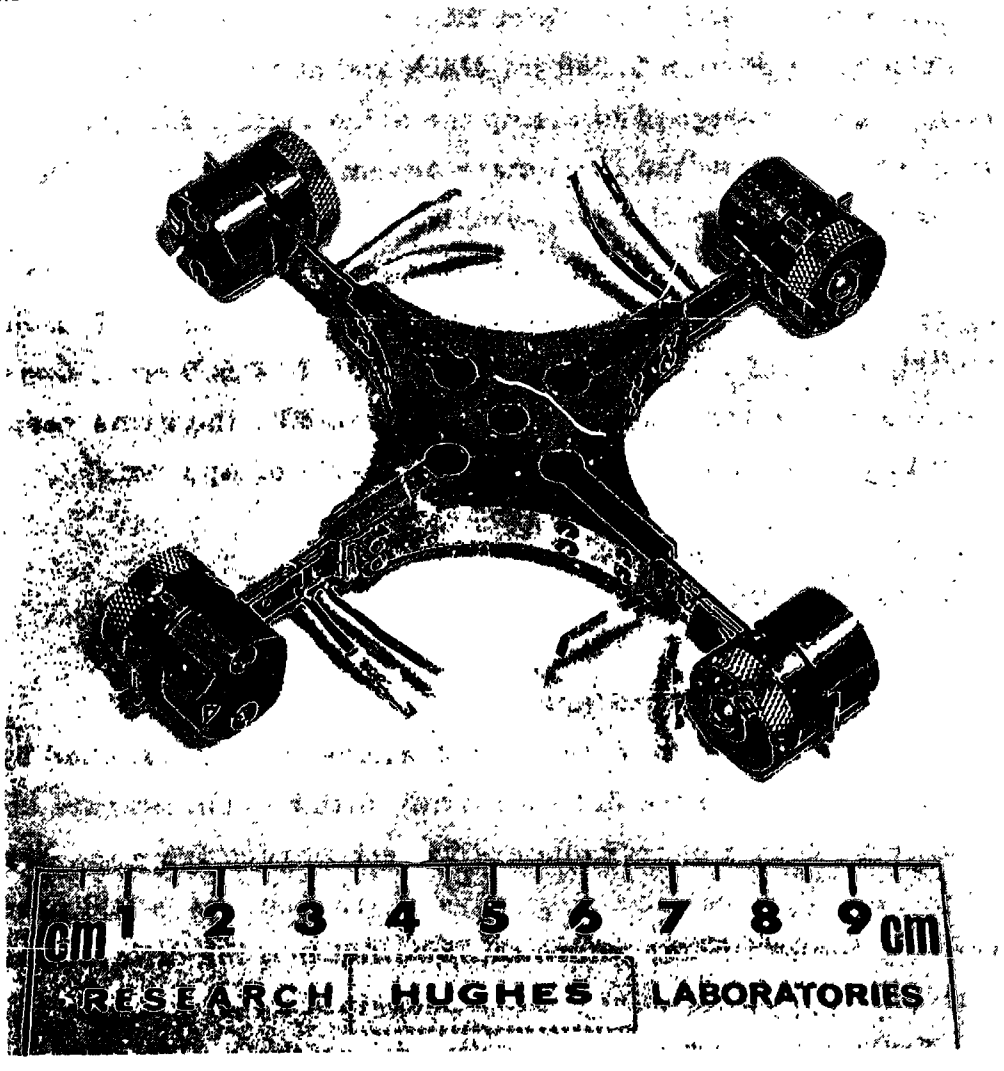

Fig. 3. Adjustable sensor.

small position adjustments on the arms. The arms are cantilever beams of aluminum with a 0.125 in. thick base where they fasten to the hub and an outer bending portion 0.030 in. thick and about 0.70 in. long. The aluminum hub is designed to clamp the arms rigidly for good cross coupling and yet allow the arm-mass assembly to be moved in and out for mass balance of the final assembly.

The detector has a resonant frequency of 88.45 Hz in the dual tuning fork or gravity gradient sensing mode (see Fig. A-2 in the Appendix), a Q of 120 and an arm length of $\ell = 5.0$ cm. Under the influence of a gravitational gradient of $\Gamma \sin 2\Omega t$, the arms respond with a vibrational amplitude of (see eq. (A-21) of Appendix)

$$\Delta = \frac{Q\ell}{(2\Omega)^2} \Gamma \cos 2\Omega t = 1.95 \times 10^{-3} \text{ cm/sec}^2 \Gamma \cos 2\Omega t \qquad (1)$$

where $2\Omega = 2\pi \times 88.45$ rad/sec.

The readout of the detector vibrations is accomplished by sensing the dynamic strains of the detector arms with barium titanate strain transducers. A pair of transducers were reversed from the arrangement shown in Fig. 3 so that opposing pairs of transducers would produce a differential output voltage which could be fed into the differential input of a Princeton Applied Research HR-8 Lock-in Amplifier.

The dynamic strain in the arms due to their deflection is a strong function of the details of the design of the detector arms, and is difficult to calculate accurately because of the complex mechanical structure used. The relationship predicted in Ref. 3 is

$$\epsilon = \frac{(b + L)\, c}{(L^3/3 + bL^2 + b^2 L)} \Delta = 0.026 \text{ cm}^{-1} \Delta \qquad (2)$$

where $b = 0.3$ cm is the radius of the end mass, $L = 1.8$ cm is the length of the arm, and $c = 0.038$ cm is the half thickness of the arm.

The barium titanate strain transducers extend over a considerable portion of the arm; therefore, they measure an averaged value of the strain, which is a maximum at the hub and zero at the end. This average measured strain was estimated as

$$\epsilon_t = 0.6\,\epsilon = 0.016\ \mathrm{cm}^{-1}\,\Delta \ . \qquad (3)$$

The transducers used on the detector had been calibrated on a test setup which compared them with a resistive strain gauge using pure longitudinal strains at 1600 Hz. The transducer factor obtained under these conditions was about $\sigma = 0.7 \times 10^5$ V/unit strain. Thus the voltage output from this sensor should be approximately

$$V = \sigma\epsilon_t = 1.1 \times 10^3\ \mathrm{V/cm}\ \Delta = 2.2\ \mathrm{V/sec}^2\ \Gamma \cos 2\Omega t \ . \qquad (4)$$

NONGRAVITATIONAL COUPLING

It is obvious that in order to detect the very weak ac gravitational forces being generated by the rotating mass quadrupole, the generator and detector must be well shielded from each other to prevent acoustic and electromagnetic coupling. The detector is highly sensitive to acoustic noise with a frequency component at its resonance frequency, but experience has shown that the acoustic noise can be eliminated by placing the detector in a vacuum chamber at a few milliTorr.

Although an ideal detector is theoretically insensitive to vibrations of the mounting structure,[3] in practice a small amount of the vibrations in the mount leak into the gradient sensing mode. Because of this, an effort must be made to keep the detector mount vibrations at a low level. This was accomplished by suspending the detector in the chamber with a spring, and the chamber from the ceiling by another spring. The generator was isolated from the workbench by compression springs, and the iron shield plate was vibrationally isolated from both the generator and detector by its own support springs (see Fig. 4).

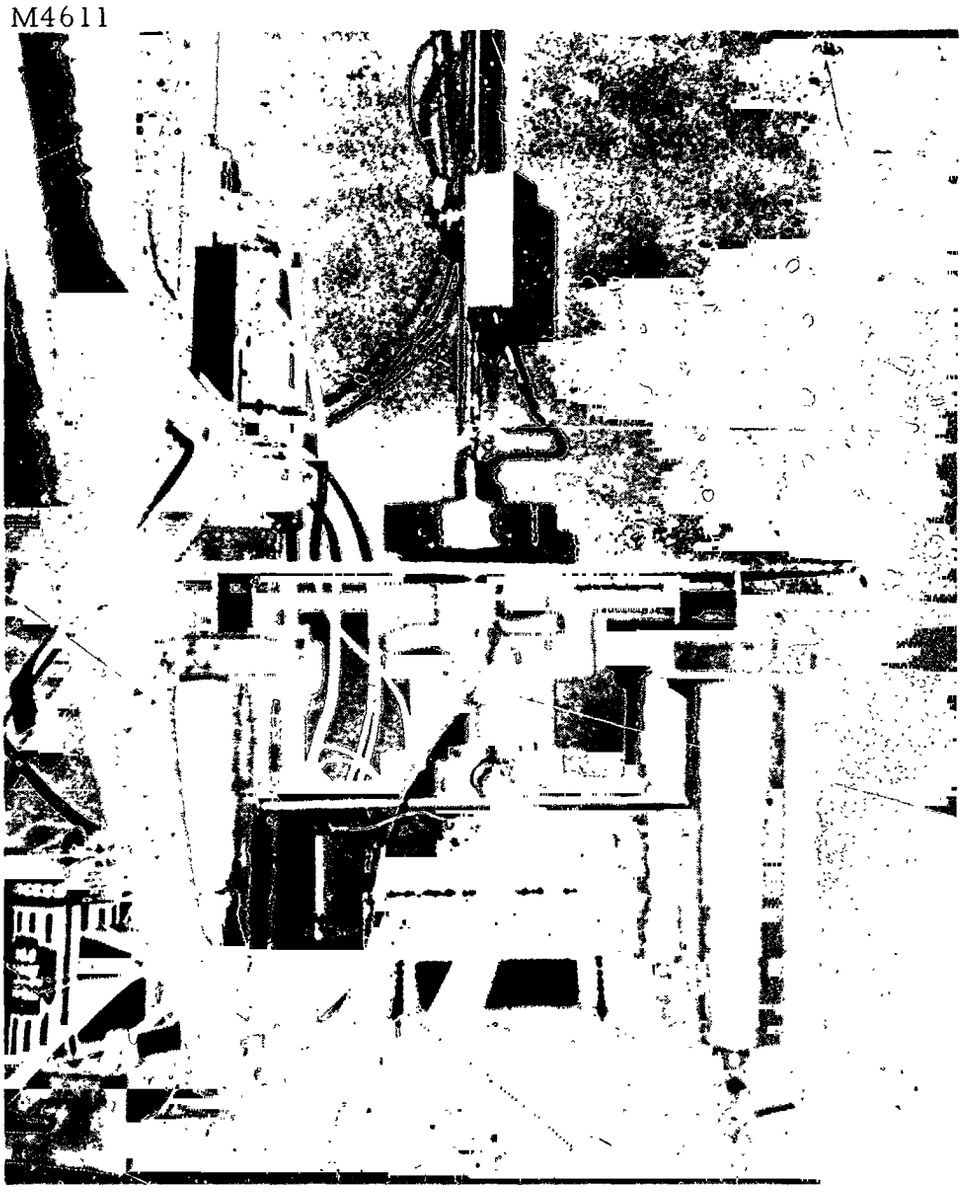

Fig. 4. Relative position of generator and detector.

Electromagnetic coupling can occur in two ways: (1) by direct interaction of the rotating magnetic fields of the motor with the arms of the detector; (2) by stray electromagnetic voltages or currents entering the detector output leads or the preamplifier. The electromagnetic coupling into the output electronics is easily checked, since it is independent of the resonant response of the detector and was found to be unobservable even in the single ended mode of operation, although all data were taken with a differential input to insure that pickup was not a problem.

Direct coupling of the rotating magnetic fields around the generator motor into the detector was found to be a major problem. At first it was not well understood, since the detector arms were of aluminum and the detector masses of brass. This interaction was originally eliminated by using a phase locked asynchronous drive. In this mode of operation of the generator, the generator motor is driven by currents at some higher frequency, typically 200 Hz, so they do not excite the detector resonant mode. The amplitude of the drive voltage is controlled by a servo loop so that the rotor remains at a constant speed of 44 rps. The servo loop is so tight that both the frequency and the phase of the rotor are held tightly to the phase of a reference signal from a precise oscillator (General Radio Frequency Synthesizer). It was later discovered that the detector had been assembled with stainless steel screws; when they were replaced by brass screws, the magnetic coupling was eliminated and it was possible to take good data using synchronous drive on the generator.

One important factor aided greatly in the problem of eliminating the nongravitational coupling between the generator and the detector. Because of the double mass in the mass quadrupole, the generator is rotated at <u>half</u> of the detector frequency. Therefore, predominantly all of the acoustic and electromagnetic energy produced by the generator is at a frequency which is outside the detector response frequency; only that small portion of the energy which is harmonically generated at twice the rotation frequency must be shielded against.

The generator was designed specifically for the problem of determining the nongravitational coupling effects. If four aluminum slugs are put in the mass holder, the generator has no time varying mass quadrupole moment and therefore no dynamic gravitational gradient field; however, it still retains all of its electromagnetic and acoustic properties. A test run was made at 5 cm separation distance using the four aluminum slugs. The generator speed was varied from 43 to 45 rps, so that the detector mode frequency of 88 Hz was not missed. The detector output remained at 0 ± 4 nV. The rotor was then deliberately unbalanced so that the acoustic output was noticeably increased and the test was rerun, with the same results. These experiments demonstrated that the response of the detector structure and sensor electronics to nongravitational forces arising from all sources, including the generator, was less than 4 nV.

DETECTOR CALIBRATION

After the test for nongravitational coupling, two of the aluminum slugs were replaced with tungsten slugs, resulting in a mass difference of 1012 g. The rotor was rebalanced and the generator and detector were placed 5 cm apart. The theoretical calculations presented in the Appendix indicate that at this distance, and with this size detector, a 1012 g effective mass should produce an equivalent gravitational force gradient of

$$\Gamma \sin 2\Omega t = 1.25 \times 10^{-7} \sin 2\Omega t \quad \text{sec}^{-2} \ . \tag{5}$$

The dynamic gradient has an amplitude of about 0.04 of the earth's gravitational force gradient.

From the theory of operation of the sensors,[3] this gradient should cause the gravitational gradient sensing mode of the detector to oscillate with an amplitude of (see eq. (1))

$$\Delta = 2.5 \times 10^{-10} \cos 2\Omega t \quad \text{cm} \ . \tag{6}$$

Although the amplitude of these motions is extremely small, of the order of 0.01 of the diameter of an atom, they are easily measured if piezoelectric strain transducers are used. Similar sensing techniques used on the gravitational radiation detectors at the University of Maryland[4] have measured motions down to 10^{-14} cm.

The motion induced in the detector causes an average strain in the arms of

$$\epsilon_t = 3.9 \times 10^{-12} \cos 2\Omega t \ . \qquad (7)$$

If we assume that the transducer calibration is $\sigma = 0.7 \times 10^5$ V/strain, the predicted output of these sensors under excitation by a generator with a 1 kg mass difference at a 5 cm separation distance would be

$$V = 2.2 \text{ V/sec}^2 \ \Gamma \cos 2\Omega t = 270 \cos 2\Omega t \quad \text{nV (predicted)}, \qquad (8)$$

or an rms voltage of 190 nV.

When the test was run, the actual measured output voltage of one arm of the sensor under these conditions was 97 ± 3 nV (rms). This is much larger than the output voltage fluctuations of 4 nV under the control conditions using the four aluminum masses, and is half the predicted output. The exact reason for this lower output is not known, but it is assumed that it is a result of the difficulty in obtaining an accurate calibration of the strain transducers, or in calculating the strain from the deflection Δ. The gravity gradient input to detector voltage output relationship for the adjustable detector obtained from this calibration is

$$V = 1.1 \text{ V/sec}^2 \ \Gamma \cos 2\Omega t \ . \qquad (9)$$

VERIFICATION OF GRAVITATIONAL COUPLING

Although the control experiments with the four aluminum slugs and the balanced and unbalanced rotor indicated that the nongravitatonal coupling was negligible, it was still possible that the replacement of the aluminum slugs with the tungsten slugs could change the magnetic moment or balance of the generator and cause nongravitational coupling. In order to further insure that the voltage output seen was caused only by gravitational gradient coupling, a run of data was taken at various separation distances and with various mass quadrupole moments. (One of the aluminum slugs froze in its hole in the generator during the preliminary work so it was possible to try only four different mass quadrupole arrangements.)

At the start of the experiment, the phase of the lock-in detector was adjusted to give a maximum output with the tungsten slugs and was not adjusted or peaked during the remainder of the data run. The quadrature voltage was monitored periodically to insure the detection of any phase shift in the signal induced by any variation in the relative strength of the gravitational coupling and any synchronous nongravitational coupling. No quadrature component was detected during the data runs.

With the tungsten slugs in the generator, a set of data was taken while the separation distance was varied from 4.8 cm to 12 cm. The generator was then stopped and the tungsten slugs replaced with brass slugs, resulting in an effective mass difference of 406.0 gm. Without adjustment to the sensor electronics, a second set of data was taken from 4.8 cm to 10 cm. The generator was again stopped and the brass slugs removed, leaving a void or relative mass difference of - 200 gm. The phase knob of the lock-in detector was switched exactly 180° to account for the effective negative mass, or 180° signal phase difference, and the third set of data taken from 4.8 cm to 8 cm. When aluminum slugs were placed in all four holes, the output was 0 ± 3 nV. The data are plotted in Fig. 5.

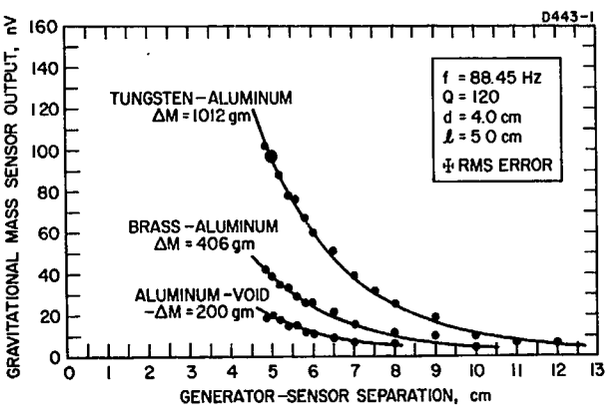

Fig. 5. AC gravitational coupling between rotating mass quadrupole and cruciform gravitational mass sensor.

Curves of detector output versus separation distance were then calculated and plotted in Fig. 5 for various mass quadrupole moments using the theoretical equations (A-15) and (A-16) derived in the Appendix. For conversion of the calculated equivalent gravitational gradient field to sensor voltage output, we used the calibration point at 5 cm and 97 nV (larger data point). The two lower curves are the upper curve multiplied by 0.4 and 0.2, respectively.

The excellent agreement of the data with the theoretical predictions in amplitude and phase for various conditions of mass quadrupole moment and separation distance indicates that only gravitational energy was being transmitted from the generator to the detector. The minimum dynamic gravitational gradient field observed during this test was about 6×10^{-9} sec^{-2} (6 Eötvös units) or 0.002 of the earth's gradient. The effective acceleration on the 5 cm long detector arms due to this field was

$$a = \Gamma \ell = 3 \times 10^{-8} \text{ cm/sec}^2 = 3 \times 10^{-11} \text{ g's} \qquad (10)$$

and the effective force level on the 20 gm detector masses was

$$F = ma = 6 \times 10^{-7} \text{ dynes} \quad . \qquad (11)$$

SUMMARY

We have constructed a generator of 88 Hz gravitational gradient fields and used the fields to calibrate the response of a dynamic gravitational gradient sensor. The test involved the transmission of gravitational signals over distances up to 12 cm.

APPENDIX

GRAVITATIONAL INTERACTIONS BETWEEN A CRUCIFORM DETECTOR AND A ROTATING MASS QUADRUPOLE

The model which we will use to calculate the gravitational interaction between a rotating mass quadrupole and a resonant cruciform gravitational mass sensor is shown in Fig. A-1. The generator is assumed to be two spherical masses of mass M separated by a distance 2d and rotated about their center of mass at a constant angular frequency $\dot{\theta} = \Omega$. The detector is assumed to be four spherical masses of mass m on orthogonally disposed massless arms of length ℓ. The sensor is supported from above so that its center of mass is at a height h directly above the center of mass of the generator. The particular mode of the sensor used to sense the gravitational gradient forces is the dual tuning fork mode (see Fig. A-2). It was shown in previous analyses[3] that this mode does not respond to vibrational forces at the mount nor to the direct gravitational force field, but only to the gradient of the gravitational force field.

The forces on the sensor resulting from the gravitational interaction between the rotating masses M_c and the sensor masses m_i typically consist of

$$F_{ic} = -\frac{G M m}{R_{ic}^2} \qquad \begin{array}{l} i = 1 \text{ to } 4 \\ c = a, b \\ m_i = m \\ M_c = M \end{array} \qquad \text{(A-1)}$$

where

$$R_{ic}^2 = h^2 + r_{ic}^2 \qquad \text{(A-2)}$$

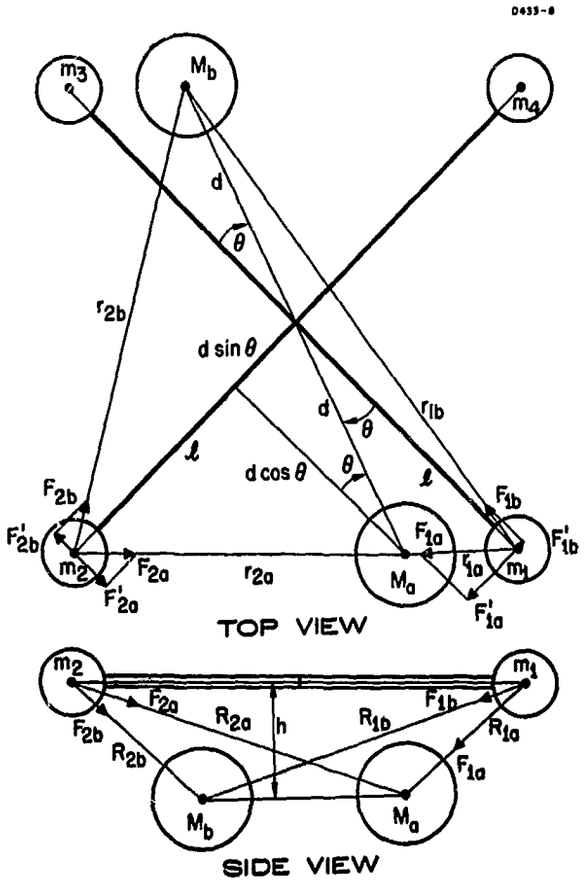

Fig. A-1. Model for gravitational interaction calculation.

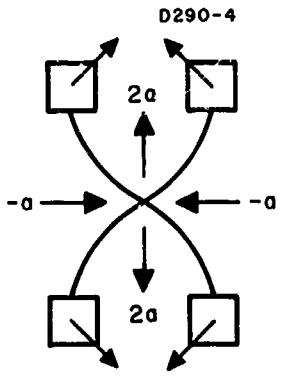

Fig. A-2.
Gravity gradient
sensing mode.

and

$$
\begin{aligned}
r_{3a}^2 &= r_{1a}^2 = \ell^2 + d^2 - 2\ell d \cos\theta \\
r_{3b}^2 &= r_{1b}^2 = \ell^2 + d^2 + 2\ell d \cos\theta \\
r_{4a}^2 &= r_{2a}^2 = \ell^2 + d^2 - 2\ell d \sin\theta \\
r_{4b}^2 &= r_{2b}^2 = \ell^2 + d^2 + 2\ell d \sin\theta \quad .
\end{aligned}
\tag{A-3}
$$

However, the components of the forces which drive the sensing mode of the detector are the tangential components of the forces F_{ic}

$$
\begin{aligned}
F'_{3a} &= F'_{1a} = \frac{G M m}{R_{1a}^3} d \sin\theta \\
F'_{3b} &= F'_{1b} = -\frac{G M m}{R_{1b}^3} d \sin\theta \\
F'_{4a} &= F'_{2a} = -\frac{G M m}{R_{2a}^3} d \cos\theta \\
F'_{4b} &= F'_{2b} = \frac{G M m}{R_{2b}^3} d \cos\theta
\end{aligned}
\tag{A-4}
$$

where the sense of the forces is taken to be positive in the clockwise direction.

The resultant force F'_i on each of the arms due to the forces F'_{ic} is given by

$$F_3' = F_1' = F_{1a}' + F_{1b}' = GMmd \left[\frac{1}{R_{1a}^3} - \frac{1}{R_{1b}^3} \right] \sin\theta \tag{A-5}$$

$$F_4' = F_2' = F_{2a}' + F_{2b}' = -GMmd \left[\frac{1}{R_{2a}^3} - \frac{1}{R_{2b}^3} \right] \cos\theta \quad .$$

The response of the detector arms to these resultant forces has been presented in a previous work by Bell, Forward, and Morris.[3] Taking a simplified version of their equations (38) through (41), we obtain

$$m\ddot{\Delta}_i + d\dot{\Delta}_i + k\Delta_i = F_i' \qquad i = 1 - 4 \tag{A-6}$$

where Δ_i is the deflection of the i^{th} arm, k is the spring constant, and d is the damping.

These four equations (A-6) describe the individual motions of the four arms; however, the vibrations of interest are the motions of the gravity gradient sensing mode (see Fig. A-2). The equation for this mode is obtained by the following linear combination of the individual arm motions[5]

$$\Delta_g = \frac{1}{2} (\Delta_1 - \Delta_2 + \Delta_3 - \Delta_4) \tag{A-7}$$

where the normalization factor of 1/2 is used so that the detector energy expressed in terms of the four arm amplitudes is equivalent to the detector energy expressed in terms of the four vibrational mode amplitudes (gravity gradient, torsional, and two translational).[5]

If we add the equations for the four arm motions (eqs. (A-6)) in this manner, we obtain the equation of motion for the gravity gradient sensing mode

$$m\ddot{\Delta}_g + d\dot{\Delta}_g + k\Delta_g = \frac{1}{2}\,(F_1' - F_2' + F_3' - F_4') = F_g \qquad \text{(A-8)}$$

where

$$F_g = G\,Mmd\left[\left(\frac{1}{R_{1a}^3} - \frac{1}{R_{1b}^3}\right)\sin\theta + \left(\frac{1}{R_{2a}^3} - \frac{1}{R_{2b}^3}\right)\cos\theta\right]. \qquad \text{(A-9)}$$

Because R_{ic} is a function of the angle θ, the resultant force F_g has a complex behavior with the angle of rotation. To calculate the components of the resultant force as a function of frequency, we will expand the terms in R_{ic}^{-3}. Letting

$$R^2 = \ell^2 + d^2 + h^2 \quad , \qquad \text{(A-10)}$$

we can write the resultant force F_g as

$$F_g = G\,Mmd\left\{\left[(R^2 - 2\ell d\cos\theta)^{-3/2} - (R^2 + 2\ell d\cos\theta)^{-3/2}\right]\sin\theta + \left[(R^2 - 2\ell d\sin\theta)^{-3/2} - (R^2 + 2\ell d\sin\theta)^{-3/2}\right]\cos\theta\right\}. \qquad \text{(A-11)}$$

Bringing R^2 out from the denominator and letting $\Lambda = (\ell d/R^2)$, we obtain

$$F_g = \frac{G\,Mmd}{R^3}\left\{\left[(1 - 2\Lambda\cos\theta)^{-3/2} - (1 + 2\Lambda\cos\theta)^{-3/2}\right]\sin\theta + \left[(1 - 2\Lambda\sin\theta)^{-3/2} - (1 + 2\Lambda\sin\theta)^{-3/2}\right]\cos\theta\right\}. \qquad \text{(A-12)}$$

We now expand each term using the binomial expansion theorem; however, because the expansion parameter Λ can be as high as $1/3$ when the

generator and detector are separated by 4.5 cm, it is necessary to take the expansion out to the seventh order.

$$F_g = \frac{G\,Mmd}{R^3}\left\{\left[6\Lambda\cos\theta + 35\Lambda^3\cos^3\theta + \frac{693}{4}\Lambda^5\cos^5\theta + \frac{6435}{8}\Lambda^7\cos^7\theta\right]\sin\theta + \left[6\Lambda\sin\theta + 35\Lambda^3\sin^3\theta + \frac{693}{4}\Lambda^5\sin^5\theta + \frac{6435}{8}\Lambda^7\sin^7\theta\right]\cos\theta\right\}. \quad \text{(A-13)}$$

(The even order terms drop out because of the symmetry.) If we rearrange the above equation and use the trigonometric identities

$$\begin{aligned} 2\sin\theta\cos\theta &= \sin 2\theta \\ 2(\cos^3\theta\sin\theta + \sin^3\theta\cos\theta) &= \sin 2\theta \\ 16(\cos^5\theta\sin\theta + \sin^5\theta\cos\theta) &= 5\sin 2\theta + \sin 6\theta \\ 32(\cos^7\theta\sin\theta + \sin^7\theta\cos\theta) &= 7\sin 2\theta + 3\sin 6\theta\ , \end{aligned} \quad \text{(A-14)}$$

we can obtain the expression

$$F_g = \frac{6\,G\,Mm\ell d^2}{R^5}\left\{\left(1 + \frac{35}{12}\Lambda^2 + \frac{1155}{128}\Lambda^4 + \frac{15015}{512}\Lambda^6\right)\sin 2\Omega t + \left(\frac{231}{128}\Lambda^4 + \frac{6435}{512}\Lambda^6\right)\sin 6\Omega t\right\} \quad \text{(A-15)}$$

where we brought out a factor of $6\Lambda = 6\ell d/R^2$ from behind the brackets. This expression shows that the interaction force between the generator and detector is complicated at close distances of separation and depends upon the sizes of the generator and detector, as well as the separation distance. This expression also shows that in addition to responding to the gravitational force gradient or the second order gradient of the

potential at 2Ω, the detector will also respond to the sixth order gradient of the potential at 6Ω. Because of the symmetry of the generator-detector combination, the intermediate higher order gradients are not observable.

In order to relate the equation for the effective force on the gravitational gradient sensing mode of the detector (A-15) to the previous work, we define an equivalent gravitational force gradient by the relation

$$\Gamma = F_g/2m\ell \qquad \text{(A-16)}$$

where m is the effective mass and 2ℓ is the effective length of the gravitational gradient sensing mode.

The effective gravitational force gradient (A-16) was computer calculated for various values of the separation distance h, and the results for the amplitudes of the two frequency components are plotted in Fig. A-3. For this curve it was assumed that the detector had an effective radius of 5 cm, and the generator consisted of two 1 kg masses on a radius of 4 cm. At the nominal separation distance of 5 cm, the effective gravitational force gradient resulting from the generator is 1.24×10^{-7} sec^{-2}. This is about 0.04 of the earth's gradient. These two relatively small masses have a relatively large gradient because we are able to bring the center of mass of the detector very close to the center of mass of the generator.

At distances greater than 12 cm, the only important term in (A-16) is the first, and the effective gravitational gradient is given by the formula

$$\Gamma = \frac{3\,GMd^2 \sin 2\Omega t}{(h^2 + d^2 + \ell^2)^{5/2}} \approx \frac{3\,GMd^2}{h^5} \sin 2\Omega t \ . \qquad \text{(A-17)}$$

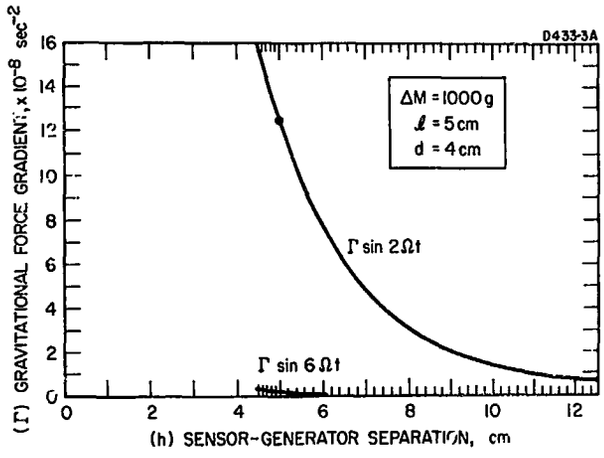

Fig. A-3. Calculated equivalent gravitational force gradient.

The gradient is falling off as d^2/h^5 rather than as $1/h^3$ because the detector is only sensitive to the dynamic gradient being generated by the rotating mass quadrupole moment of the generator and is not sensitive to the static gradient of its monopole moment which does fall off as $1/h^3$.

If we choose the rotation speed Ω of the generator so that the detector senses the gravitational force gradient fields being generated at twice the rotation speed

$$\frac{k}{m} = (2\Omega)^2 \quad , \tag{A-18}$$

then the gravitational forces at 2Ω are seen to be driving terms in the equation of motion of the vibrational mode (eq. (A-8)):

$$\ddot{\Delta}_g + \frac{d}{m}\dot{\Delta}_g + (2\Omega)^2\Delta_g = 2\Gamma\ell \sin 2\Omega t \quad . \tag{A-19}$$

The solution to this equation is well known as

$$\Delta_g = -2\Gamma\ell \frac{Q}{(2\Omega)^2} \cos 2\Omega t \tag{A-20}$$

where Δ_g is the amplitude of the vibrational mode and $Q = 2\Omega m/d$ is the quality factor of the resonance.

In practice we do not measure the mode amplitude directly, but instead measure the amplitude of one of the arms

$$\Delta_l = \frac{1}{2}\Delta_g = -\Gamma\ell \frac{Q}{(2\Omega)^2} \cos 2\Omega t \quad . \tag{A-21}$$

REFERENCES

1. R. L. Forward, "Gravitational Mass Sensor," Proc. Symp. on Unconventional Inertial Sensors (Farmingdale, New York, 1963), pp. 36-60.

2. R. L. Forward, "Rotating Gravitational and Inertial Sensors," Proc. AIAA Unmanned Spacecraft Meeting (Los Angeles, Calif., 1965), pp. 346-351.

3. C. C. Bell, R. L. Forward, and J. R. Morris, "Mass Detection by Means of Measuring Gravity Gradients," presented at AIAA Second Annual Meeting, San Francisco, Calif., 26-29 July 1965; also AIAA Paper 65-403.

4. J. Weber, "Gravitational Waves," in Gravitation and Relativity, H.-Y. Chiu and W. F. Hoffman, Eds., (W. A. Benjamin, Inc., New York, 1964), p.100, Chap. 5.

5. C. C. Bell, J. R. Morris, J. M. Richardson, and R. L. Forward, "Vibrational Mode Behavior of Rotating Gravitational Gradient Sensors," to be presented at the AIAA/JACC Guid. and Control Spec. Conf., Seattle, Washington, 15-17 August 1966.

N66 36778

ATTACHMENT F

NONIDEAL BEHAVIOR OF ROTATING GRAVITATIONAL MASS SENSORS

The following attachment was published as a Research Report and has been submitted to the AIAA for publication in the Journal of Spacecraft and Rockets.

HUGHES RESEARCH LABORATORIES
Malibu, California

a division of hughes aircraft company

Research Report No. 354

NONIDEAL BEHAVIOR OF ROTATING GRAVITATIONAL MASS SENSORS

D. Berman
Theoretical Studies Department

June 1966

TABLE OF CONTENTS

PRECEDING PAGE BLANK NOT FILMED.

LIST OF ILLUSTRATIONS

PRECEDING PAGE BLANK NOT FILMED

ABSTRACT

A mathematical model of a nonideal gravitational mass sensor was formulated from basic Lagrangian principles. The model was checked against existing sensor behavior theory by consideration of the simplified "ideal" case. Next, a special case of the nonideal sensor was studied, where the center of mass of the sensor was held constant. This case was of academic interest, because it offered basic insight into the coupling effect of sensor imperfections and the gravity signal. Finally, the general nonideal equations were computer mechanized. Typical results are presented which consist of a wide variety of external disturbances and sensor parameter values. Specific hardware design considerations were then studied and indicated the desirability of weak sensor-to-platform coupling and high manufacturing precision.

BLANK
PAGE

I. INTRODUCTION

Gravitational mass sensors have been under development at Hughes Research Laboratories since 1964. Figure 1 shows a typical mechanical design. The description and operating behavior of these devices already appear in the literature.[1,2] However, all previous analyses have been concerned with operation of an "ideal" sensor. In this paper, a general mathematical description of a gravitational mass sensor has been formulated, including the nonideal effects of manufacturing imperfections and external disturbances. Manufacturing imperfections may include deviations among sensor arm masses, lengths, and spring constants. In addition, the inability to locate the center of geometry at the center of mass (C.G. offset) should be considered. External disturbances can include translational oscillations introduced at the mounting of the central hub. Equations are derived which are sufficiently general to describe sensor behavior under these effects.

It is important to understand nonideal sensor behavior because sensor imperfections may cause distortions of the gravity signal. Analysis of an ideal sensor does not predict these distortions or the "noise" which results from sensor imperfections. External disturbances acting upon an "ideal" sensor do not disturb the gravity signal in any way. Therefore, in order to eliminate the mechanical noise which is generated in a real gravitational device, the nonideal effects must be thoroughly understood.

II. DERIVATION OF GENERAL EQUATIONS

This section outlines the mathematical steps which lead from the Lagrangian description of the physical system to working differential equations, which are ultimately solved in later sections. Based on the cruciform gravitational sensor shown in Fig. 1, the model used for analysis is described by Fig. 2. The symbols are defined as follows:

m_n = mass of arm n

a_n = arm length of arm n n = 1, 2, 3, 4

h = center of mass offset.

M 3615

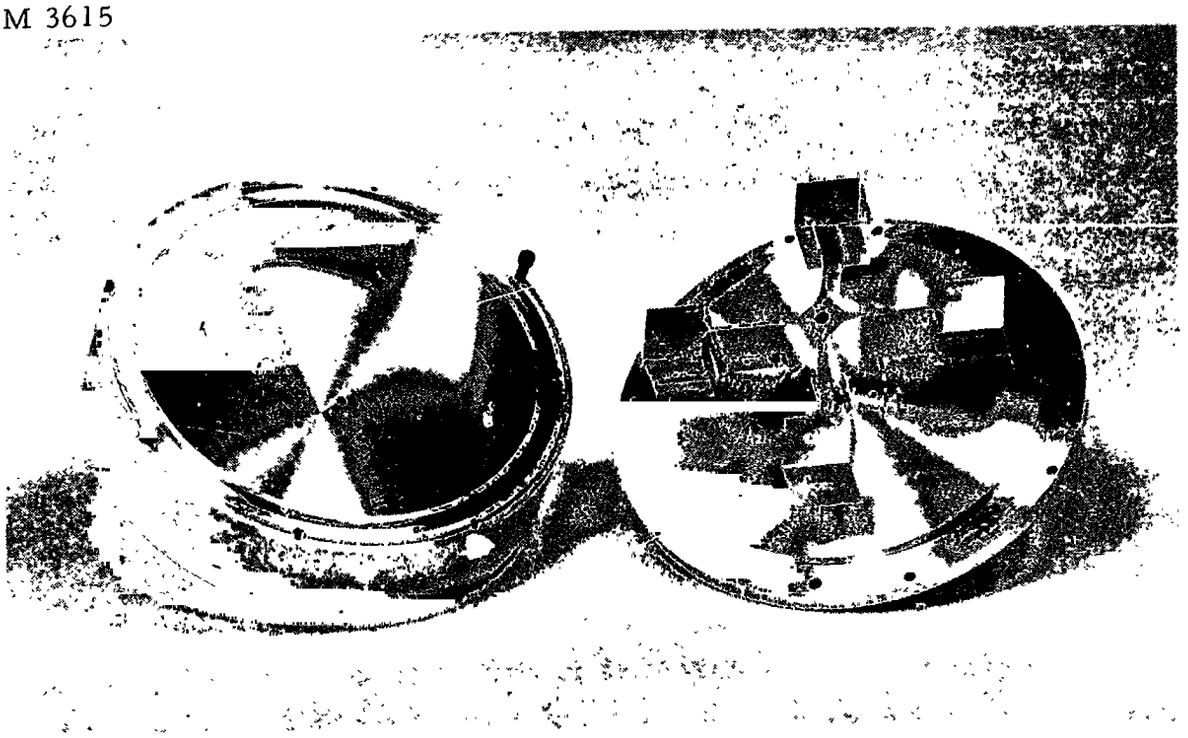

Fig. 1. Cruciform gravitational mass sensor.

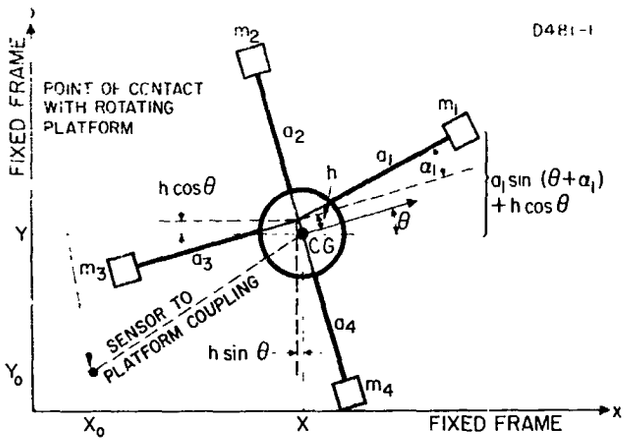

Fig. 2. Model of gravitational mass sensor used for analysis.

Each of the four arms on a central hub is a separate spring-mass system. The pivot points for the arms are assumed to coincide at a point located a distance h from the center of mass of the sensor.

The sensor should be rotated at around 50 rps; to accomplish this, the sensor is coupled to a rotating platform. The platform is maintained at the desired angular frequency, which is transmitted to the sensor. However, the platform-to-sensor coupling transmits both the rotation and the external mechanical disturbances to the sensor. Hence, the coupling is designed to have large translational flexibility.

The type of coupling assumed in this analysis is such that the translational restoring force on the sensor is relative to a fixed frame of reference. This coupling, for example, is the result of suspending the sensor on a long wire in a gravitational environment (Fig. 3). The situation here resembles a pendulum with small displacement. The translational (coupling) forces on the sensor are independent of the rotation.

All sensor motion is assumed to take place in a plane. Sensor motion is thus completely described by the following seven generalized coordinates:

X, Y	=	coordinates of hub center of mass with respect to the fixed x-y frame
θ	=	angular position of hub with respect to fixed x-y frame
α_1, α_2, α_3, α_4	=	position of arms with respect to a coordinate system on the hub.

Lagrangian methods will now be employed to describe the seven motions of the sensor. Lagrange's equation is a second-order differential equation which expresses a relationship between total kinetic energy T and generalized force F[3, 4]:

$$\frac{d}{dt}\left(\frac{\partial T}{\partial \dot{\psi}}\right) - \frac{\partial T}{\partial \psi} = F_{\psi} \quad . \tag{1}$$

Here ψ represents each of the independent variables selected as the generalized coordinates. There is one Lagranian equation for each coordinate:

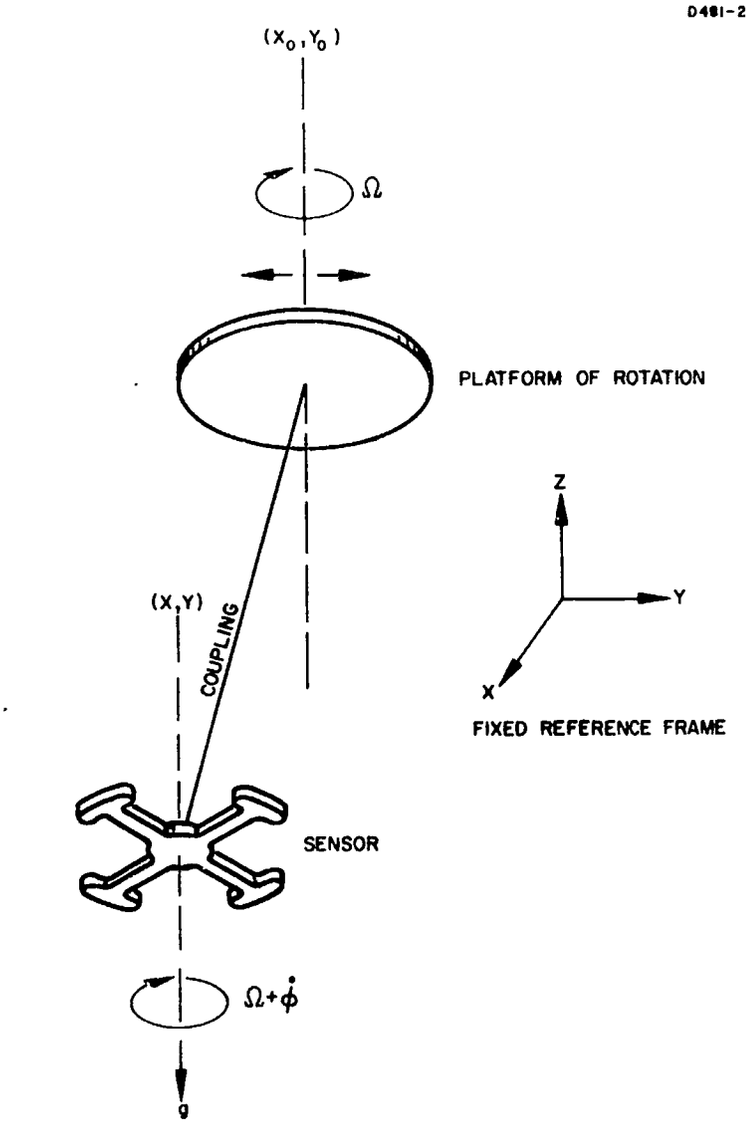

Fig. 3. Relationship among sensor, platform of rotation, and fixed reference frame.

$$\psi = X,\ Y,\ \theta,\ \alpha_1,\ \alpha_2,\ \alpha_3,\ \alpha_4 \quad .$$

In eq. (1), T is the total kinetic energy of the system (hub plus the four arms) and F is the generalized force associated with each of the coordinates (i.e., $F_n = -k\alpha_n$ is the restoring force on each arm, where k is the spring constant of the arm).

The total kinetic energy T is difficult to write in terms of the generalized coordinates, but is written easily in terms of the x_n - y_n coordinates of the fixed frame:

$$T = \frac{1}{2}\sum_{n=1}^{4} m_n\left(\dot{x}_n^2 + \dot{y}_n^2\right) + \frac{1}{2}M\left(\dot{X}^2 + \dot{Y}^2\right) + \frac{1}{2}I\dot{\theta}^2 \tag{2}$$

where

x_n, y_n ≡ coordinates of arm n in fixed frame
M ≡ mass of central hub
I ≡ moment of inertia of hub.

We must now express x_n, y_n in terms of the generalized coordinates: α_n, X, Y, θ. From strictly geometric considerations, Fig. 2 produces the following relationships between the two systems:

$$z_n = Z + ihe^{i\theta} + i^{n-1} a_n e^{i(\theta+\alpha_n)} \quad . \tag{3}$$

Complex variable notation is used extensively in order to greatly simplify the mathematics.[5]

$$\begin{aligned} z_n &= x_n + iy_n \\ Z &= X + iY;\ \ \bar{Z} = X - iY \\ e^{i\theta} &= \cos\theta + i\sin\theta \quad . \end{aligned} \tag{4}$$

In addition, wherever the subscript n is indicated, it is implied that n runs from 1 to 4. Thus, eq. (3) actually represents eight separate equations: the four x_n and the four y_n.

The time derivatives of x_n, y_n in terms of the generalized coordinates are

$$\dot{z}_n = \dot{Z} + \left[i^n a_n (\dot{\theta} + \dot{\alpha}_n) e^{i\alpha_n} - h\dot{\theta} \right] e^{i\theta} \quad . \tag{5}$$

At this point, it is theoretically possible to sum the squares of (5) as indicated in eq. (2); however, eq. (1) may be expanded more easily, since T is not required explicitly. Only certain partial derivatives of T are required. We may thus evaluate (1) without writing T explicitly.

Inspection of eq. (1) indicates that we require fourteen partial derivatives of T: $\partial T/\partial x$, $\partial T/\partial \dot{x}$, $\partial T/\partial Y$, etc... . The partials of T with respect to the dotted terms are (from eq. (2) and (5)

$$\frac{\partial T}{\partial \dot{X}} = \Sigma m_n \dot{x}_n + M\dot{X} \quad .$$

$$\frac{\partial T}{\partial \dot{Y}} = \Sigma m_n \dot{y}_n + M\dot{Y} \tag{6}$$

$$\frac{\partial T}{\partial \dot{\theta}} = \Sigma m_n \left(\dot{x}_n \frac{\partial \dot{x}_n}{\partial \dot{\theta}} + \dot{y}_n \frac{\partial \dot{y}_n}{\partial \dot{\theta}} \right) + I\dot{\theta}$$

$$\frac{\partial T}{\partial \dot{\alpha}_n} = m_n \left(\dot{x}_n \frac{\partial \dot{x}_n}{\partial \dot{\alpha}_n} + \dot{y}_n \frac{\partial \dot{y}_n}{\partial \dot{\alpha}_n} \right) \quad .$$

The partials of T with respect to the undotted terms are

$$\frac{\partial T}{\partial X} = \frac{\partial T}{\partial Y} = 0$$

$$\frac{\partial T}{\partial \theta} = \Sigma m_n \left(\dot{x}_n \frac{\partial \dot{x}_n}{\partial \theta} + \dot{y}_n \frac{\partial \dot{y}_n}{\partial \theta} \right) \tag{7}$$

$$\frac{\partial T}{\partial a_n} = m_n \left(\dot{x}_n \frac{\partial \dot{x}_n}{\partial a_n} + \dot{y}_n \frac{\partial \dot{y}_n}{\partial a_n} \right) .$$

The partials of $\dot{x}_n$, $\dot{y}_n$ with respect to $\dot{\theta}$, θ, $\dot{a}_n$, a_n are now required; this represents 32 separate calculations. These are immediately available from eq. (5) and are

$$\frac{\partial \dot{z}_n}{\partial \theta} = \left[i^n a_n (\dot{\theta} + \dot{a}_n) e^{i a_n} - h\dot{\theta} \right] i e^{i\theta}$$

$$\frac{\partial \dot{z}_n}{\partial \dot{\theta}} = \left(i^n a_n e^{i a_n} - h \right) e^{i\theta} \tag{8}$$

$$\frac{\partial \dot{z}_n}{\partial a_n} = i^{n+1} a_n (\dot{\theta} + \dot{a}_n) e^{i(a_n + \theta)}$$

$$\frac{\partial \dot{z}_n}{\partial \dot{a}_n} = i^n a_n e^{i(a_n + \theta)} .$$

We may now evaluate the basic Lagrangian equation (eq. (1)).

Direct substitution of eq. (6) and (7) and the above partial derivatives (eq. (8)) into (i) yields

$$M\ddot{X} + \Sigma m_n \ddot{x}_n = F_x \tag{9}$$

$$M\ddot{Y} + \Sigma m_n \ddot{y}_n = F_y \tag{10}$$

$$I\ddot{\theta} + \Sigma m_n \left[\ddot{x}_n \frac{\partial \dot{x}_n}{\partial \dot{\theta}} + \ddot{y}_n \frac{\partial \dot{y}_n}{\partial \dot{\theta}} + \left\{ \frac{d}{dt}\left(\frac{\partial \dot{x}_n}{\partial \dot{\theta}} \right) - \frac{\partial \dot{x}_n}{\partial \theta} \right\} \dot{x}_n + \left\{ \frac{d}{dt}\left(\frac{\partial \dot{y}_n}{\partial \dot{\theta}} \right) - \frac{\partial \dot{y}_n}{\partial \theta} \right\} \dot{y}_n \right] = F_\theta \tag{11}$$

$$m_n \left[\ddot{x}_n \frac{\partial \dot{x}_n}{\partial \dot{a}_n} + \ddot{y}_n \frac{\partial \dot{y}_n}{\partial \dot{a}_n} + \left\{ \frac{d}{dt}\left(\frac{\partial \dot{x}_n}{\partial \dot{a}_n} \right) - \frac{\partial \dot{x}_n}{\partial a_n} \right\} \dot{x}_n + \left\{ \frac{d}{dt}\left(\frac{\partial \dot{y}_n}{\partial \dot{a}_n} \right) - \frac{\partial \dot{y}_n}{\partial a_n} \right\} \dot{y}_n \right] = F_n \,. \tag{12}$$

Considerable simplification is afforded by noting the following relationships among the partial derivatives:

$$\frac{d}{dt}\left(\frac{\partial \dot{z}_n}{\partial \dot{\theta}} \right) = \frac{\partial \dot{z}_n}{\partial \theta}$$

$$\frac{d}{dt}\left(\frac{\partial \dot{z}_n}{\partial \dot{a}_n} \right) = \frac{\partial \dot{z}_n}{\partial a_n} \,. \tag{13}$$

Using these relationships, the third and fourth Lagrangian expressions (eq. (11) and (12)) become

$$I\ddot{\theta} + \Sigma m_n \left(\ddot{x}_n \frac{\partial \dot{x}_n}{\partial \dot{\theta}} + \ddot{y}_n \frac{\partial \dot{y}_n}{\partial \dot{\theta}} \right) = F_m \tag{14}$$

$$m_n\left(\ddot{x}_n \frac{\partial \dot{x}_n}{\partial \dot{a}_n} + \ddot{y}_n \frac{\partial \dot{y}_n}{\partial \dot{a}_n}\right) = F_n \quad . \tag{15}$$

In order to obtain $\ddot{x}_n$ and $\ddot{y}_n$, one additional time-derivative of (5) is required. The results are given below:

$$\ddot{z}_n = \ddot{Z} - h(\ddot{\theta} + i\dot{\theta}^2)\, e^{i\theta} + i^n a_n \left[\ddot{\theta} + \ddot{a}_n + i(\dot{\theta} + \dot{a}_n)^2\right] e^{i(\theta+a_n)} \quad . \tag{16}$$

We now have all the required terms for the equations of motion in terms of the generalized coordinates X, Y, θ, a_n. Equation (16), in addition to the required partial derivatives, must be substituted into (9), (10), (14), and (15).

Up to this point, no approximations have been imposed; all expressions have been exact. However, before we continue, it is necessary to utilize certain known physical properties of the sensor in order to simplify (16). We will thus depart from an exact solution, obtaining a solution which is as valid as the following assumptions.

It is known that the arm displacements are very small ($a_n \lesssim 10^{-8}$ cm). In addition, the first and second derivatives of a_n are of the form $\dot{a}_n = \omega a_n$; $\ddot{a}_n = \omega^2 a_n$ (where $\omega \sim 10^2$ rad/sec) such that they too are small. Therefore, any terms involving products of a_n, $\dot{a}_n$, $\ddot{a}_n$ are considered second order and are assumed to be negligible (i.e., a_n^2, $\dot{a}_n \times a_n$, $\dot{a}_n^2$, etc.). This process will result in a set of linear differential equations.

Similarly, an assumption regarding the rotation θ will be made. The sensor is being driven at a constant angular velocity Ω. Any deviation in rotation from Ω will be a small value. Hence,

$$\theta = \Omega t + \phi \tag{17}$$

where $\phi/\Omega \ll 1$. Products of ϕ and any other small terms (a_n, etc.) will be neglected.

In simplifying (16) the following type of trigonometric expansion for small angles is used:

$$\sin\theta = \sin(\Omega t + \phi) = \sin\Omega t + \phi\cos\Omega t$$

$$\cos(\theta + \alpha_n) = \cos(\Omega t + \phi + \alpha_n) = \cos\Omega t - (\phi + \alpha_n)\sin\Omega t \quad . \tag{18}$$

Using the above assumptions and trigonometric expressions, eq. (16) becomes

$$\ddot{z}_n = \ddot{Z} + \left\{\left[a_n(\ddot{\alpha}_n - \Omega^2\alpha_n) + i\Omega(2\dot{\alpha}_n + \Omega)\right]i^n - h\left[\ddot{\phi} - \Omega^2\phi + i\Omega(2\dot{\phi} + \Omega)\right]\right\} e^{i\Omega t} \tag{19}$$

where α_n in (19), (20), and (21), actually includes ϕ; i.e., $\alpha_n = \alpha_n + \phi$. It is also desirable to rewrite the partial derivatives (eq. (8)) utilizing the assumptions and trigonometric expansions discussed above. This is done as follows. Only the derivatives with respect to the dotted terms are rewritten, since the others will never be required (see (14) and (15)):

$$\frac{\partial\dot{z}_n}{\partial\dot{\theta}} = \left[i^n a_n(1 + i\alpha_n) - h(1 + i\phi)\right] e^{i\Omega t}$$

$$\frac{\partial\dot{z}_n}{\partial\dot{a}_n} = i^n a_n\left[1 + i\,\alpha_n\right]e^{i\Omega t} \quad . \tag{20}$$

III. IDEAL SENSOR

Before attempting to find the general solution for the nonideal sensor, it is of interest to determine what (9), (10), (14), and (15), produce for a special, simplified case. This case is referred to as the "ideal sensor," and has the following properties:

$$m_1 = m_2 = m_3 = m_4 = m$$

$$a_1 = a_2 = a_3 = a_4 = a$$

$$h = 0 \ .$$

The setting of $h = 0$ reduces (19) to the following form (note that there are no subscripts on the a's; $a_n = a$);

$$\ddot{z}_n = \ddot{Z} + i^n e^{i\Omega t}[a(\ddot{\alpha}_n - \Omega^2 \alpha_n) + i\Omega(2\dot{\alpha}_n + \Omega)] \quad . \tag{21}$$

Equation (21) is substituted into (9), yielding the expression for $\ddot{X}$ of the ideal sensor, with all of the terms in the generalized coordinates. Equation (9) indicates that (21) is first multiplied by m_n. However, under the assumption of the ideal sensor, $m_n = m$; when the summation is performed, m factors out. Equation (9) thus becomes

$$\frac{M'}{\sqrt{2}ma}\ddot{X} - [\ddot{\alpha}_+ - 2\Omega\dot{\alpha}_- - \Omega^2\alpha_+] \sin\Omega t - [\ddot{\alpha}_- + 2\Omega\dot{\alpha}_+ - \Omega^2\alpha_-] \cos\Omega t = \frac{F_x}{\sqrt{2}ma} \tag{22}$$

where

$$\alpha_+ \equiv \frac{1}{\sqrt{2}}(\alpha_1 - \alpha_3)$$
$$\alpha_- \equiv \frac{1}{\sqrt{2}}(\alpha_2 - \alpha_4) \tag{23}$$
$$M' \equiv M + 4m \ .$$

The a_+ and a_- correspond to certain vibrational modes of the sensor. Appendix I gives a physical interpretation of all the sensor vibrational modes.

In exactly the same way in which (21) was substituted into (9) to obtain (22), eq (21) is substituted into (10), yielding:

$$\frac{M'}{\sqrt{2}ma}\ddot{Y} - \left[\ddot{a}_- + 2\Omega\dot{a}_+ - \Omega^2 a_-\right]\sin\Omega t + \left[\ddot{a}_+ - 2\Omega\dot{a}_- - \Omega^2 a_+\right]\cos\Omega t = \frac{F_y}{\sqrt{2}ma} \tag{24}$$

Equations (22) and (24) are the equations of motion, in generalized coordinates, for the X-Y coordinates of the center of mass of the sensor.

Using the simplified forms for $\ddot{x}_n$ and $\ddot{y}_n$ (eq. (21) for the ideal sensor), eq. (15) immediately yields

$$\ddot{a}_n + \ddot{\phi} + \ddot{Z}e^{i\Omega t} = \frac{F_n}{ma} \quad . \tag{25}$$

These are the equations of motion of the four arms of the sensor in terms of the generalized coordinates. An ideal sensor has already been analyzed. Therefore, we take this opportunity to compare the reduced case of the nonideal sensor equations with the results previously established. For this reason, we solve for the natural frequencies of the various modes of sensor vibration (Appendix I). We thus consider only the spring forces on the arms (no gravitational or damping forces), plus the coupling forces corresponding to those described in Fig. 3.

Hence, the generalized forces* are

$$F_n = -ka^2\alpha_n$$
$$F_x = -KX \qquad (26)$$
$$F_y = -KY \quad .$$

The first of the vibrational modes which we will compare with Ref. 1 is the gravity sensing mode defined by (see Appendix I)

$$\alpha_g = \frac{1}{2}(\alpha_1 - \alpha_2 + \alpha_3 - \alpha_4) \quad ; \qquad (27)$$

substituting (27) into (25), the result is

$$\ddot{\alpha}_g + \frac{k}{m}\alpha_g = 0 \quad . \qquad (23)$$

This result indicates that the gravity mode is insensitive to any motions (induced or otherwise) of the central hub. This is obvious because neither X, Y, nor θ appears in (28). The gravity mode natural frequency is constant:

$$\omega_g^2 = \frac{k}{m} \quad . \qquad (29)$$

(These results are identical to those obtained in Ref. 1.)

The next vibrational modes we will compare are the right and left hand circulating translational modes, defined as (see Appendix I)

*Since the generalized coordinate α_n is an angle, the generalized force associated with this coordinate is a torque. Therefore, a^2 (arm length) appears in the expression for F_n.

$$a_R = \frac{1}{2}(a_1 + ia_2 - a_3 - ia_4)$$
$$a_L = \frac{1}{2}(a_1 - ia_2 - a_3 + ia_4) \quad . \tag{30}$$

Substituting (26) into (25)

$$\ddot{a}_n + \ddot{\phi} + \omega_g^2 a_n = -i^n \ddot{\bar{Z}}\, e^{i\Omega t} \quad . \tag{31}$$

The equation for the right hand translational mode (from (30)) follows immediately:

$$\ddot{a}_R + \omega_g^2 a_R = i\ddot{\bar{Z}}\, e^{-i\Omega t} \quad . \tag{32}$$

The translational mode is thus directly influenced by the translational motions of the hub (X, Y), and the natural frequency is not constant as in the case of the gravitational mode. To solve (32), we obtain Z from (22) and (24). Multiplying (24) by i and adding to (22) yields (using (26))

$$\ddot{a}_R + 2i\Omega\dot{a}_R - \Omega^2 a_R = \frac{M'}{2m}\left(\ddot{\bar{Z}} + \frac{K}{M'}\bar{Z}\right) i\, e^{-i\Omega t} \quad . \tag{33}$$

We now assume solutions of the form[6]

$$a_R = |a_R|\, e^{i\omega t} \quad , \tag{34}$$

and proceed to find ω ($|a_R|$ = const.). Substituting (34) into (32) yields, for Z,

$$i\ddot{\bar{Z}} = |a_R|(\omega_g^2 - \omega^2)\, e^{i(\omega+\Omega)t} \quad . \tag{35}$$

Equations (34) and (35) are substituted into (33) to yield the final result for the translational mode frequencies of the ideal sensor*:

$$(\omega \pm \Omega)^4 + \frac{M'}{2m}(\omega_g^2 - \omega^2)\left[(\omega \pm \Omega)^2 - \Omega_m^2\right] = 0 \qquad (36)$$

where $\Omega_m^2 = K/M'$. Equation (36) is discussed thoroughly in Ref. 1, but it will be plotted here for completeness. We now take the special case: $\Omega_m = 0.9\,\omega_g$. Then, dividing through (36) by ω_g^4 results in

$$(\omega \pm \Omega)^4 + \frac{M'}{2m}(1 - \omega^2)\left[(\omega \pm \Omega)^2 - 0.81\right] = 0 \qquad (37)$$

where all frequencies (ω, Ω) are normalized with respect to ω_g. Numerical evaluation of (37) results in four separate and distinct modes, indicating a splitting of the two basic translational modes. These four cases are plotted in Fig. 4, demonstrating the effect of the rotational frequency Ω in splitting the two basic translational modes.

This completes the exploration of the special case of the ideal sensor. All results check exactly with the previous work established in Ref. 1.

*Since the left hand translational mode is the complex conjugate of the right hand (eq. (30)), the solution to the left hand case is the same, with the sign of Ω reversed. Hence, the more general expression for the four translational modes contains $\pm\Omega$.

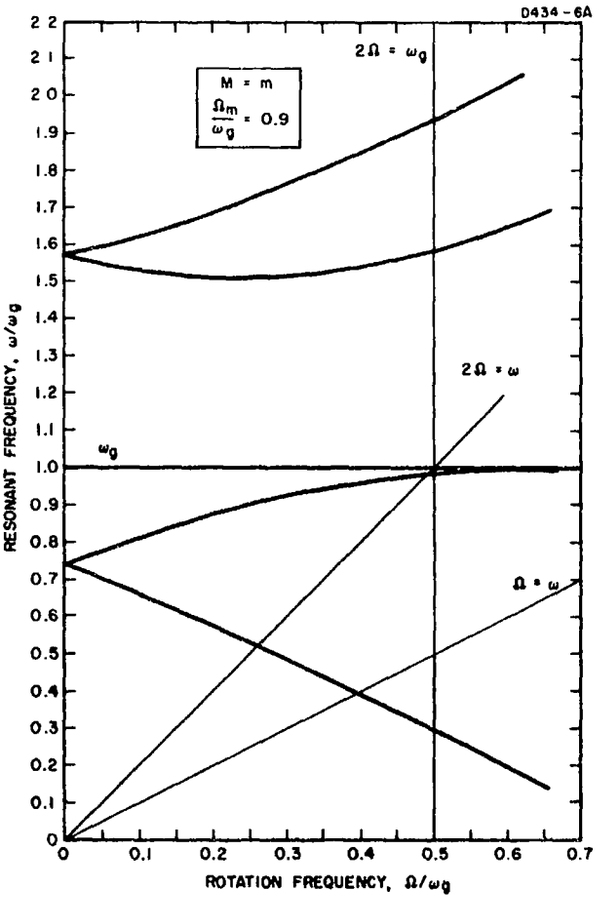

Fig. 4. Translational modes predicted for the ideal sensor.

IV. NONIDEAL SENSOR: FIXED CENTER OF GRAVITY

We now return to (19) and proceed to establish the sensor motion equations for the general, nonideal case. Here, we allow for variations among the arm masses, spring constants, etc., and offset center of mass. Substitution of (19) into (15) yields the equations of motion for the four arms of the nonideal sensor:

$$a_n(\ddot{a}_n + \ddot{\phi}) + i^n \ddot{\bar{Z}} e^{i\Omega t} - i^n h\left[\Omega^2 a_n + \ddot{\phi} - i\Omega(\Omega + 2\dot{\phi})\right] = \frac{F_n}{m_n a_n}. \quad (38)$$

Equation (38) is similar to (25), with two important differences. First, eq. (38) contains terms in h, allowing for a displaced center of gravity. Second, the m's and a's now contain subscripts, allowing each arm to depart from the others in length and mass. Therefore, when we form the gravity sensing mode (eq. (27)), we will not obtain a simple equation of the form (28). Other terms will appear in the mode equation and couple it to the motions of the individual arms. (eq. (38)). This phenomenon will be demonstrated below. At this point, it can already be seen that the time-varying motions of the center of mass of the sensor influence the gravitational mode. This was not true for the ideal sensor, where the gravitational mode was found to be independent of sensor center of gravity motions. It is thus the manufacturing imperfections which allow noise signals to enter the gravity mode.

We now choose a special case of a nonideal sensor in order to demonstrate how small sensor imperfections can disturb the gravity signal. The special case corresponds to a sensor with a fixed center of mass, and rotating at constant angular velocity:

$$Z = \phi = 0$$

$$\theta = \Omega t \quad . \quad (39)$$

Physically, this case is somewhat unrealistic because it is extremely difficult to maintain the sensor center of mass fixed in space. The case is instructive, however, because it offers an analytic solution (closed form) of the general problem. In other words, the fixed center of gravity is of interest as an introductory case; it provides a basic understanding of why and how the gravity signal is disturbed by the sensor imperfections.

The generalized forces F_n will now contain not only the spring force, but also damping D and gravity G forces (since the generalized coordinate α_n is an angle, the generalized forces are torques):

$$F_n = -k_n a_n^2 \alpha_n - a_n^2 D_n \dot{\alpha}_n + G_n m_n a_n \quad . \tag{40}$$

The subscript on the k_n indicates that differences exist among the spring constants of the arm. Substituting (39) and (40) into (38) yields, for the arm motions,

$$\ddot{\alpha}_n + \frac{D_n}{m_n}\dot{\alpha}_n + \frac{k_n}{m_n}\alpha_n = \frac{1}{a_n}G_n \quad . \tag{41}$$

We will assume equal damping coefficients, such that

$$\frac{D_1}{m_1} = \frac{D_2}{m_2} = \ldots, \text{ etc. } = \gamma \quad . \tag{42}$$

Only the effects of errors in the arm natural frequencies will be explored:

$$\frac{k_n}{m_n} = \omega_n^2 \equiv (1 + \epsilon_n)\omega_g^2 \quad . \tag{43}$$

Where ϵ_n = deviation from ω_g^2 of arm n natural frequency squared.

The gravity mode equation (from (27) and (41) is

$$\ddot{\alpha}_g + \gamma\dot{\alpha}_g + \omega_g^2\alpha_g + \frac{\omega_g^2}{2}(\epsilon_1\alpha_1 - \epsilon_2\alpha_2 + \epsilon_3\alpha_3 - \epsilon_4\alpha_4)$$

$$= \frac{1}{2a}(G_1 - G_2 + G_3 - G_4) \quad . \tag{44}$$

It is observed that equation (44) contains a set of driving terms resulting from the errors ϵ_n. Therefore, the mode is disturbed because of the variations among the arm natural frequencies. It was demonstrated in Ref. 2 (see Appendix II) that

$$G_1 - G_2 + G_3 - G_4 = 4a\Gamma \sin 2\Omega t \tag{45}$$

where Γ is the gravitational gradient being sensed.

Using (45), the solution to (44) was obtained. Since G_n is a series of sines and cosines, we know that α_n must also be a series of sines and cosines. However, only those terms which are at frequency 2Ω are of interest. The other frequency terms are filtered and do not disturb the signal. The procedure for an analytic solution to (44) is outlined, but the step-by-step algebra is not presented. Equation (41) is a set of constant coefficient, second order differential equations whose solutions are straightforward. Considering only 2Ω driving terms on the right-hand side of (41), the α_n are also of 2Ω frequency. These results for α_n are substituted into the right-hand side of (44), thereby driving the gravity mode (α_g) at a frequency 2Ω. Equation (44) then contains five driving terms with different amplitudes and phases, all at the same frequency of 2Ω. These five terms are combined into one sinusoidal term by first reducing them to one sine and one cosine term, both at the same frequency and phase. The amplitude of the signal $|\alpha_g|$ is then the square root of the sum of the squares of the amplitudes of these two sine and cosine terms. The final result, for the amplitude of the disturbed gravity mode signal (at 2Ω), is as follows:

$$|a_g|_{2\Omega} = \left\{ \frac{\frac{\omega^2}{Q^2}\left[\sum \frac{\epsilon_n}{(1+\epsilon_n-\omega^2)^2+\omega^2/Q^2}\right]^2 + \left[2 - \sum \frac{\epsilon_n(1+\epsilon_n-\omega^2)}{(1+\epsilon_n-\omega^2)^2+\omega^2/Q^2}\right]^2}{(1-\omega^2)+\frac{\omega^2}{Q_2}} \right\}^{1/2} \tag{46}$$

where

$$\omega \equiv \frac{2\Omega}{\omega_g}$$

$$\epsilon_n \equiv \frac{\epsilon_n}{2}$$

$$Q \equiv \frac{\omega_g}{\gamma} = \frac{\omega_g m}{D} \quad .$$

Equation (46) is plotted in Fig. 5 (for Q = 100). The amplitude represents the actual signal which would be received in an attempt to sense a gravity gradient with a sensor with a fixed center of mass. The errors ϵ_n used in the plot of Fig. 5 were selected at random in the range from 0 to 5%. The distortion of the ideal signal is evident from the figures, being very pronounced in the cases of the larger values of ϵ_n.

It should be emphasized that the foregoing case of the fixed center of gravity sensor is of academic interest only. Real sensors do not have a fixed center of gravity. By fixing the center of gravity, we are in effect decoupling the arms from each other so that they act independently. With the center of gravity free, the sensor response, both in theory and practice, is found to have a response which is different from that of the fixed center of mass case.

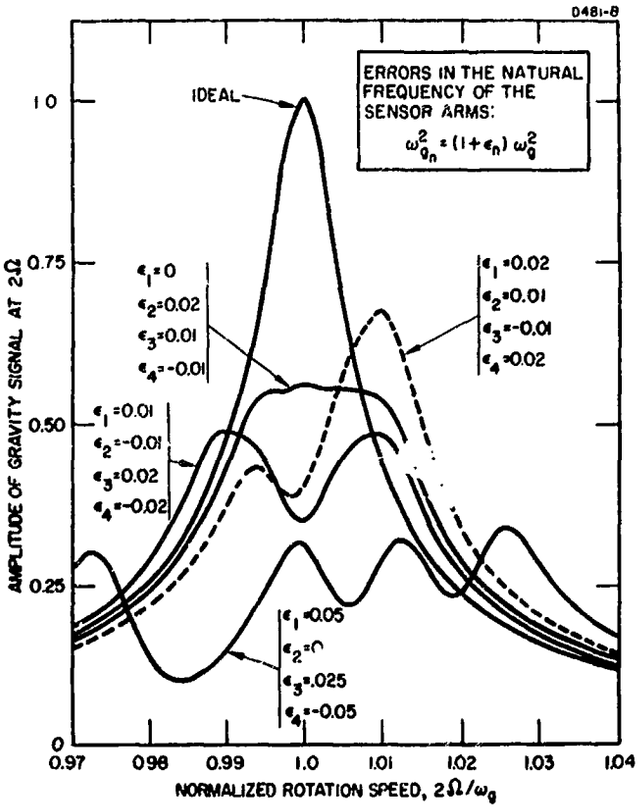

Fig. 5. Fixed center of gravity gravitational mass sensor. Effect of nonideal sensor on gravity signal 2Ω.

V. EXTERNAL DISTURBANCES

Before we can proceed to the general solution of the nonideal sensor (eq. (38)), the nature of the disturbance vibrations must be thoroughly understood. In the realistic case of a nonideal sensor, the center of gravity is not fixed, but is mounted to the rotating platform by some type of flexible coupling (Fig. 3). The sensor motion is therefore influenced by the external disturbances which the platform applies through the flexible coupling. Assume that the axis through the platform of rotation is vibrating in the X-Y plane. This axis may be vibrating in the fixed frame of reference because of inherent bearing effects (refer to Fig. 7) or because of effects which are completely external to the entire system (from a space vehicle, etc.).

In general, these vibrations (and therefore the sensor response) may consist of many different frequencies. However, only one frequency concerns us — the gravity sensing frequency 2Ω. Therefore, we are interested only in that part of the disturbance which can ultimately produce a 2Ω forcing function in the sensor vibrational modes.

Any arbitrary disturbance may be represented by the following Fourier expansion[6]:

$$X_o = \sum_{r=0}^{\infty} (p_r \sin r\Omega t + q_r \cos r\Omega t)$$

$$Y_o = \sum_{r=0}^{\infty} (u_r \sin r\Omega t + v_r \cos r\Omega t) \quad . \tag{47}$$

where the coefficients are constants.

To determine what components of (47) contribute to the sensor vibrational modes, it is necessary to work in a frame of reference rotating with the sensor. The relationship between the fixed-frame coordinates (X, Y) and rotating coordinates (defined now as X_1, Y_1) is

$$X_i = X \cos \Omega t + Y \sin \Omega t$$

$$Y_i = X \sin \Omega t - Y \cos \Omega t \quad . \tag{48}$$

Transformation of (47) by (48) gives rise to the following types of driving terms

$$X_{10},\ Y_{10} = f \left\{ \begin{array}{l} \sin r\Omega t \sin \Omega t \\ \sin r\Omega t \cos \Omega t \\ \cos r\Omega t \sin \Omega t \\ \cos r\Omega t \cos \Omega t \end{array} \right\} \tag{49}$$

We now ask the following question: What values of r in (49) will produce an oscillatory term of frequency 2Ω ? The answer follows from the trigonometric identity:

$$\sin r\Omega t \sin \Omega t = \frac{1}{2} \cos (r\Omega - \Omega)t - \frac{1}{2} \cos (r\Omega + \Omega)t \quad . \tag{50}$$

All four terms of (49) expand similarly into sines or cosines of the same two frequencies indicated in (50). Hence, r is found from the simple relation

$$\begin{array}{l} r\Omega - \Omega = 2\Omega \\ \qquad\qquad \text{or} \quad r = 1,\ 3 \quad . \\ r\Omega + \Omega = 2\Omega \end{array}$$

Thus, only the Ω and 3Ω terms of an arbitrary disturbance can influence sensor vibrational mode response.

The tranformation of Ω and 3Ω disturbances into 2Ω driving terms of the sensor modes may be explained physically. We recall that any translational motion may be decomposed into a right- and left-hand circular motion (Fig. 6(a)). Sensor response is most easily understood

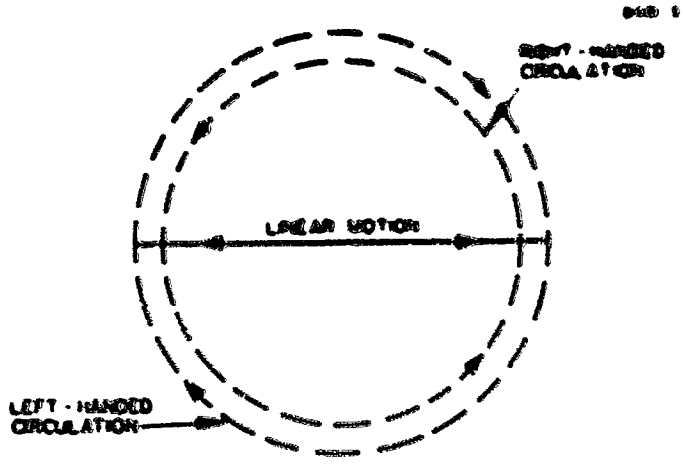

Fig. 6(a)
Translational motion decomposes into right and left-hand circulation

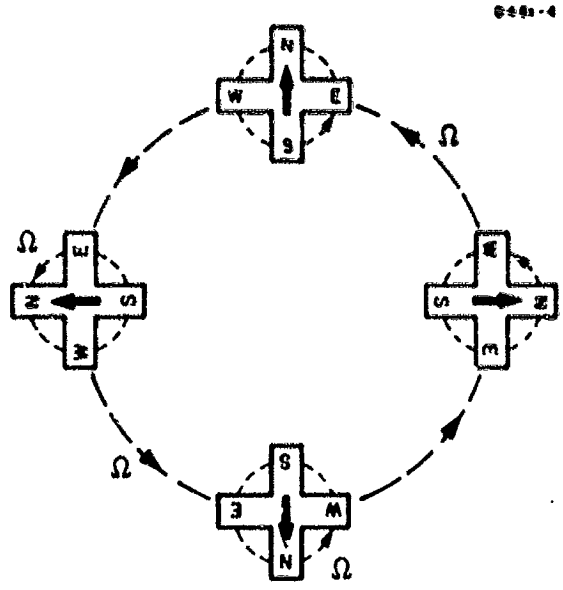

Fig. 6(b).
Positive circulation produces no vibrational effect in rotating reference frame.

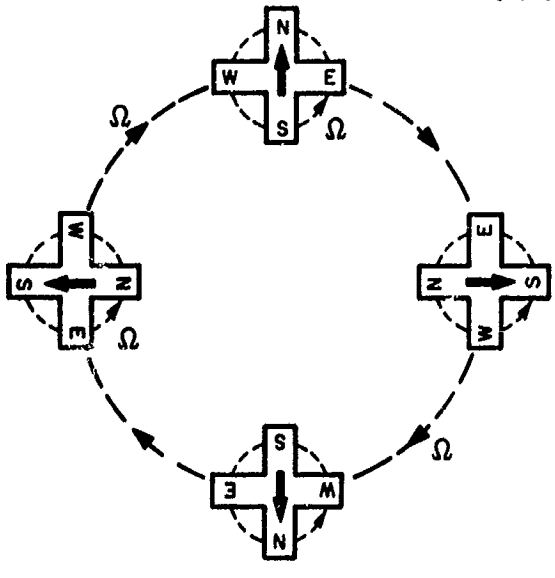

Fig. 6(c).
Negative circulation induces a vibrational mode forcing function at twice the frequency of rotation.

by considering the general disturbance to be a superposition of circular motions. When the motion is circular, the force induced on the sensor arms is purely centrifugal and therefore is readily appreciated.

Let us separate an Ω disturbance oscillation into a positive circulation (in the direction of sensor spin) and a negative circulation (opposite to the spin). Figure 6(b) and (c) shows the separate effects on the sensor. Note that in the case of positive circulation, the force vector always points from S to N, regardless of the sensor orientation. The centrifugal force is constant in the rotating frame; therefore, positive circulation (of Ω) has no effect on sensor arm vibration. The arms merely experience a constant acceleration.

However, now consider the negative component of (an Ω) circulation. This circular motion is opposite to that of the spin, as shown in Fig. 6(c). Note that the induced force vector points sometimes from S to N and sometimes from N to S, depending on sensor orientation. In the sensor-fixed frame, the centrifugal force reverses direction twice during one complete cycle. Hence, a vibrational mode forcing function of frequency 2Ω is produced.

The foregoing physical conclusions on positive and negative circulation are easily verified mathematically. Positive circulation (of Ω) is described by the expressions (from (47)):

$$X_o = q_1 \cos \Omega t$$
$$Y_o = u_1 \sin \Omega t$$
$$u_1 = q_1 = q \quad .$$

This motion is transformed into the rotating coordinate system by the use of (48). The result is the forcing function of the sensor vibrational modes:

$$X_{10} = q \cos^2 \Omega t + q \sin^2 \Omega t = q$$
$$Y_{10} = q \cos \Omega t \sin \Omega t - q \sin \Omega t \cos \Omega t = 0 \quad .$$

We see that the forcing function is a constant. Hence, there is only a constant force on the sensor modes, and no vibrational effect. It is of practical importance that Ω positive circulation does not drive the vibrational modes. It seems that inherent bearing vibrations belong to this class of motions, and do not influence sensor response. Figure 7 shows a cross section of a rotating shaft and bearing. Within the bearing, the shaft experiences translational motion, in addition to spin. If the stabilizing action of the bearing is the same in all directions (such as with a magnetic bearing), the translational shaft motion will be positive circular (at Ω).

Negative Ω circulation is expressed mathematically (from (47)) as follows:

$$X_o = p_1 \sin \Omega t$$
$$Y_o = v_1 \cos \Omega t$$
$$v_1 = p_1 = p \quad .$$

Transforming into the sensor-fixed reference frame (from (48)),

$$X_{10} = p \sin \Omega t \cos \Omega t + p \cos \Omega t \sin \Omega t$$
$$= p \sin 2\Omega t$$
$$Y_{10} = p \sin^2 \Omega t - p \cos^2 \Omega t = - p \cos 2\Omega t \quad .$$

We thus obtain the expected result that 2Ω driving terms are created from negative circulation of frequency Ω.

Similar considerations as outlined above indicate that for a 3Ω circulation, the positive component contributes to the vibrational mode response at 2Ω.

The transformation of external disturbances into vibrational mode driving forces has been thoroughly considered. We have seen how an arbitrary disturbance oscillation is converted into 2Ω forcing functions of the sensor-fixed reference frame. The most general expression for 2Ω forcing functions is

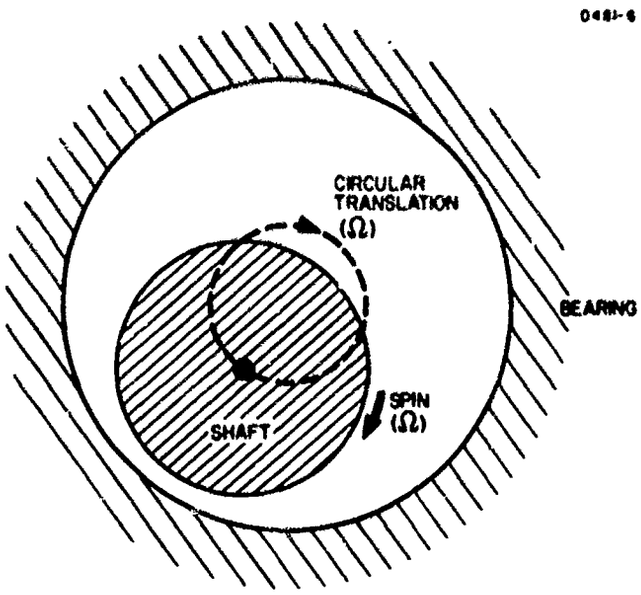

Fig. 7. Inherent bearing vibrations give rise to positive circulation motions, which have no effect on sensor response.

$$X_{10} = p \sin 2\Omega t + q \cos 2\Omega t$$

$$Y_{10} = u \sin 2\Omega t + v \cos 2\Omega t \quad . \tag{51}$$

The proper choice of p, q, u, and v will describe any disturbance motion in terms of vibrational mode driving functions. This will be the expression used to drive the general nonideal sensor equations solved in the next section.

VI. NONIDEAL SENSOR: GENERAL CASE

The general solution of eq. (38) is now obtained. This will be the most realistic case physically, since it includes the nonideal effects of sensor imperfections, as well as nonrigid coupling between sensor and rotating platforms (Fig. 3). Vibrational mode driving disturbances will be of frequency 2Ω, as described in Section V.

In this section, the solution is formulated in terms of a 12-by-12 determinant. The determinant is actually evaluated numerically on the computer (the results are given in Section VII).

Deviations in rotational speed will be neglected; constant angular velocity of the sensor is assumed. This assumption appears to be reasonable, since the first-order quantitative effects of the nonideal sensor imperfections are observable at constant angular speed. The following analytical results verify this. The assumption of constant rotational speed means that

$$\phi = 0 \ .$$

The nonideal effect to be explored is that resulting from a center of gravity offset. As explained before, this implies that the center of mass of the sensor does not coincide with the center of geometry. Referring to Fig. 2, we allow h to have some nonzero value. For the moment, all other nonideal effects are zero (sensor arm masses and lengths are equal).

The equations of motion for the arms are obtained from (38):

$$\ddot{\alpha}_n + i^n \ddot{\bar{Z}} e^{i\Omega t} - i^n h\Omega^2(\alpha_n - i) = \frac{F_n}{ma^2} \ . \qquad (52)$$

(X, Y, and h are normalized to "a"; i.e., $X/a \rightarrow X$).

Using eqs. (27), (40), and (45), the gravitational mode is constructed from (52):

$$\ddot{a}_g + \gamma \dot{a}_g + \omega_g^2 a_g = h \frac{\Omega^2}{2} (a_2 - a_4) + 2\Gamma \sin 2\Omega t \quad . \tag{53}$$

Thus, a nonzero h couples the a_- mode [$a_- = (a_2 - a_4)/2$] into the gravity mode. Since a_- depends on X, Y, the motions of the sensor center of gravity will now affect the gravity gradient signal. This is the first indication of how external disturbances produce noise in the gravity sensing mode. Noise is introduced because of the sensor imperfections. We recall that for the case of the ideal sensor, the signal was compietely free from noise regardless of the translational motion of the sensor.

The equations for X, Y are derived just as they were before (eqs. (22) and (24)), except that h is nonzero. The first step is to evaluate F_x and F_y. In evaluating the total forces on the sensor (see Figs. 2 and 3), the damping effects D_m plus the effects of external disturbances (X_o, Y_o) are included:

$$\begin{aligned} F_x &= - D_m \dot{X} - K(X - X_o) \\ F_y &= - D_m \dot{Y} - K(Y - Y_o) \quad . \end{aligned} \tag{54}$$

The X_o, Y_o describe translational motion of the rotating platform, thus causing the external disturbance. The equations for X, Y are thus

$$\frac{1}{2m} [M'\ddot{X} + D_m \dot{X} + K(X - X_o)] = (\ddot{a}_+ - 2\Omega \dot{a}_- - \Omega^2 a_+ - 2\Omega^2 h) \sin \Omega t + (\ddot{a}_- + 2\Omega \dot{a}_+ - \Omega^2 a_-) \cos \Omega t \tag{55a}$$

$$\frac{1}{2m}[M'\ddot{Y} + D_m\dot{Y} + K(Y - Y_o)] = (\ddot{a}_- + 2\Omega\dot{a}_+ - \Omega^2 a_-)\sin\Omega t$$
$$- (\ddot{a}_+ - 2\Omega\dot{a}_- - \Omega^2 a_+ - 2\Omega^2 h)\cos\Omega t \quad . \tag{55b}$$

Comparing (55) with (22) and (24), it is seen that h introduces only two addition terms in the X, Y equations.

a_+ and a_- appear on the right-hand side of (55). Therefore, it is convenient to form the equation of these modes from (52):

$$\ddot{a}_+ + \gamma\dot{a}_+ + \omega_g^2 a_+ = \ddot{X}\sin\Omega t - \ddot{Y}\cos\Omega t + h\Omega^2$$
$$\ddot{a}_- + \gamma\dot{a}_- + \omega_g^2 a_- = \ddot{X}\cos\Omega t + \ddot{Y}\sin\Omega t - \frac{h\Omega^2}{2}(a_2 + a_4) \quad . \tag{56}$$

The equations are still not completely in mode form, because of the $(a_2 + a_4)$ term. However, note that

$$(a_2 + a_4) = a_t - a_g \tag{57}$$

where a_t is the torsional mode (see Appendix I):

$$a_t = \frac{1}{2}(a_1 + a_2 + a_3 + a_4) \quad . \tag{58}$$

Writing the equation of the torsional mode (from (47)),

$$\ddot{a}_+ + \gamma\dot{a}_t + \omega_g^2 a_t = \frac{h\Omega^2}{2}(a_4 - a_2) \quad . \tag{59}$$

The four a equations are now completely described by combinations of the four sensor vibrational modes. The result is a set of six coupled differential equations (the four arm equations and the two X, Y equations). The solution to these provides a complete description of all

sensor motions. Before proceeding with the solution, it is convenient to transform X and Y into a rotating frame of reference (X_1, Y_1) by use of (48). Rewriting the four mode equations (eqs. (53), (56), and (59)) using the definitions of (48) yields

$$\begin{aligned}
&\ddot{a}_g + \gamma a_g + \omega_g^2 a_g = h\Omega^2 a_- - 2\Gamma \sin 2\Omega t \\
&\ddot{a}_t + \gamma \dot{a}_t + \omega_g^2 a_t = -h\Omega^2 a_- \\
&\ddot{a}_- + \gamma \dot{a}_- + \omega_g^2 a_- = \ddot{X}_1 + 2\Omega \dot{Y}_1 - \Omega^2 X_1 - \frac{h\Omega^2}{2}(a_t - a_g) \\
&\ddot{a}_+ + \gamma \dot{a}_+ + \omega_g^2 a_+ = \ddot{Y}_1 - 2\Omega \dot{X}_1 - \Omega^2 Y_1 + h\Omega^2 \quad .
\end{aligned} \tag{60}$$

The X, Y equations (eqs. (55a) and (55b)) are also simplified by the application of (48):

$$\frac{M'}{2m}\left[(\ddot{Y}_1 - 2\Omega\dot{X}_1 - \Omega^2 Y_1) + \gamma_m(\dot{Y}_1 - \Omega X_1) + \Omega_m^2(Y_1 - Y_{10})\right] = \ddot{a}_+ - 2\Omega\dot{a}_- - \Omega^2 a_+$$

$$\frac{M'}{2m}\left[(\ddot{X}_1 + 2\Omega\dot{Y}_1 - \Omega^2 X_1) + \gamma_m(\dot{X}_1 + \Omega Y_1) + \Omega_m^2(X_1 - X_{10})\right] = \ddot{a}_- + 2\Omega\dot{a}_+ - \Omega^2 a_- \tag{61}$$

where

$\Omega_m^2 \equiv$ natural frequency for sensor translation $= \frac{K}{M'}$

$\gamma_m \equiv$ damping coefficient of sensor translation $= \frac{D_m}{M'}$.

Equations (60) and (61) will now be solved. At this point it should be made clear that the solutions sought are those which arise from 2Ω driving forces of the vibrational modes. Noise at other frequencies is not important, since the 2Ω gravitational signal can be distorted only by 2Ω noise.

For this reason also, only 2Ω driving terms arising from the external disturbance are being considered (eq. (51).

Thus, we seek solutions of the form[6]

$$\psi = A_\psi \sin 2\Omega t + B_\psi \cos 2\Omega t \tag{62}$$

where ψ is used to represent each of the six variables:

$$\psi = \alpha_g,\ \alpha_t,\ \alpha_+,\ \alpha_-,\ X_1,\ Y_1 \quad .$$

When (62) and (51) are substituted into (60) and (61), two sets of algebraic equations result: one set results from equating the coefficients of the sine terms, and the other from equating the coefficients of the cosine terms. In other words, each of the six differential equations (60) and (61) becomes two algebraic equations. This algebraic set of twelve simultaneous equations is now presented. Consider first the eight equations arising from the four differential equations of the vibrational modes (eq. (60)):

$$\begin{aligned}
&(1 - 4\Omega^2)A_g - 2\frac{\Omega}{Q}B_g = h\Omega^2 A_- - 2\Gamma \\
&(1 - 4\Omega^2)B_g + 2\frac{\Omega}{Q}A_g = h\Omega^2 B_- \\
&(1 - 4\Omega^2)A_t - 2\frac{\Omega}{Q}B_t = -h\Omega^2 A_- \\
&(1 - 4\Omega^2)B_t + 2\frac{\Omega}{Q}A_t = -h\Omega^2 B_- \\
&(1 - 4\Omega^2)A_- - 2\frac{\Omega}{Q}B_- = -5\Omega^2 A_x - 4\Omega^2 B_y - \frac{h\Omega^2}{2}(A_t - A_g) \\
&(1 - 4\Omega^2)B_- + 2\frac{\Omega}{Q}A_- = -5\Omega^2 B_x + 4\Omega^2 A_y - \frac{h\Omega^2}{2}(B_t - B_g) \\
&(1 - 4\Omega^2)A_+ - 2\frac{\Omega}{Q}B_+ = -5\Omega^2 A_y + 4\Omega^2 B_x \\
&(1 - 4\Omega^2)B_+ + 2\frac{\Omega}{Q}A_+ = -5\Omega^2 B_y - 4\Omega^2 A_x \quad .
\end{aligned} \tag{63}$$

The four remaining algebraic equations are produced by the two differential equations of sensor translational motion, the X_1, Y_1 equations (61).

$$\frac{M'}{2m}\left[(\Omega_m^2 - 5\Omega^2)A_2 + 4\Omega^2 B_1 + \frac{\Omega}{Q_m}(-2B_y - A_x) - \Omega_m^2 u\right] = -5\Omega^2 A_+ + 4\Omega^2 B_-$$

$$\frac{M'}{2m}\left[(\Omega_m^2 - 5\Omega^2)B_2 - 4\Omega^2 A_1 + \frac{\Omega}{Q_m}(2A_y - B_x) - \Omega_m^2 v\right] = -5\Omega^2 B_+ - 4\Omega^2 A_-$$

$$\frac{M'}{2m}\left[(\Omega_m^2 - 5\Omega^2)A_1 - 4\Omega^2 B_2 + \frac{\Omega}{Q_m}(-2B_x + A_y) - \Omega_m^2 p\right] = -5\Omega^2 A_- - 4\Omega^2 B_+$$

$$\frac{M'}{2m}\left[(\Omega_m^2 - 5\Omega^2)B_1 + 4\Omega^2 A_2 + \frac{\Omega}{Q_m}(2A_x + B_y) - \Omega_m^2 q\right] = -5\Omega^2 B_- + 4\Omega^2 A_+ \quad . \tag{64}$$

In the previous two sets (eqs. (63) and (64)), normalization has been performed with respect to ω_g. In other words,

$$\frac{\Omega}{\omega_g} \rightarrow \Omega; \quad \frac{\Omega_m}{\omega_g} \rightarrow \Omega_m, \quad \text{also,} \quad Q_m \equiv \frac{\omega_g}{\gamma_m} \quad .$$

Solution for the twelve unknowns of (eq. (63) and (64)) (the six A's and six B's) is straightforward by determinant techniques.[7] The determinant of the coefficients of the unknowns in (63) and (64) is presented in Table I. There are twelve columns, each corresponding to one of the unknowns; each of twelve rows corresponds to one of the equations in (63) and (64). The column to the far right consists of the inhomogeneous parts of (63) and (64) and is not part of twelve-by-twelve determinant of coefficients. This column contains the driving terms (or forcing functions) of the system; the top one is a result of gravitational gradients, and the bottom four are a result of external vibrational disturbances.

Solution by the method of determinants proceeds (by Cramer's rule) as follows. Call the original determinant as it stands $\{\theta\}$. Then let $\{A_g\}$

TABLE I

Determinant of the Coefficients of the Unknowns

	A_g 1	B_g 2	A_t 3	B_t 4	A_- 5	B_- 6	A_+ 7	B_+ 8	A_1 9	B_1 10	A_2 11	B_2 12	Inhomogeneous Parts
1	$(1 - 4\Omega^2)$	$\frac{2\Omega}{Q}$	0	0	$-h\Omega^2$	0	0	0	0	0	0	0	$-\frac{2\Gamma}{\omega_g^2}$
2	$\frac{2\Omega}{Q}$	$(1 - 4\Omega^2)$	0	0	0	$-h\Omega^2$	0	0	0	0	0	0	0
3	0	0	$(1 - 4\Omega^2)$	$\frac{2\Omega}{Q}$	$+h\Omega^2$	0	0	0	0	0	0	0	0
4	0	0	$\frac{2\Omega}{Q}$	$(1 - 4\Omega^2)$	0	$+h\Omega^2$	0	0	0	0	0	0	0
5	$\frac{h\Omega^2}{2}$	0	$\frac{h\Omega^2}{2}$	0	$(1 - 4\Omega^2)$	$\frac{2\Omega}{Q}$	0	0	$5\Omega^2$	0	0	$4\Omega^2$	0
6	0	$\frac{h\Omega^2}{2}$	0	$\frac{h\Omega^2}{2}$	$\frac{2\Omega}{Q}$	$(1 - 4\Omega^2)$	0	0	0	$5\Omega^2$	$-4\Omega^2$	0	0
7	0	0	0	0	0	0	$(1 - 4\Omega^2)$	$\frac{2\Omega}{Q}$	0	$-4\Omega^2$	$5\Omega^2$	0	0
8	0	0	0	0	0	0	$\frac{2\Omega}{Q}$	$(1 - 4\Omega^2)$	$4\Omega^2$	0	0	$5\Omega^2$	0
9	0	0	0	0	0	$-4\Omega^2 \frac{2m}{M'}$	$5\Omega^2 \frac{2m}{M'}$	0	$-\frac{\Omega}{Q_m}$	$4\Omega^2$	$(\Omega_m^2 - 5\Omega^2)$	$-\frac{2\Omega}{Q_m}$	$\Omega_m^2 u$
10	0	0	0	0	$4\Omega^2 \frac{2m}{M'}$	0	0	$5\Omega^2 \frac{2m}{M'}$	$-4\Omega^2$	$-\frac{\Omega}{Q_m}$	$\frac{2\Omega}{Q_m}$	$(\Omega_m^2 - 5\Omega^2)$	$\Omega_m^2 v$
11	0	0	0	0	$5\Omega^2 \frac{2m}{M'}$	0	0	$4\Omega^2 \frac{2m}{M'}$	$(\Omega_m^2 - 5\Omega^2)$	$-\frac{2\Omega}{Q_m}$	$\frac{\Omega}{Q_m}$	$-4\Omega^2$	$\Omega_m^2 p$
12	0	0	0	0	0	$5\Omega^2 \frac{2m}{M'}$	$-4\Omega^2 \frac{2m}{M'}$	0	$\frac{2\Omega}{Q_m}$	$(\Omega_m^2 - 5\Omega^2)$	$4\Omega^2$	$\frac{\Omega}{Q_m}$	$\Omega_m^2 q$

be the determinant $\{\mathcal{D}\}$ with the first column replaced by the column of inhomogeneous parts. In addition, let $\{B_g\}$ be the determinant with the second column replaced by the inhomogeneous column. Then it follows by Cramer's rule that

$$A_g = \frac{\{A_g\}}{\{\mathcal{D}\}} \; ; \; B_g = \frac{\{B_g\}}{\{\mathcal{D}\}} \quad . \tag{65}$$

The amplitude of the 2Ω component of the gravitation mode of vibration will be denoted by $|a_g|$. Then

$$|a_g| = [A_g^2 + B_g^2]^{1/2} \quad . \tag{66}$$

A digital computer program was written (Appendix III) to solve the three determinants $\{\mathcal{D}\}$, $\{A_g\}$, and $\{B_g\}$, and to facilitate the other indicated calculations in (65) and (66). The program allows determination of $|a_g|$ for all rotational frequencies Ω and any combination of sensor parameters and disturbance motions. Moreover, specific gravitational gradient values may be introduced simultaneously with the external disturbances in order to obtain this combined effect on nonideal sensor behavior. In other words, noise cannot be expected to simply add to the gravity gradient signal in a linear manner. It is more likely that the noise plus gravitational effects will couple in a complex way to produce a resulting signal which differs considerably from the sum of the two effects taken separately. The program is designed to demonstrate this effect.

Although these results are specifically for a nonzero h (and all other nonideal effects are zero), they are really quite a bit more general.

Equation (52), for example, is of the same form if, instead of $h \neq 0$, there were sensor arm imperfections of the type $\epsilon_1 = \epsilon_3 = 0$ and $\epsilon_2 = -\epsilon_4$. In other words, the $h \neq 0$ results are also indicative of sensor behavior under a particular combination of errors among the arm natural frequencies. Hence, the results represent sensor response not only for an offset center of gravity, but also for other sensor imperfections of the same order of magnitude as indicated. The parameter h may be considered a general "asymmetry" coefficient which describes the sensor degree of departure from the "ideal" case.

VII. COMPUTER RESULTS

The result of the computer program will now be discussed. In the first case of interest, the sensor was excited with a gravitation gradient, assuming the sensor was ideal. The proper combination of input data is then Γ = a nonzero value, and h = 0. The result is shown in Fig. 8, where the values used for the other input parameters are listed. This result, with a sharp, clear resonance at $\Omega = 0.5$, is that expected for an ideal sensor. It was found that the gravity signal is unaltered by any arbitrary choice of p, q, u, or v (eq. (51)), indicating that no type of external disturbance can influence the gravity signal of an ideal sensor. This agrees with the previous results for an ideal sensor and those obtained in Ref. 1.

The following computer results all correspond to nonideal sensor behavior under applied external disturbances (in the absense of a gravity gradient). For these cases, h = nonzero values and $\Gamma = 0$. The type of disturbance considered first was a linear vibrational motion of the rotating platform, at the same frequency and phase as the rotation itself. The results for this type of disturbance were typical of many types of random translational disturbances of the platform shown in the following figures.

The computer results for nonideal sensor behavior under the application of the external linear disturbance are shown in Fig. 9. The amplitude of the resulting signal in the gravitational mode a_g is referred to as "noise" because it is purely a function of the disturbances and sensor imperfections. This signal in no way represents a gravitational gradient, since none was included for this case. The abscissa in Fig. 9 is rotational frequency, and the ordinate is the noise amplitude (at 2Ω), normalized to the magnitude of the disturbance vibration X_o. In other words, if the noise-to-disturbance ratio is 1.0, every micron of platform vibration is transmitted directly to produce 1 μ sensor arm displacement. Therefore, if the absolute value of arm displacement is to be known, the absolute value of the disturbance motion must be known. However, the

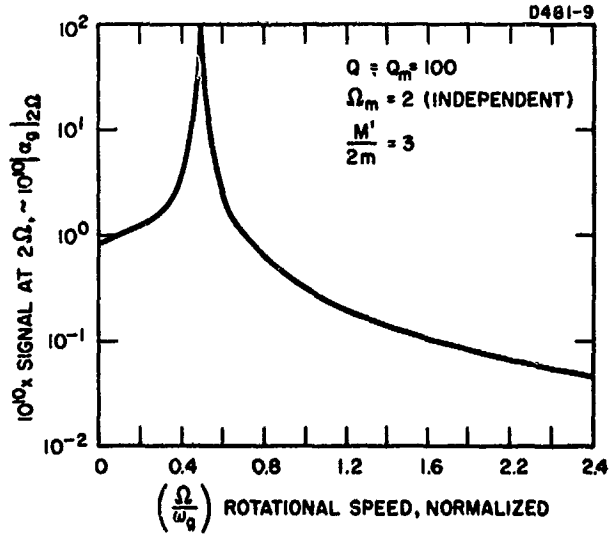

Fig. 8. 2Ω signal from a perfect sensor (regardless of any type of external disturbance). A plot of 10^{10} x actual signal for a $\Gamma/\omega_g^2 = 10^{-10}$ (for example, one earth gradient and ω_g = 100 cps).

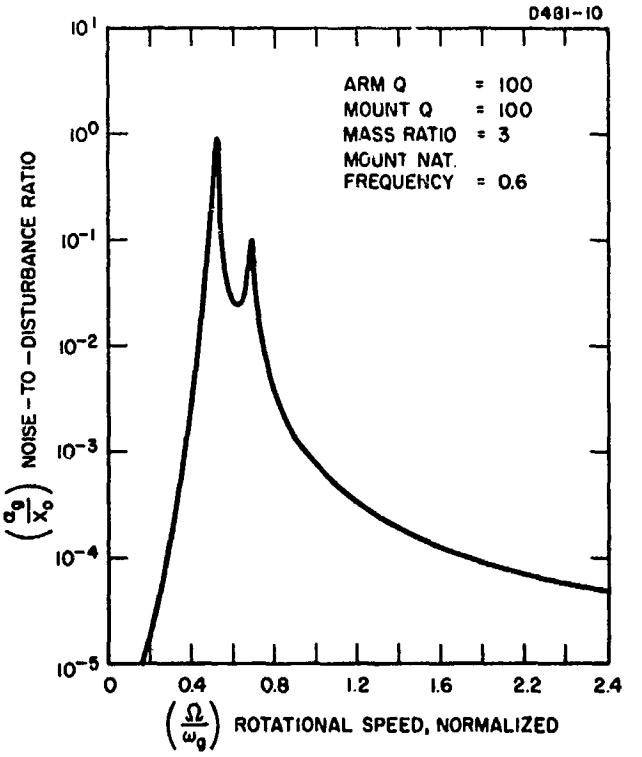

Fig. 9.
Noise in a 2Ω signal (gravitational mode) due to the disturbances at the mount of a sensor with 1% asymmetry (gravity absent). Disturbance consists of a translational vibration of the rotating platform, at the same frequency and phase as the rotation.

value of the ratio itself is important because it allows the study of sensor behavior over the range of values of the key sensor design parameters (such as Ω_m, h, etc.). The results may then be considered relative to any desired value of X_o. The curve in Fig. 9 shows two peaks. The largest peak is at $\Omega = 0.5$ and is associated with the sensor arm natural frequency. The second peak is at $\Omega = 0.66$, which is near the sensor-platform coupling (mount) natural frequency of 0.60.

Many curves such as that shown in Fig. 9 may be generated, each with a different value of some key sensor parameter (or different type of external disturbance). The dependence of sensor behavior on that parameter (or disturbance) may then be established. Figure 10, for example, is the sensor response under application of an elliptical motion of the rotating platform (at rotational frequency). The natural frequency of the mount for this case was taken as $\Omega_m = 0.3$. It is seen that a resonant peak now appears in the vicinity of $\Omega = 0.3$, while the major peak is still at $\Omega = 0.5$. An elliptical motion of the platform is also the basis of Fig. 11. Here, the mount frequency is $\Omega_m = 0.9$, and again a resonant peak is associated with the mount frequency as well as the gravitational mode. Figures 12 and 13 demonstrate sensor response to arbitrarily imposed platform disturbances. In other words, the platform is assumed to experience random vibrations in two dimensions. Figure 12 is for $\Omega_m = 1.0$, and Fig. 13 is for $\Omega_m = 2.0$. In these results, as many as four distinct resonant peaks can be observed. In addition to the gravitational mode resonance and mount resonance, other sensor vibrational modes (Appendix I) experience resonance. These particular results (Figs. 9 through 13) are typical of the vast variety of cases which may be examined with the aid of the computer program in Appendix III. Any combination of sensor parameters and external disturbances may be considered.

The final set of computer results is shown in Fig. 14. The original program was modified so that the gravitational mode response at gravity-sensing frequency ($\Omega/\omega_g = 0.5$) could be calculated directly.

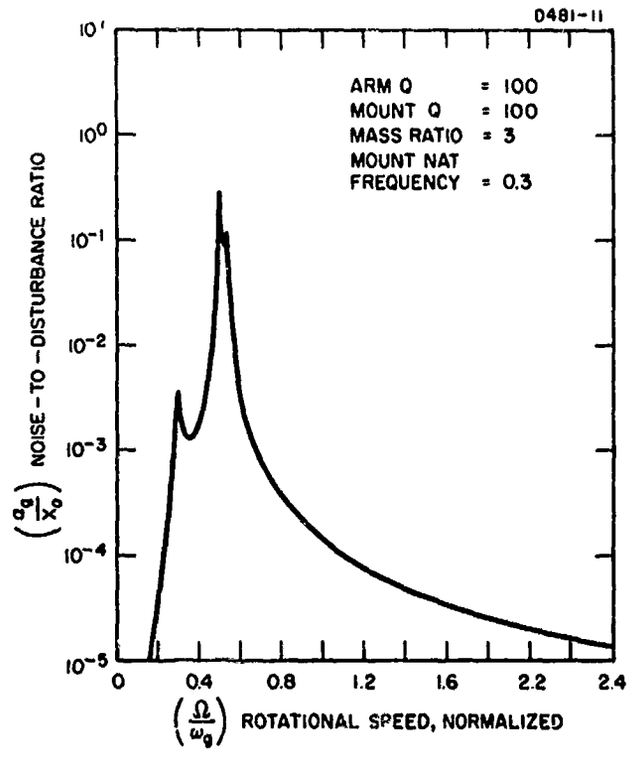

Fig. 10.
Noise in the 2Ω signal (gravitational mode) due to disturbances at the mount of a sensor with 1% asymmetry (gravity absent). Single frequency elliptic disturbance.

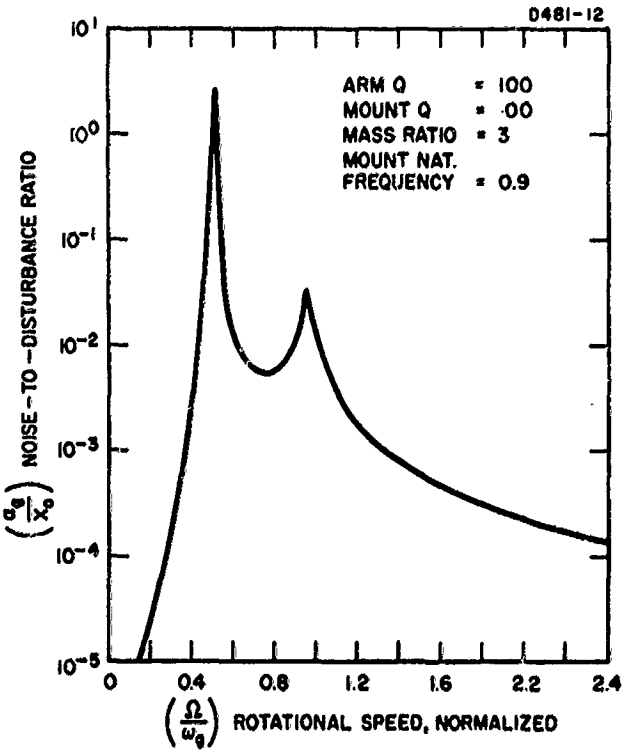

Fig. 11.
Noise in the 2Ω signal (gravitational mode) due to disturbances at the mount of a sensor with 1% asymmetry (gravity absent). Single frequency elliptic disturbance.

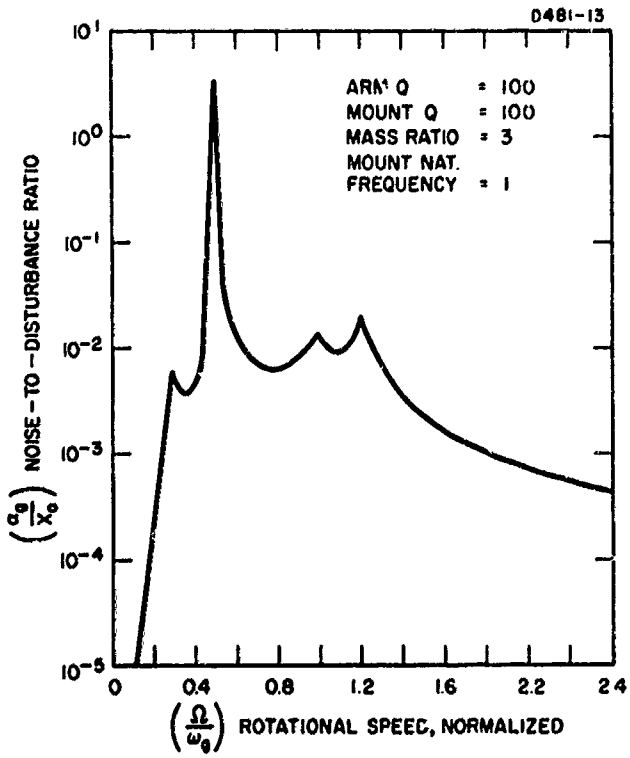

Fig. 12.
Noise in the 2Ω signal (gravitational mode) due to disturbances at the mount of a sensor with 1% asymmetry (gravity absent). Multiple frequency, complex random motion disturbance.

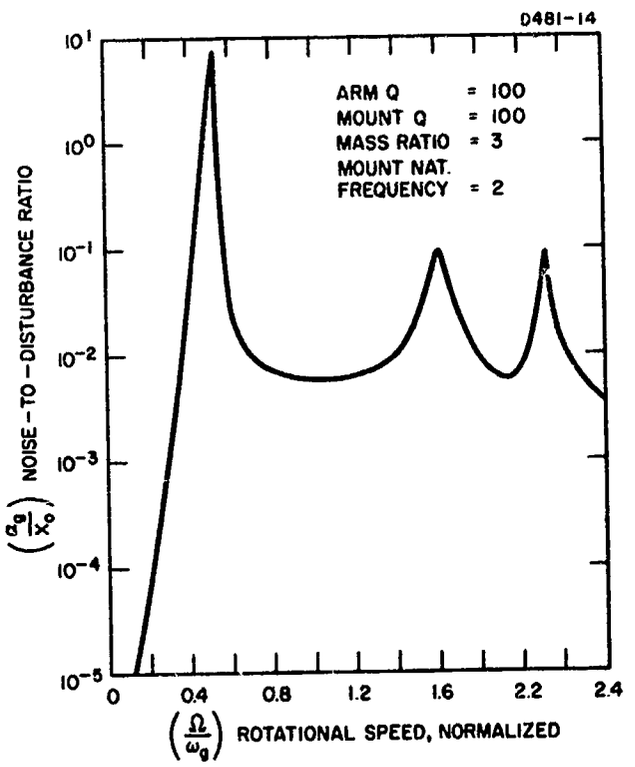

Fig. 13.
Noise in the 2Ω signal (gravitational mode) due to disturbances at the mount of a sensor with 1% asymmetry (gravity absent). Multiple frequency, complex random motion disturbance.

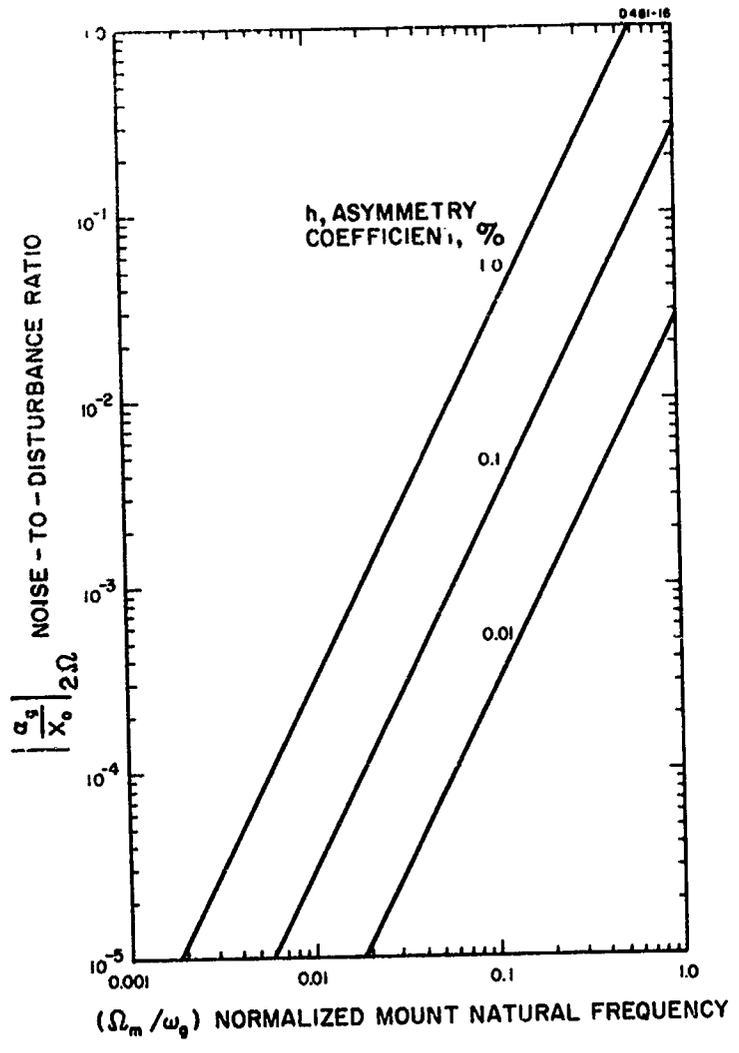

Fig. 14. Gravitational mode response (at gravity-sensing frequency) due to external disturbance of Ω negative circulation.

These results may be interpreted as a cross-plot of the $\Omega/\omega_g = 0.5$ peaks from such curves as those in Figs. 9 through 13.

This particular data display (Fig. 14) clearly shows the interaction of parameters affecting sensor response. Sensor-to-platform coupling is described by Ω_m (the mount natural frequency), and h is the sensor asymmetry coefficient (c.g. offset). The ordinate represents the noise-to-disturbance ratio for $\Omega = 0.5$ (i.e., the magnitude of noise at the gravity sensing rotational speed for any magnitude of disturbance). The external disturbance was taken to be a negative circulation at the same frequency as sensor rotation (i.e., Ω).

Figure 14 shows some dramatic results. When the mount natural frequency is reduced from 1.0 to 0.01, the noise reduction is four orders of magnitude. Further reduction in Ω_m could reduce the noise even more, as linear extrapolation of Fig. 14 demonstrates. Therefore, it is highly desirable to maintain the weakest possible coupling between sensor and driving platform, so that vibrations from the platform do not influence sensor response.

The effect of h on noise generation appears to be linear over the entire range of values studied. Each order-of-magnitude reduction in h resulted in a corresponding order-of-magnitude reduction in noise. The absolute value of h in actual sensor hardware is dependent on manufacturing precision.

VIII. CONCLUSION

In this paper we have analyzed (1) the disturbance of sensor vibrational modes, and (2) the design of the sensor in order to minimize the disturbance effect.

We have succeeded in developing the Lagrangian description of a rotating mass sensor and have calculated the noise level in the gravity-sensing signal for any given combination of external disturbance and sensor asymmetry.

We have shown that any translational disturbance may be considered as a combination of positive and negative circulations. The results indicated that positive circulation at Ω contributes nothing to sensor vibrational mode response, while negative circulation at Ω creates undesirable 2Ω driving forces. Positive circulation at 3Ω also contributes to 2Ω vibrational mode response.

It has also been suggested that inherent bearing vibrations at Ω belong to the Ω positive circulation class, and hence do not influence sensor behavior. It is thus expected that only those excitations which are external to the entire system pose potential interference problems.

If there are components in the disturbance which can influence vibrational mode response (as there are in linear, elliptical, etc., motions), the noise in the gravity-sensing mode can be diminished by

- Reducing the magnitude of the external disturbance
- Reducing the sensor-to-platform coupling
- Reducing manufacturing imperfections.

Figure 14 shows the effect of these three considerations on gravity-mode response to disturbance vibrations. It was shown that optimum sensor design could suppress the noise level by several orders of magnitude.

ACKNOWLEDGMENT

The author wishes to thank Dr. Robert L. Forward, under whose direction this work was conducted. Dr. Forward's contribution to gravitational science has established the principles on which this paper is based.

PRECEDING PAGE BLANK NOT FILMED.

APPENDIX I

SENSOR VIBRATIONAL MODES

The vibrational motion of the four sensor arms may be described in terms of four modes of oscillation. Each mode corresponds to a particular combination of amplitude and phase of the four arms. The existence of the vibrational modes was established in Ref. 1, along with mode behavior under ideal conditions. The following is the physical description of the four modes, as taken from Ref. 1.

The four primary modes of vibration are the gravity gradient sensing mode (Fig. I-1(a)):

$$a_g = \frac{1}{2}(a_1 - a_2 + a_3 - a_4) \quad ; \tag{I-1}$$

the torsional mode (see Fig. I-1(b)):

$$a_T = \frac{1}{2}(a_1 + a_2 + a_3 + a_4) \quad ; \tag{I-2}$$

and the two orthogonal translational modes (see Fig. I-1(c)):

$$a_+ = \frac{1}{\sqrt{2}}(a_1 - a_3) \tag{I-3}$$

$$a_- = \frac{1}{\sqrt{2}}(a_2 - a_4) \quad . \tag{I-4}$$

The two translational modes can also be expressed in terms of right and left hand circulating translational modes which are complex combinations of the orthogonal modes

PRECEDING PAGE BLANK NOT FILMED.

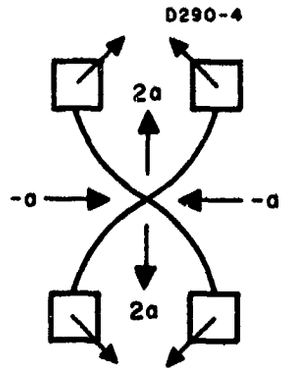

(a)

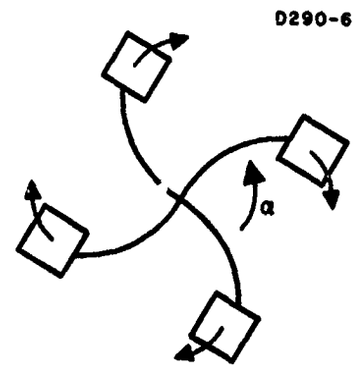

(b)

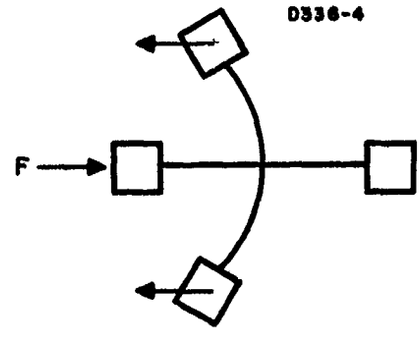

(c)

Fig. I-1. Operating mass sensor.

$$a_R = \frac{1}{\sqrt{2}}(a_+ + ia_-) = \frac{1}{2}(a_1 + ia_2 - a_3 - ia_4) \qquad \text{(I-5)}$$

$$a_L = \frac{1}{\sqrt{2}}(a_+ - ia_-) = \frac{1}{2}(a_1 - ia_2 - a_3 + ia_4) \qquad \text{(I-6)}$$

where the complex number i indicates a 90° phase lag in the response of the arm vibrating in that particular mode. This second form of the translational modes is used in the study of the mode behavior in a rotating system.

BLANK
PAGE

APPENDIX II

CALCULATION OF GRAVITATIONAL GRADIENT FORCES

The sensor forces created by a gravitational gradient were calculated in Ref. 2 and are outlined below.

If the sensor is rotating in the vicinity of a large mass, as shown in Fig. II-1, gravitational forces will exist between each mass of the sensor and the large mass, which has a magnitude

$$F_{gn} = \frac{g m_n \mathcal{m}}{R_n^2} \qquad \text{(II-1)}$$

where

F_{gn} ≡ total gravitational force for each sensor mass; n = (1, 2, 3, 4, and 6)

m_n ≡ mass of each sensor portion evaluated

$\mathcal{m}$ ≡ sensed mass

R_n ≡ distance between $\mathcal{m}$ and m_n

g ≡ universal gravitation constant $= 6.670 \times 10^{-8}$ (cm^2/g^2) dyne.

The portion of this force which acts upon the cantilever spring is the tangential portion which is evaluated for mass 1 as follows:

$$m_1 G_1 = - \frac{F_{g1} R \sin \theta_1}{R_1} \qquad \text{(II-2)}$$

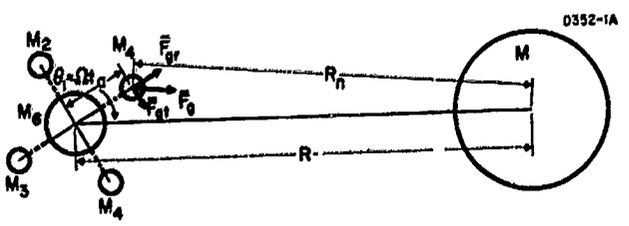

Fig. II-1. Operating mass sensor.

or a gravitational acceleration of

$$G_1 = - \frac{g\mathcal{M}R \sin \theta_1}{R_1^3} \quad . \tag{II-3}$$

Since any variation of the rotation speed from Ω due to gravitational forces will appear as a g^2 perturbation on the force, θ_1 can be approximated by Ωt. ($\Omega \equiv$ rotational angular velocity.) Therefore,

$$G_1 \approx - \frac{g\mathcal{M}R \sin \Omega t}{R_1^3} \tag{II-4}$$

where

$$\left(\frac{1}{R_1}\right)^3 = \frac{1}{(R^2 + a^2 - 2Ra \cos \Omega t)^{3/2}} \quad . \tag{II-5}$$

If (II-5) is now expanded binomially, the higher power sine and cosine terms may be replaced by their corresponding multiple angle identities. All terms of like frequency are then collected, and only the terms with the lowest power of a/R are kept in each frequency. Equation (II-4) becomes

$$G_1 = - \frac{g\mathcal{M}}{R^2}\left[\sin \Omega t + \frac{3}{2}\left(\frac{a}{R}\right)\sin 2\Omega t + \frac{15}{8}\left(\frac{a}{R}\right)^2 \sin 3\Omega t + \frac{35}{16}\left(\frac{a}{R}\right)^3 \sin 4\Omega t\right] \tag{II-6}$$

Similarly, for the other three arms:

$$G_2 = - \frac{g\mathcal{M}}{R^2}\left[\cos \Omega t - \frac{3}{2}\left(\frac{a}{R}\right)\sin 2\Omega t - \frac{15}{8}\left(\frac{a}{R}\right)^2 \cos 3\Omega t + \frac{35}{16}\left(\frac{a}{R}\right)^3 \sin 4\Omega t\right] \tag{II-7}$$

$$G_3 = -\frac{g\mathcal{M}}{R^2}\left[-\sin\Omega t + \frac{3}{2}\left(\frac{a}{R}\right)\sin 2\Omega t - \frac{15}{8}\left(\frac{a}{R}\right)^2 \sin 3\Omega t + \frac{35}{16}\left(\frac{a}{R}\right)^3 \sin 4\Omega t\right] \tag{II-8}$$

and

$$G_4 = -\frac{g\mathcal{M}}{R^2}\left[-\cos\Omega t - \frac{3}{2}\left(\frac{a}{R}\right)\sin 2\Omega t + \frac{15}{8}\left(\frac{a}{R}\right)^2 \cos 3\Omega t + \frac{35}{16}\left(\frac{a}{R}\right)^3 \sin 4\Omega t\right] . \tag{II-9}$$

APPENDIX III

COMPUTER PROGRAM

We present here the digital computer program used to solve the 12-by-12 determinant and to perform the other calculations indicated in Section VII. It is recalled that the solution to the six differential equations of sensor motion was presented in determinant form. In the following computer program,* the input data and corresponding statement numbers are as follows:

Statement Number			
180	Q	=	sensor arm inverse damping coefficient
190	Q_m	=	damping coefficient for sensor translational motion
200	$\frac{M'}{2m}$	=	sensor-to-arm mass ratio
210	Ω_m	=	natural frequency of sensor translation (normalized to ω_g)
220	Γ	=	gravitation gradient being sensed (normalized to ω_g^2)
230	p	=	external disturbances (normalized to arm length, a)
240	q		
250	u		
260	v		
170	h	=	linear distance between center of mass and center of geometry of sensor (normalized to arm length, a)
310	Ω	=	sensor rotational frequency (normalized to ω_g).

*Programmed by C. R. Buckey, Hughes Research Laboratories.

```
100   LET  N=12
110   DIM  A(12, 12), B(12), V(12)
120   FØR  I=I TØ 12
130   FØR  J=1 TØ 12
140   LET  A(I, J)=0
150   NEXT J
160   NEXT I
170   LET  H=.01
180   LET  Q1=100
190   LET  Q2= 100
200   LET  M1= 1/3
210   LET  Ø1 =.6
220   LET  G=0
230   LET  A1=1
240   LET  A2 =0
250   LET  B1=0
260   LET  B2=-1
270   PRINT "Q=";Q1;"Q0=";Q2;"M RATIØ=";M1
280   PRINT "ØMEGA0=";Ø1;"G=";G;"A10=";A1
290   PRINT "A20=";A2;"B10=";B1;"B20=";B2
300   PRINT "H=";H
310   FØR  Ø=.1 TØ 3 STEP .1
315   FØR  I=1 TØ 12
316   FØR  K=1 TØ 12
317   LET  A(I, K)=0
318   NEXT K
319   NEXT I
320   LET  W1=1-(4*Ø*Ø)
330   LET  W2 =2*Ø/Q1
340   LET  W3=H*Ø*Ø
350   LET  W4=Ø*Ø
360   LET  W5=Ø/Q2
370   LET  W6=Ø1*Ø1-5*W4
380   FØR  I=1 TØ 8
390   LET  A(I, I)=W1
400   NEXT I
410   LET  A(1, 2)=-W2
420   LET  A(1, 5)=-W3
430   LET  A(2, 1)=W2
440   LET  A(2, 6)=-W3
450   LET  A(3, 4)=-W2
460   LET  A(3, 5)=W3
470   LET  A(4, 3)=W2
480   LET  A(4, 6)=W3
490   LET  A(5, 1)=-W3/2
500   LET  A(5, 3)=W3/2
```

```
510  LET A(5,6)=-W2
520  LET A(5,9)=5*W4
530  LET A(5,12)=4*W4
540  LET A(6,2)=-W3/2
550  LET A(6,4)=W3/2
560  LET A(6,5)=W2
570  LET A(6,10)=5*W4
580  LET A(6,11)=-4*W4
590  LET A(7,8)=-W2
600  LET A(7,10)=-4*W4
610  LET A(7,11)=5*W4
620  LET A(8,7)=W2
630  LET A(8,9)=4*W4
640  LET A(8,12)=5*W4
650  LET A(9,6)=-4*W4*M1
660  LET A(9,7)=5*W4*M1
670  LET A(9,9)=-W5
680  LET A(9,10)=4*W4
690  LET A(9,11)=W6
700  LET A(9,12)=-2*W5
710  LET A(10,5)=-A(9,6)
720  LET A(10,8)=5*W4*M1
730  LET A(10,9)=-4*W4
740  LET A(10,10)=-W5
750  LET A(10,11)=2*W5
760  LET A(10,12)=W6
770  LET A(11,5)=A(10,8)
780  LET A(11,8)=A(10,5)
790  LET A(11,9)=W6
800  LET A(11,10)=-2*W5
810  LET A(11,11)=W5
820  LET A(11,12)=-4*W4
830  LET A(12,6)=A(11,5)
840  LET A(12,7)=A(9,6)
850  LET A(12,9)=2*W5
860  LET A(12,10)=W6
870  LET A(12,11)=4*W4
880  LET A(12,12)=W5
890  FØR I=1 TØ 12
900  LET B(I)=0
910  NEXT I
920  LET B(1)=-G
930  LET B(9) = Ø1*Ø1*A2
940  LET B(10)=Ø1*Ø1*B2
950  LET B(11)=Ø1(Ø1*A1
960  LET B(12)=Ø1*Ø1*B1
970  FØR K=1 TØ N-1
980  LET L=K
990  FØR I=N TØ K+1 STEP -1
1000 LET S=ABS(A(K,K))
```

```
1010IF  ABS(AI, K))<=S THEN 1040
1020  LET S=A(I, K)
1030  LET L=I
1040  NEXT I
1050  LET V(K)=L
1060  IF L=K THEN 1120
1070  FØR I=K TØ N
1080  LET S=A(K, I)
1090  LET A(K, I)=A(L, I)
1100  LET A(L, I)=S
1110  NEXT I
1120  LET S=A(K, K)
1130  FØR I=N TØ K+1 STEP -1
1140  LET A(K, I)=A(K, I)/A(K, K)
1150  NEXT I
1160  FØR I=N TØ K+1 STEP -1
1170  FØR L=N TØ K+1 STEP -1
1180  LET A(I, L)=A(I, L)-A(I, K)*A(K, L)
1190  NEXT L
1200  NEXT I
1210  NEXT K
1280  LET K=1
1290  LET I=V(K)
1300  LET S=B(K)
1310  LET B(K)=B(I)
1320  LET B(I)=S
1330  LET B(K)=B(K)/A(K, K)
1340  IF K=N THEN 1410
1350  FØR I=N TØ K+1 STEP -1
1360  LET B(I)=B(I)-A(I, K)*B(K)
1370  NEXT I
1380  LET K=K+1
1390  IF K=N THEN 1330
1400  GØTØ 1290
1410  FØR I=N TØ 1 STEP -1
1420  LET K=N
1430  LET S=0
1440  IF K=I THEN 1480
1450  LET S=S+A(I, K)*B(K)
1460  LET K=K-1
1470  GØTØ 1440
1480  LET B(I)=B(I)-S
1490  NEXT I
1500  PRINT Ø;SQR(B(1)↑2+B(2)↑2)
1510  NEXT Ø
1520  END
```

Modification to get cross-plot of (a_g/X_o) versus Ω_m at constant $\Omega = 0.5$ (Fig. 14):

```
1510  NEXT Ø1
310   FØR 0 ← Ø1=0 TØ 1 STEP .05
265   LET Ø=.5
1500  PRINT Ø1; SQR(B(1)↑2+B(2)↑2)
295   PRINT "Ø=";Ø
```

REFERENCES

1. C. C. Bell, J. R. Morris, J. M. Richardson, and R. L. Forward, "Vibrational mode behavior of rotating gravitational gradient sensors," submitted to J. Spacecraft and Rockets, 1966.

2. C. C. Bell, R. L. Forward, and J. R. Morris, "Mass Detection by Means of Measuring Gravity Gradients," presented at AIAA Second Annual Meeting, San Francisco, 26-29 July 1965; also AIAA Paper No. 65-403.

3. K. R. Symon, Mechanics (Addison-Wesley Publishing Co., Reading, Mass., 1957).

4. R. A. Becker, Introduction to Theoretical Mechanics (McGraw-Hill, New York, 1954).

5. R. V. Churchill, Complex Variables and Applications (McGraw-Hill, New York, 1960).

6. I. S. Sokolnikoff and R. M. Redheffer, Mathematics of Physics and Engineering (McGraw-Hill, New York, 1958).

7. L. A. Pipes, Matrix Methods for Engineering (Prentice-Hall, Englewood Cliffs, New Jersey, 1963).

PRECEDING PAGE BLANK NOT FILMED.